SPIM

Thèse de Doctorat

école doctorale **sciences pour l'ingénieur et microtechniques**

UNIVERSITÉ DE FRANCHE-COMTÉ

Development and metrological characterization of a high-performance Cs cell atomic clock based on coherent population trapping

■ Moustafa ABDEL HAFIZ

SPIM

Thèse de Doctorat

école doctorale **sciences pour l'ingénieur et microtechniques**

UNIVERSITÉ DE FRANCHE-COMTÉ

N° X X X

THÈSE présentée par

MOUSTAFA ABDEL HAFIZ

pour obtenir le

Grade de Docteur de
l'Université de Bourgogne Franche-Comté

Spécialité : **Sciences pour l'ingénieur**

Development and metrological characterization of a high-performance Cs cell atomic clock based on coherent population trapping

Soutenue publiquement le 01 juin 2017 devant le Jury composé de :

JAKOB REICHEL	Rapporteur	Professeur des Universités
THOMAS ZANON-WILLETTE	Rapporteur	Maître de Conférences
CHRISTOPH AFFOLDERBACH	Examinateur	Chercheur
NOËL DIMARCQ	Examinateur	Directeur de Recherche CNRS
GAËLLE LUCAS-LECLIN	Examinatrice	Maître de Conférences
PHILIPP TREUTLEIN	Examinateur	Professeur
VINCENT GIORDANO	Directeur de thèse	Directeur de Recherche CNRS
RODOLPHE BOUDOT	Encadrant de thèse	Chargé de Recherche CNRS

Remerciements

Je remercie chaleureusement tous les membres du jury pour avoir examiné mes travaux avec intérêt, et d'avoir contribué à la correction et à l'amélioration de ce manuscrit. Je m'excuse auprès d'eux, et d'avance auprès du lecteur intéressé, pour la longueur de l'ouvrage. Pour ma défense, l'histoire de l'horloge CPT de FEMTO est longue à raconter et pleine de rebondissements.

Les travaux présentés dans ce manuscrit ont été financés par le Labex FIRST-TF et par la région Franche-Comté. Ils sont une brique d'un projet collaboratif réunissant les experts européens des horloges atomiques à cellule basés à l'INRIM, au LNE-SYRTE, à l'UNINE et enfin à FEMTO-ST, laboratoire d'accueil de ma thèse.

Je tiens en premier lieu à remercier énormément Rodolphe Boudot pour m'avoir encadré avec autant d'implication durant ma thèse. Il a tout simplement été le mentor idéal. A la fois bienveillant et exigeant, j'ai pu tout au long de mon séjour à FEMTO-ST compter sur une inépuisable source de bonne humeur, de motivation et de bons conseils. J'ai beaucoup appris auprès de lui sur le domaine du temps-fréquence et sur la vie de chercheur en général. Il s'est montré soucieux de mon épanouissement au sein du laboratoire et dans ma carrière future...
Bon, en vrai, ça a été un vrai calvaire de travailler plus de trois ans avec Rodolphe, de l'entendre sans cesse chanter des "chauuuuuuuud cacao..." ou d'émettre d'autres sons d'aliéné. J'ai été harcelé et humilié à longueur de temps tout simplement parce que j'ai besoin d'un petit peu plus de temps de sommeil que la moyenne. Désolé Rodolphe d'avoir passé mes week-ends à dormir, au lieu de profiter du soleil de la Franche-Comté et de finir mes nuits au labo !

Sinon, il me reste à remercier mes co-bureaux, Alexandre Didier (que j'ai entre autres indubitablement rétamé au ping-pong, ou c'était l'inverse peut-être ?), Eric Kroemer (j'ai du voir grâce à lui toutes les vidéos de chat qui existent sur le net), Maël Souidi (toujours fatigué et incohérent les lundis de la semaine, le reste du temps ça allait), Lucas Groult (merci de ne pas m'avoir noyé ou transpercé d'une flèche ou de m'avoir envoyé un rapace me crever les yeux la nuit merci merci...), et ma co-bureau à mi-temps Aryanne Kroemer, avec qui j'ai partagé d'agréables moments, des blagues pourries, mais aussi mes angoisses quand j'en avais, et un sacré paquet de choco princes.

Pour mon plus grand bonheur, je n'ai jamais été seul à travailler sur les "horloges en mousse", j'ai bénéficié notamment de l'aide précieuse de Pan Da sur les questions de synthèse micro-ondes et de son extrême sympathie, de l'infinie sagesse de Vincent Maurice (également Ze creator de blagues pourries) et de sa maîtrise du Python. J'ai eu l'immense joie de travailler également avec Jaroslav Rutkowski, Rémy Vicarini, Grégoire Coget et Michael Petersen.

Je remercie d'un bloc les nombreux collègues qui m'auront aidé à résoudre un problème durant ma thèse ou à passer la période douloureuse de la rédaction, en salle de manip', au détour d'un couloir ou encore en salle de pause, j'ai nommé : Jacques Millo, Clément Lacroûte, Yann Kersalé, Vincent Giordano (qui m'a accessoirement officiellement encadré), Enrico Rubiola, François Vernotte, Ahmed Bakir, Jean-Michel Friedt, Emile Carry, Marion Delehaye, Valérie Pétrini, Benoît Dubois, Serge Grop, Yannick Gruson... et les nombreux autres que j'ai eu la paresse de mentionner tellement la liste est longue.

Merci à mes camarades qui furent ou qui sont encore thésards (bon courage à eux) et dont la présence qui ont été un soutien permanent. Merci donc pour en nommer certains, à Baptiste Maréchal, Carolina Cardelas, Nesrine Belkadi, Lyes Djoumi, Mouloud Ourak, Jérémy Bon, Etienne Vaillant, Guillaume Wong, Nikolay Vorobiev, Christophe Fluhr.

Un grand merci à Cyrus Rocher et Philippe Abbé qui ont assuré à eux seuls la réalisation de quasi-toutes les cartes électoniques et les pièces mécaniques constituant les organes vitaux de l'horloge ! Merci à Fabienne Cornu et Sarah Djaouti d'avoir enduré tous les aléas des aspects administratifs avec bonne humeur.

J'ai eu l'occasion durant ma thèse d'approcher et d'échanger avec un grand nombre d'acteurs du temps-fréquence dans le monde, et je tiens à leur témoigner ma reconnaissance, notamment à Peter Yun, Stéphane Guérandel, Jean-Marie Danet, Denis Brazhnikov, Salvatore Micalizio, Claudio E. Calosso, et surtout un énorme merci à Emeric De Clercq d'avoir toujours répondu à mes interrogations les plus profondes avec une grande modestie et un humour tordant.

Je remercie enfin mes parents, ma soeur et mon frère, mes piliers depuis toujours.
Je remercie Hafsa ma moitié.

Résumé

Introduction Les horloges atomiques répondent à un besoin pour des systèmes nécessitant une référence de fréquence de grande stabilité pendant des durées que les oscillateurs mécaniques ou piézoélectriques ne peuvent maintenir. Les horloges atomiques micro-ondes sont composées d'un oscillateur généralement à quartz stabilisé en fréquence sur une référence atomique, qui est la fréquence de transition d'un atome vers un de ses états excités. Les horloges atomiques sont massivement utilisées dans l'industrie pour les applications de synchronisation des télécommunications et de navigation par satellite. La demande croissante de références de fréquence dans des domaines de plus en plus hétérogènes, et notamment dans les systèmes embarqués, a encouragé le développement d'horloges atomiques d'architecture et de principe de fonctionnement différents, donnant en plus des exigences sur les performances de l'horloge, des contraintes en termes de coût, de volume et de consommation d'énergie.
En particulier, le projet européen MClocks, financé par EURAMET et dirigé par S. Micalizio (INRIM), cadre de ma thèse, avait pour but de développer des horloges atomiques compactes visant des stabilités de l'ordre de quelques 10^{-13} à 1 s d'intégration, et de l'ordre de quelques 10^{-15} à 10^5 s d'intégration.

Contexte Le développement de l'horloge à piégeage cohérent de population (CPT) de haute performance présentée dans cet ouvrage a été initiée à FEMTO-ST en 2011, avec la thèse de mon prédécesseur Xiaochi Liu. L'objectif initial était de monter une horloge CPT comparable à l'horloge CPT du LNE-SYRTE (décrite dans ce manuscrit) à l'aide d'une architecture simplifiée utilisant une source laser unique modulée en fréquence au lieu de deux lasers asservis en phase. Mon prédécesseur X. Liu monta un premier prototype d'horloge CPT présentant de forts contrastes grâce à une architecture alliant un laser modulé en fréquence via un modulateur électro-optique d'intensité, et un schéma de pompage optimisé initialement proposé par le groupe de Happer, et nommé push-pull optical pumping (PPOP). Alors que la thèse de X. Liu s'est focalisée sur l'étude spectroscopique de l'horloge CPT, mes travaux se sont orientés vers la caractérisation métrologique poussée de l'horloge, et vers la poursuite de son développement en vue de l'amélioration de ses performances, en régime continu d'abord, puis en régime impulsionnel.

Stabilité court terme La stabilité court terme d'une horloge atomique CPT dépend généralement du rapport signal/largeur de la résonance et du niveau de bruit de photodétection à la fréquence de modulation. Ce sont deux fronts sur lesquels j'ai travaillé durant ma thèse. De forts contrastes de résonance CPT ont ainsi pu être obtenus en combinant l'utilisation d'un modulateur électro-optique d'intensité pour la génération de deux raies optiques quasi-pures et séparées de la fréquence hyperfine de l'état fondamental du Cs, et du schéma de pompage PPOP. Cette dernière technique permet de repomper les atomes piégés dans les sous-niveaux Zeeman extrêmes du spectre hyperfin du Cs, et ainsi de repeupler les sous-niveaux d'intérêt ($m = 0$), insensibles au champ magnétique au premier ordre. Une étude spectroscopique détaillée nous a permis de déterminer les paramètres expérimentaux (puissance optique, température de cellule, champ magnétique, point de fonctionnement du modulateur électro-optique) optimisant la résonance CPT. L'horloge CPT présente à ce jour une stabilité de fréquence de $2\ 10^{-13}\ \tau^{-1/2}$ pour des temps d'intégration allant jusqu'à la centaine de secondes. Ce niveau de stabilité est à notre connaissance la meilleure jamais atteinte par une horloge CPT, et se tient parmi les meilleures performances établies par les horloges atomiques à cellule en général.

Un budget de bruit de détection détaillé nous a permis d'identifier les limitations de la stabilité de fréquence à court terme comme étant le bruit d'intensité et de fréquence laser (AM-FM, puis dans une moindre mesure AM-AM et FM-AM).

Stabilité moyen/long terme La stabilité moyen/long terme d'une horloge atomique CPT est limitée par les fluctuations des paramètres expérimentaux agissant sur les niveaux d'énergie des états atomiques. Nous avons tout particulièrement mesuré l'effet des variations du champ magnétique statique, de la température de cellule, de la puissance et de la fréquence laser, ainsi que d'autres paramètres pertinents, sur la fréquence d'horloge. A partir de ces niveaux de sensibilité d'horloge, et des mesures de fluctuations typiques des paramètres expérimentaux, nous en avons déduit une estimation de la contribution de ces différents paramètres à la stabilité moyen terme de la fréquence d'horloge. Cette étude nous a permis de dégager les deux facteurs limitants principaux de l'horloge CPT: la puissance laser et, dans une moindre mesure, la température de cellule.
Plusieurs solutions ont été étudiées pour surmonter ces limites, comme :

- l'utilisation d'une cellule de Cs contenant un mélange de gaz tampon présentant un ratio optimisé annulant la dépendance de la fréquence d'horloge à la température de cellule au premier ordre.
- la réduction des fluctuations de puissance laser via un système de stabilisation de puissance à deux niveaux.
- la réduction, voire l'annulation de la sensibilité de la fréquence d'horloge à ces variations de puissance laser par le choix de paramètres expérimentaux adaptés, ou via une interrogation CPT en lumière pulsée (Ramsey CPT).

La stabilité d'horloge atteint un palier flicker à $2\ 10^{-14}$.

Moyens expérimentaux utilisés Au fur et à mesure du développement de l'horloge, plusieurs ajustements furent à l'origine d'améliorations des performances de l'horloge en continu :

- la mise en place d'un étage supplémentaire d'isolation optique a permis de réduire les effets de retour lumineux vers la diode laser sur le bruit de fréquence de ce dernier.
- la mise en place d'un système de stabilisation de la fréquence laser basé sur une technique originale de spectroscopie sub-Doppler mettant en jeu simultanément les deux raies CPT a permis de limiter les déplacements d'horloge dus aux fluctuations de la fréquence laser.
- la mise en place d'un système de stabilisation de puissance laser pour limiter les effets de déplacement lumineux de puissance.

Interrogation Ramsey-CPT Le choix de l'utilisation du régime impulsionnel a été motivé par le fait que, en régime continu, la largeur de résonance CPT croît avec la puissance laser, dégradant de ce fait la stabilité de l'horloge pour les fortes puissances. En régime impulsionnel, la largeur des franges de Ramsey ne dépend que du temps noir, période séparant deux impulsions lumineuses, autorisant alors à priori de travailler avec des fortes intensités laser et obtenir de signaux de forte amplitude sans conséquence sur la largeur des franges. De plus, la discontinuité de l'interaction de la lumière avec les atomes permet de réduire la sensibilité de la fréquence d'horloge aux variations de l'intensité lumineuse. Dans notre cas, nous avons observé une réduction de cette sensibilité d'un facteur 25 par rapport au régime continu. Une stabilité à $2.3\ 10^{-13}\ \tau^{-1/2}$ jusqu'à 100 s d'intégration a été démontrée dans ce régime, d'un niveau comparable à ce qui avait été obtenu en régime continu. La principale limite à la stabilité court terme de l'horloge a été identifiée comme étant le bruit d'amplitude laser (AM-AM). Nous pensons que l'implémentation d'un asservissement de puissance laser fonctionnant dans le régime impulsionnel pourrait lever cette limitation induite par le bruit AM-AM.

Travaux annexes Cette thèse reporte aussi une étude expérimentale et théorique, menée en profondeur pour identifier les phénomènes physiques complexes mis en jeu dans la spectroscopie sub-Doppler bi-fréquence, mettant en avant la contribution significative d'états noirs CPT Zeeman et hyperfins, ainsi que d'effets de pompage optique. La plateforme constituée par l'horloge a été utilisée pour mener des tests de physique plus amont, incluant la caractérisation par spectroscopie CPT d'une cellule centimétrique de césium avec un revêtement anti-relaxant OTS (octadecyltrichlorosilane) en vue d'une utilisation dans des cellules micro-fabriquées développées à FEMTO-ST pour des horloges atomiques miniatures. Le temps de relaxation de la cohérence hyperfine fut mesuré à 0.5 ms, correspondant à un nombre de 12 rebonds des atomes contre les parois de cellule avant relaxation.

Conclusions Les performances de l'horloge CPT sont en accord avec les spécifications du projet MClocks concernant la stabilité de fréquence court terme, mais la stabilité moyen terme demeure encore à être améliorée. Néanmoins, il a été démontré durant ma thèse que l'architecture proposée pourrait légitimement répondre au besoin de références atomiques compactes et haute performance naissant dans l'industrie des télécommunications et de la navigation. Plusieurs pistes restent à explorer dans le futur, impliquant une meilleure compréhension des effets de puissance laser dans les horloges CPT ainsi que des déplacements collisionnels dus à la présence de gaz tampon.

Contents

Introduction

The advent of quantum mechanics [1] in the beginning of the 20th century has revolutionized our knowledge of matter and nature at small scales and energies. Quantum mechanics differs from classical physics in that objects can be considered as waves and particles (wave-particle duality), their energy and momentum being discretized, and that precision with which quantities can be known is limited by the uncertainty principle. From this approach arose the well-known Bohr's relation stipulating that an atom being on an energy level E_1 can be transferred to a higher excited state E_2 by absorbing the energy of an incident exciting electromagnetic field such that $E_2 - E_1 = h\nu$ with h the Planck's constant and ν the wave frequency. The same atom, relaxing to the lowest state energy level, will re-emit spontaneously a photon with frequency ν.

In time and frequency metrology, this principle has been exploited for the development of atomic clocks consisting to stabilize the frequency of a local oscillator onto a well-defined atomic transition frequency. With the progress of microwaves technology during the second World War, the first Cs beam clock was demonstrated in 1955 in NPL by Essen and Parry [2]. In 1967, the 13th General Conference of Weights and Measures redefined the second as "the duration of 9 192 631 770 periods of the radiation corresponding to the transition between two hyperfine levels of the ground state of the ^{133}Cs atom (at rest and in a null magnetic field)."

In the fifties, the discovery of optical pumping [3] by Alfred Kastler has introduced the possibility to manipulate and spin-polarize atoms with coherent pumping light, respecting well-defined quantum selection rules. This technique has allowed to initiate light spectroscopy and to explore energy levels of a wide variety of atoms or molecules. During the next decades, outstanding progress in laser science and technology, offering narrow, tunable and highly coherent light sources with increased reliability, power and now modest cost [4], has allowed to perform exciting atomic physics experiments by resolving features in atomic and molecular spectra with an unprecedented resolution and accuracy. Laser spectroscopy has later paved the way towards tremendous and remarkable developments such as the demonstration of laser cooling and trapping techniques [5–7], the realization of Bose-Einstein condensation in alkali gases [8–10], the development of ultra-stable cavity-stabilized lasers [11] using Pound-Drever-Hall techniques [12] or the emergence of femtosecond lasers allowing to construct a bridge between optical or microwave frequencies [13]. All these breakthrough systems and technologies have contributed greatly to increase our knowledge about light-matter interaction and to prove fundamental aspects of quantum mechanics.

In time and frequency metrology, these remarkable progress have conducted over the last decade to the demonstration of optical atomic frequency standards with exceptional frequency stabilities in the range of a few $10^{-16}\ \tau^{-1/2}$ and accuracies flirting the 10^{-18} level [14–18]. These impressive performances make today the second the physical unit defined by far with the best precision and make such clocks, that can even now be compared over long-distance fiber links [19, 20], exquisite tools to perform exciting fundamental physics tests, geodesy [21] or time-frequency comparisons.

Besides these exceptional performances, the transfer and valorization of atomic clocks for industrial applications has always been a challenging objective due to their complexity, volume, power consumption and cost. Yet, there exists without any doubt a wide variety of applications, including satellite-based navigation systems, network synchronization, secure data communications, oil exploration, defense systems, which require field-deployable atomic clocks combining excellent fractional frequency stability, low power consumption and small size.

In this domain, microwave vapor cell atomic clocks have become attractive candidates. In particular, well-known lamp-based microwave Rb vapor cell atomic clocks based on the optical-microwave double resonance technique have been widely used for decades, including for space applications [22, 23]. The advent of high-performance narrow-line semiconductor diode lasers has later allowed to improve the stability performances of these clocks by at least one order of magnitude. In recent years, relevant efforts have been pursued in different laboratories, especially in Europe, to push to limit the performances of vapor cell clocks by adopting original interrogation schemes including mainly pulsed optical pumping (POP) and coherent population trapping (CPT), often associated with a pulsed Ramsey scheme. These efforts have led to the demonstration of ultra-compact vapor cell clocks demonstrating short-term fractional frequency stability as low as a few $10^{-13}\ \tau^{-1/2}$ [24–26].
Stimulated by these promising laboratory-prototypes has started in 2013 an ambitious European project, named Mclocks [27], funded by EURAMET and led by S. Micalizio (INRIM). The main objective of this project, combining expertise and experience of main vapor cell clocks makers in Europe, was to pursue the development of three types of high-performance vapor cell microwave clocks matching the upcoming demanding requirements of industrial and technical applications.
The first clock was a pulsed optically pumped (POP) Rb clock, with a targeted fractional frequency stability of a few 10^{-13} at 1 s and in the 10^{-15} range at 10^5 s. The second one was a vapor cell clock based on cold atoms (Rubiclock [28]) targeting performances comparable to that of the POP Rb clock in the short term but with better long-term performance and an accuracy within an order of magnitude of that of primary standards. The third clock technology, heart of my thesis, proposed to investigate the potential of an alternative vapor cell clock based on CPT. Coherent population trapping involves complex atom-field interaction phenomena whose rigorous explanation requires the quantum mechanics formalism. The CPT phenomenon, discovered by Gozzini and Alzetta [29] in Pisa in 1976, occurs by connecting two ground-state energy levels of an atomic specie to a common excited state using two phase-coherent optical fields frequency-split by the atomic ground state hyperfine frequency. Atoms are then trapped through a destructive quantum interference process in a particular coherent superposition of both ground states, named dark state, modifying significantly the atomic vapor response and absorption. This two-photon transition process allows to detect in an "all-optical" way atomic resonances greatly narrower than the natural linewidth of optical transitions, making this phenomenon interesting for the development of compact and high-stability atomic clocks.

In the Mclocks project, the objective was to study the possibility of realizing a simple-architecture CPT-based clock, with high potential for compacity and providing short-term performances competitive with the clocks described above. The development of two CPT clocks was engaged in a collaborative partnership. The first CPT clock, based on a recently proposed novel double-modulation technique, was implemented at LNE-SYRTE, Paris. The second CPT clock, based on a technique named push-pull optical pumping (PPOP), has been developed in FEMTO-ST and was the main objective of my PhD thesis.
My PhD thesis has conducted to the development, optimization and metrological characterization of a high-performance and simple-architecture CPT-based Cs vapor cell atomic clock. This clock combines basically a distributed-feedback (DFB) diode laser, a pigtailed electro-optic modulator for optical sidebands generation, an acousto-optic modulator, a Michelson delay-line and polarization orthogonalizer system, a Cs vapor cell and electronics. While absolutely no frequency measurements had been performed at starting date of my work, my PhD thesis ended with the demonstration of a CPT clock with a short-term fractional frequency stability at the level of $2\ 10^{-13}\ \tau^{-1/2}$ up to 100 s averaging time, ranking among best vapor cell frequency standards.

Chapter 1 of this manuscript reminds the basic principle of atomic clocks, their applications and describes metrological tools used to characterize performances of frequency references. An overview on compact atomic clocks, including commercial and laboratory-prototype devices, is reported to fix the context of my work.
Chapter 2 describes basics of CPT physics and dresses an overview of optimized CPT pumping schemes used to maximize the number of atoms onto the clock transition in high-performance CPT frequency

standards.
Chapter 3 reports an in-depth description and characterization of the clock experimental setup.
Chapter 4 reports metrological characterization and fractional frequency stability performances of the CPT clock operating in the continuous-wave (CW) regime. A detailed short-term and mid-term noise budget is reported.
In Chapter 5, the clock setup is studied and tested using a Ramsey-like pulsed interrogation technique. Performances in this regime are compared to those obtained in the CW regime.
Chapter 6 describes auxiliary experiments performed using our CPT clock setup. This includes the characterization of an octadecyltrichlorosilane (OTS) wall-coated Cs vapor cell as well as an in-depth experimental and theoretical investigation on dual-frequency sub-Doppler spectroscopy in Cs vapor cells.

Chapter 1

Compact atomic clocks: applications, definitions, overview

In this chapter, I emphasize the need for atomic clocks and present the various applications they are involved in. I expose the basics of atomic clocks and define metrological tools used to characterize the performances of frequency standards, including mainly Allan deviation, phase noise and frequency noise power spectral densities. The basic expression defining the Allan deviation of an atomic clock is given. From this, the content of this manuscript focuses mainly on compact atomic clocks. An overview on different compact and high-performance atomic clocks, including Cs beam standards, passive hydrogen masers (PHM), Rb vapor cell clocks, clocks based on coherent population trapping and compact cold atom clocks, is reported. Commercially-available clocks and new-generation laboratory clock prototypes are separately presented. This overview allows me in the end of this chapter to introduce the context and main achievements of my thesis work.

1.1 Applications

Timekeeping issues have become inescapable in a wide range of nowadays applications. Exchanging data packets ever faster and without errors implies the clocks of a communicating network to keep synchronized more and more accurately. More generally, a multitude of industrial fields, including telecommunications, navigation, defense and space applications, require stable and reliable frequency standards. Atomic clocks are ideal candidates to assume this role. Indeed, unlike quartz crystal oscillators which are subject to drift in large time scales, atomic standards are able to keep a stable frequency over several months averaging time.

In particular, the field of telecommunications itself represents a huge market estimated at about 327 billion euros in 2010, pushed by an important demand for rapid data transfer via optical fibers and for wireless communications. The requirements include high-speed data, broadband transmission, high capacity to support an important number of simultaneous users, global mobility, scalable quality of service, and the service should be provided at low cost for operators and subscribers.

Atomic clocks are also key elements in positioning systems. The market revenue was estimated at around 9.8 billion dollars in 2013, and the number of GPS-enabled subscribers is expected to raise. In satellite-based global positioning system (GPS, GLONASS, GALILEO), the observable of interest is the delay between two events. The GPS receiver measures the difference between two dates: the arrival time of an electromagnetic wave packet incoming from a satellite, and the time of its emission, included in the signal data. The distance between the receiver and the satellite is given from the product of the measured time delay and the light velocity. Since the latter is a fundamental constant, the accuracy in the measurement of the distance satellite/receiver depends in principle only on the accuracy of the measured value of the delay. Actually, variations in optical index along the wave path and relastivistic effects have to be taken into account and corrected. A measurement of the wave traveling time between the receiver and at least 4 different satellites allows to determine the position of the receiver with high accuracy. The error in the obtained value highly depends on how well the satellites and the receptor are time-synchronized. A difference of one microsecond can lead to a positioning error of 300 m. Satellite navigation has opened opportunities to develop a large panel of new generation atomic clocks with particular attention paid to their system design, compacity, low complexity, high robustness and reliability. The full deployment of GALILEO (expected in 2020) will open three markets for high performance time and frequency products: the space segment requiring space-qualified devices to be placed onboard of satellites, the ground segment where accurate clocks synchronise the onboard clocks, and the market consisting of signal receivers for positioning and timing, which could be found in military systems, GPS receivers, unmanned aerial vehicles (UAVs), telecom networks and hand-held test and measurement devices.

One can find atomic clocks in several similar applications including very long baseline interferometry (VLBI) [30] for geodesy and astrometry purposes, where the observable is the delay between the reception of a signal from an extragalactic radio source between at two radio observatories at least. One can also enumerate undersea sensing for oil and gas deposits exploration [31]. They are also likely to be present in data transfer securing, including quantum cryptography [32, 33], or even more "fancy" applications such as secure commercial transactions. Indeed, the use of atomic clocks for synchronizing emission of multiple simultaneous commercial orders would prevent from abuses in high-frequency trading (HFT) [34, 35].

Atomic clocks also permit advances in the definition of physical quantities and rude testing of general laws of fundamental physics. The second is by far the system international (SI) base unit we know to realize with the highest accuracy. One smart effort would then be to try to define all other SI base units exclusively from the second using the Einstein equivalence principle, and the fundamental physical constants. In that way, the exactitude of the realization of the second would be reported to the other SI units. This reasoning led, for example, to the definition of the meter from the speed of light in 1983. Currently, only three of the seven SI base units remain independent: the second, the kilogramm, and the Kelvin.

On the contrary, advances in the accuracy of the second realization allowed the development of experiments setting ever lower upper bounds to an eventual drift of the fundamental constants, such as the fine structure constant [36], the gravitational constant [37, 38] or the proton-to-electron mass

ratio [39].
A lot of these applications would not have been made possible without the emergence of high-performance atomic clocks. Besides, the increased demand for highly stable timekeeping led to the study and development of new architectures of atomic clocks taking into account new constraints on their size, cost and power consumption, even at the expense of stability.
The MClocks project [27] was started in 2013 in this context, aiming the development of atomic clocks combining high stability performances and low size and power consumption to allow them to be suitable in a large field of industrial applications.

1.2 Atomic clocks

1.2.1 Basic principle

An atomic clock consists of three main blocks (see Fig. 1.1):

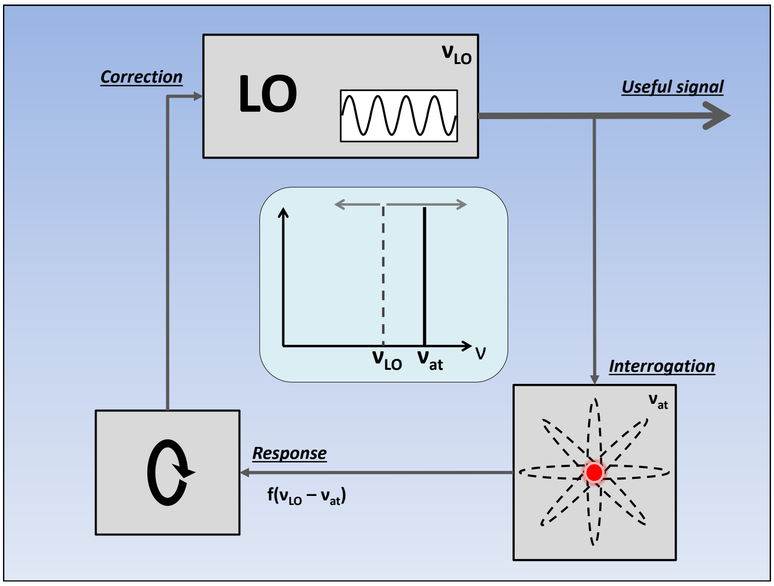

Figure 1.1: General operation principle of an atomic clock

- **A local oscillator** (LO) which delivers a signal oscillating at frequency ν_{LO}. The LO can be a frequency-multiplied quartz oscillator or a sapphire oscillator in microwave clocks, or a laser in optical clocks.

- **An atom or an atomic ensemble** which is "interrogated" by a fraction of the latter signal. It acts as a frequency reference. Indeed, we assume that an unperturbed atom, isolated from external perturbations like interaction with other particles or any static or dynamic field, presents well-defined energy states. Thus the transition frequencies between these states are well known and are the same for all atoms of the same kind, since they are all identical. The atomic "response" is a signal function of the frequency difference between the local oscillator output (at ν_{LO}) and the atomic transition (at ν_{at}).

- **A servo electronics** which collects and analyzes the atomic "response", and delivers a correction signal to the local oscillator, so that its transmitting frequency ν_{LO} is maintained on the atomic line.

1.2.2 Characterization tools

I will describe in this section relevant metrological tools characterizing the performances of atomic clocks in the time and frequency domain. We invite the reader to refer to abundant literature in this domain [40–44] for further information.

1.2.2.1 Generalities

The performances of a clock are mainly defined by two criteria: its accuracy and its fractional frequency stability (Allan deviation). According to [42], "accuracy is the extent to which a given measurement, or the average of a set of measurements for one sample, agrees with the definition of the quantity being measured. It is the degree of "correctness" of a quantity. Frequency standards have varying degrees of accuracy. The International System (SI) of units for time and frequency (second and Hz, respectively) are obtained in laboratories using very accurate frequency standards called primary standards. A primary standard operates at a frequency calculable in terms of the SI definition of the second: "the duration of 9,192,631,770 periods of the radiation corresponding to the transition between the two hyperfine levels of the ground state of the cesium atom 133"[45]." Due to the recent progress in the field of trapped atoms [15, 46–48] and ions [17, 49–51], and the very high accuracy and stability reached by optical clocks using this technique, a new definition of the second based on optical clocks seems relevant and is currently discussed [52]. "Reproducibility is the ability of a single frequency standard to produce the same frequency, without adjustment, each time it is put into operation. From the user's point of view, once a frequency standard is calibrated, reproducibility confers the same advantages as accuracy.

The stability describes the amount something changes as a function of parameters such as time, temperature, shock, and the like." Figure 1.2 illustrates the notions of accuracy and stability for a frequency source.

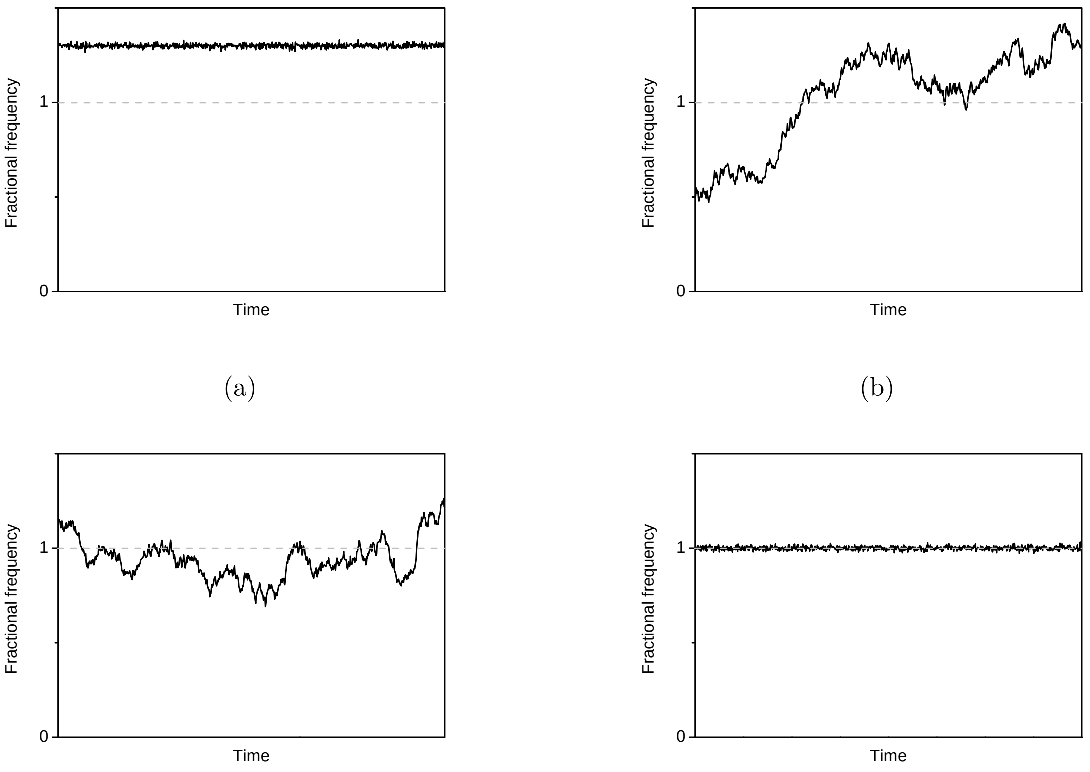

(a) (b)

(c) (d)

Figure 1.2: Stability and accuracy for a frequency source. (a) Stable but not accurate. (b) Neither stable nor accurate. (c) Not stable but accurate. (d) Stable and accurate. Here, the frequency standard is assumed to be defined as 1 in fractional.

In general, an oscillator output signal $V_{clock}(t)$ can be represented by:

$$V_{clock}(t) = V_0 \sin(2\pi\nu_0 t + \varphi(t)) \tag{1.1}$$

where V_0 is the signal amplitude, ν_0 its average frequency and $\varphi(t)$ corresponds to its phase fluctuations. We will assume V_0 to be a constant value, because the amplitude noise is generally negligible when compared to phase fluctuations.

An ideal oscillator would deliver a purely harmonic signal at frequency ν_0. In that case, $\varphi(t)$ would simply be a constant term that can be reduced to zero when applying the correct translation of the time axis. However, real clock signals differ from a pure sinusoid, because of the addition of unwanted noise that can be random, periodic or even monotonic (drifts). This divergence from the ideal case is evaluated in the time-dependent phase term $\varphi(t)$. The stability of a clock can be characterized either in the time domain or in the frequency domain.

1.2.2.2 Time domain

Let us define the instantaneous phase $\Phi(t)$ and the instantaneous frequency $\nu(t)$ as:

$$\Phi(t) = 2\pi\nu_0 t + \varphi(t) \tag{1.2}$$

$$\nu(t) = \frac{1}{2\pi}\frac{d\Phi(t)}{dt} = \nu_0 + \frac{1}{2\pi}\frac{d\varphi(t)}{dt} \tag{1.3}$$

The signal variations can be characterized either by the phase $\varphi(t)$ or by the frequency $\nu(t)$ fluctuations. We introduce now another quantity, the instantaneous fractional frequency fluctuations $y(t)$, that is more convenient to quantify the oscillator deviance from an ideal frequency reference and to compare it with other clocks, whatever their transmitting frequencies.

$$y(t) = \frac{\nu(t) - \nu_0}{\nu_0} = \frac{1}{2\pi\nu_0}\frac{d\varphi(t)}{dt} \tag{1.4}$$

The Allan variance $\sigma_y^2(\tau)$ is a mathematical quantity widely used to estimate a clock frequency stability in the time domain [41, 42, 53]. It is computed from a frequency data sample as following (see Fig. 1.3). Data are sliced into regular time intervals of length τ. $\overline{y}_k$ is the averaged value of the fractional frequency fluctuations $y(t)$ over the sample k.

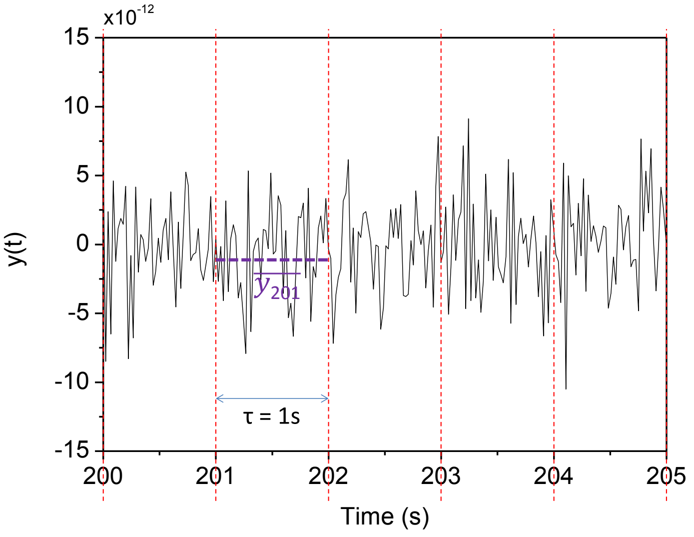

Figure 1.3: Example of frequency data sampling. y_k is the frequency averaged from time $k\tau$ to $(k+1)\tau$.

The Allan variance σ_y^2 is defined for an averaging time τ as:

$$\sigma_y^2(\tau) = \frac{1}{2}\langle(\overline{y}_{k+1} - \overline{y}_k)^2\rangle_k \tag{1.5}$$

where $\langle x \rangle_k$ means the mean of x over all the k samples.
The Allan deviation $\sigma_y(\tau)$ is generally represented in a log-log scale, and the line slope gives information on the noise mechanisms taking place, as shown in Fig. 1.4. It turns out to be a relevant quantity to compare the performances of different clocks, whatever their kind or transmission frequency.

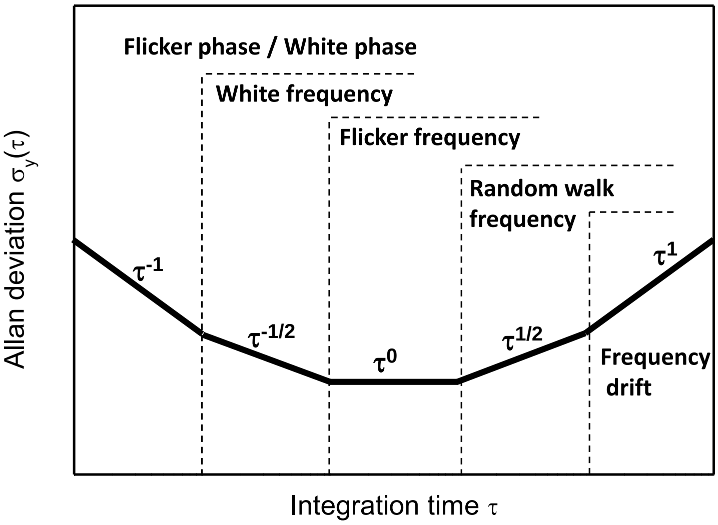

Figure 1.4: Allan deviation slopes in log-log scale for different noise mechanisms.

1.2.2.3 Frequency domain - link with the Allan variance

In the frequency domain, an evaluation of the clock stability is given by the power spectral density (PSD) of the fractional frequency fluctuations $S_y(f)$. This quantity represents the repartition of $y(t)$ in the Fourier frequency domain. $S_y(f)$ can be written as a power law such as:

$$S_y(f) = \sum_{\alpha=-2}^{+2} h_\alpha f^\alpha \tag{1.6}$$

The Allan variance can also be calculated knowing the frequency noise repartition in the frequency domain.

$$\sigma_y^2(\tau) = 2\int_0^{+\infty} S_y(f)\frac{sin^4(\pi\tau f)}{(\pi\tau f)^2}df \tag{1.7}$$

Using Eq. (1.6) in (1.7):

$$\sigma_y^2(\tau) = 2\int_0^{+\infty} \sum_{\alpha=-2}^{+2} h_\alpha f^\alpha \frac{sin^4(\pi\tau f)}{(\pi\tau f)^2}df \tag{1.8}$$

The quantity S_y of an oscillator signal can be experimentally obtained from the PSD of its phase fluctuations S_φ, measured by a signal source analyzer. The relationship between these spectral densities is [44]:

$$S_y(f) = \frac{f^2}{\nu_0^2} S_\varphi(f) \tag{1.9}$$

Table 1.1 resumes the relationships between S_y, S_φ and σ_y^2 for periodic signals dominated by the main kinds of noises.

Table 1.1: Different kinds of noises and their representative coefficients, exponents and their relationship in the Fourier frequency and in the time domains. f_h is the upper cut-off frequency, that has to be finite in the case of phase flicker and white noise (otherwise the integral in Eq. (1.8) diverges).

Noise mechanisms	$\mathbf{S_y(f)}$	$\mathbf{S_\varphi(f)}$	$\mathbf{S_y \leftrightarrow S_\varphi}$	$\sigma_{\mathbf{y}}^{\mathbf{2}}(\tau)$
Random walk frequency noise	$h_{-2}f^{-2}$	$b_{-4}f^{-4}$	$h_{-2} = \frac{b_{-4}}{\nu_0^2}$	$\frac{2}{3}\pi^2\tau\ h_{-2}$
Flicker frequency noise	$h_{-1}f^{-1}$	$b_{-3}f^{-3}$	$h_{-1} = \frac{b_{-3}}{\nu_0^2}$	$2\ln 2\ h_{-1}$
White frequency noise	h_0	$b_{-2}f^{-2}$	$h_0 = \frac{b_{-2}}{\nu_0^2}$	$\frac{1}{2\tau}\ h_0$
Flicker phase noise	$h_1 f$	$b_{-1}f^{-1}$	$h_1 = \frac{b_{-1}}{\nu_0^2}$	$\frac{1.038+3\ln(2\pi f_h\tau)}{4\pi^2\tau^2}\ h_{+1}$
White phase noise	$h_2 f^2$	b_0	$h_2 = \frac{b_0}{\nu_0^2}$	$\frac{3f_h}{4\pi^2\tau^2}h_{+2}$

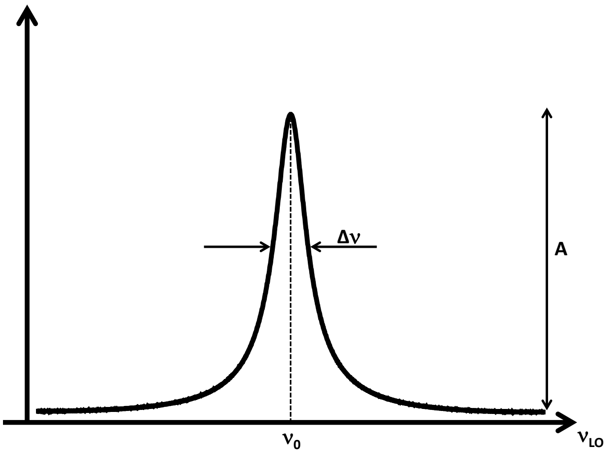

Figure 1.5: Typical clock resonance signal. A: amplitude of the signal. $\Delta\nu$: resonance linewidth. ν_0: carrier frequency.

1.2.2.4 Frequency stability of an atomic clock

The frequency noise for an atomic clock is generally a white noise for several decades of averaging time. The short-term fractional frequency stability of an atomic clock can be approximated by:

$$\sigma_y(\tau) \approx \frac{\Delta\nu}{\nu_0}\frac{1}{SNR}\tau^{-1/2} \approx \frac{1}{Q}\frac{1}{SNR}\tau^{-1/2} \tag{1.10}$$

where $\Delta\nu$ is the resonance linewidth, ν_0 its carrier frequency, $Q = \frac{\nu_0}{\Delta\nu}$ the resonator quality factor and SNR the measured signal-to-noise ratio in a 1 Hz bandwidth. Equation (1.10) reveals the general recipe to improve the short-term stability of an atomic clock: a high resonance amplitude, a narrow line, a high carrier frequency and a low noise level. Figure 1.5 illustrates the main characteristics of a resonance signal.

Atomic transitions frequencies are sensitive to environment, such as the surrounding static and dynamic electromagnetic fields or temperature. Indeed, the atomic levels suffer from frequency shifts which depend on the amplitude of the perturbation. As a consequence, atomic clocks frequency stability becomes limited by the impact of the experimental parameters at high averaging times. In section 2.1.3.3, I will expose and detail the effect of parameters with the highest contribution to vapor cell clocks stability.

1.3 High performance and compact atomic clocks

1.3.1 Introduction

There exists a wide variety of atomic clocks developed worldwide. In this manuscript, I will focus on so-called compact atomic clocks. These clocks, combining reduced volume and power consumption as well as an excellent frequency stability, are of great interest to be used in industrial applications. I will first present a non-exhaustive overview of commercially-available compact atomic clocks, including the Cs beam standard, the PHM and the Rb standard. These clocks are already used today in space applications, instrumentation, synchronization of telecommunications and in laboratory experiments. Then, I will report a few new-generation high-performance lab-prototype atomic clocks. In particular, I will describe double-resonance Rb clocks, atomic clocks based on coherent population trapping (CPT) and cold atom clocks. Note that many other types of compact atomic clocks are being developed. Among them can be cited the trapped atom clock on a chip (TACC) [54], CSACs [55–57], compact ion clocks [58–60] or transportable optical clocks[61]. Since their principles or applications fields are far different from my thesis subject, these technologies will not be described further in this manuscript.

1.3.2 Commercial clocks

1.3.2.1 The Cs beam standard

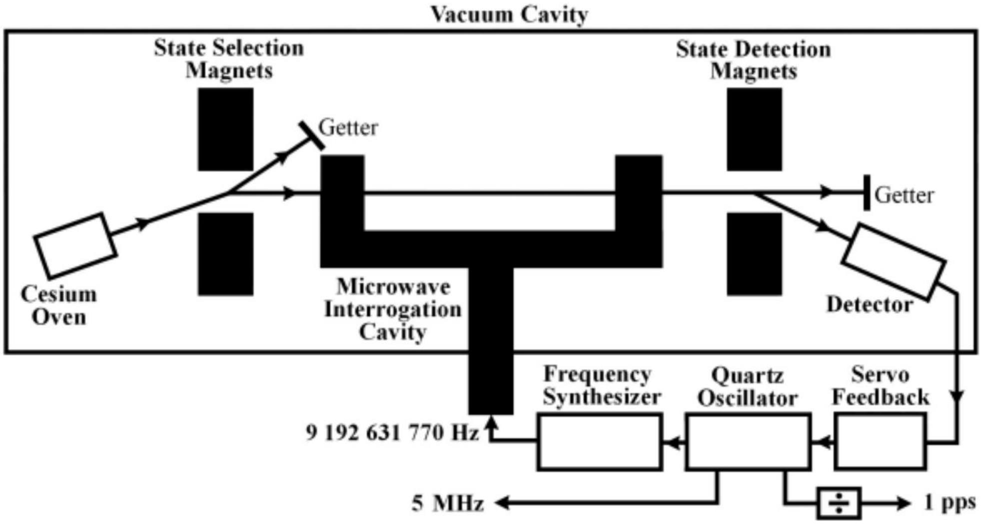

Figure 1.6: Simplified representation of a Cs beam standard. Extracted from [43].

A diagram of a Cs beam standard is shown in Fig. 1.6. The principle is sketched in Fig. 1.7. A beam of cesium atoms is produced in an oven. Commercial Cs beam standards [62, 63] currently use magnetic deflexion to separate the atomic populations of the ground states $|i\rangle$ and $|f\rangle$. After collimation, the beam crosses a first area with a magnetic field gradient. This splits the beam into two arms. Each arm contains cesium atoms in a specific ground energy level. After this state preparation, one of the arms (atoms in state $|i\rangle$) is selected and sent to a Ramsey cavity, where atoms experience twice a microwave interrogation field, separated by a free evolution area. If the microwave frequency is exactly tuned to the Cs hyperfine frequency, a maximum number of atoms transit to the upper ground level $|f\rangle$ after Ramsey interrogation. A second magnetic selection area is placed after the cavity and a detector is placed such that it detects the atoms that have transited to state $|f\rangle$

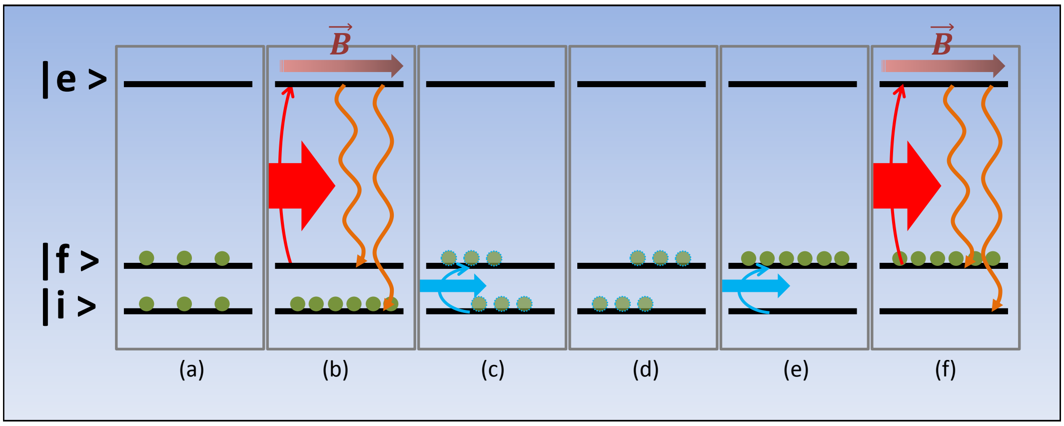

Figure 1.7: Atomic population during the different Ramsey scheme steps of a Cs beam standard. (a) At equilibrium the atoms are evenly distributed over the ground states. (b) Magnetic selection or optical pumping of atoms in state $|i\rangle$. (c) Microwave is switched on. Atoms are brought into a superposition of the ground states. (d) The microwave is switched off. The atoms evolve freely. (e) Second microwave pulse. At resonance, a maximum of atoms have transited to state $|f\rangle$. (f) Magnetic selection or optical detection of the atoms that changed energy level after crossing the Ramsey cavity.

after crossing the Ramsey cavity. The signal is maximum at resonance. Figure 1.8 shows a typical Ramsey spectrum observed with a Cs beam standard. For example, the high-performance version Cs standard from Microsemi (5071A) [63] exhibits a fractional frequency stability lower than $5\ 10^{-12}$ at 1 s averaging time and lower than $8.5\ 10^{-14}$ at 10 000 s averaging time. Note that Cs beam standards using optical pumping for selecting atoms in one of the ground states exist [64, 65], but there is no commercial version at the moment, due to the difficulty of procuring reliable laser diodes. In ref [66] was demonstrated at LNE- SYRTE a state-of-the-art Cs beam standard with optical pumping and detection showing a frequency stability of $3.5\ 10^{-13}\ \tau^{-1/2}$ until at least 10^5 s.

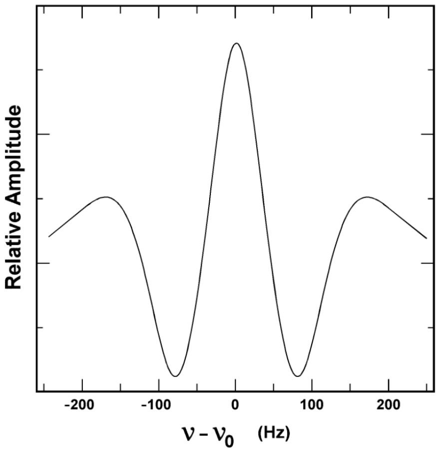

Figure 1.8: Typical Ramsey central fringe observed in a Cs beam standard. Extracted from [67].

1.3.2.2 The passive hydrogen maser (PHM) clock

In passive hydrogen masers [69–72] hydrogen vapor is sent through a magnetic selection stage that only selects H atoms in a specific ground state. These atoms enter a storage quartz bulb, included in a microwave resonant cavity. Some atoms experience spontaneous relaxation with emission of a wave oscillating at around 1.420 GHz. Stimulated emission and amplification of the signal occurs when the external signal is frequency-locked to the atomic transition. Figure 1.9 shows the operation principle of a an active hydrogen maser. The main difference between an active and a passive standard is

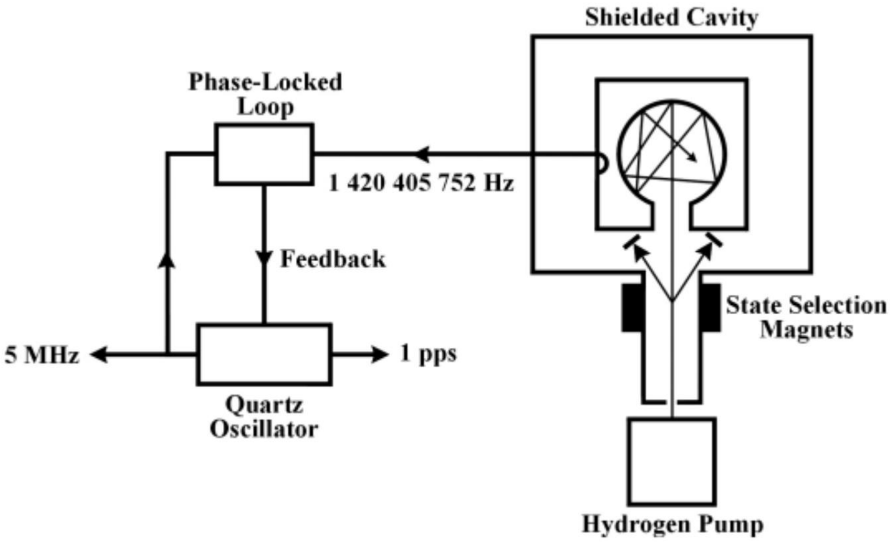

Figure 1.9: Diagram of an active hydrogen maser clock. The main difference with a PHM is that the clock signal is directly emitted by the atoms in an active standard, whereas it is an external signal in a PHM clock. Extracted from [68].

that in an active standard, the clock signal is directly emitted by the atoms. Figure 1.10 is a typical resonance obtained with a passive hydrogen maser.

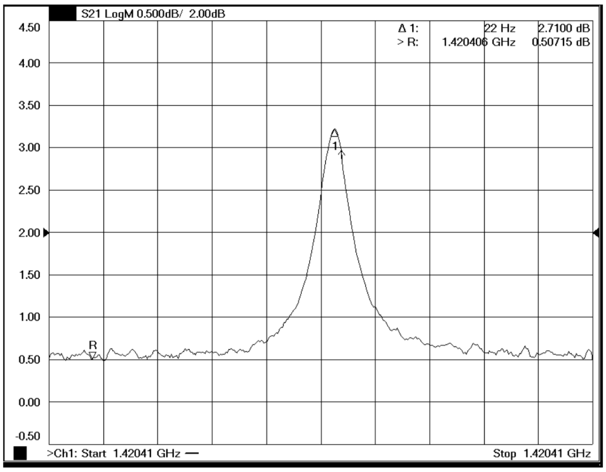

Figure 1.10: Typical resonance from a passive maser hydrogen clock. Extracted from [71].

The typical performances announced for the PHM from T4Science (pH Maser 1008) are 5 10^{-13} at 1 s averaging time and 4 10^{-15} at 1 d [70].

1.3.2.3 The rubidium frequency standard

The double resonance technique The optical-microwave double resonance technique involves a 3-level system. Let us denote $|i\rangle$ and $|f\rangle$ the ground levels of Rb, and $|e\rangle$ an excited state (see Fig. 1.11). In continuous regime, the microwave and optical fields are permanently on. The atoms are initially (before the fields are switched on) equally distributed in both ground states. The optical frequency links states $|f\rangle$ and $|e\rangle$. The light pumps the atoms in state $|i\rangle$, the specific ground state which does not interact with the optical field. After a while, in steady state conditions, the atomic population in state $|f\rangle$ is greatly depleted. Atomic absorption of the light is decreased. When the microwave frequency is at resonance, i.e. it is equal to the ground state splitting, state $|f\rangle$ is repopulated. Optical absorption is increased again at resonance. An error signal is generated by modulating the LO frequency around the microwave resonance and demodulating the detection signal.

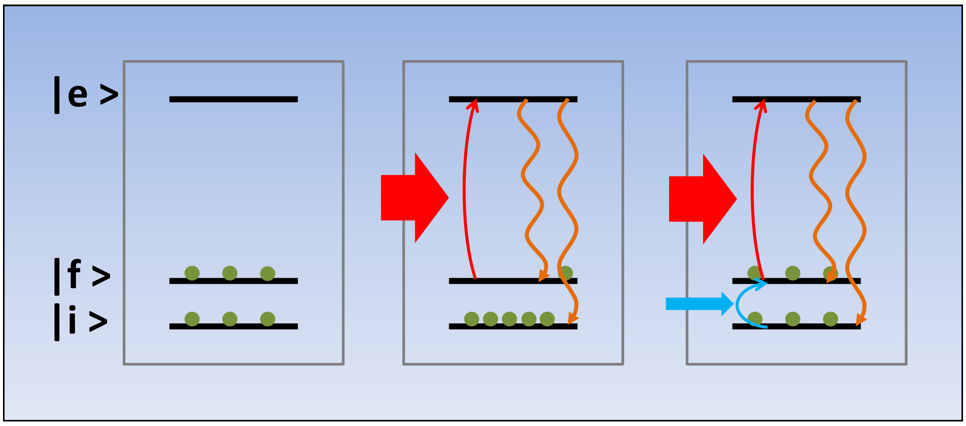

Figure 1.11: Principle of double resonance. Left: atomic ensemble at equilibrium. Fields are turned off. Center: the optical field is turned on. The microwave is absent or detuned from hyperfine resonance. Optical absorption is low. Right: both optical and microwave fields are on. Optical absorption is increased.

Rubidium atomic frequency standard (RAFS) A schema of the RAFS is shown in Fig. 1.12. In this compact and inexpensive atomic clock [22, 73–76], light is emitted from a Rb discharge lamp and crosses a first Rb cell, that acts like a narrow band filter. The filtered light crosses a second Rb cell and the transmitted power is measured with a photodiode. When the Rb vapor in the second cell is exposed to a field oscillating at exact hyperfine transition frequency (around 6.834 GHz for ^{87}Rb), the light transmission through the cell is decreased. The LO is then frequency-locked on the minimal transmission point. Figure 1.13 shows an example of resonance spectrum of a RAFS.

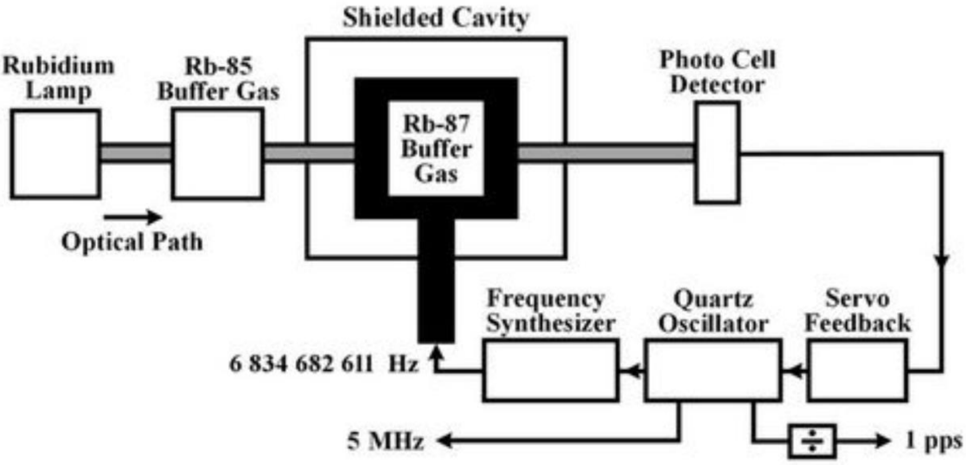

Figure 1.12: Diagram of a Rb standard. Extracted from [77]

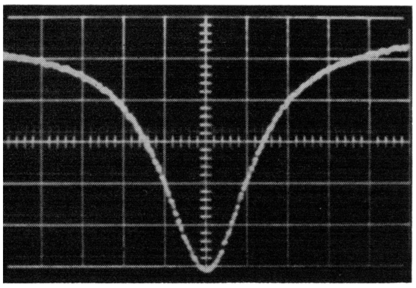

Figure 1.13: Example of resonance spectrum of a Rb atomic frequency standard. The larger abscissa divisions are three parts in 10^9. Extracted from [78].

The commercially-available RAFS from Microsemi (XPRO) [75] and from spectratime (LPFRS-01)

[76] show a fractional frequency stability of 10^{-11} at 1 s and lower than 3 10^{-11} at 1 month averaging time.

1.3.2.4 Overview on commercial compact atomic clocks

Table 1.2 summarizes the performances, power consumption and volume of compact commercial frequency standards described above. Comparing these clocks in terms of size or power consumption, Rb standards are much smaller than Cs beams or PHMs, and are also more energy efficient. However, in terms of stability performances, PHMs rank first, well ahead of Cs beams and RAFS.

Table 1.2: Characteristics of commercial atomic clocks. N.C.: non-communicated

Frequency standard	$\sigma_y(1\,\mathrm{s})$	$\sigma_y(10\,\mathrm{s})$	$\sigma_y(100\,\mathrm{s})$	$\sigma_y(10\,000\,\mathrm{s})$	σ_y (1 mth)	Power supply (W)	Volume (L)	Weight (kg)
Cs beam [62, 63]	5-12 10^{-12}	3.5-8.5 10^{-12}	8.5-27 10^{-13}	8.5-27 10^{-14}	10^{-14}	45 - 50	30	30
PHM [69, 72, 79]	5-20 10^{-13}	2-6 10^{-13}	5-20 10^{-14}	7-50 10^{-15}	N.C.	80-90	46-50	18-33
* Rb clock [75, 76]	10^{-11}	3 10^{-12}	10^{-12}	N.C.	1-4 10^{-11}	10	0.2-0.4	0.29

* Note that some space-qualified Rb clocks have been demonstrated to exhibit record stability performances up to 10^{-15} at 20 days averaging time [23, 73].

To date, there is a real need for new-generation industrial applications to develop high-performance atomic clocks with improved fractional frequency stability while keeping similar size and power consumption. Optical clocks are the most accurate and stable clocks available nowadays, but their development is still at the level of laboratory prototypes in terms of size, cost, power consumption and repeatability. Furthermore, their performances are far higher than the requested specifications in common telecommunication or navigation systems, and the latters are currently not well-adapted to optical frequencies yet. The H-maser is the leader in terms of mid-term and long-term stabilities, but it remains bulky, expensive and highly energy consuming.

A valid alternative is represented by vapor-cell clocks that have been studied and developed in several National Metrological Institutes (NMIs) and research laboratories. These clocks are attractive candidates because they combine compactness, reliability, low cost and power consumption, with frequency stabilities comparable to a H-maser. Over the last years, performances of these clocks have been greatly improved thanks to the use of advanced interrogation techniques and to the benefits of narrow-linewidth laser diodes. The following subsection describes their main representatives.

1.3.3 Lab prototype clocks

1.3.3.1 Double resonance clocks

In the following, I will distinguish Rb clocks operating in the continuous and in the pulsed regimes.

Continuous Rb double-resonance (DR) clock Today, to the best of our knowledge, the best CW Rb vapor cell clock developed worldwide is the Rb clock developed in Université de Neuchâtel (UNINE, Switzerland) [26, 80, 81]. Figure 1.14 shows the architecture of this clock.

The set-up combines a laser block, the physics package and a local oscillator. The laser is a distributed feedback (DFB) laser emitting at the Rb D_2 line (780 nm). It is frequency stabilized using an evacuated Rb cell. The core of the physics package consists of a Rb glass cell of 25 mm length and diameter. The cell contains a mixture of argon and nitrogen with pressure ratio $r(Ar/N_2) = 1.6$. The cell volume, which is crossed by the laser beam and microwave, is terminated by a stem that acts like a reservoir for metallic Rb. The cell is placed inside a compact magnetron-type microwave cavity with volume less than 45 cm^3. The latter resonates at the Rb clock transition frequency, at around 6.8 GHz. A static magnetic field is applied in order to split Zeeman transitions and isolate the clock transition. The ensemble is surrounded by a double-layer magnetic shield. The LO relies on an oven controlled crystal oscillator (OCXO) and on a microwave synthesis chain to generate the 6.835 GHz GHz signal for the interrogation stage. The working principle of the clock is the same as for RAFS (see subsection 1.3.2.3), except that the Rb discharge lamp is replaced by a laser diode.

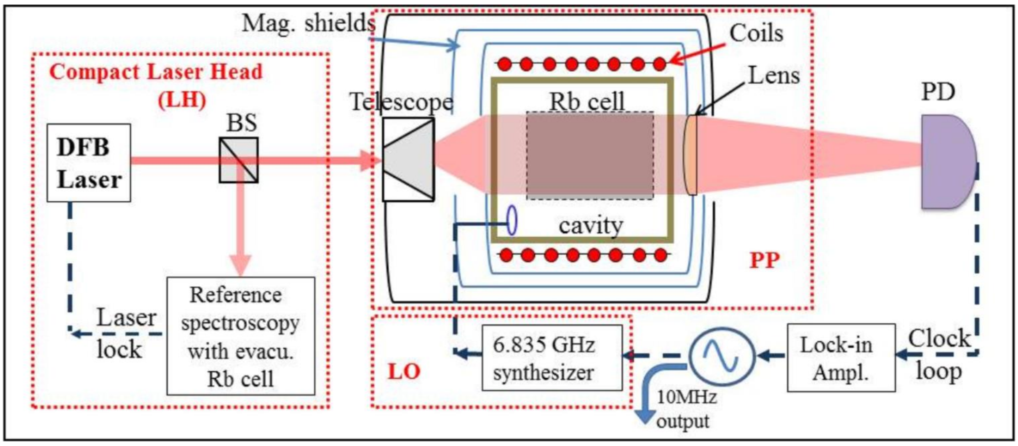

Figure 1.14: Schema of the POP clock set-up at UNINE. Extracted from [82].

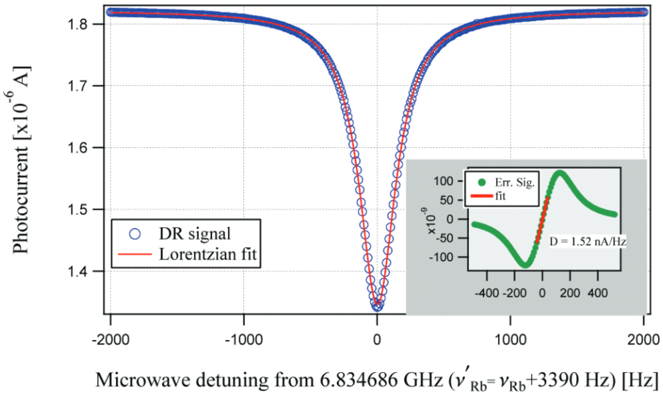

Figure 1.15: Typical spectroscopic signal achieved with the double resonance clock at UNINE. The amplitude is 0.48 µA, the background level is 1.82 µA, the contrast is 26 % and the linewidth 334 Hz. The inset shows the corresponding error signal exhibiting a discriminator slope close to zero microwave detuning of 1.52 nA/Hz. Extracted from [26].

Figure 1.15 shows a spectrum of the clock signal obtained in continuous regime. Figure 1.16 shows the demonstrated stability of UNINE DR clock to date. The clock short-term frequency stability is $1.4\ 10^{-13}\tau^{-1/2}$, while the shot noise limit is $4.9\ 10^{-14}\tau^{-1/2}$. The limitation is attributed by the authors to frequency modulation (FM)-to-amplitude modulation (AM) conversion of laser FM noise in the vapor cell. At longer averaging times, the measured stability is around $1.4\ 10^{-14}$ at 100 s and $5.5\ 10^{-14}$ at 10 000 s. The authors claim that the mid term limitation is due to temperature fluctuations of the vapor cell stem. The biparted geometry of the cell induces enhanced temperature sensitivity [83]. The authors anticipate the stability to reach levels below $1\ 10^{-14}$ if the stem volume is reduced and the physics package is under vacuum.

Rb pulsed optically pumped (POP) clock INRIM (Torino, Italy) has proposed the pulsed approach for a Rb clock. Instead of maintaining a continuous interaction with atoms, a Ramsey interrogation [84] is applied. One of the key properties of this scheme is that the mutual influence of laser and microwave signals is greatly reduced compared with a continuous approach: the clock transition takes place in the dark, when the pumping light is off and the coupling of laser fluctuations to the atomic frequency is negligible. The Ramsey interaction allows to obtain clock signal linewidth independent from the laser intensity and the microwave power. Additionally, the light shift is reduced in comparison with the classical double resonance continuous approach.

Firstly, INRIM investigated the approach in great detail with microwave detection [85]: the magnetization created in the atomic medium by the Ramsey pulses excites a microwave field that can be detected as a maser emission after the second pulse when the atoms are placed in a high-Q cavity. The

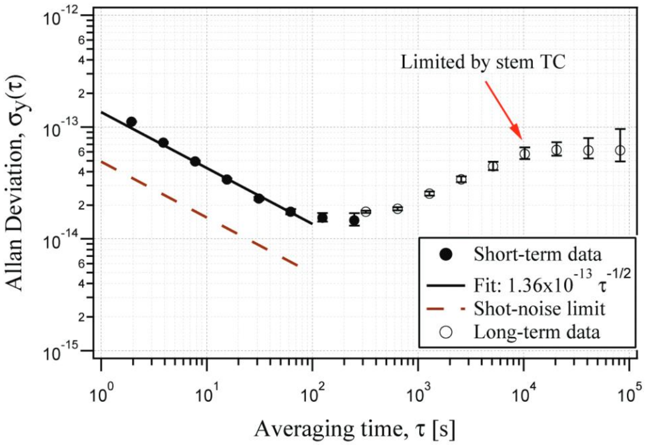

Figure 1.16: Allan deviation of the continuous double resonance Rb clock at UNINE. Legend is given in inset. Extracted from [26].

best performance of short-term frequency stability of this system is achieved at high laser intensity (10 mW/cm^2), and was measured to be 1.2 10^{-12} $\tau^{-1/2}$ after a drift removal of 6 10^{-14} per day. This performance is close to the thermal noise limited stability, which is 1 10^{-12} $\tau^{-1/2}$.
Later, S. Micalizio et al. at INRIM proposed a compact pulsed Rb vapor cell atomic clock prototype [24, 86] with optical detection. In this case, the atomic reference is observed on the laser absorption signal at the end of the cell. The laser is switched on during the detection window, but it is used as a probe. The interest in using optical detection is motivated by the fact that the signal-to-noise ratio is then shot-noise-limited, resulting in an improvement by more than an order of magnitude compared with the thermal noise that sets the ultimate stability limit of the passive maser approach. A higher signal-to-noise ratio of the signal can be detected, because energy of an optical photon is higher than energy of a microwave photon. Consequently, the short-term frequency stability can be improved. Moreover, the microwave cavity does not play a role in the detection and a high-Q cavity is no longer required. The mid-long frequency stability is also improved because cavity-pulling is negligible. A simplified representation of the experimental set-up is shown in Fig. 1.17.

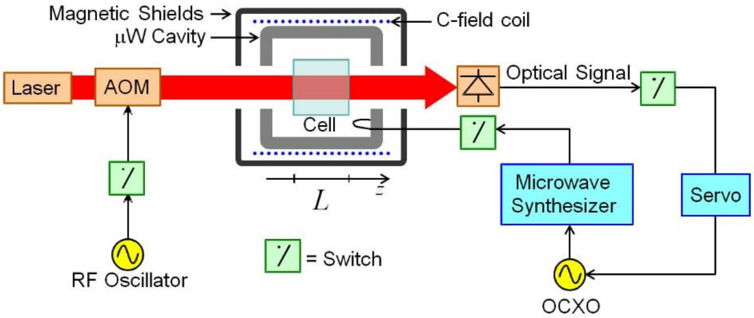

Figure 1.17: Schema of the POP clock set-up at INRIM. Extracted from [87].

The set-up is quite similar to the one at UNINE: it combines an optical part, a physics package and electronics. The physics package is organized in a layer structure. From the inner to the outer part of the package, one finds a buffer gas-filled Rb quartz cell, a microwave cavity, a solenoid, a first heater, a first magnetic shield, then a second heater and two other magnetic shields. The cell is 20 mm diameter and length, and presents two symmetrical stems. It is filled with ^{87}Rb vapor and a mixture of N_2 and Ar with a pressure ratio of 1.6 and a total pressure of 25 Torr. The cavity is made from molybdenum and resonates at the ground state hyperfine frequency for ^{87}Rb. The choice of the cell size has been a compromise between being small compared with the cavity volume to ensure homogeneity of the microwave field, and being large enough so that the number of atoms in the vapor is high. The laser diode is a 20 MHz-linewidth DFB laser emitting at the Rb D_2 line. It is stabilized via a saturated absorption set-up. The pulse sequence is generated with an acousto-optic modulator (AOM) that also

compensates for the buffer gas-induced optical frequency shift [88].
The operation principle of this clock is the same as described for the CW DR clock, except that the pumping, interrogation and detection steps are performed sequentially. The pulse sequence is shown in Fig. 1.18.

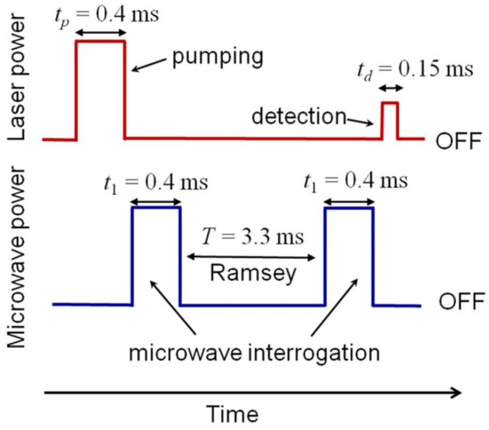

Figure 1.18: Representation of the pulse sequences in the POP clock with optical detection. Extracted from [24].

A first laser pulse of duration t_p is sent on the atoms in order to massively populate one of the clock ground levels. Any persistant microwave coherence is destroyed during this step, avoiding residual light shift. The laser is switched off. A sequence of two microwave pulses of duration t_1, separated by a free evolution time T where the fields are off, is then performed. A second laser pulse of width t_d is used to probe the atomic population in the lower level of the optical transition after microwave interrogation. When sweeping the LO frequency and detecting optical transmission, one can observe Ramsey fringes like shown in Fig. 1.19.

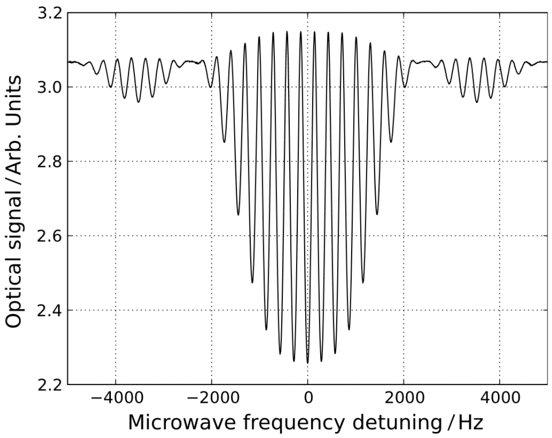

Figure 1.19: Typical Ramsey fringes obtained with the POP clock, with parameters $t_p = 0.44$ ms, $t_1 = 0.4$ ms, $T = 3.3$ ms and $t_d = 0.15$ ms. Extracted from [24].

Figure 1.20 shows the performances of INRIM POP clock. The measured short-term fractional frequency stability is 1.7 10^{-13} $\tau^{-1/2}$ until 1000 s averaging time. A small bump that the authors attribute to air conditioning appears at 200 s. The stability reaches the level of 6 10^{-15} after 2000 s averaging time. The short-term stability is limited by the laser phase noise converted into amplitude noise. This contribution could be strongly reduced according to the authors by using a 1 MHz linewidth laser and using a more stable current supply. The contribution from phase noise of the local oscillator is the second limitation and it can also be reduced with the use of recently developed frequency synthesizers [89, 90] and an optimized timing sequence. The mid- and long term stabilities are limited by temperature fluctuations and inhomogeneity in the vapor cell.
Although only the POP clock from INRIM has been described in this paragraph, there are other

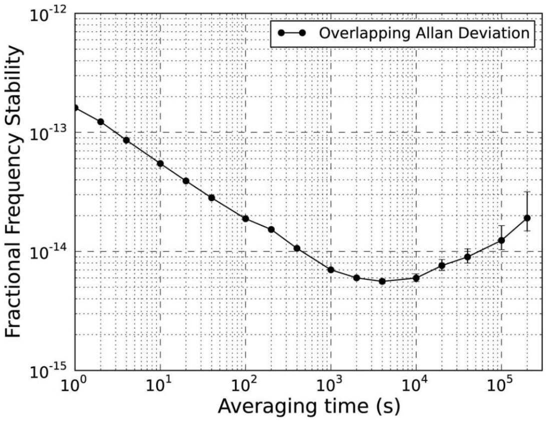

Figure 1.20: Allan deviation of the POP clock at INRIM. Extracted from [83].

pulsed Rb clocks developed, in particular at UNINE (Neuchâtel) [91] (yielding 2.1 10^{-13} at 1 s) and at SIOM (Shanghai) [92, 93] (demonstrating 3.5 10^{-13} at 1 s and 4.9 10^{-15} at 2000 s).

1.3.3.2 CPT clocks

One drawback of double resonance clocks is that they require a microwave cavity with particular design to ensure the vapor feels an homogenous electromagnetic field, hence limiting the set-up compacity. In CPT clocks, two laser fields, resonant with optical transitions sharing the same excited state, are sent through the atomic vapor. The microwave interrogating field is optically carried [94]. Thus, no microwave cavity is needed. When the laser frequency difference equals the lower states splitting, the atoms are pumped in a quantum superposition of these states, which is uncoupled from the light fields, yielding a decrease in atomic absorption. The CPT phenomenon will be detailed in section 2.1. In CPT clocks, main solutions to generate the optical lines required for CPT interaction are the use of a directly-modulated laser, the use of an externally-modulated laser or the use of two phase-locked lasers. In the following, I present a non-exhaustive state-of-the-art for CPT clocks operating in continuous and pulsed regimes.

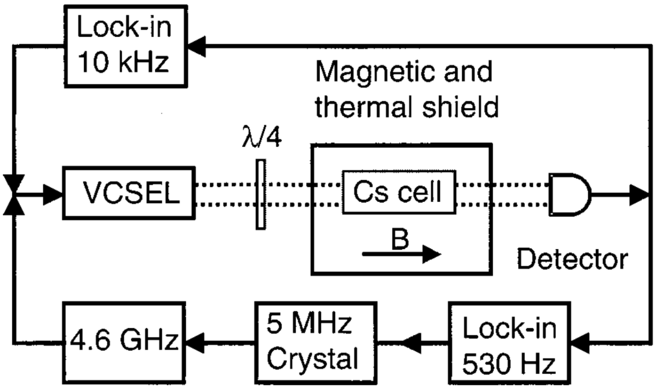

Figure 1.21: Architecture of a CPT clock with modulation of the VCSEL injection current. Extracted from [95].

CPT clocks in continuous regime Knappe et al. developped at NIST (Boulder) an ultra-compact CPT clock [95]. The interrogating optical field is produced by a VCSEL, emitting on the Cs D_2 line (852 nm) and frequency modulated by directly modulating its injection current. The clock architecture is shown in Fig. 1.21. The VCSEL injection current is modulated at half the Cs hyperfine frequency (4.596 GHz). The beam is circularly polarized using a quarter-wave plate and sent through a Cs cell filled with buffer gas. A photodiode detects the laser power transmitted through the cell. The photodiode signal is exploited in order to stabilize both the laser and the LO frequencies on the bottom of the absorption line and on the maximum of the CPT resonance, respectively. An example of CPT spectrum is shown in Fig. 1.22. Figure 1.23 shows the Allan deviation for this clock. The fractional frequency stability is of the order of $10^{-11}\ \tau^{-1/2}$ for about 100 s averaging time with a cell filled with Ne buffer gas only and for 1000 s with a cell filled with a Ne-Ar buffer gas mixture.

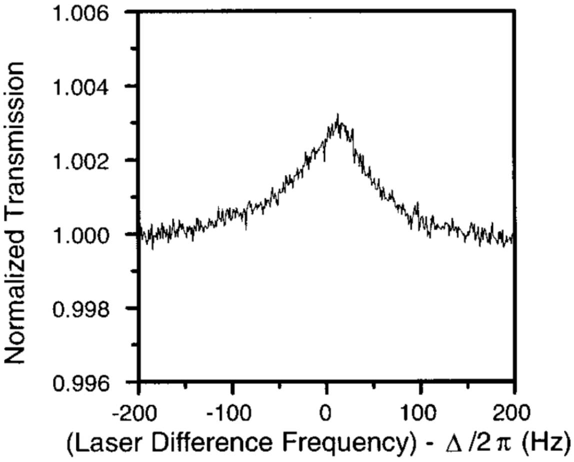

Figure 1.22: Example of spectrum of the dark resonance absorption signal. Extracted from [95].

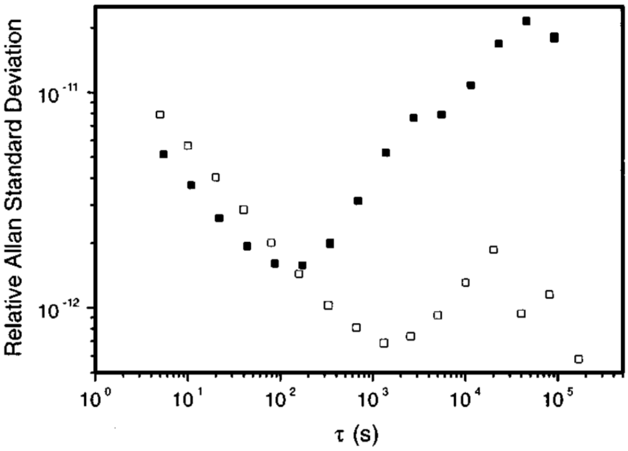

Figure 1.23: Allan deviation of the miniature CPT clock with a cell containing 9.7 kPa of Ne (filled squares) or 5.3 kPa of a Ne-Ar mixture (empty squares). Extracted from [95].

A wide variety of CPT clocks with simple architectures also exists. The reader can for example refer to [96] for a Rb CPT clock with Ne-Ar buffer gas showing a fractional frequency stability of $3.5\ 10^{-11}$ $\tau^{-1/2}$ until 2000 s averaging time, or to [97] for a Rb CPT clock with a cell coated with antirelaxation coating showing $2\ 10^{-11}\ \tau^{-1/2}$ until a few thousands of seconds averaging time. Over the last decade, the implementation of CPT, associated with micro-electro-mechanical systems (MEMS) and VCSEL laser technology, has allowed the advanced miniaturization of atomic clocks. These new-generation ultra-compact clocks can exhibit an Allan deviation of 10^{-11} at one day averaging time, while fitting in around 15 cm^3 and consuming about 150 mW. A wide competition exists in this domain [55, 56, 98–100] and even a commercial chip-scale atomic clock (CSAC) is available from Microsemi (CSAC SA.45s) [57]. Considering that CSAC is part of a different specific domain, I decided not to develop it further in the manuscript.

In the most common approach, atoms in CPT clocks interact with circularly polarized light. In this case, numerous atoms are lost in extreme Zeeman sublevels and do not participate to the clock transition. This leads to CPT resonances with poor contrasts. To circumvent this issue, different CPT optimized pumping schemes were proposed in the literature to maximize the number of atoms that participate to the clock transition. This aspect will be detailed in section 2.3. In that sense, a polarization-selective method was developed by M. Zhu for detecting a CPT resonance signal in a vapor cell [101]. The method uses a single laser beam with frequency modulation to induce CPT resonance and to control the laser power-induced shifts of the atomic energy levels. The method provides high CPT resonance contrasts.

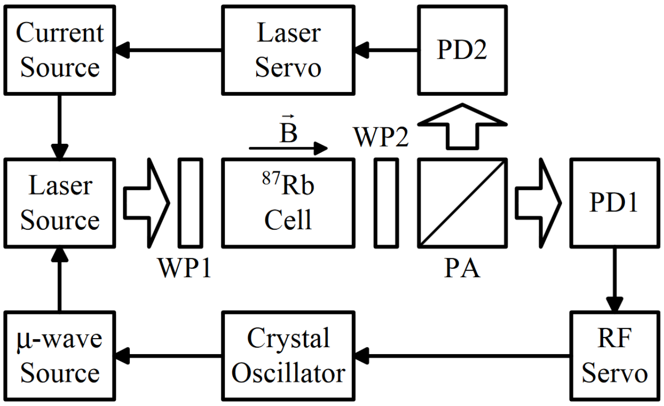

Figure 1.24: Block diagram of the polarization-selective CPT experiment set-up: PA is a polarization analyzer. WP1 and WP2 are two waveplates. PD 1 and PD2 are photo-detectors. Extracted from [101].

The set-up is shown in Fig. 1.24. A single diode laser is frequency modulated by coupling a microwave signal into the injection current. The ±1 order sidebands serve as the CPT generation and CPT detection frequencies while the higher order sidebands compensate for eventual laser power-induced shifts of the clock transition. The first waveplate (WP1) converts the linear polarization of the laser output beam to the desired elliptical polarization so that most of the power is in the σ^+ polarization for CPT generation. The second waveplate (WP2), which is a combination of three linear waveplates, converts the circular polarizations of the laser fields emerging from the absorption cell into the desired linear polarizations, and provides the necessary relative phase shift between the two orthogonal polarizations. The waveplate WP2 and the polarization analyzer (PA) are aligned so that the polarization analyzer blocks most of the power in the high-order modulation sidebands and the CPT resonance signal is symmetric. Figure 1.25 shows the detected CPT resonance with this setup. The linewidth is 218 Hz and the contrast is 22 %. As shown in Fig. 1.26, this CPT-based rubidium vapor cell frequency standard demonstrated a measured short-term stability of $1.4\ 10^{-12}\tau^{-1/2}$ up to 100 s averaging time.

The CPT clock with polarization modulation [102–104], developed very recently at LNE-SYRTE (Paris) in the frame of the MClocks project, aims to propose a simple set-up using an optimized polarization scheme. Only one laser is used and it is phase modulated to obtain both needed frequency components to perform CPT interaction. A novel pumping scheme inspired from M. Huang's and J. Camparo's work [105] is implemented and allows to increase the clock signal. The technique basically consists in slowly modulating the laser beam polarization and the LO microwave phase synchronously. The experimental set-up is shown in Fig. 1.27. A monochromatic beam is emitted by a DFB at the Cs D_1 line. It is frequency modulated via an electro-optic phase modulator (EOPM) at half the Cs ground hyperfine frequency (4.596 GHz). The first-order optical sidebands are separated by the hyperfine splitting and are used to perform CPT. One acousto-optic modulator (AOM1) is used to stabilize the light power, whereas another one (AOM2) compensates for the optical shift due to the presence of buffer gas in the CPT cell. A liquid crystal polarization rotator (LCPR) is used to control the beam polarization. The latter is synchronously modulated with the phase of the microwave driving the EOPM to produce the double modulation scheme. The beam is then expanded to 9 mm×16 mm section and crosses a 25 mm diameter and 50 mm length Cs vapor cell filled with 15 Torr of a N_2-Ar

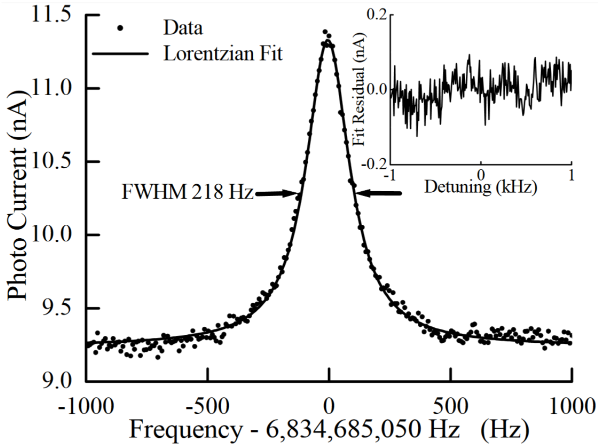

Figure 1.25: CPT resonance signal detected using the polarization-selective method. A Lorentzian line shape is fit to the experimental data. The fit residual is shown in inset. Extracted from [101].

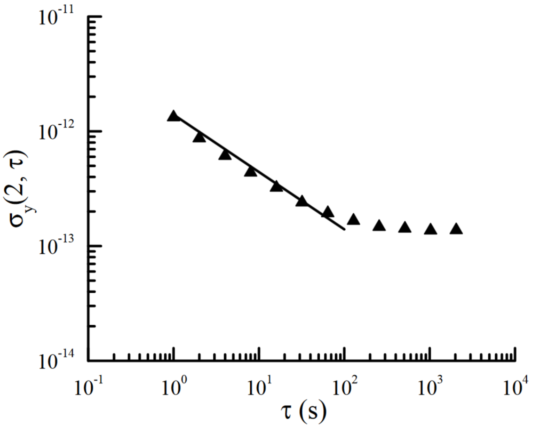

Figure 1.26: Allan deviation of the CPT-based Rb frequency standard using polarization-selective method. Black triangles are the measured Allan deviation. The solid line is 1.4 10^{-12} $\tau^{-1/2}$. Extracted from [101].

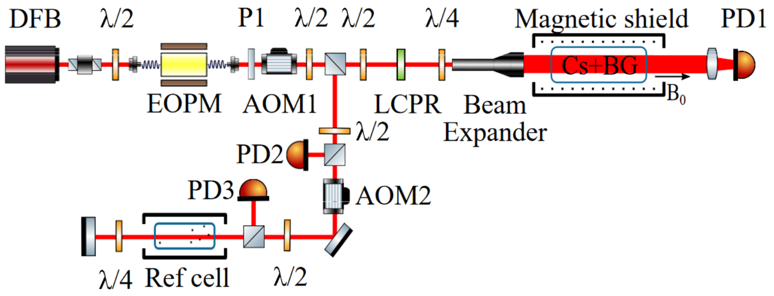

Figure 1.27: Architecture of the double modulation clock. Extracted from [102].

mixture. The cell is stabilized in temperature and a solenoid provides an axial magnetic field to set the quantization axis and to split the Zeeman sublevels. Two magnetic shielding layers prevent magnetic field fluctuations in the cell. The sequence used to perform the double modulation scheme is represented in Fig. 1.28. The microwave frequency is modulated at frequency $F_M = \frac{1}{t_{F_M}}$. The beam polarization is simultaneously modulated with the microwave phase at frequency $f_m = \frac{1}{t_m}$. The absorption signal is averaged over a time t_w at the end of each LO frequency step. The obtained CPT spectrum is shown in black in Fig. 1.29. This signal is synchronously demodulated at frequency F_M to get the error signal shown in red.

For a total incident laser power of 163 µW and a cell temperature of 35.1 °C, the CPT contrast is

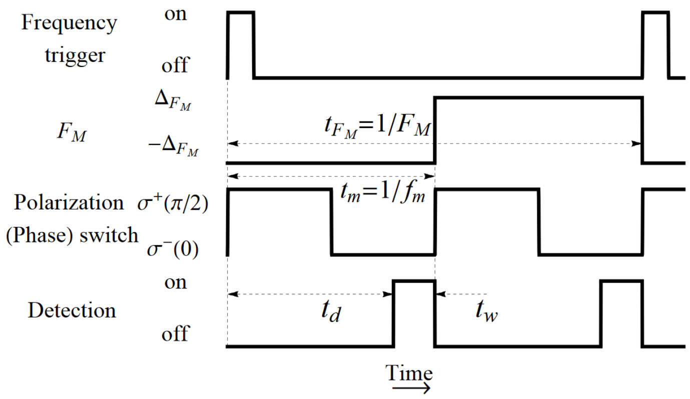

Figure 1.28: Time sequence of the double modulation clock. Extracted from [102].

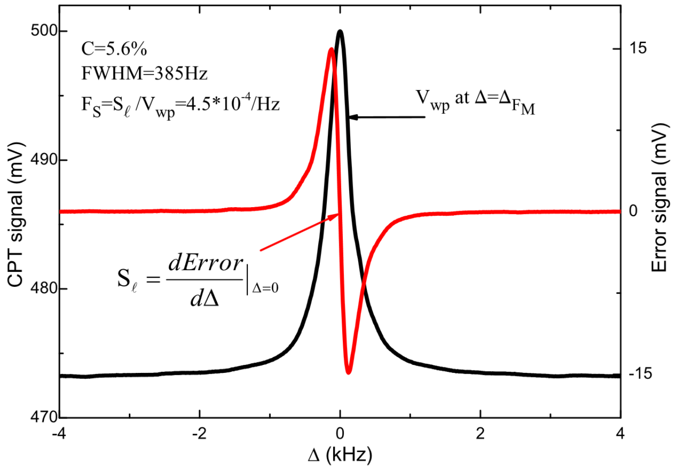

Figure 1.29: Black line: CPT spectrum acquired with the double modulation clock. Red line: Error signal. Extracted from [102].

5.6 % and the linewidth is 385 Hz. The latest published stability measurement to date is shown in Fig. 1.30. The preliminary stability level is 3.2 10^{-13} $\tau^{-1/2}$ until 20 s averaging time. Then it follows a line with slope 1.6 10^{-14} $\tau^{1/2}$ for several thounsands seconds. The main limitation as well as at 1000 s appears to be due to the microwave power fluctuations, inducing fluctuations of the EOPM output optical spectrum. Their contribution is estimated to be 2.26 10^{-13} and 4.2 10^{-13} at 1 s and 1000 s, respectively.

It should be noted that INRIM also developed a CPT-maser. The full description is given in [106]. When the alkali-metal vapor is placed in a resonant cavity and is crossed by two resonant laser fields, the oscillation of the atomic magnetization due to CPT coherence is responsible for stimulated emission, which can be detected with an antenna. A fractionnal frequency stability of around 3 10^{-12} $\tau^{-1/2}$ up to 100 s averaging time was reported with this set-up.

Pulsed CPT clocks One of the best CPT clocks [25, 107, 108] is being developed at LNE-SYRTE (Paris). This work was first initiated by T. Zanon-Willette et al. [109–111], inspired by J. E. Thomas et al. [112]. It combines an optimized CPT pumping scheme (lin per lin [113], described in section 2.3) and a pulsed Ramsey-like interrogation technique allowing the detection of narrow Ramsey-CPT fringes. Furthermore, reducing the interaction time between atoms and the laser field allows to significantly reduce the light shift effects [109]. The clock architecture is shown in Fig. 1.31.

The CPT cell is 5 cm long and 2 cm diameter. It is filled with a Cs vapor and a N_2-Ar buffer gas mixture with pressure ratio $\frac{P_{Ar}}{P_{N_2}} = 0.6$ and total pressure 21 Torr. It is surrounded by a solenoid supplying a static magnetic field to set the quantization axis, a heating device and two layers of magnetic shielding. The laser beams that generate CPT are produced by two phase-locked external

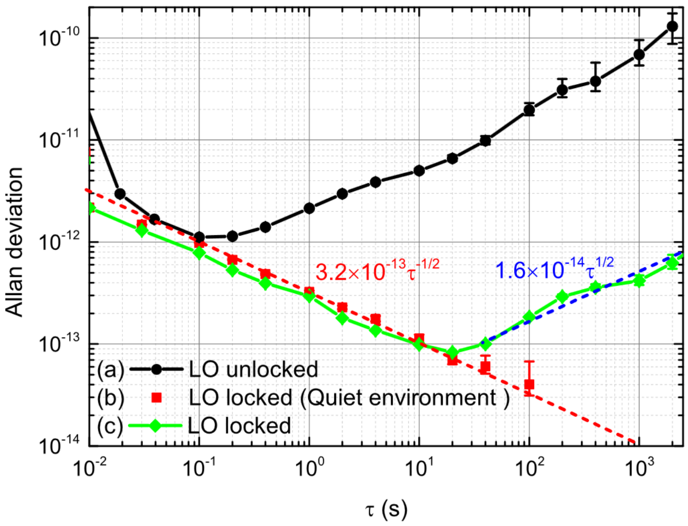

Figure 1.30: LO measured frequency stability when (a) free running, (b) and (c) locked on the atomic resonance. (b) is the best record in quiet environment, (c) is a longer record. The dashed lines are asymptoted lines with slopes 3.2 10^{-13} $\tau^{-1/2}$ for red line and 1.6 10^{-14} $\tau^{1/2}$ for blue line. Extracted from [102].

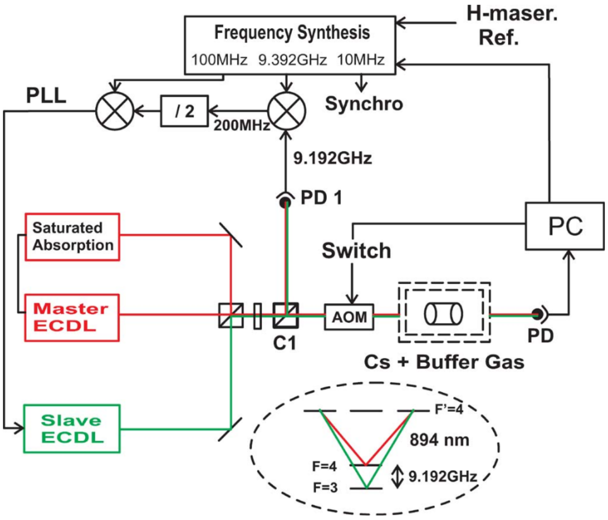

Figure 1.31: Architecture of the pulsed CPT clock at LNE-SYRTE. PLL: phase-locked loop. C1: polarizing beam splitter. PD 1: fast photodiode. Extracted from [111].

cavity diode lasers (ECDL). The master laser is frequency stabilized on the $|F=4\rangle \rightarrow |F'=4\rangle$ resonance of the Cs D_1 line using saturated absorption on an annex evacuated Cs cell. The slave laser is phase locked to the master laser using an optical phase-locked loop (OPLL). A frequency offset of about 9.192 GHz is maintained between the lasers, and it is compared to a 9.392 GHz signal from a low noise frequency synthesizer. The resulting 200 MHz signal is used in the optical PLL. The laser beams are superimposed via a beam splitter. An acousto-optic modulator compensates for the optical shift of atomic resonances due to buffer gas in the CPT cell. It is also used to switch the light on and off, in order to generate the Ramsey pulse sequence. A photodiode detects the transmitted light through the CPT cell, and the signal is processed by a computer. This allows to observe Raman-Ramsey fringes with a narrow central line. The typical timing sequence is shown in Fig. 1.32a.

This sequence consists of an alternance of a bright time of duration τ_p, in which lasers are on, and a dark time of duration T_R, where the lasers are switched off. During bright times, atoms are pumped in the CPT state. After the dark period where atoms are free to evolve at the hyperfine clock frequency, follows the interrogation step of duration τ_d: at the beginning of the following bright pulse, the microwave signal carried by the laser fields interferes with the atomic coherence. Destructive

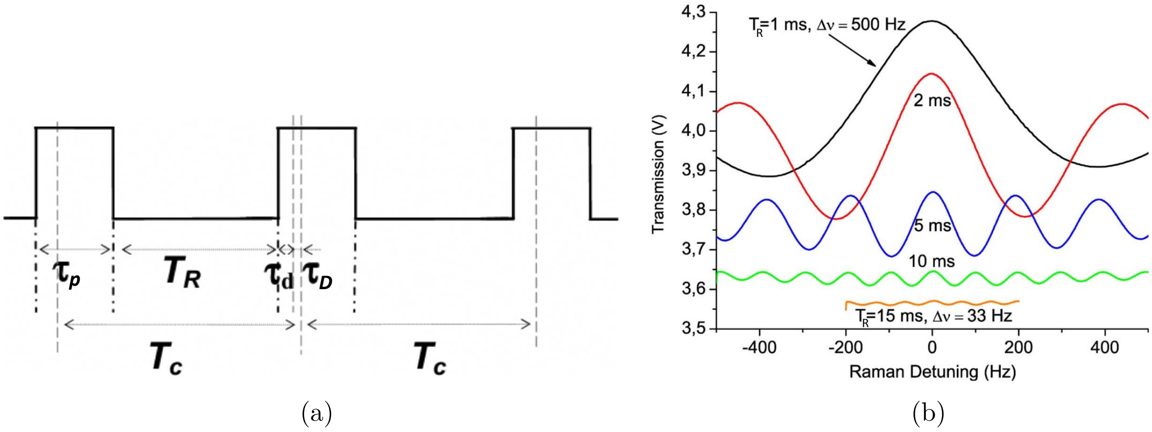

(a) (b)

Figure 1.32: (a) Time sequence of the pulsed CPT clocks, and (b) Ramsey fringes obtained for different free evolution times. Extracted from [111].

interference induces an escape of atoms from the CPT state. During the following detection step of period τ_D the optical transmission through the atomic vapor is measured and averaged. Figure 1.32b shows experimental Ramsey fringes obtained with different free evolution times. Figure 1.33 shows the measured clock short-term frequency stability.

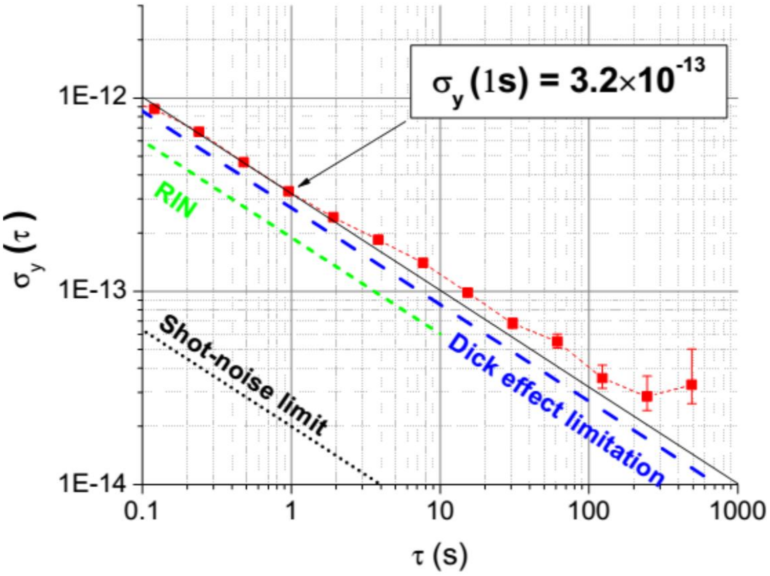

Figure 1.33: Allan deviation of the pulsed CPT clock. Red squares: measured stability. Black solid line: asymptote of experimental data with slope 3.2 10^{-13} $\tau^{-1/2}$. Blue dashed line: Dick effect contribution (2.7 10^{-13} $\tau^{-1/2}$). Green short-dashed line: contribution of the signal-to-noise ratio. Dark dotted line: shot noise contribution. Extracted from [107].

A value of around 3.2 10^{-13} $\tau^{-1/2}$ is measured up to 200 s averaging time. The major limitations for short-term stability are shown to be the LO phase noise via Dick effect, and then the laser RIN. At longer term, the clock stability remains higher than 3 10^{-14}, limited essentially by magnetic field fluctuations and intensity light shifts [114].

Note that NIST has started a few years ago the development of a cold atom CPT clock described in [115]. This clock is to date limited to a level of 4 10^{-11} $\tau^{-1/2}$ up to 1000 s averaging time.
Cold atom technology has also been proposed to develop other kinds of compact atomic clocks that are not based on CPT. An example is given in the following.

1.3.3.3 Cold atoms

HORACE [116, 117] is a compact cold cesium atom clock developed in LNE-SYRTE (Paris, France) for space applications and onboard systems. The operation of this clock is different from fountains since the laser cooling, the microwave interrogation and the detection are all sequentially performed inside a spherical microwave cavity. A representation of the set-up is given in Fig. 1.34.

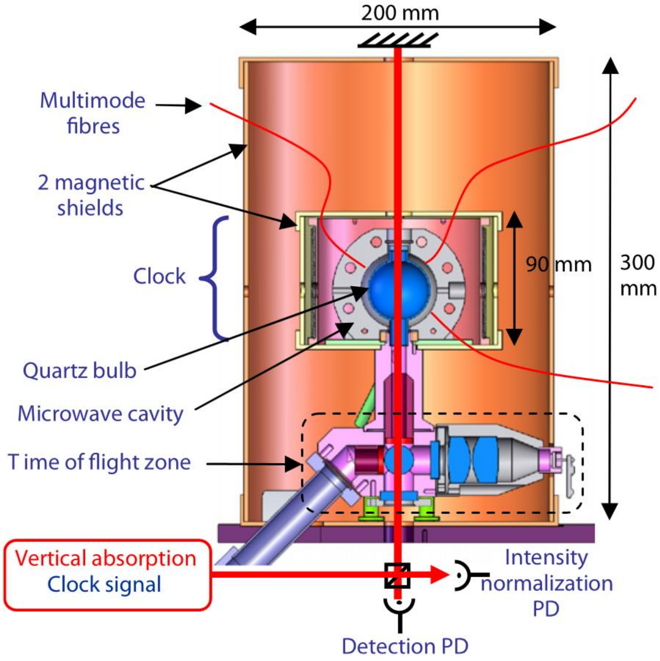

Figure 1.34: Set-up of the Horace clock. Extracted from [117].

The optical molasses is produced in a spherical oxygen-free high thermal conductivity (OFHC) copper cavity. In order to perform laser cooling, this cavity is fed with 6 multimode optical fibers in the (1,1,1) configuration. Its walls are optically polished in order to reflect and scatter the 852 nm cooling light. The microwave cavity acts here as a reflecting sphere for the laser field and averages power imbalances between multimode fibers. Two slits (1 mm×4 mm) provide symmetrical microwave coupling. The cavity operates a TEM011 mode with a quality factor of about 5000. This cavity is surrounded by a solenoid creating a 10∼20 mG vertical static magnetic field to raise the Zeeman degeneracy. A blown quartz bulb is used to prevent interactions between Cs atoms and copper cavity walls. As it shifts cavity resonance by several 100 MHz, each cavity has to be made, polished and tuned for a given bulb. This bulb is glued to a laser soldered Titanium apparatus. An ion pump maintains a residual pressure below 10^{-8} mbar in the vacuum chamber and in the bulb. A glass cell containing liquid Cs acts as a reservoir which can be heated up to increase Cs pressure in the bulb. A time-of-flight detection zone, located 9 cm below the cavity, allows to perform atomic velocity diagnostics.

The operation principle of HORACE is described in the following: atoms are first laser-cooled with 6 optical fibers disposed in each direction. No specific optics is used to shape the light beams, or equilibrate their intensities. The polished copper surface of the microwave cavity itself acts as a spherical reflector and light is sent isotropically to the atoms. Temperatures as low as 35 µK are observed, much lower than the Doppler limit. This allows to trap in an optical molasses about 10^7 atoms in 100 ms. The atoms are then prepared in one of the ground states by optical pumping. In a second step, the microwave field is generated in the cavity to probe the clock transition. It can be continuous or a Ramsey sequence. This step duration is limited by the free falling time of atoms inside the cavity of about 50 ms on earth. The next step is optical interrogation. Only atoms that have transited from the initial state to the other hyperfine ground state absorb the interrogating light. Figure 1.35 shows a typical Ramsey spectrum in pulsed regime. Figure 1.36 shows the frequency stability of HORACE.

The achieved clock frequency stability is 2.2 10^{-13} $\tau^{-1/2}$ for the short term and a level of 4 10^{-15} is reached at 5000 s averaging time. Atomic shot noise is limiting. The interaction time with light is not

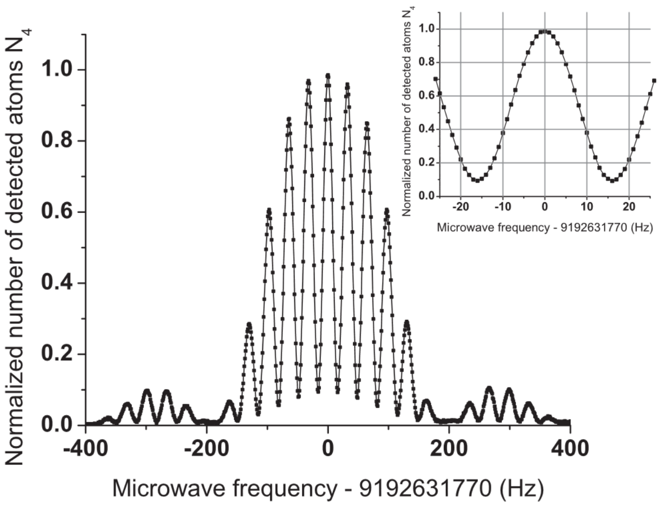

Figure 1.35: Typical Ramsey fringes obtained with HORACE in pulsed mode. Inset: central fringe magnified. The linewidth is 18 Hz, the contrast is 90 %.

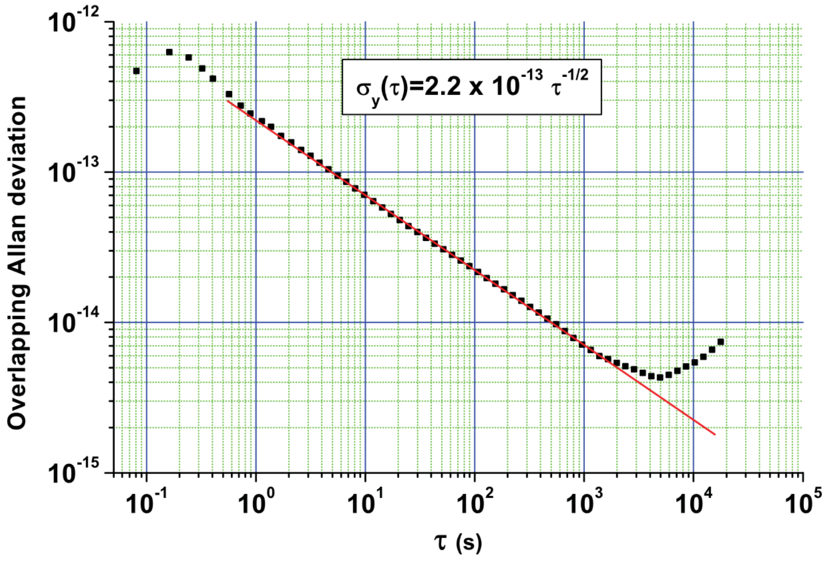

Figure 1.36: Fractional frequency stability of HORACE. Extracted from [117].

limited by temperature aspects and is only due to the falling time of atoms in the cavity.

Recently, MuClock, an industrial compact version of HORACE using Rb atoms, has been developed and commercialized by Muquans, a spin-off from Institut d'Optique and Observatoire de Paris. The datasheet is available at [28]. The choice of Rb atoms was mainly motivated by the fact that the D_2 line wavelength for Rb (780 nm) is easily reachable by second harmonic generation from simple widely-used and reliable telecom wavelength fiber components. The required interrogation laser beam is obtained by frequency-doubling an amplified seed laser operating at 1560 nm. The expected stability is less than $3\ 10^{-13}$ at 1 s averaging time and less than $2\ 10^{-15}$ at 1 day. The whole device size is 120 cm × 51 cm × 40 cm. For comparison, the passive hydrogen maser from T4Science [70] presents a frequency stability of $5\ 10^{-13}$ at 1 s averaging time and $4\ 10^{-15}$ at 1 d, and a size of 53 cm × 47 cm × 20 cm.
A measurement campain has been performed in 0 g conditions in a plane to circumvent the limitation of falling time of Rb atoms. The results showed a great increase of the number of cooled atoms as well as the absorption contrast. For a Ramsey time $T_R = 50$ ms, they gained a factor of 1.4 in the number of trapped atoms and 1.7 in contrast, compared to measurements performed on the ground. For $T_R = 80$ ms, the gains in number of trapped ions and contrast were 4 and 8, respectively.

1.3.4 Summary

Table 1.3: Summary of the state of the art vapor cell atomic clocks performances. We inserted in this table the achieved performances of the CPT clock I developed during my thesis for information. N.C. : non-communicated

Clock	FWHM (Hz)	Contrast (%)	σ_y (1 s)	σ_y (10 000 s)	Shot noise limit (1 s)
HORACE / MuClock	12.5	65	$<3\ 10^{-13}$	$<3\ 10^{-15}$	$1\ 10^{-13}$
POP (INRIM)	152	28	$1.7\ 10^{-13}$	$6\ 10^{-15}$	$2\ 10^{-14}$
CW DR (UNINE)	334	26	$1.4\ 10^{-13}$	$5.5\ 10^{-14}$	$4.9\ 10^{-14}$
Pulsed CPT (LNE-SYRTE)	152	15	$3.2\ 10^{-13}$	N.C.	$2\ 10^{-14}$
Double modulation CPT (LNE-SYRTE)	385	5.6	$3.2\ 10^{-13}$	N.C.	$3.4\ 10^{-14}$
PPOP CPT CW (FEMTO-ST)	538	31.8	$2.1\ 10^{-13}$	N.C.	$1.6\ 10^{-14}$
PPOP CPT pulsed (FEMTO-ST)	134	17	$2.3\ 10^{-13}$	N.C.	$2.7\ 10^{-14}$

The performances of the best vapor cell atomic clocks are resumed in Table 1.3 and in Fig. 1.37. We observe that the short-term frequency stability levels of all compact vapor cell clocks are comparable. They are all in the 1-3 10^{-13} $\tau^{-1/2}$ range. At longer averaging times, CPT clocks suffer from excess frequency fluctuations as compared to double-resonance clocks or cold atom clocks (HORACE/Rubiclock). This is mainly due to the higher sensitivity of the CPT resonance to light shifts.

1.3.5 Context and resume of my thesis work

The development of a high-performance CPT clock has started in FEMTO-ST in 2010 with the thesis of X. Liu [119]. Starting from discussions with our colleagues E. de Clercq and S. Guérandel from LNE-SYRTE, the concept was to propose the development of a new CPT clock with performances comparable to those demonstrated by the pulsed CPT clock developed at LNE-SYRTE (a few 10^{-13} $\tau^{-1/2}$), but with a simplified architecture using a single modulated instead of two phase-locked lasers. During his thesis, my predecessor X. Liu assembled a first non-optimized clock experiment platform and demonstrated the detection of high-contrast CPT resonances in buffer gas-filled Cs vapor cells [120] with an optimized CPT pumping scheme, initially proposed by Happer's group and named push-pull optical pumping (PPOP) [121]. Nevertheless, only first basic CPT spectroscopy measurements were performed during his thesis. Absolutely no frequency measurements had been performed yet at the starting date of my thesis.

During my thesis, in the frame of the MClocks project, I contributed to pursue the development, optimization and detailed metrological characterization of the single-laser CPT clock based on the PPOP technique. This clock combines mainly a DFB laser diode, a pigtailed electro-optic modulator for sidebands generation, an acousto-optic modulator, a Michelson system to produce the PPOP scheme, a buffer gas-filled Cs vapor cell, a photodetector and electronics to pilot the set-up. I did perform first frequency stability tests, later improved and optimized in the CW and in the pulsed regimes, reporting a detailed noise budget to highlight the main limitations of the clock. This clock is to date at the level of 2.1 10^{-13} $\tau^{-1/2}$ up to 100 s averaging time, ranking among the best vapor cell frequency standards. These performances are to our knowledge the best performances ever reported for a CPT-based atomic clock. I will detail my contribution on clock aspects in chapters 3, 4, and 5.

During my thesis, I also demonstrated an original laser frequency stabilization technique based on dual-frequency Doppler-free spectroscopy. This technique, involving complex physical processes involving coherent population trapping and optical pumping, can lead under proper conditions to a significant sign reversal of the Doppler-free dip and greatly enhance the absorption of the vapor cell. This method has allowed a significant improvement of our laser frequency stability. A detailed experimental and theoretical investigation, described in section 6, supported by E. de Clercq (LNE-SYRTE) and D. Brazhnikov (ILP) has been performed, to explore the physics involved in such a scheme.

The clock set-up has also become a reliable platform to perform various auxiliary physical experiments.

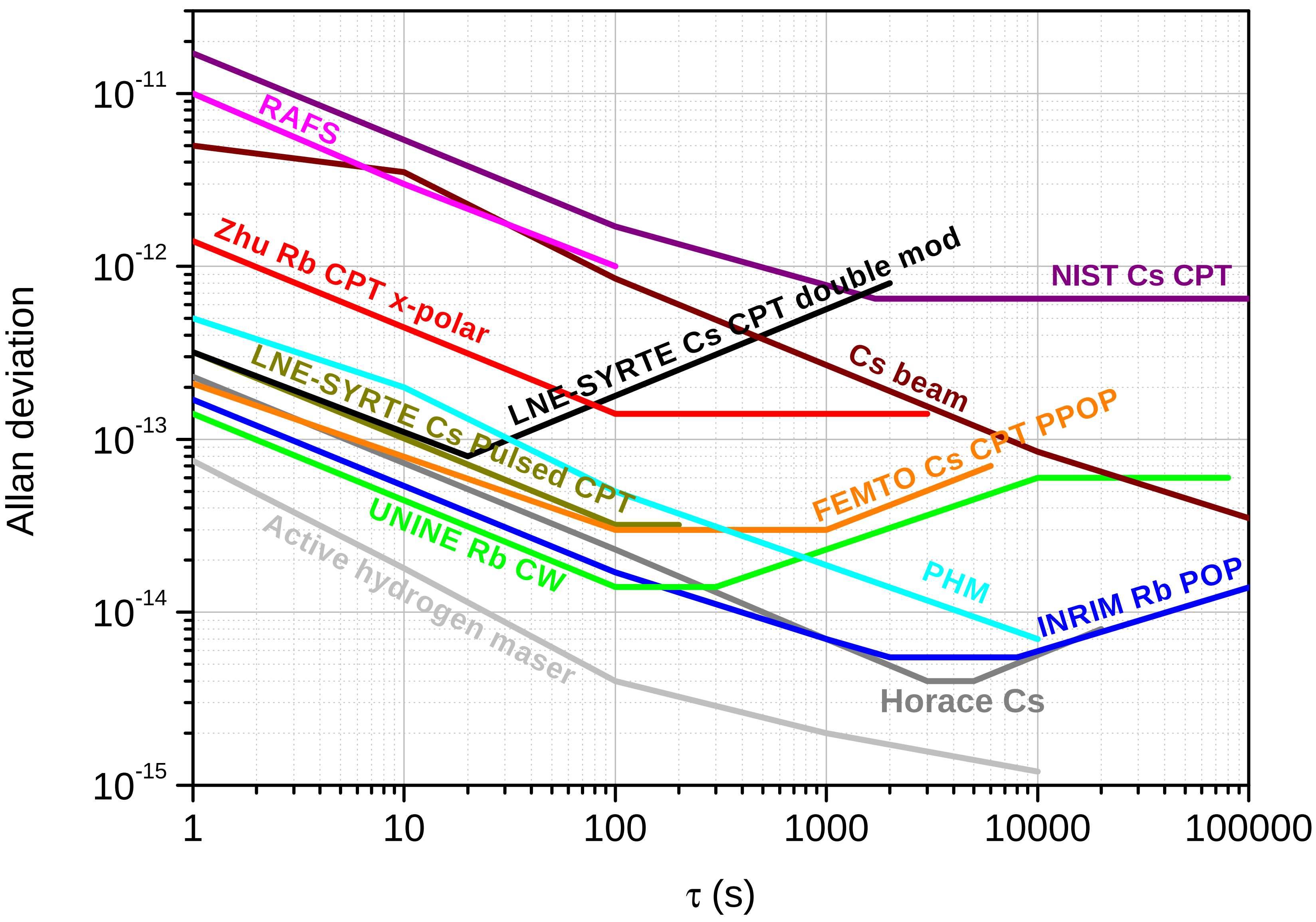

Figure 1.37: State of the art of compact atomic clocks. Extracted from [102] for the SYRTE Cs CPT double-modulation clock, from [95] for the NIST CPT clock, from [75] for the RAFS, from [63] for the Cs beam standard, from [101] for the Rb CPT clock using a polarization-selective method, from [107] for the LNE-SYRTE pulsed CPT clock, from [118] for the FEMTO PPOP CPT clock, from [26] for the CW Rb clock from UNINE, from [117] for HORACE, from [70] for the passive hydrogen maser, from [83] for the POP clock from INRIM and from [79] for the active hydrogen maser.

In that sense, I have reported the characterization of a Cs vapor cell coated with octadecyltrichlorosilane (OTS) using CPT spectroscopy. This is reported in chapter 6. The clock set-up has also been used to perform the characterization of Cs vapor microfabricated cells developped at FEMTO-ST. These aspects, reported in the thesis of V. Maurice [122], will not be developed in this manuscript to preserve its clarity and coherence.

Chapter 2

Basics on CPT physics for CPT clocks

This chapter presents the basics of the CPT physics. A brief theoretical description of the CPT phenomenon through the dressed atom approach is reported. Expressions of the CPT resonance main characteristics (linewidth, amplitude) are given. In the following, main CPT resonance frequency shifts, including the Zeeman shift, the collisional frequency shift and the light shift, are briefly introduced. A comparison between the use of the alkali D_1 and D_2 lines for CPT interaction is discussed. The last part of the chapter is dedicated to the description of a wide variety of optimized CPT polarization schemes proposed in the literature, all aiming to maximize the number of atoms in the clock transition. This overview will allow me to explain the choice we did of using push-pull optical pumping for our CPT clock.

2.1 The CPT phenomenon

2.1.1 CPT observation

The coherent population trapping phenomenon was first observed by Alzetta et al. [29, 123] in a sodium vapor cell illuminated with a multimode dye laser tuned on the D_1 line.

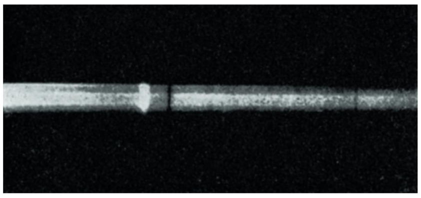

Figure 2.1: Photography of dark lines observed in a sodium vapor cell in presence of a magnetic field inhomogeneity. Figure extracted from [124].

The cell was placed in an inhomogenous axial magnetic field in order to convert the Zeeman frequency splitting amplitude into the z spatial coordinate. This resulted in the emergence of dark lines inside the fluorescent cell where the frequency difference between the two modes of the laser matched a hyperfine transition. This is shown in Fig. 2.1. This observation led to describe this phenomenon as dark resonances.

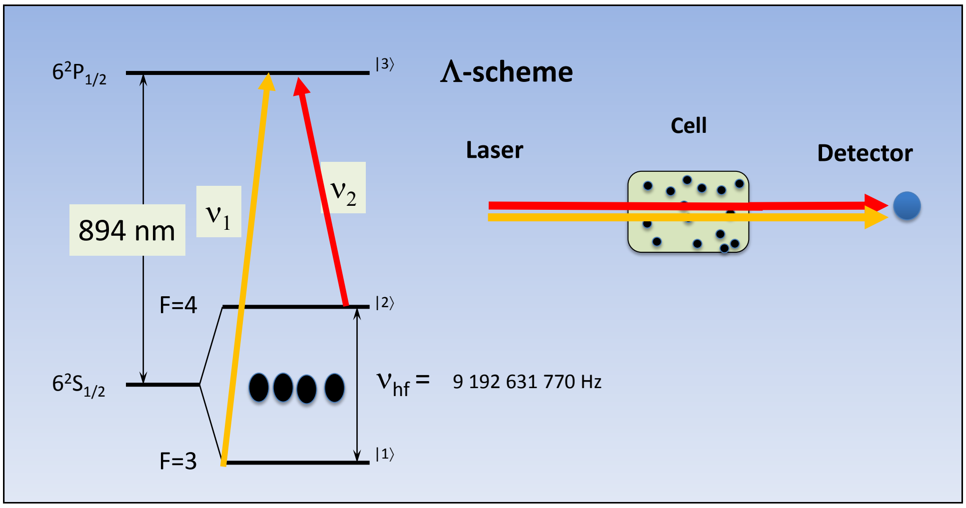

Figure 2.2: Representation of the Cs D_1 line as a three-level system and CPT excitation by two laser fields. The atoms are trapped in a coherent superposition of both ground states, represented here by an imaginary level between the two ground levels.

Figure 2.2 describes the CPT phenomenon for Cs atoms as a simplified three-level scheme. Coherent population trapping occurs if the following conditions are fulfilled:

- An isolated three-level atomic system (or as close as possible).
- Two coherent fields linking both ground states to the same excited state.
- The frequency difference between the fields equals the ground state hyperfine splitting.

In these conditions, the atomic system enters in a coherent superposition of both ground states, that is non absorbing for the exciting fields. When shining the atoms and measuring the transmitted light, a CPT peak emerges in the bottom of the absorption line, as represented in Fig. 2.3.

2.1.2 Interpretation

Here is one possible interpretation that gives a simple and qualitative explanation and leads to a clear evidence of the CPT phenomenon. It uses the dressed atom representation, i.e. the atomic

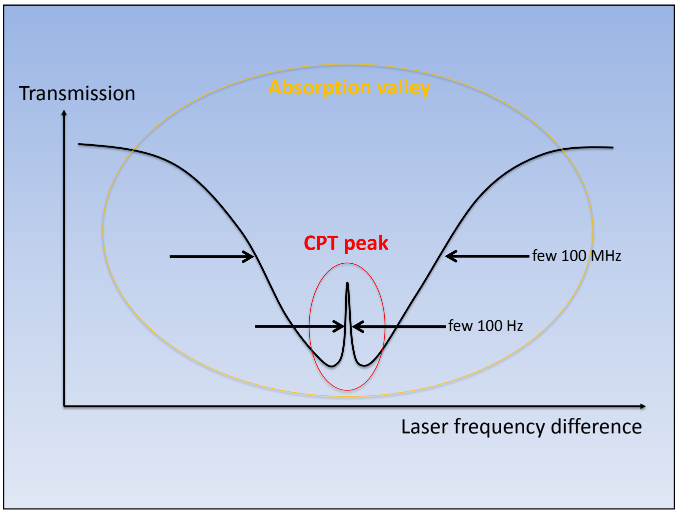

Figure 2.3: Representation of a CPT spectrum in the bottom of an optical absorption resonance line. The magnitude given for the resonances widths is for a centimeter-scale vapor cell filled with a few tens of Torr of buffer gas.

system dressed with the interacting photons [125]. Consider a three-level atomic system as shown in Fig. 2.2 , in presence of a bichromatic field with angular frequencies ω_1 and ω_2, corresponding to the $|1\rangle \rightarrow |3\rangle$ and the $|2\rangle \rightarrow |3\rangle$ transitions, respectively. The system {atom+photons} is considered in a stationnary state, and let N_1 and N_2 be the number of photons at each frequency when the atom is in the excited state.

The atom can either relax to state $|1\rangle$ by emitting one photon at ω_1 or to state $|2\rangle$ by emitting one photon at ω_2. We can thus use three states describing the whole system {atom + photons} at any time, and let us name them $|1, N_1+1, N_2\rangle$, $|2, N_1, N_2+1\rangle$ and $|3, N_1, N_2\rangle$, where state $|i, J, K\rangle$ stands for a system where the atom is in state $|i\rangle$ with energy level E_i and is surrounded by J photons with angular frequency ω_1 and K photons with angular frequency ω_2.

The hamiltonian of the system can be written in this basis as:

$$H = \hbar \begin{pmatrix} \Delta_1 & 0 & \Omega_{R1} \\ 0 & \Delta_2 & \Omega_{R2} \\ \Omega_{R1} & \Omega_{R2} & -i\frac{\Gamma^*}{2} \end{pmatrix} \tag{2.1}$$

where $\Delta_i = \omega_i - E_i/\hbar$ is the angular frequency detuning of field i from $|i\rangle \rightarrow |3\rangle$ resonance, Ω_{Ri} is the Rabi frequency associated with transition $|i\rangle \rightarrow |3\rangle$, Γ^* is the relaxation rate from state $|3\rangle$ to any of the lower states. For simplicity, we shifted the absolute zero energy level to the value $E_3 + \hbar\,(N_1\omega_1 + N_2\omega_2)$. Also notice that the hamiltonian H is non-hermitic. Let us assume that the term $-i\frac{\Gamma^*}{2}$ takes account of spontaneous emission.

The CPT phenomenon is highlighted when the hamiltonian of this system is expressed in a more convenient basis involving states $|C\rangle$ and $|NC\rangle$ (for coupled and non-coupled), defined as following:

$$|NC\rangle = \frac{\Omega_{R2}}{\Omega_R}\,|1, N_1+1, N_2\rangle - \frac{\Omega_{R1}}{\Omega_R}\,|2, N_1, N_2+1\rangle \tag{2.2}$$

$$|C\rangle = \frac{\Omega_{R2}}{\Omega_R}\,|2, N_1, N_2+1\rangle + \frac{\Omega_{R1}}{\Omega_R}\,|1, N_1+1, N_2\rangle \tag{2.3}$$

where we introduced $\Omega_R = \sqrt{\Omega_{R1}^2 + \Omega_{R2}^2}$.

The hamiltonian written in the basis $\{|NC\rangle, |C\rangle, |3, N_1, N_2\rangle\}$ is:

$$H = \hbar \begin{pmatrix} \frac{\Omega_{R1}^2\Delta_2 + \Omega_{R2}^2\Delta_1}{\Omega_R^2} & \frac{\Omega_{R1}\Omega_{R2}}{\Omega_R^2}(\Delta_1 - \Delta_2) & 0 \\ \frac{\Omega_{R1}\Omega_{R2}}{\Omega_R^2}(\Delta_1 - \Delta_2) & \frac{\Omega_{R1}^2\Delta_1 + \Omega_{R2}^2\Delta_2}{\Omega_R^2} & \Omega_R \\ 0 & \Omega_R & -i\frac{\Gamma^*}{2} \end{pmatrix} \tag{2.4}$$

From Eq. (2.4), it is easy to see that when the microwave resonance condition is fulfilled, that means when $\Delta_1 - \Delta_2 = 0$, the hamiltonian does not couple the state $|NC\rangle$ to any of the two other states. At exact microwave resonance, the system is trapped into this state and interaction with the exciting fields is blocked. Atoms trapped in state $|NC\rangle$ become transparent to the incident light and do not emit fluorescence. That is why it is commonly called 'dark state'.

When the microwave detuning is finite, a coupling between $|NC\rangle$ and $|C\rangle$ appears, and because a coupling already exists between $|C\rangle$ and $|3\rangle$ the atoms initially trapped in the dark state leak to the others, and they become absorbing to light again.

2.1.3 CPT resonance characteristics

In the following, I will consider CPT in Cs vapor cells. In Fig. 2.4 are presented a typical CPT spectrum and the resonance main characteristics. A is the resonance signal amplitude, y_0 is the off-resonance transmission value, and $\Delta\nu$ is the full width at half maximum (FWHM) of the resonance. It is useful to define the resonance contrast as $C = A/y_0$.

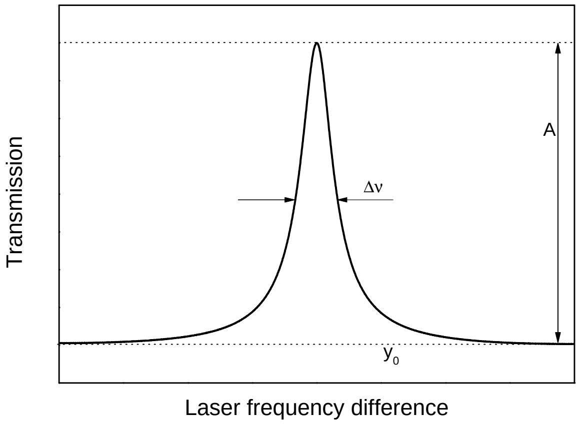

Figure 2.4: Example of a CPT resonance spectrum.

For passive atomic clocks, in which white frequency noise is the dominant noise source, the Allan deviation $\sigma_y(\tau)$ is given by [124]:

$$\sigma_y(\tau) = \frac{\Delta\nu}{\nu_0}\frac{\xi}{SNR}\tau^{-1/2} \tag{2.5}$$

where ν_0 is the clock frequency, ξ is a constant of order unity related to how the resonance is measured and SNR is the measured signal-to-noise ratio in a 1 Hz bandwidth. Thus, a high frequency stability is achieved for high signal amplitudes and low linewidths.

When photons are detected, one can express the shot-noise limited signal-to noise ratio as [124]:

$$SNR = C\sqrt{\frac{P_{det}}{2h\nu_L}} \tag{2.6}$$

where P_{det} is the optical power hitting the photodetector at the output of the cell, h is the Planck constant and ν_L is the laser central frequency. From Eqs (2.5), we find that there are two main routes for improving the short-term stability of a CPT clock: narrowing the resonance line and maximizing the signal-to-noise ratio.

2.1.3.1 CPT signal amplitude

It can be shown that the CPT signal amplitude A is proportionnal to the difference of the atomic population in the excited state at resonance ρ_r and far from resonance ρ_{nr} [126–128]:

$$A = n_{at}\left(\rho_r - \rho_{nr}\right)\Gamma^* = \frac{\Omega_{R1}^2\Omega_{R2}^2}{\Gamma^{*2} + 4\Delta_0^2}\,\frac{1}{\gamma_{12} + \frac{\Omega_R^2}{2\Gamma^*}} \tag{2.7}$$

where n_{at} is the atomic density in the vapor, $\Delta_o = \Delta_1 = \Delta_2$ is the optical detuning (assumed to be the same for both laser fields) and γ_{12} is the relaxation of hyperfine coherence. According to Eq. (2.7) and assuming light fields with equal intensities ($\Omega_{R1} = \Omega_{R2}$), the signal amplitude varies quadratically with laser power at small intensities, and then linearly at high intensities.

2.1.3.2 CPT linewidth

The natural shape of a CPT resonance spectrum is Lorentzian, with a linewidth given by the spontaneous decay rate from the excited state. However, in practice, the width of spectral lines are affected by atomic motion (Doppler broadening), collisions (pressure broadening) and radiation intensity (power broadening).

We consider the beam covers the whole cell diameter. The Doppler effect is attributed to the frequency shift of the radiation emitted by an atom in motion. In the lab frame, the frequency ν of a photon emitted by an atom moving with velocity v is well approximated by:

$$\nu = \nu_0\left(1 + \frac{v}{c}\cos\theta\right) \tag{2.8}$$

where ν_0 is the radiation frequency expressed in the frame where the atom is at rest, c is the light velocity, and θ is the angle between the directions of the atom's motion and of the photon propagation. This approximation is valid for non-relativistic velocities of the atom ($v \ll c$). In vapor cells, the velocity of atoms is isotropically distributed due to thermal agitation, resulting in a Boltzmann distribution for values of θ. The sum of the frequency shifts of radiation emitted by all the atoms in the vapor yields a broadening of the overall resonance line. The Doppler broadening is suppressed in the particular case where the motion of atoms is contained in a region of space of dimension L, such that $L < \lambda/2$, where λ is the transition wavelength [129]. This is the Dicke regime. In this regime, only the natural-linewidth Lorentzian resonance spectrum is visible on the top of a Doppler piedestal of weak amplitude. For a Cs vapor cell with microwave interrogation, the Dicke regime is reached for an atomic containment lower than around 1.6 cm. This can be done, either by using a cm-scale vapor cell or even smaller, or by introducing a pressure of buffer gas that ideally does not interact with the alkali atoms, but turns the atomic motion from ballistic to diffusive. Besides, the natural width of atomic resonances in a pure alkali-metal vapor cell is dramatically broadened by the limited time-of-flight of alkali atoms before they collide with the cell walls. Thus, the effect of buffer gas is also to rise the interaction time between light and atoms and to reduce the inelastic bounces occurrences on the cell walls, yielding a reduction of the atom-walls collisional broadening.

As long as the absorption follows a Beer-Lambert law (the medium is opically thin), and when the Doppler broadening is negligible, the CPT linewidth $\Delta\nu$ in a vapor cell with buffer gas can be written as [130]:

$$\Delta\nu = \frac{1}{\pi}\left(\gamma_{12} + \frac{\Omega_R^2}{\Gamma^*}\right) \tag{2.9}$$

From Eq. (2.9), we can infer that the CPT linewidth increases linearly with incident laser intensity. Extrapolation at null intensity gives the hyperfine relaxation rate γ_{12}, which is given by:

$$\gamma_{12} = \gamma_{nat} + \gamma_w + \gamma_{se} + \gamma_{bg} \tag{2.10}$$

γ_{nat} is the natural relaxation rate of the CPT coherence. When the transition of concern is in the microwave domain, it is negligible compared to the other terms and we will omit it from now on.

γ_w is the contribution from collisions of the alkali atoms with the cell walls. Its expression in a cylindrical cell is given by [126]:

$$\gamma_w = \left[\left(\frac{2.4}{R}\right)^2 + \left(\frac{\pi}{L}\right)^2\right] D\,\frac{P_0}{P} \tag{2.11}$$

where R is the cell radius, L its length, D is the diffusion coefficient of the alkali atoms in the buffer gas at the vapor temperature T, P is the buffer gas pressure at temperature $T_0 = 273.15\,\mathrm{K}$ and $P_0 = 1\,\mathrm{atm}$ is the reference pressure. Table 2.1 gives the values of the diffusion coefficient for N_2 and Ar buffer gas.

Table 2.1: Values of the diffusion coefficient D_0 of Cs in N_2 and Ar at $T_0 = 273.15\,\mathrm{K}$, of the Cs-buffer gas collisional cross section (independent of pressure) [131, 132] and of the Cs-buffer gas relative mean velocities at 308 K. We assume a dependence for D_0 such that $D = D_0(T/T_0)^{3/2}$ [133].

Buffer gas	D_0 [cm^2/s]	σ_{bg} [10^{-25} m/s]	$\overline{v_{rbg}}$ [m/s]
N_2	0.087	0.6	$30.29\sqrt{T}$
Ar	0.134	1.04	$26.27\sqrt{T}$

γ_{se} stands for the broadening due to collisions between alkali atoms with exchange of their spins. Its expression is:

$$\gamma_{se} = \frac{6I+1}{8I+4}\,\overline{v}_{th} n_{at} \sigma_{se} \tag{2.12}$$

where I is the nuclear spin (7/2 for Cs), σ_{se} is the atom-atom cross section for spin exchange ($2.18\ 10^{-18}\,\mathrm{m}^2$ for Cs-Cs) and $\overline{v}_{th} = \sqrt{\frac{8k_BT}{\pi\mu_{Cs-Cs}}}$ (k_B is the Boltzmann constant and $\mu_{Cs-Cs} = \frac{M}{2} \approx 1.1\ 10^{-25}\,\mathrm{kg}$ is the reduced mass of a 2-Cs atoms system, M is the mass of a ^{133}Cs atom) the mean atomic velocity.

γ_{bg} is the contribution from collisions of alkali atoms with buffer gas atoms. It is expressed as:

$$\gamma_{bg} = \frac{P}{k_BT}\overline{v_{rbg}}\sigma_{bg} \tag{2.13}$$

where $\overline{v_{rbg}} = \sqrt{\frac{8k_BT}{\pi\mu_{Cs-bg}}}$ ($\mu_{Cs-bg} = \frac{M\ M_{bg}}{M+M_{bg}}$ being the reduced mass of the Cs atom-buffer gas particle system, M_{bg} is the mass of a buffer gas particle) is the mean relative velocity between alkali atoms and buffer gas atoms and σ_{bg} is the collisional cross section between them. Values of σ_{bg} and $\overline{v_{rbg}}$ are reported in Table 2.1.

For a 5 cm-long and 2 cm-diameter Cs vapor cell filled with a 15 Torr N_2-Ar buffer gas mixture ($r(Ar/N_2) = 0.6$), at 35 °C, the CPT resonance broadening due to collisions of alkali atoms with the walls is of the order of $\gamma_w = 38\,\mathrm{rad/s}$. The contribution from Cs collisions with buffer gas is also around $\gamma_{se} = 61\,\mathrm{rad/s}$. The one from collisions with buffer gas atoms is around 20 rad/s. The total CPT linewidth at null laser intensity ($\Omega_R = 0$) is then around 38 Hz. Relaxation times ($1/\gamma$) are reported in Fig. 2.5 as a function of the cell temperature and of the total pressure of buffer gas.

2.1.3.3 CPT resonance frequency shifts

Zeeman shift A static magnetic field is set in the vapor, in order to set the quantization axis and to lift the Zeeman degeneracy. The dependence of the Zeeman sublevels energy with the axial magnetic field (oriented along the beam propagation axis), when it is low enough, is given by the Breit-Rabi formula [134, 135]:

$$E_{F,m_F} = -\frac{\Delta E}{2\,(2I+1)} - m_F g_I \mu_B \pm \frac{\Delta E}{2}\left(1 + \frac{4m_F}{2I+1}x + x^2\right)^{1/2} \tag{2.14}$$

where F and m_F are respectively the atomic angular momentum and the magnetic quantum number, $\Delta E = h\nu_0$ is the hyperfine energy separation, $I = 7/2$ for ^{133}Cs is the nuclear spin, g_I is the nuclear Landé factor and μ_B is the Bohr magneton. ± stands for + if $F = I + \frac{1}{2}$ and for − if $F = I - \frac{1}{2}$. x is a dimensionless quantity with value:

$$x = (g_J + g_I)\,\frac{\mu_B B}{\Delta E} \tag{2.15}$$

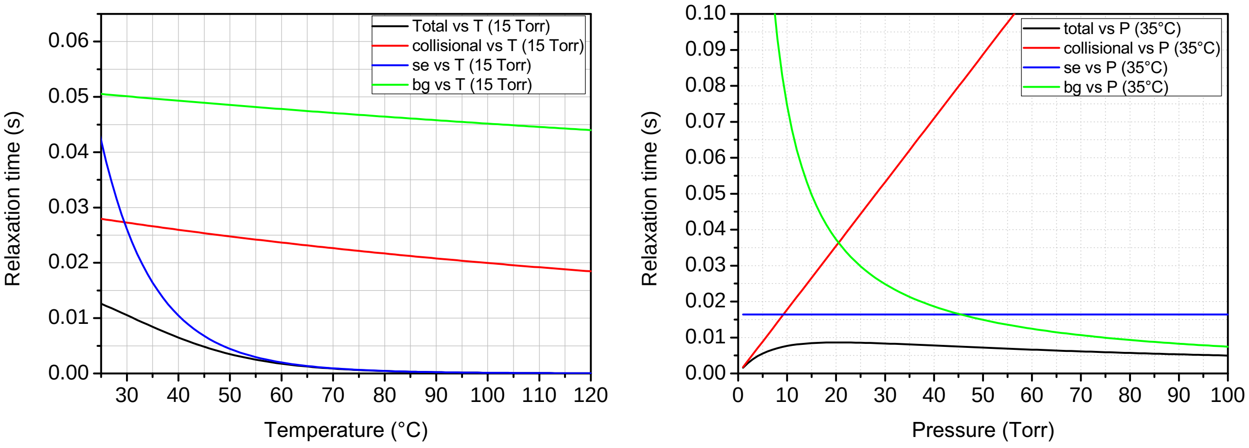

(a) (b)

Figure 2.5: CPT resonance relaxation time versus the cell temperature and N_2-Ar buffer gas pressure, for a cell with diameter = 2 cm, length = 5 cm, $r(Ar/N_2) = 0.6$.

with g_J is the electronic Landé factor, and B the magnetic field. In particular the clock transition frequency ν_{00} ($m_{F=3} = m_{F=4} = 0$) varies like:

$$\nu_{00}(x) = \nu_0 \left(1 + \frac{x^2}{2}\right) \tag{2.16}$$

where $x = 3.049\,575\,6 \; 10^{-4}/\mathrm{G}$ for Cs. We obtain:

$$\nu_{00}(B) = \nu_0 + 427.453\,30 B^2 \tag{2.17}$$

If the magnetic field in the vapor is set at 100 mG, the required magnetic field stability level to maintain the magnetic contribution to the 0-0 resonance fractional frequency fluctuations lower than 10^{-14} is of the order or 1 µG. If the clock apparatus is displaced and rotated, the maximum amplitude of the geomagnetic field variation along the quantization axis is of the order of 1 G. Then, in order to keep the frequency stability under the 10^{-14} level, the cell has to placed in a magnetic shielding with attenuation coefficient higher than 10^6. Sensitivity of the other Zeeman transitions to magnetic field is much higher since it contains a first-order term. For example, the transition with $m_{F=3} = m_{F=4} = 1$ varies as $700\,840.64B$ at first order. To maintain the same level of frequency stability for the 1-1 resonance, the magnetic fluctuations must be 4 orders of magnitude lower (around 130 pG). Such level of stability is not easily reachable in practice. In a vapor cell clock, a static magnetic field is applied with enough amplitude to separate the Zeeman resonances and to resolve only the 0-0 CPT line.

Collisional shift The presence of buffer gas in the vapor cell induces a frequency shift of the clock resonance. It is explained by the distorsion of the electronic cloud of Cs atoms in the vicinity of a buffer gas atom, yielding a displacement of the hyperfine energy levels. It has been experimentally observed that, for light buffer gas such as He, Ne or N_2, this collisional shift is dominated by repulsive Pauli interactions, and it is positive. On the contrary, for heavier buffer gas atoms such as Ar, Kr or Xe, the collisional shift is governed by attractive Van der Waals interaction, and it is negative. This frequency shift is of the order of a few hundred Hz/Torr, and this coefficient varies with temperature within a few Hz/(Torr K). In practice, in a limited pressure and temperature range, the collisional shift is generally approximated by a linear function of temperature and pressure. In the domain of vapor cell atomic clocks, we will assume that, in a limited temperature range, the collisional frequency shift of the clock transition $\Delta\nu_{bg}$ is given by [136]:

$$\Delta\nu_{bg} = P_0 \left[\beta + \delta\,(T - T_0) + \gamma\,(T - T_0)^2\right] \tag{2.18}$$

where P_0 is the buffer gas pressure measured at the reference temperature $T_0 = 273\,\mathrm{K}$ and T is the cell temperature. β [Hz/Torr] is the first-order pressure coefficient, δ [Hz/(Torr K)] and γ [Hz/(Torr K^2)] are the first and second-order thermal coefficients, respectively. The values of β, δ and γ depend on the buffer gas. Experimentally measured values for some buffer gas are given in Table 2.2. Values for other buffer gas can be found in literature [137, 138].

Table 2.2: Measured values of buffer gas-induced frequency shift coefficients for Cs. [137–139]

Buffer gas	β[Hz/Torr]	δ[Hz/(Torr K)]	γ[mHz/(Torr K^2)]
Ne	686(14)	0.266(6)	−1.68(5)
N_2	922.5(48)	0.824(6)	−2.51(3)
Ar	−194.4(16)	−1.138(10)	0.0(3)
Kr	−1450(50)	−1.9(5)	N.C.
Xe	−2350(50)	6.2(5)	N.C.
He	1185(46)	1.49(15)	N.C.
CH_4	−1050(30)	−1.47(9)	N.C.

In the presence of Ne, the quadratic dependence of the buffer gas frequency shift with temperature is high. The dependence with temperature is canceled at first order for a value of $T_{inv} = 79(3)\,°\mathrm{C}$. This configuration is of great interest for miniature CPT atomic clocks. In general, the development of vapor cell atomic clocks requires the use of a mixture of buffer gas of two kinds. An appropriate choice of the partial pressures allows to obtain a so-called inversion temperature T_{inv}, for which the clock frequency sensitivity to temperature fluctuations is canceled at first order [136, 139, 140]. When a mixture of buffer gas 1 and 2 is used, Eq. (2.18) becomes:

$$\Delta\nu_{bg} = P_0 \left[(r_1\beta_1 + r_2\beta_2) + (r_1\delta_1 + r_2\delta_2)(T - T_0) + (r_1\gamma_1 + r_2\gamma_2)(T - T_0)^2 \right] \tag{2.19}$$

where β_i, δ_i and γ_i are the pressure and temperature coefficients for buffer gas $i.r_i$ stands for the mole fraction of buffer gas i ($r_i = \frac{P_i}{P}$). Let us define the ratio r as $r = \frac{r_2}{r_1}$. We can thus retrieve Eq. (2.18) by defining the effective coefficients β, δ and γ such that:

$$\beta = \frac{\beta_1 + \beta_2 r}{1 + r} \tag{2.20}$$

$$\delta = \frac{\delta_1 + \delta_2 r}{1 + r} \tag{2.21}$$

$$\gamma = \frac{\gamma_1 + \gamma_2 r}{1 + r} \tag{2.22}$$

Using the definition of r and matter conservation ($r_1 + r_2 = 1$) in Eq. (2.19), one can easily derive:

$$\frac{d\Delta\nu_{bg}}{dT} = P_0 \left[\frac{\delta_1 + \delta_2 r}{1 + r} + 2\frac{\gamma_1 + \gamma_2 r}{1 + r}(T - T_0) \right] \tag{2.23}$$

Equation (2.23) zeroes for $T = T_{inv}$, defined such that:

$$r = -\frac{\delta_1 + 2\gamma_1 (T_{inv} - T_0)}{\delta_2 + 2\gamma_2 (T_{inv} - T_0)} \tag{2.24}$$

or such that:

$$T_{inv} = T_0 - \frac{\delta_1 + r\delta_2}{2(\gamma_1 + r\gamma_2)} \tag{2.25}$$

Figure 2.6 shows the pressure ratio r to use as a function of the desired inversion temperature, for a cell filled with a buffer gas mixture consisting in Ar and N_2. The relationship is [128]:

$$r(Ar/N_2) = 0.724(12) - 0.004\,41(9)\,(T_{inv} - T_0) \tag{2.26}$$

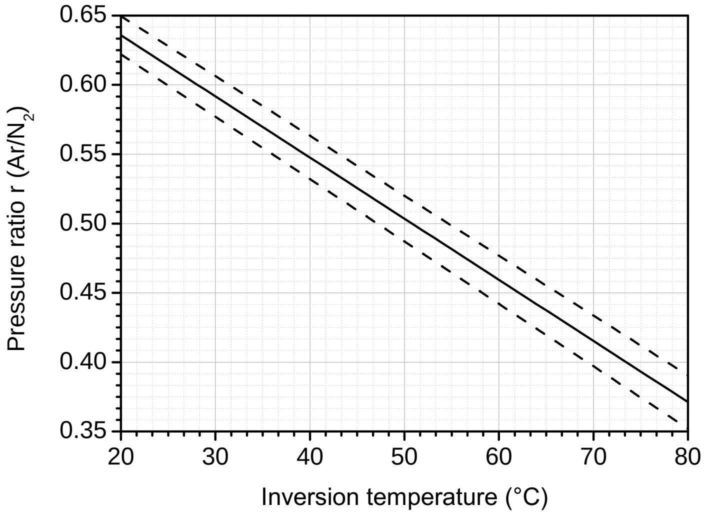

Figure 2.6: Pressure ratio between Ar and N_2 as a function of the inversion temperature.

Light shift It is well known that the energy levels of a two-level system are perturbed when interacting with a nearly resonant light (finite microwave detuning). This light shift is called AC Stark effect. Its expression is given by [141, 142]:

$$\Delta\nu_{ls} \propto -\Omega_R^2 \frac{\Delta}{\Delta^2 + (\Gamma^*/2)^2} \tag{2.27}$$

where Ω_R is the corresponding transition Rabi frequency, Δ the microwave detuning and Γ^* the excited state decay rate. We note that at first order, the dependence of the light shift with light intensity is linear and the dependence with detuning is dispersive. There is no light shift when the radiation is exactly at resonance.

When dealing with CPT in a 3-level system with two resonant fields, the first solution one could think of, is to sum the energy shifts from each optical transition involved in the CPT interaction [126]. If we suppose the light intensity for both frequency components are equal, then the light shift is a linear function of the total laser intensity.

$$\Delta\nu_{ls} \propto -\left(\Omega_{R1}^2 - \Omega_{R2}^2\right) \frac{\Delta_0}{\Delta_0^2 + (\Gamma^*/2)^2} \tag{2.28}$$

where Ω_{R1} and Ω_{R2} are the Rabi frequencies and Γ^* is the excited state decay rate. However, as it will be seen in Fig. 4.14 and discussed in D. Miletic's thesis [143], when probing a large intensity range, the CPT resonance central frequency does not behave linearly with the light intensity. This reflects the complexity of light shift effect in CPT experiments. In [128], O. Kozlova studied the impact of several experimental parameters on the CPT resonance frequency shift. She explained that the AC Stark effect should be reduced in CPT since the ground states are partially decoupled from light. She also reported that light-induced shifts in CPT involve several causes resulting in distortion of the CPT peak, such as a finite optical detuning, an overlap between the buffer gas-broadened optical lines, temperature-induced optical frequency shifts, etc... The reader can refer to O. Kozlova's manuscript for more details about her experiments.

We will keep in mind that light intensity-induced shifts in CPT are more complex than summing independently the AC Stark shifts from both optical fields involved in CPT, and that the light shift coefficient is dependent on the experimental parameters. One crucial step in the development of a CPT clock is to try to find a cancellation point for the light shift coefficient.

2.1.4 Optical broadening and frequency shifts

For the D_1 optical resonance in Cs, the Dicke regime is set for atomic ensembles contained in a region of space with dimension $d < 450\,\text{nm}$. This is not achieved in practice and the optical absorption lines of Cs, even in presence of buffer gas, are Doppler-broadened. Moreover, collisions with buffer gas atoms are responsible for additional broadening and also frequency shift of the optical resonances. The absorption line can be fitted by a Voigt profile, which is the convolution of a Lorentzian profile (natural and collisional contributions) and a Gaussian profile (Doppler contribution).
The total linewidth of the optical resonance $\frac{\Gamma^*}{2\pi}$, for a Cs cell in the presence of a pressure P of buffer gas, is given by:

$$\frac{\Gamma^*}{2\pi} = \frac{\Gamma}{2\pi} + \beta_{opt}P + \Delta\nu_D \tag{2.29}$$

where $\frac{\Gamma}{2\pi}$ is the Cs D_1 resonance natural linewidth (4.575 MHz [135]), β_{opt} is the collisional broadening coefficient for Cs in the considered buffer gas, in Hz/Torr, and $\Delta\nu_D$ is the Doppler broadening. The Doppler broadening is given by [144]:

$$\Delta\nu_D = \frac{2\nu_{D_1}}{c}\sqrt{\frac{2k_BT\ln 2}{M}} \tag{2.30}$$

where $\nu_{D_1} = 335.12\,\text{THz}$ is the frequency of the D_1 transition, $c = 2.9979\ 10^8\,\text{m/s}$ is the speed of light, M is the mass of a Cs atom and T is the cell temperature. At 35 °C, the Doppler broadening is 360 MHz.
In Table 2.3, the values of β_{opt} are given for N_2 and for Ar. For an Ar/N_2 buffer gas mixture with $r(Ar/N_2) = 0.6$ and a total pressure of 15 Torr, the resulting β_{opt} coefficient is 17.38 MHz/Torr and the collisional broadening is around 260 MHz. We thus expect a total linewidth for the optical lines of around 625 MHz.
The optical frequency shift S_o in presence of a pressure P of buffer gas is simply:

$$S_o = aP \tag{2.31}$$

where a (values given in Table 2.3) is the optical transition collisional shift due to buffer gas. A detailed calculation of this shift will be given in section 3.6.1.

Table 2.3: Measured values for the optical shift and broadening coefficients [88].

Buffer gas	a [MHz/Torr]	β_{opt} [MHz/Torr]	Temperature of measurement [K]
N_2	−7.69(1)	15.82(5)	318
Ar	-6.47(3)	18.31(16)	313

2.2 Cs D_1 line versus D_2 line

Alkali atoms are the best candidates to perform CPT. Their outermost electron is single and it is in an s-orbital, which bring alkali atoms as close as possible from a simple and isolated three-level system. Figure 2.7 details the tree structure of Cs D_1 and D_2 lines.
The choice of ^{133}Cs as the clock atomic reference can be justified by the fact that:

- ^{133}Cs is non radioactive.
- The ground state hyperfine splitting is high, and it is historically the main reason for defining the second value from the Cs hyperfine frequency (the second is defined as the duration of 9 192 631 770 oscillations of the radiation corresponding to the transition between the hyperfine levels of ^{133}Cs ground state). The highest is the clock frequency and the highest is its quality factor.
- The excited state hyperfine splitting is higher for Cs than for other atoms like Rb for example.

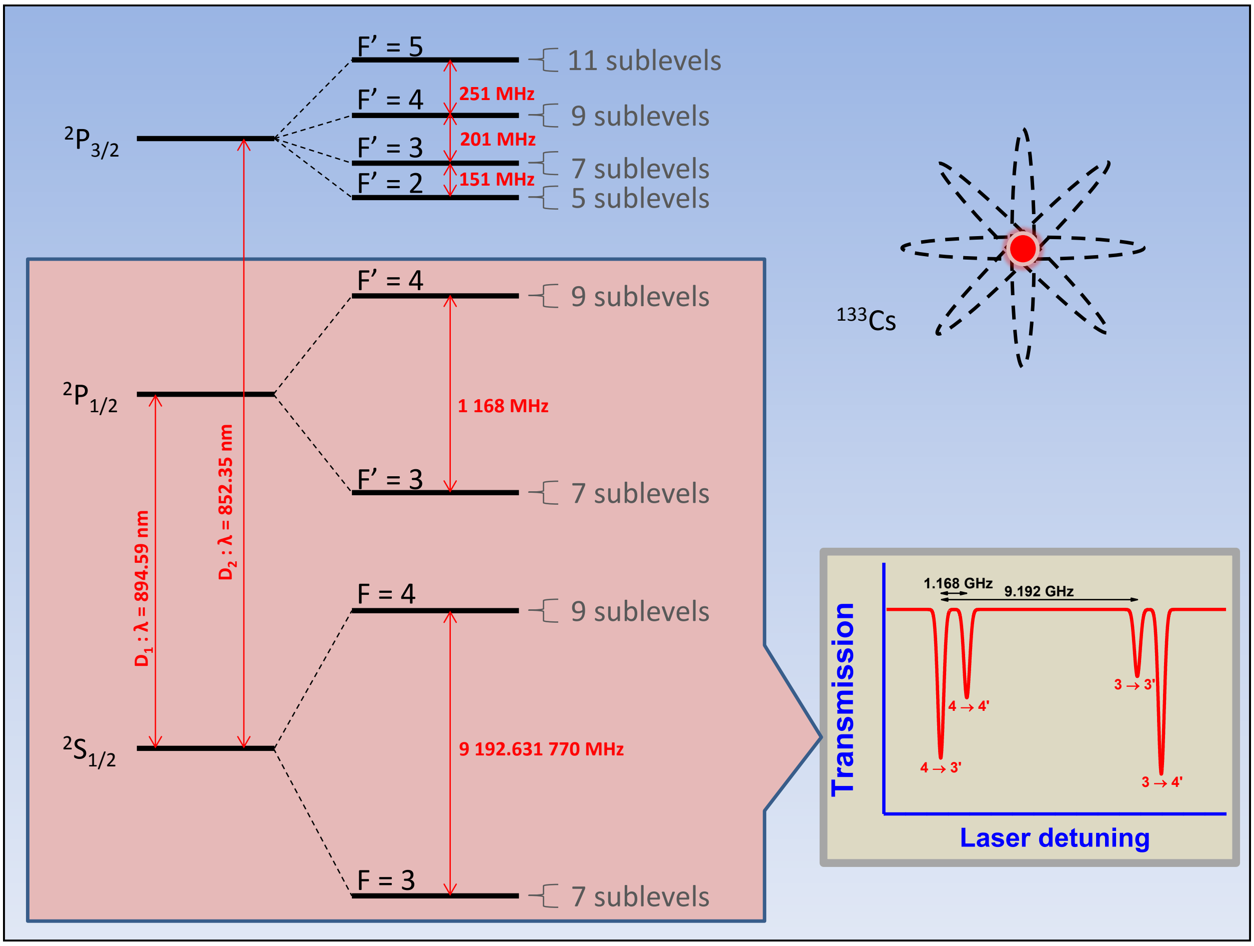

Figure 2.7: Energy diagram for the ^{133}Cs D_1 and D_2 lines.

Furthermore, the D_1 line presents a simpler tree structure than the D_2 line (there are less hyperfine levels in the excited state, and they are well-separated by 1.167 GHz), avoiding possible leaks of atoms to unwanted states. Choosing the D_1 line then allows to obtain higher amplitudes for the absorption signal [145]. It is thus possible to perform CPT using both ground states and one excited state of the Cs D_1 line. All the experiments described in the manuscript are performed using the $F' = 4$ excited state, unless it is clearly specified. Indeed, the associated absorption line is deeper, leading to CPT resonances with a lower background level and higher contrasts. However each of these states present an additional Zeeman subdivision which is revealed in the presence of a static magnetic field: these Zeeman sublevels are split because their energy level vary differently with the magnetic field, as shown in Fig. 2.8.

The $m = 0$ sublevels energy present a quadratic dependence to magnetic field, whereas the other ones present a linear dependence at first order. Being less sensitive to magnetic field, $m = 0$ sublevels are more suitable for clock applications. A static magnetic field is then generally deliberately applied in the vapor cell in order to lift the Zeeman degeneracy. Only atoms involved in the magnetic first order insensitive hyperfine transitions are selected. We will see in section 2.3 that this magnetic selection affects the number of atoms that participate to the clock resonance, and it brings new constraints on the employed light polarization in order to repopulate the states of interest.

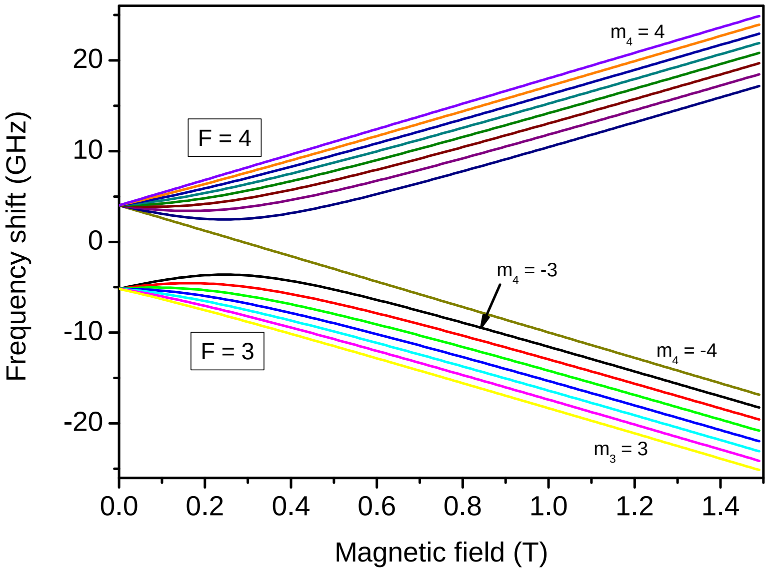

Figure 2.8: Zeeman splitting of the ground states for ^{133}Cs.

2.3 CPT signal optimization

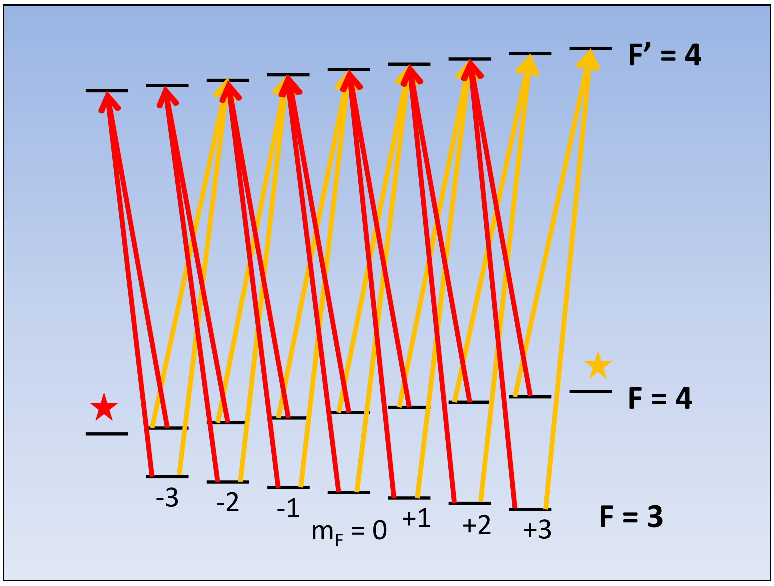

Figure 2.9: Scheme of the Zeeman degeneracy showing the possible CPT excitations with a single right (orange) or left (red) circular polarization. The excited state is F' = 4. Trap states are indicated with a colored star.

From Eq. (1.10) one can easily understand that improving the short-term stability of a CPT clock implies, among others, to increase the resonance signal. The quantum selection rules impose the Cs atoms to be excited by a circularly polarized light in order to bring them to the 0-0 CPT state. Indeed, the vertical $|4,0\rangle \rightarrow |4',0\rangle$ transition is forbidden [146]. The 0-0 resonance is thus in principle out of reach using linearly polarized light. However, using single circularly polarized light instead, the atoms progressively populate the extreme Zeeman sublevels of the ground state (labeled with stars in Fig. 2.9) by a pumping effect, at the expense of the central ones which are much less sensitive to the surrounding magnetic field. A large number of them are trapped in these extreme states, and the clock 0-0 resonance signal is limited.

Many alternative excitation schemes have been thought in order to lift the trap states and increase the clock signal contrast. In the following is presented a non exhaustive list of them. I will first describe a few methods based on particular polarization configurations of light (lin par lin, lin per lin, PPOP, double modulation) resulting in the generation of a so-called double-lambda scheme that allows to repopulate the central Zeeman sublevels. I will also mention a few other methods that have been reported to produce high contrast clock resonances (polarization-selective detection and feedback spectroscopy).

2.3.1 Double lambda schemes

The objective of optimized pumping schemes is to maximize the atomic population in the central Zeeman sublevels in order to increase the clock resonance signal compared to when a single circular polarized light is used. In double-lambda configuration, two orthogonal circular polarizations interact with the atomic vapor simultaneously and central CPT states are favored. In Fig. 2.10a are represented the CPT resonances excited by double-lambda schemes. There are two main kinds of them:

- the first one is the $|3,0\rangle - |4,0\rangle$ (0-0) dark state. It can be excited either via the $|4,-1\rangle$ excited state (pink arrows) or via $|4,1\rangle$ (purple arrows).
- the second kind involves two ground states from different hyperfine levels with Δm = 2. They are the $|3,-1\rangle - |4,1\rangle$ CPT state and the $|3,1\rangle - |4,-1\rangle$ one. They are highlighted in dark and light blue respectively in Fig. 2.10a.

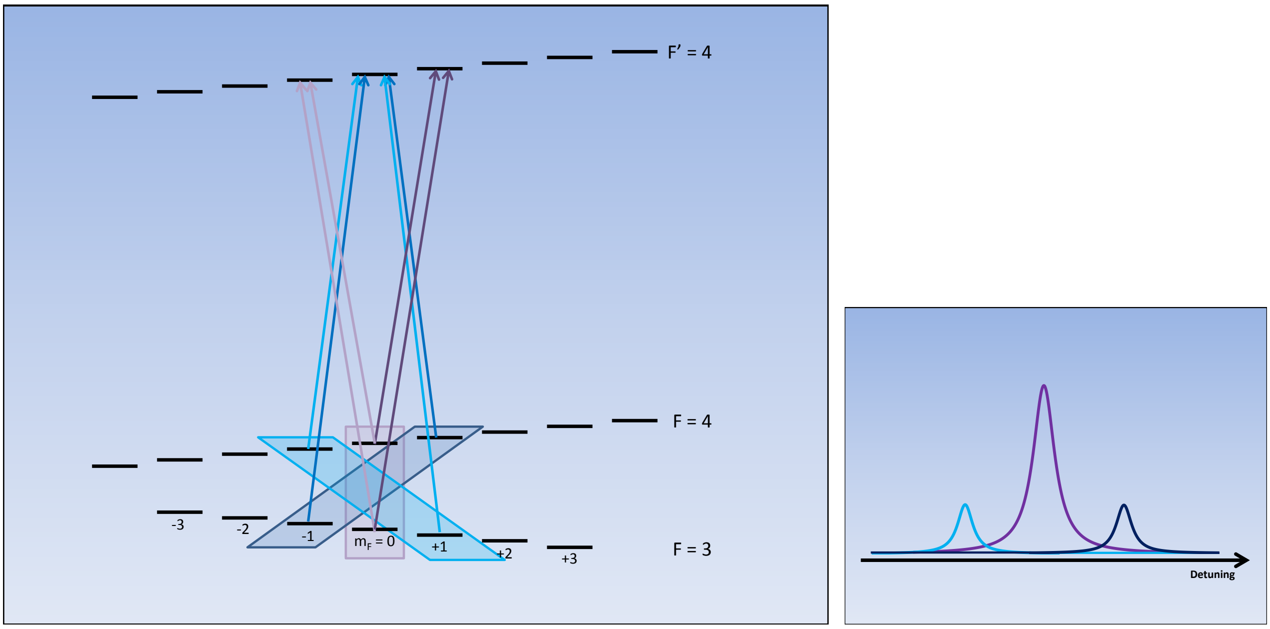

(a) (b)

Figure 2.10: (a) Scheme of the possible clock CPT states excitations in a double-lambda configuration and (b) the typical associated resonances observed. Each single color in (a) represents a possible CPT excitation. The pink and purple arrows represent 0-0 CPT states. The light and dark blue arrows are $\Delta_m = 2$ CPT resonances. The purple curve in (b) corresponds to both 0-0 resonances. It does not appear for a lin par lin polarization scheme.

These two types of resonances ($\Delta m = 2$ and 0-0) present a different sensitivity to magnetic field. From the Breit-Rabi formula (Eq. (2.14)), we find that the 0-0 resonance frequency (ν_{00}) dependence to magnetic field is quadratic,

$$\nu_{00} \approx \nu_0 + 427B^2 \tag{2.32}$$

with B in G and ν_0 is the hyperfine splitting frequency (9 192 631 770 Hz), whereas the $\Delta m = 2$ resonances also present a linear component:

$$\nu_{\Delta m=2} \approx \nu_0 \pm 1116.5B + 400.7B^2 \tag{2.33}$$

At high magnetic fields it is possible to resolve the different resonances which are simultaneously present in most of the optimized pumping schemes that will be described in the following. This may result at high magnetic fields in the broadening of the CPT resonance, or even in a splitting at very high fields as represented in Fig. 2.10b.

2.3.2 Lin par lin

In the lin par lin configuration, described in [147] for ^{87}Rb, both optical fields that produce CPT are linearly polarized along the same axis. A linearly polarized light can be decomposed into two orthogonal circularly polarized components. Then, the double-lambda schemes of Fig. 2.10a are in principle observable. However the double-lambda involving $m = 0$ is not observed in practice. This is due to opposite Clebsch Gordan coefficients of the involved transitions and to the relative phase of the electromagnetic fields [120]. As a consequence, the central resonance spectrum only consists of the combination of the blue resonances in Fig. 2.10. High contrast resonances have been reported [147, 148] in lin par lin configuration for low buffer gas pressures. However, the use of this polarization scheme presents several drawbacks: as already seen in previous section, the $\Delta m = 2$ CPT resonances are sensitive to the magnetic field at first order inducing broadening of the resulting transmission peak, or even splitting. Furthermore, asymmetry in this peak should appear in the case of unbalanced field intensities in the two involved lambda schemes, resulting in a global shift of the resonance. For example, to stabilize a $\Delta m = 2$ resonance fractional frequency fluctuations below $1\ 10^{-15}$, the magnetic field has to be stabilized within a 8.2 nG-wide interval. On the other hand, a 0.22 µG-wide interval is needed to stabilize a 0-0 resonance frequency at the same level (assuming a 50 mG static magnetic field), which makes a factor of 26 between the two kinds of resonances.

2.3.3 Interferences between 0-0 resonances

The optimized polarization schemes presented in the following (lin per lin, PPOP, double modulation) are intended to allow interaction of the lambda schemes with the $m = 0$ states. Only a qualitative description of the method will be exposed in the manuscript. It relies on the work from Y-Y. Jau et al [121, 149]. In this interpretation, atoms in the 0-0 CPT state can be represented by the mean projection S_z of the single electrons spin along the magnetic field direction axis. Figure 2.11 shows the evolution of S_z with time.

The electrons spin z-component oscillates at the hyperfine frequency ν_0. The probability to absorb a photon is proportional to $1 - 2s_zS_z$, where s_z is the projection of the photon spin on the z-axis (1 for a right circularly polarized photon, -1 for a left polarized one). Then the relative probabilities to absorb a right circularly polarized photon (p_+) or a left circularly polarized photon (p_-) are equal to:

$$p_+ = \sin^2\left(\frac{2\pi\nu_0 t}{2}\right) \tag{2.34}$$

$$p_- = \cos^2\left(\frac{2\pi\nu_0 t}{2}\right) \tag{2.35}$$

As a consequence, the dark state is preserved only if the interactions with the orthogonal circularly polarized lights occur alternatively and at the clock frequency. It can be seen as a constructive interference between the dark state produced by the respective polarized lights. At the opposite, when the interaction with the beams occurs at the same time, the CPT states created by the two polarization components mutually destruct each other.

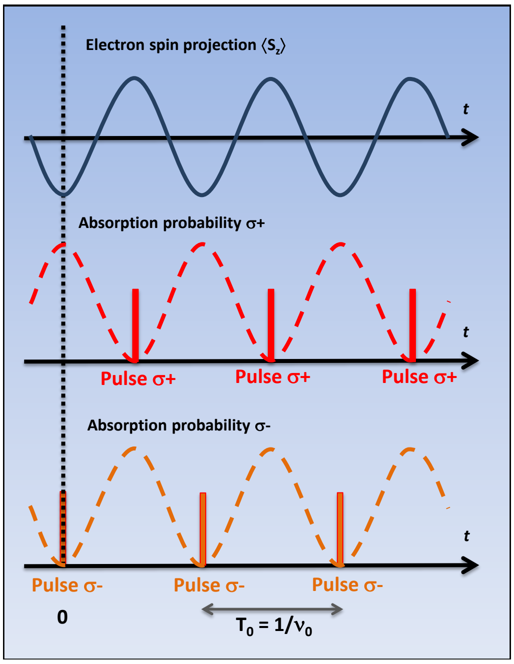

Figure 2.11: Probability of absorbing left or right circular polarized lights for an atom in a CPT state, as a function of time. The atom is represented by its single electron spin projection along the z axis.

2.3.3.1 Lin per lin

In lin per lin configuration [113, 150], both optical fields frequency separated by the hyperfine frequency are linearly and orthogonally polarized. They can decompose into two orthogonal circularly polarized components, and the obtained superposition of states for one lambda is common to the other. They interfere constructively, allowing the observation of the 0-0 resonance. The Δm = 2 peaks are resolved only for high magnetic fields. Lin per lin configuration allows the detection of high contrast CPT clock resonances. The major drawback is that this pumping scheme forces to spatially separate the frequency components of the exciting electromagnetic field. Another solution proposed in [151, 152] is the use of a dual-frequency and dual-polarization optically-pumped vertical external-cavity semiconductor laser (VECSEL) to generate the interrogating field.

2.3.3.2 Push Pull Optical Pumping (PPOP)

The PPOP scheme [120, 121] is more suitable for a compact CPT clock where the same beam contains both required frequencies. In this scheme the atoms are crossed by a bichromatic field, with each component containing both orthogonal circular polarizations. A phase delay corresponding to half the hyperfine period is introduced between both polarized lights. In this condition the scheme is equivalent to lin per lin [113, 120]. The 0-0 CPT states produced by both polarizations are common, yielding a high clock 0-0 resonance contrast.

To produce this polarization set-up, the bichromatic beam is sent to a Michelson-like set-up shown in Fig. 2.12. The input beam is linearly polarized and split into two arms of equal amplitude by a polarizing beam splitter. The two components have orthogonal polarizations axis. They pass once through QWPs such that their polarization axis are at 45° from the QWP slow axis. After reflection by the mirrors, they cross the QWPs a second time. The beams polarization axis have rotated 90°. They finally recombine again in the PBS cube. A last QWP turns the output perpendicular linear polarizations to orthogonal circular ones.

One of the mirrors is fixed while the other one can be translated in order to adjust the arm length. In order to ensure a constructive interference between the two CPT states excited by the orthogonally polarized beams, the associated coherences have to oscillate in phase. This is achieved when the optical path difference between the two arms is $(\frac{1}{2}+p)\lambda$, where $\lambda = 32.635\,\mathrm{mm}$ is the hyperfine

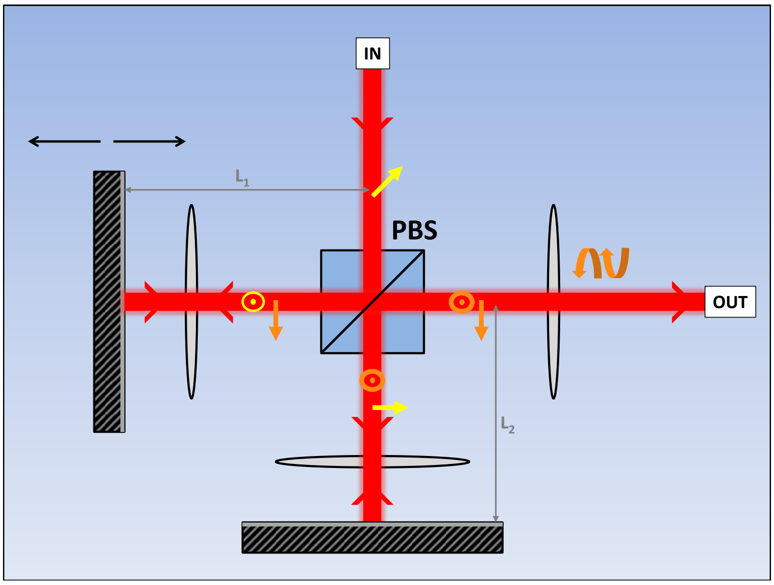

Figure 2.12: Schema of the delay-line system to produce the PPOP scheme from a linearly polarized light. The input beam contains both resonant frequencies. It is linearly polarized 45° from the polarizing beam splitter (PBS) principal axis. Each arm of the interferometer contains a quarter wave plate, and a mirror. One of the mirrors can be translated along the beam promagation axis. Another quarter wave plate is placed at the output of the system.

wavelength for Cs and p is a positive integer. Since the beams make a round trip along the arms of the delay-line, constructive interference occurs when the length difference between them in mm is:

$$L_1 - L_2 = \frac{\lambda}{2}\left(p + \frac{1}{2}\right) \tag{2.36}$$

For Cs, Eq. (2.36) becomes:

$$L_1 - L_2[\mathrm{mm}] = 8.1587 + p\ 16.317 \tag{2.37}$$

As the CPT coherence is in the microwave domain, we expect the clock behavior not to be critically sensitive to length fluctuations of the path difference between the two arms. This will be confirmed in subsection 4.3.5.

2.3.3.3 Double modulation

The CPT clock with double modulation [103] has been recently proposed as an alternative to PPOP and lin per lin schemes. The goal here is also to produce an alternance of orthogonal circularly polarized light like in PPOP, but without making any beam separation. This is a pure time alternance, generated by a polarization modulator. Another difference is that the polarization modulation frequency is low compared to the hyperfine frequency (a few kHz).

This scheme is inspired from the observation of M. Huang and J. Camparo [105]. The observation of a CPT resonance doublet due to destructive interference has been reported if no particular attention is given to the phase relationship between the laser frequencies. The CPT states produced by each circular polarization alternance add constructively, on the condition that the dephasing between the exciting fields is pi-modulated synchronously with the beam polarization, yielding a single CPT resonance peak with high contrast [103, 104, 153] (see the CPT sequence in Fig. 1.28). This excitation requires no physical splitting of the beam, promising a highly compact set-up with an all-linear architecture.

2.3.4 Polarization-selective detection method (PSDM)

The aim of the polarization-selective detection method, proposed by M. Zhu [101], is to increase the CPT resonance contrast by selectively reducing the power of off-resonant light that reaches the photodetector. It is based on the atomic vapor dichroism and birefringence, inducing a selective Faraday polarization rotation of the light participating to CPT. In Zhu's experiment, the laser current is directly modulated. Thus, the laser source contains both bands resonant with the atomic transitions and additional harmonics that do not participate to CPT. The light is initially linearly polarized. A first waveplate turns the polarization into circular. After crossing the CPT cell, the light component that is involved in CPT experiences a different phase shift from the non-resonant light. A second waveplate converts the polarization states to linear. An analyzer placed before the photodiode is disposed such that transmission of the off-resonant light is minimized. The set-up is sketched in Fig. 2.13.

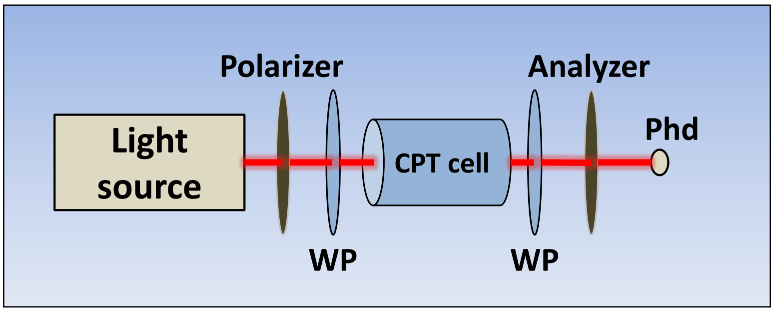

Figure 2.13: Simplified diagram of the crossed polarizers set-up. The light source contains both frequencies that excite the CPT state and additional harmonic frequencies. WP: optional waveplates (to produce circularly polarized light). Phd: photodiode.

High-contrast resonances have been observed with this method. The latter has also been adapted to a lin par lin excitation scheme in continuous regime with Cs [154] and in pulsed regime with Rb atoms [155]. The waveplates are useless in these experiments. J. Lin et al. used this technique to increase the contrasts in a pulsed double-resonance Rb clock. [92]. In reference [156], the PPOP scheme is implemented to a similar polarization selective technique. In this case, the crossed polarized beams at the CPT cell output are separately detected and substracted, resulting in a dispersive signal that cancels at exact resonance.

2.3.5 Feedback Spectroscopy

The principle of feedback spectroscopy does not involve any particular polarization conditions. The group of V. I. Yudin et al. [157] adapted this method to increase the resonance amplitude of atomic resonances. The basic principle is as follows: instead of keeping the laser intensity constant during the frequency scan, another quantity, here the atomic fluorescence, is stabilized by continuously adjusting the laser intensity during the scan. The set-up for a CPT spetroscopy experiment is pictured in Fig. 2.14.

The light source is composed from a master external cavity diode laser (ECDL) frequency locked to a Doppler-free saturated absorption resonance and injected into a slave laser diode modulated at the Rb hyperfine splitting frequency. The CPT cell transmission is detected with photodiode PD_1. The atomic fluorescence is measured with a set of photodiodes PD_2 surrounding the cell. The power level on PD_2 is stabilized by acting on an AOM that controls the laser power at the cell input. When the LO frequency approaches CPT resonance, the atomic population in the excited state (and thus the fluorescence), is strongly reduced. Intuitively, one can easily understand that, to keep the fluorescence level constant during the LO scan, the input power must be increased, raising at the same time the laser power crossing the cell, compared to conventional spectroscopy. By changing the constant parameter during spectroscopy, the authors were able to reach very high contrast and narrow resonances. Figure 2.15 compares the CPT resonance spectrum with usual spectroscopy and with the feedback spectroscopy method. The authors observed a huge increase in the resonance signal amplitude (43 times bigger) as well as a narrowing of the CPT line (from 60 kHz to 20 kHz) when closing the servo loop.

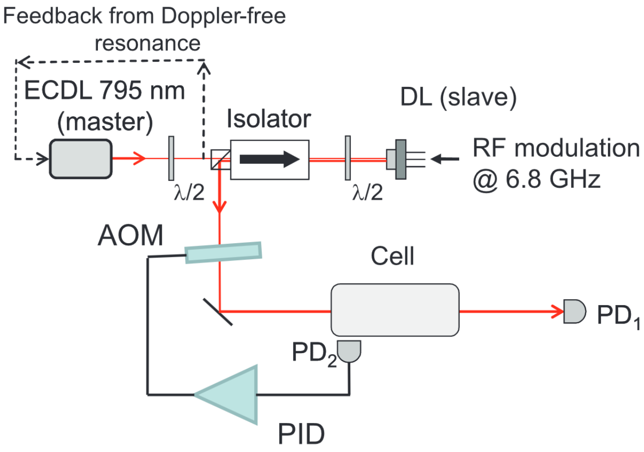

Figure 2.14: Experimental set-up of feedback spectroscopy adapted to CPT. Extracted from [157].

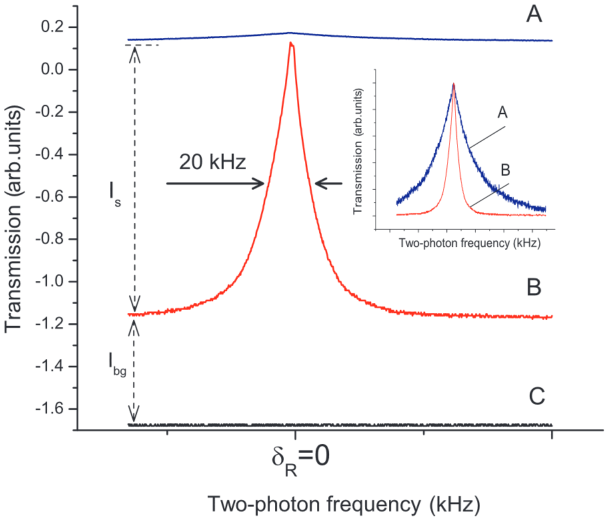

Figure 2.15: CPT transmission (A) in constant laser intensity condition, and (B) in constant fluorescence intensity. (C) is the photodiode signal when there is no light. The inset is the normalized transmission of the resonance in both cases. Extracted from [157].

2.3.6 Summary

I summarize here the principal advantages and drawbacks of the methods described in this section. The lin par lin configuration is the simplest one to realize. It only requires a polarizer before the cell entrance. Nevertheless, even if the contrasts achieved are better than for a single circular polarization scheme, they remain limited compared to other optimized polarization schemes, because the 0-0 CPT resonance is destructed. Furthermore, the resonance central frequency is highly sensitive to magnetic field, which though makes it possibly suitable for CSACs aiming modest stability performances ($\sim 10^{-11}$ at 1 day averaging time), remains inconciliable with high-performance clock applications. Lin per lin allows to reach high contrast levels. Its major drawback is that, unless a dual-frequency and dual-polarization laser is used, it requires two distinct laser sources with orthogonal polarization axis. While the latter scheme is extremely interesting for lab experimentation as only the two laser frequency components required for CPT interaction are produced by the laser sources, it remains complex (two phase-locked lasers) and voluminous, not suitable for the achievement of compact atomic clocks. PPOP and the double-modulation pumping schemes seem to be the more suitable ones for industrialization of compact CPT atomic clocks. These schemes are quite similar. They both have demonstrated high contrast resonances and are relatively easy to set up. The main advantage of the double-modulation set-up is that it allows an all-linear propagation of the interrogation laser beam, with no need for splitting it like in the PPOP set-up. Note that at the time X. Liu et al. started the development of the CPT clock based on PPOP at FEMTO-ST, the double-modulation technique had not been reported yet. The PSDM is really interesting when associated with set-ups where the laser frequency is modulated directly by modulating the current source, or when an electro-optic phase modulator is used, since a high proportion of the laser intensity (carrier and high-order sidebands) does not participate in the CPT interaction. However, as described in the next chapter, we chose in our case to modulate the laser frequency via a Mach-Zehnder electro-optic modulator. The laser intensity in the carrier is suppressed and the spectrum out of the EOM is close to a pure bichromatic spectrum. For this reason, we do not expect much benefits from the PSDM for our set-up. A priori, the feedback spectroscopy technique could be associated with anyone of the optimized pumping schemes defined before and could allow to obtain even greater contrast levels. The perspective of implementing it in our PPOP CPT experiment seems promising and exciting, and could be studied in a near future. The main difficulty will be to adapt the physics package in order to collect the cell fluorescence without any parasitic noise.

Knowing this, we opted for pursuing the development of a Cs CPT clock relying on the PPOP polarization scheme as the purpose of my thesis. Indeed, besides the "historical" reason (a lot of work had already been performed on PPOP when I first arrived at FEMTO-ST), we were convinced that the generation of CPT via PPOP, associated with a single laser source modulated via an intensity EOM would lead to high-contrast resonances, promising a clock with good short-term frequency stability, with an architecture as simple as possible, presenting great potential for compactness. The experimental set-up is described and characterized in details in the next chapter.

Chapter 3

Experimental set-up

In this chapter, I first present a general description of the CPT clock experimental set-up. For each functional block of the clock, a detailed description and characterization is given. I discuss the choices of experimental parameters and how they can affect the clock performances. In the next chapters, I will expose the main results for the CPT clock obtained in the continuous and in the pulsed regimes.

3.1 General description

The experimental set-up is represented in Fig. 3.1. A picture of the optical bench is shown in Fig. 3.2, where the main devices and the laser path are pointed.

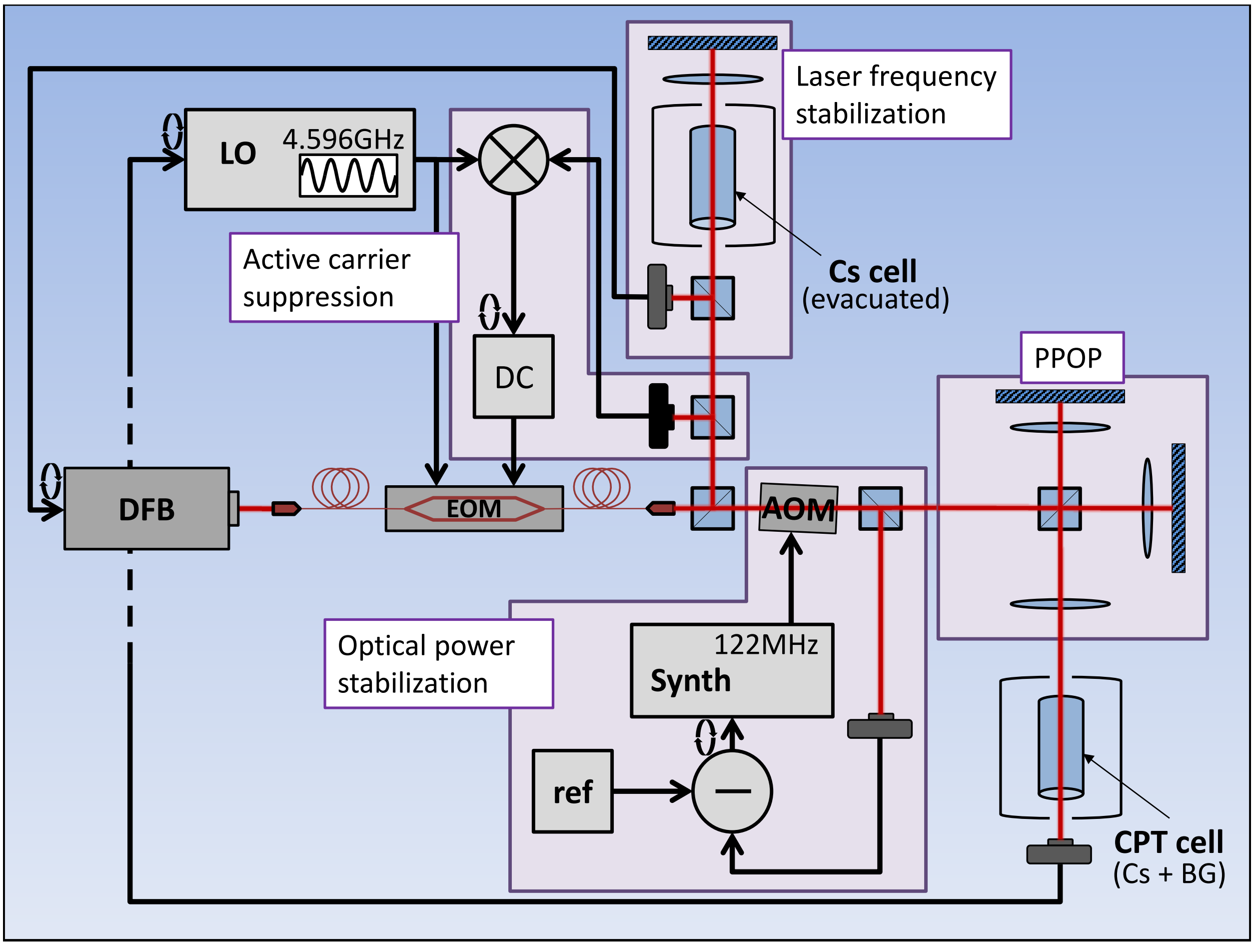

Figure 3.1: Simplified representation of the experimental set-up at FEMTO-ST. DC = stabilized voltage source. ref = ultrastable voltage reference. ⊗ = frequency mixer. ⊖ = comparator. Arrows loop: servo correction.

The CPT clock relies on a distributed feedback (DFB) laser diode emitting at the cesium D_1 line at 894.6 nm. Optical feedback is prevented with two Faraday isolators (70 dB isolation in total). It was observed that a high enough degree of isolation is critical for reaching high frequency stability performances for the laser and for the clock. The laser frequency is externally modulated via an intensity Mach-Zehnder electro-optic modulator (EOM iXblue Photline NIR-MX800-LN-10), driven by a low noise frequency synthesizer oscillating at 4.596 GHz. The first-order optical sidebands generated at the output are separated by 9.192 GHz and are used to perform the CPT interaction. The optical power contained in the carrier is measured with a fast photodiode and it is actively minimized by acting on the DC bias applied on the EOM [120]. A fraction of the output beam is transmitted to a laser frequency stabilization set-up based on Doppler-free spectroscopy in an evacuated Cs cell. The other fraction of the beam crosses an acousto-optic modulator, where only the −1 diffraction order output beam is kept. A radiofrequency (RF) wave of 122 MHz is injected into the AOM. The RF power allows to control the total intensity contained in the −1 order beam and to stabilize it. The AOM can also be used to generate pulse sequences to produce Ramsey-CPT fringes. A Michelson-like device changes the natural linear polarization of the laser field into the push-pull optical pumping scheme, where the beam combines two orthogonal circular polarizations, mutually time-delayed by half the microwave period. This particular polarization scheme allows the detection of high contrast CPT resonances. The beam diameter is expanded to about 2 cm with an afocal system involving two convergent lenses. Finally the beam crosses a glass cell containing the cesium vapor and a buffer

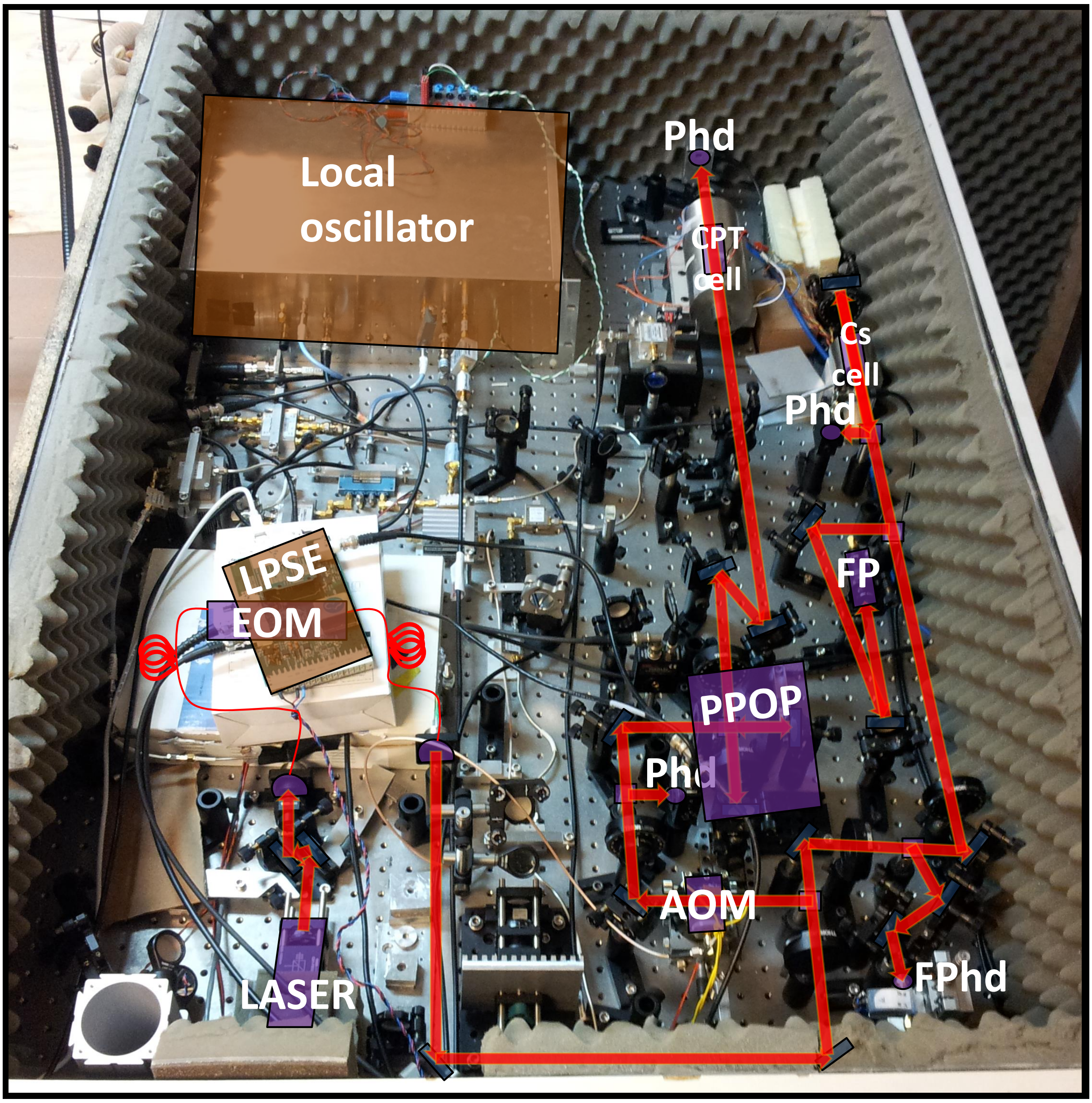

Figure 3.2: Picture of the experimental set-up. Phd: photodiode. FP: Fabry Perot cavity. LPSE: laser power stabilization electronics. EOM: Mach-Zehnder intensity modulator. PPOP: Michelson-like system. AOM: acousto-optic modulator. FPhd: fast photodiode.

gas mixture. We will call it the CPT cell. This cell is included in a physics package that ensures temperature and static magnetic environment stabilization. The transmitted light is detected with a photodiode, and the obtained CPT signal is processed by a servo to lock the synthesis output frequency on the atomic resonance.

3.2 Laser

3.2.1 Description

Optical lines needed to trap the cesium atoms into the CPT state are produced by a Distributed Feedback Laser (DFB)-type laser source (Eagleyard EYP-DFB-0895), emitting at the cesium D_1 transition wavelength (894.6 nm). This kind of laser benefits from a MHz-linewidth while taking very little space since it does not present any external cavity. Figure 3.3 is a picture of the laser ensemble. The laser diode is arranged in a TO-3 package, housing a thermistance and a Peltier module. The

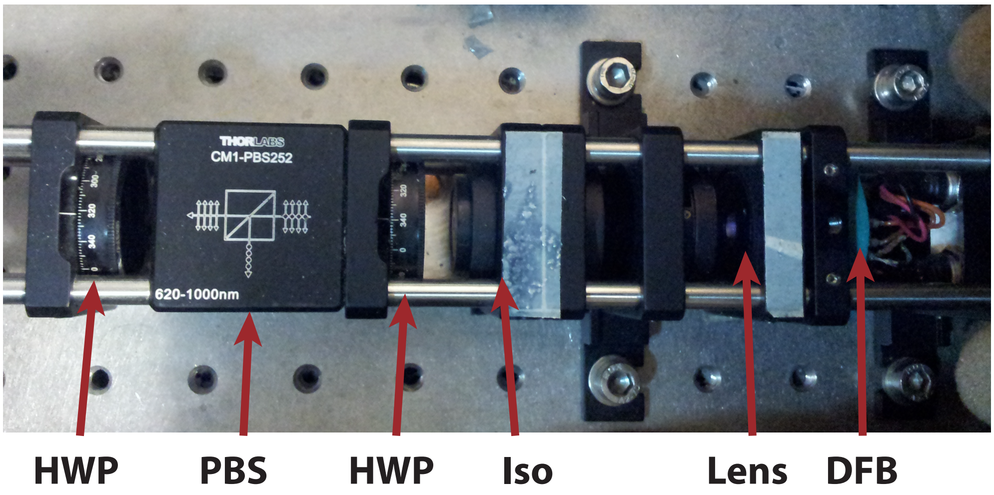

Figure 3.3: Photograph of the laser ensemble. HWP: half-wave plate. PBS: polarizing beam-splitter. Iso: optical isolator.

diode temperature is actively stabilized using a high performance commercial electronic temperature controller (LaserLabs TC 2). The Cs D_1 frequency is reached for a laser current of 192 mA and a temperature of 24.3 °C. The output power is 105 mW. The datasheet [158] mentions a frequency sensitivity to laser current of -1.1 GHz/mA and a sensitivity to temperature of -22 GHz/K. The ensemble is placed in a cage system which contains a collimating lens, an optical isolator (35 dB isolation), a half-wave plate and a polarizing beam splitter (PBS). The latter allows to collect a fraction of the beam before the EOM input. A second stage of isolation (35 dB isolation) is added to prevent laser feedback effects, which have been shown to strongly degrade the laser frequency stability. The laser frequency is stabilized by correcting the laser bias current.

3.2.2 Characterization

3.2.2.1 RIN

Figure 3.4a shows the relative intensity noise (RIN) of the DFB laser, measured as represented in Fig. 3.4b. A small fraction of the laser beam power is diverted via a PBS, and attenuated with a neutral density filter. A photodiode is placed on the beam path. The PSD of the photodiode output voltage signal S_V (in dBV^2/Hz) is measured with a Fast Fourier Transform (FFT) analyzer (HP 3561A). Another reference acquisition is done with a cap on the photodetector to take into account its intrinsic noise $S_{V_{dark}}$. The total power at the laser output is 80 mW. It is attenuated with a neutral density filter and the mean value of the photodiode signal voltage is 1.05 V. The laser RIN (in dB/Hz) is obtained as following:

$$RIN(f) = 10\log\left(\frac{10^{S_V(f)/10} - 10^{S_{V_{dark}}(f)/10}}{1.05^2}\right) \tag{3.1}$$

We observe that the dominating noise for Fourier frequencies up to around 1 kHz is flicker (f^{-1} slope). The trend is -112.5 f^{-1}dB/Hz (5.6 10^{-12} f^{-1} Hz^{-1}). A noise floor is reached after several kHz at -143 dB/Hz (5.0 10^{-15} Hz^{-1}). We measure a value of -123 dB/Hz at 10 Hz, -133 dB/Hz at 100 Hz and -143 dB/Hz at 10 kHz. According to the RIN measurement, we expect typical fractional fluctuations of the laser power at the level of 2.6 10^{-5} at 1 s integration. For example, if the laser mean power is 200 µW, the expected fluctuations of laser power would be of the order of 5 nW.

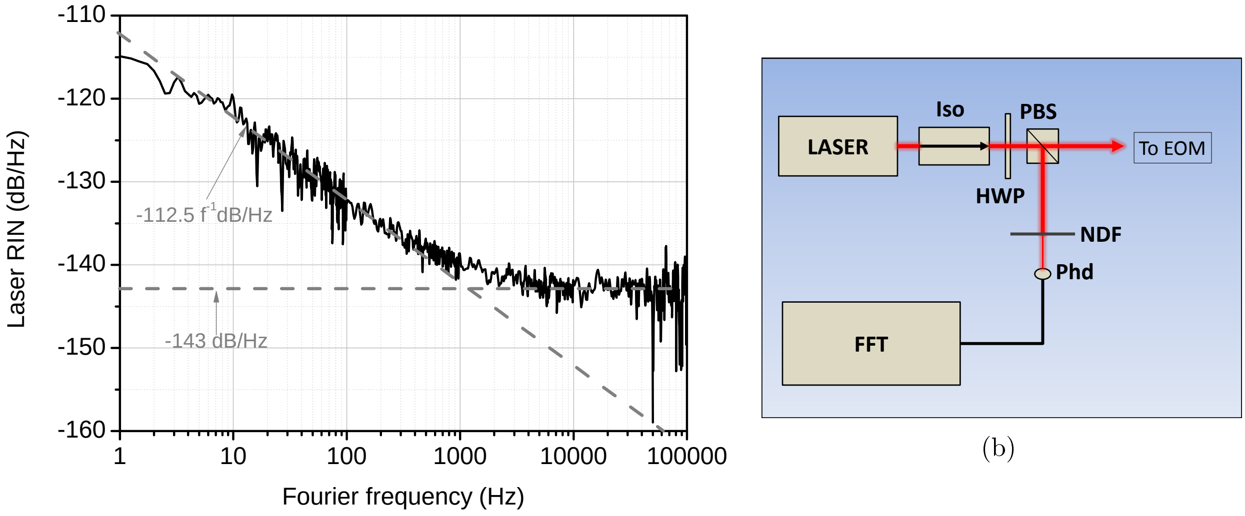

(a)

(b)

Figure 3.4: (a) Black: laser relative intensity noise in free regime for a laser output power of 80 mW. Grey dashed: asymptots with values of -112.5 f^{-1}dB/Hz ($5.6\ 10^{-12}$ f^{-1} Hz^{-1}) and -143 dB/Hz ($5.0\ 10^{-15}$ Hz^{-1}). (b) Laser RIN measurement set-up.

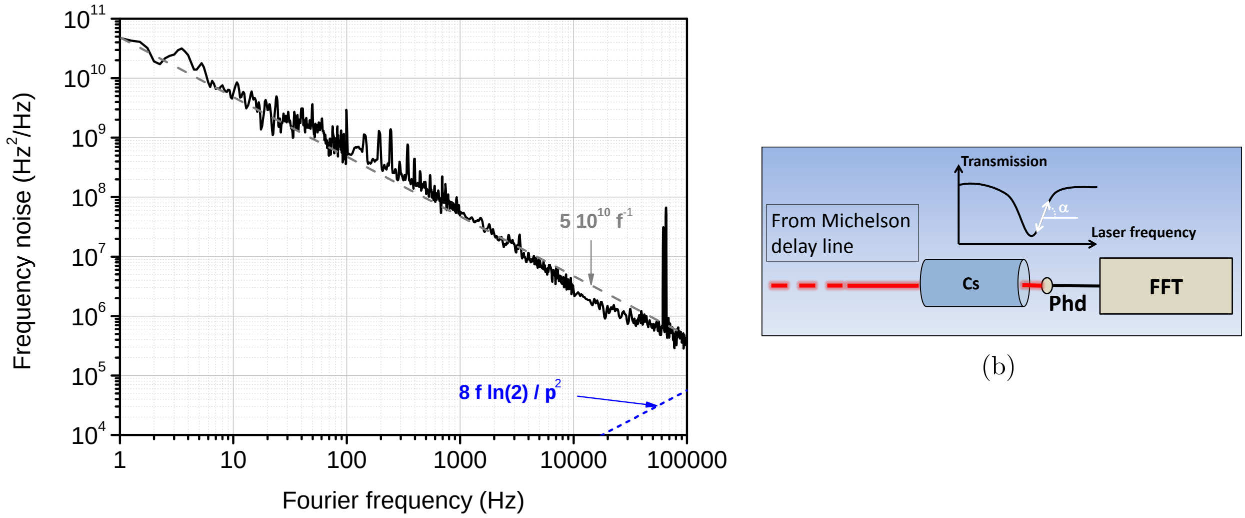

(a)

(b)

Figure 3.5: (a) Black: DFB frequency noise in free regime. Dashed: theoretical noise spectrum at the level of $5\ 10^{10}$ f^{-1} (in $\mathrm{Hz}^2/\mathrm{Hz}$). (b) Measurement set-up.

3.2.2.2 FM noise

Figure 3.5a shows the DFB FM noise in free-running regime. For this purpose, an evacuated Cs cell is placed before a photodiode as shown in Fig. 3.5b. The laser frequency is tuned at half the amplitude of a Cs absorption line. The frequency to voltage coefficient α (in V/Hz) is measured. A noise spectrum is then collected from the photodiode signal. A reference spectrum is achieved with no cell and with the same laser power hitting the photodiode. This reference spectrum is substracted from the previous one, resulting in a pure laser frequency noise, converted in the cell to amplitude noise. We multiply the obtained voltage noise data by α^2 to obtain the laser frequency noise spectrum in Fig. 3.5a. In this experiment, the analyzed light beam originates from the EOM output. No microwave signal drives the EOM. Since the noise spectra are not measured at the direct laser output, the measured data are expected to be slightly higher than the real laser noise. However, this should be closer to the frequency noise of the light crossing the vapor cell. In any case, we will assume that the laser diode frequency noise largely prevails on the additional contributions from the optics on the beam path. The spectrum is well fitted by a curve with equation $S_{\Delta\nu}(f) = 5\ 10^{10} f^{-1}\text{Hz}^{-1}$ for Fourier frequencies up to 100 kHz. We measure a value of 5 10^9 Hz^2/Hz at 10 Hz, 5 10^8 Hz^2/Hz at 100 Hz and 3 10^6 Hz^2/Hz at 10 kHz.

We can estimate from FM noise measurements the frequency stability of the laser in free regime. We use the coefficient h_{-1} of Table 1.1. Here $h_{-1} = \frac{(5\ 10^{10})}{(\nu_L)^2} = 4.6\ 10^{-19}$, where the laser frequency ν_L is 335 THz. According to Table 1.1, the Allan deviation of the laser frequency is estimated by $\sigma_y(\tau) = \sqrt{2 \ln 2\ 4.6\ 10^{-19}}$. We find $\sigma_y(\tau) = 8.0\ 10^{-10}$. A frequency stability measurement, described in subsection 3.4.1, has been performed, yielding 1.5 10^{-9} at 1 s averaging time, in reasonable agreement with the FM noise measurement.

3.2.2.3 Linewidth

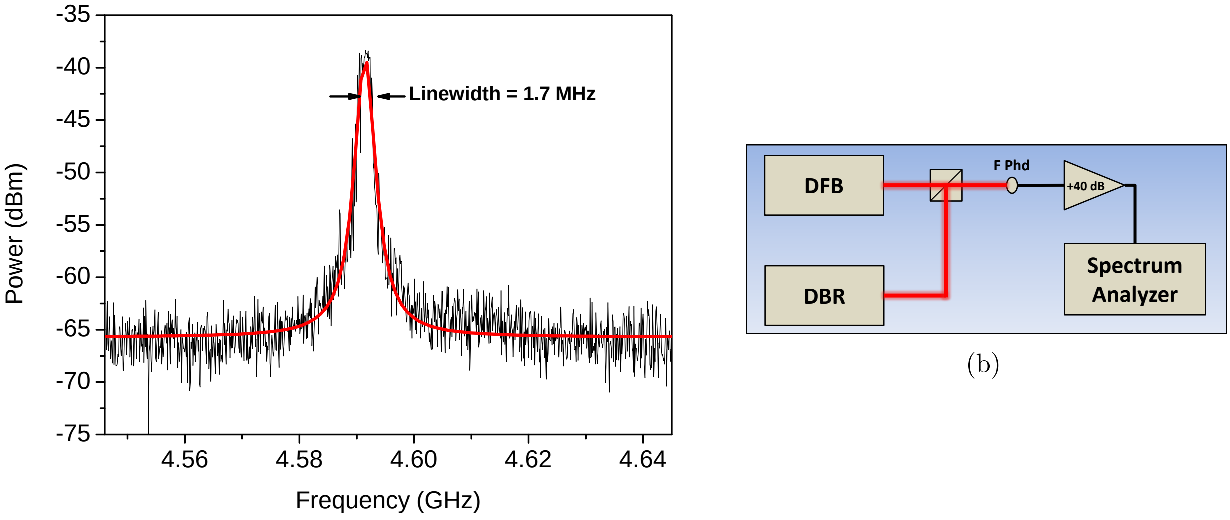

(a)

(b)

Figure 3.6: (a) Spectrum of the beatnote between the DFB laser and a DBR laser. (b) Simplified diagam of the laser linewidth measurement set-up.

We have measured the linewidth of the DFB laser output spectrum. In order to estimate it, the reflected beam out of the beamsplitter is superimposed with a beam from a distributed Bragg reflector (DBR) laser module (Vescent D2-100-DBR). The frequency difference between the two lasers is set at about 4.59 GHz. The beatnote is detected with a fast photodiode (Hamamatsu MSM G4176-03), amplified by 40 dB, and monitored on a spectrum analyzer (Agilent E4407B). The obtained spectrum is shown in Fig. 3.6a. This spectrum is fitted by a Lorentzian distribution with a full width at half maximum ($FWHM$) of 1.7 MHz. Since it is the result of the convolution of two spectra from the DFB and the DBR lasers, and if we suppose that both diodes share approximately the same linewidth, then the width of a single laser is given by $\frac{FWHM}{\sqrt{2}}$, i.e. 1.2 MHz. This value is in good agreement with the linewidth measurement of a DFB laser emitting on the Cs D$_1$ line performed by Liu et al. [159]. Di Domenico et al. demonstrated that the spectrum linewidth of a laser can be estimated from its frequency noise spectrum [160, 161]. The relationship is:

$$FWHM = \sqrt{8A \ln(2)} \tag{3.2}$$

where the quantity A is defined as the surface below the frequency noise spectrum for Fourier frequencies between $1/T_0$ and f_{limit}. T_0 is the measurement time. The signal analyzer sweep time was $T_0 = 4\,\text{ms}$ during the measurement. f_{limit} is defined as the Fourier frequency at which the PSD of laser frequency fluctuations $S_{\Delta\nu}$ crosses the line defined by $\frac{8f\ln 2}{\pi^2}$, here 300 kHz. Considering that the laser frequency noise is flicker, A can then be written:

$$A = \int_{1/T_0}^{f_{limit}} S_{\Delta\nu}(f)df = \int_{1/T_0}^{f_{limit}} h_{-1}f^{-1}df = h_{-1}\ln\left(f_{limit}T_0\right) \tag{3.3}$$

We get a value for A of $3.5\ 10^{11}\,\text{Hz}^2$. From Fig. 3.5a we note that f_{limit} is around 300 kHz. Finally we estimate from Eq. (3.2) that $FWHM \approx 1.4\,\text{MHz}$, in correct agreement with the linewidth measurement.

3.3 EOM

The laser is frequency modulated at half the Cs hyperfine frequency (4.596 GHz), so that the first order optical sidebands separation is 9.192 GHz, i.e. the clock transition frequency. An external pigtailed Mach-Zehnder modulator (iXblue Photline NIR-MX800-LN-10) with polarization-maintaining (PM) fiber and FC/APC connectors, shown in Fig. 3.7a, is used. The EOM is placed in a thermally regulated enclosure.

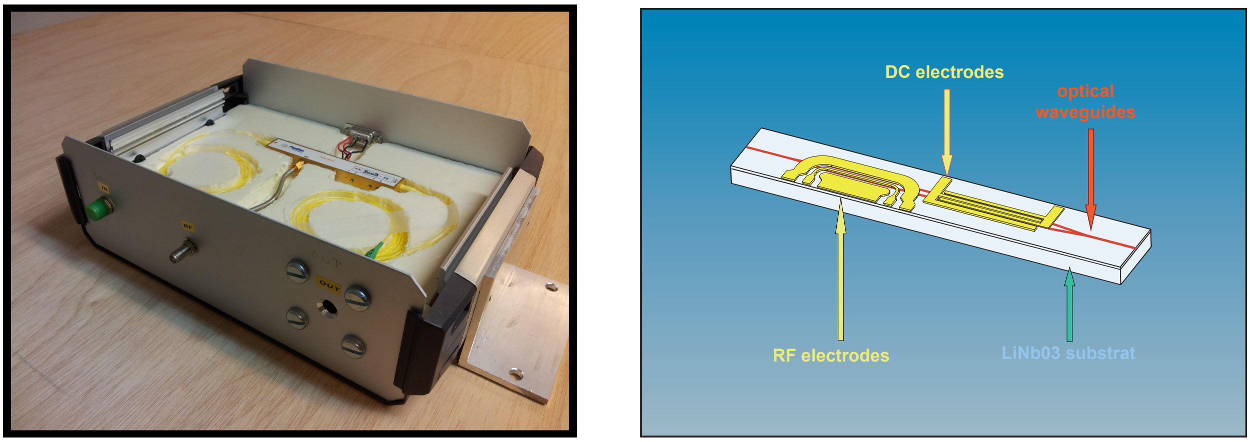

(a) (b)

Figure 3.7: (a) Picture of the EOM. The EOM package was realized by P. Abbé. (b) Functional diagram of a typical Mach-Zehnder EOM. Extracted from [162].

3.3.1 Description

The beam is injected into the EOM admission fiber, and then splits into two $LiNbO_3$ waveguides, whose refractive index depends on the applied electric field. Two electrode ensembles are arranged around the arms to apply on them a microwave field and a DC field (see Fig. 3.7b).

Owing to the interference mechanism, the power P at the output of a MZ EOM for a given input power P_0 is given by:

$$P = P_0\cos^2\left(\frac{\phi_0}{2} - \frac{\pi}{2}\frac{V}{V_\pi}\right) = \frac{P_0}{2}\left[1 - \cos\left(\phi_0 - \pi\frac{V}{V_\pi}\right)\right] \tag{3.4}$$

where ϕ_0 is a phase that results from actual length of the arms and ultimately from the manufacturing process, V is the control voltage, and V_π is the value of V needed to shift the differential phase by π. Intensity mismatch between the two arms results in a residual power at the output not included in Eq. (3.4), and expressed by the extinction ratio parameter for the modulator. In general, the so-called dark point and half-power point, shown in Fig. 3.8, are two operating conditions of great

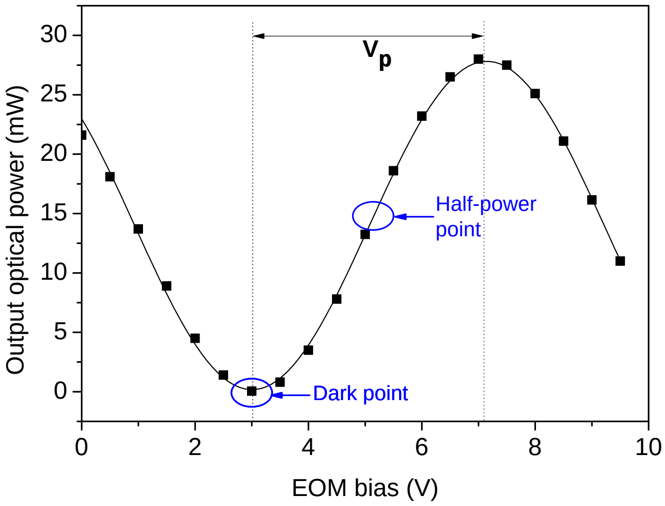

Figure 3.8: Optical power at the EOM output as a function of the bias setpoint. Black squares: data. Black line: sine fit.

interest. Here we will only focus on the dark point, which allows us to minimize the carrier power at the EOM output.

At the exact dark point, the EOM transmitted power is an even function of the control voltage. The modulator acts as a maximally-efficient frequency doubler for the microwave modulation frequency Ω. Consequently, the fundamental frequency Ω is ideally absent in the optical output. In this case, we note and replace in Eq. (3.4) $\phi_0 \to \phi_{dc}$ for the dc point and $-\pi V/V_\pi \to \phi_p \cos(\Omega t)$ for the microwave modulation. Since the operation is ideally kept at the exact dark point, it is legitimate to assume that ϕ_{dc} is a small quantity, hence to approximate $\sin\phi_{dc} \approx \phi_{dc}$ and $\cos\phi_{dc} \approx 1$. Accordingly, Eq. (3.4) rewrites as:

$$P(t) = \frac{P_0}{2}\{1 - \cos[\phi_{dc} + \phi_p \cos(\Omega t)]\} \tag{3.5}$$

$$P(t) \approx \frac{P_0}{2}\{1 - \cos[\phi_p \cos(\Omega t)] + \phi_{dc} \sin[\phi_p \cos(\Omega t)]\} \tag{3.6}$$

Further, we use the following expansions derived from the Jacobi-Anger identity:

$$\cos(z\cos\theta) = J_0(z) + 2\sum_{n=1}^{\infty}(-1)^n J_{2n}(z)\cos(2n\theta) = J_0(z) - 2J_2(z)\cos(2\theta) + ... \tag{3.7}$$

$$\sin(z\cos\theta) = -2\sum_{n=1}^{\infty}(-1)^n J_{2n-1}(z)\cos[(2n-1)\theta] = 2J_1(z)\cos\theta - 2J_3(z)\cos(3\theta) + ... \tag{3.8}$$

$J_i(z)$ are Bessel functions of the first kind. The power at the modulator output is given by:

$$P(t) = \frac{P_0}{2}[1 - J_0(\phi_p) + 2\phi_{dc}J_1(\phi_p)\cos(\Omega t) + 2J_2(\phi_p)\cos(2\Omega t) - 2\phi_{dc}J_3(\phi_p)\cos(3\Omega t) + ...] \tag{3.9}$$

Equation (3.9) evidences that the beam power at the EOM output is spectrally distributed over the laser carrier frequency ν_L and frequencies corresponding to $\nu_L + n\frac{\Omega}{2\pi}$ where n is a relative integer. The power repartition between the carrier and the sidebands depend on the microwave modulation depth ϕ_p and on the DC dephasing ϕ_{dc} between the arms of the Mach-Zehnder interferometer.

In the following, I will expose the results of the EOM characterization and define the experimental conditions we chose for the laser modulation.

3.3.2 EOM characterization

3.3.2.1 Carrier suppression

Exctinction ratio and half-wave voltage A power meter is placed at the output of the EOM when no microwave field is applied on the latter. The optical power is measured as a function of the applied bias voltage (see Fig. 3.8).
The measured half-wave voltage is $V_\pi = 4.14\,\mathrm{V}$. This is low enough to ensure that at least one carrier suppression point can be found using a variable voltage source with 10 V maximum output. The extinction ratio is 27.5 dB. With this, we are confident that the laser spectrum out of the EOM is very close to the one from two phase locked distinct laser sources.

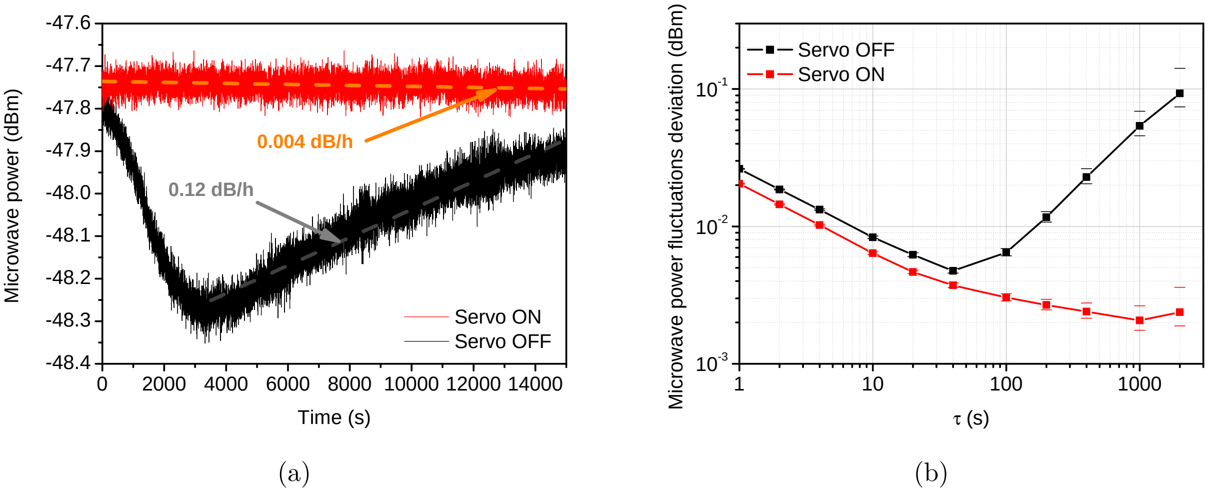

(a) (b)

Figure 3.9: (a) Microwave power at 4.6 GHz contained in the EOM optical output with (red) and without servo (black) and (b) associated deviation.

Stabilization The EOM bias voltage is delivered by a stabilized voltage generator. It is initially set to suppress the carrier at the output of the EOM, at the darkpoint shown in Fig. 3.8. Nevertheless, without any active stabilization, this setpoint is likely to drift due to temperature fluctuations, photorefractive effects, static charges accumulation, etc., that induce fluctuations of the Mach-Zehnder optical path difference. This limits the stability of carrier suppression. The black line of Fig. 3.9a shows the carrier power evolution with time, when the stabilization loop is open. We observed a typical drift of the carrier suppression of 0.12 dB/h. It is then necessary to lock the bias voltage so that it follows the carrier suppression point. To this aim, a dark point stabilization set-up, shown in Fig. 3.10, is implemented.
For this purpose, a fraction of the EOM output beam is sent to a fast photodiode and the collected microwave signal is amplified, filtered around 4.6 GHz to select only the term in Eq. (3.9) that oscillates at Ω, and then mixed with the 4.596 GHz signal coming from the LO driving the EOM. The mixer is saturated at the LO input, and receives a small signal $V_{\mu w}\cos(\Omega t)$ at the RF input, where $V_{\mu w}$ is proportionnal to ϕ_{dc}. In this condition, it operates as a synchronous detector. The output signal, after low-pass filtering with a 1.9 MHz bandwidth, is $V_{out} = \frac{2}{l_m} V_{\mu w}$, where l_m is the single-sideband modulation loss of the mixer, and the factor 2 is due to the overlapping of the lower and upper sidebands in the synchronous conversion. The resulting error voltage V_{out} crosses zero at the carrier minimization point. A servo loop is then used to stabilize this EOM setpoint by adjusting permanently the bias voltage. The electric diagram of the EOM carrier suppression stabilization box is given in appendix Fig. D.1. The red line of Fig. 3.9a shows the carrier power evolution when the suppression setpoint is stabilized. It is reduced to the level of 0.004 dB/h, i.e. a factor of 30 improvement. FFT measurements of the error signal generated by the servo in closed or open loop conditions are shown in Fig. 3.11, and attest a servo bandwidth of 10 kHz.

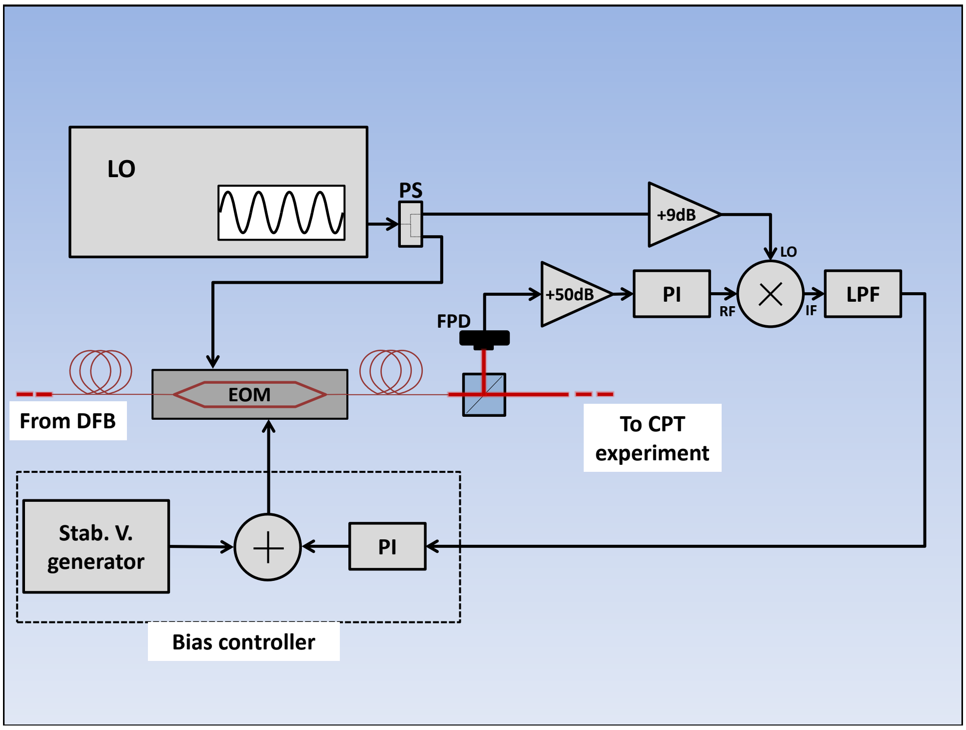

Figure 3.10: Scheme of the carrier suppression setpoint stabilization set-up. FPD = fast photodiode. BPF = band-pass filter at 4.6 GHz. LPF = low-pass filter with 1.9 MHz cut-off frequency. PI = proportional integrator. PS = power splitter. ⊗ = frequency mixer. ⊕ = summer. 50 dB = amplifiers (AML412L2001 + NEXTEC NBL00419). 50 dB = amplifier (ZX60-8008E+). Stab. V. generator = variable voltage source relied on an ultrastable low drift reference voltage (LM399).

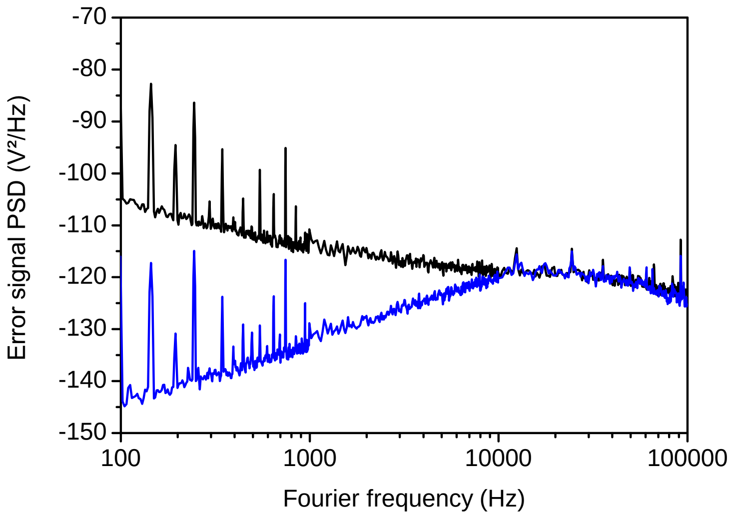

Figure 3.11: FFT spectrum of the error signal from the EOM setpoint stabilization servo in locked (blue) and unlocked (black) conditions.

A critical weakness in this setup is identified and has to be taken care of. Since the RF mixer is used as a synchronous detector in our experiment, the effective setpoint depends on the value of the DC offset voltage of the mixer. Then the mixer has to be chosen such that this offset is as low as possible. Nevertheless, a static offset can be compensated by adding "artificially" a voltage to the error signal sent to the PI servo. In this case, fluctuations of this offset value would become the major issue, participating to the instability of the light intensity interacting with the vapor.

Monitoring The relative power contained in the carrier and the first order bands is continuously monitored with the help of a 10 GHz **F**ree **S**pectral **R**ange (FSR) scanning Fabry Perot (FP) interferometer (Thorlabs SA210). Examples of Fabry Perot spectra are shown in Fig. 3.12a. While scanning the FP cavity length, the different orders of the EOM output are revealed as transmission peaks, in a pattern repeated every free spectral range (FSR) of the cavity (see the schematic representation in Fig. 3.12c). The peaks amplitudes corresponding to the carrier and the first order lateral bands are measured as a function of the DC control voltage. The result is shown in Fig. 3.12b.

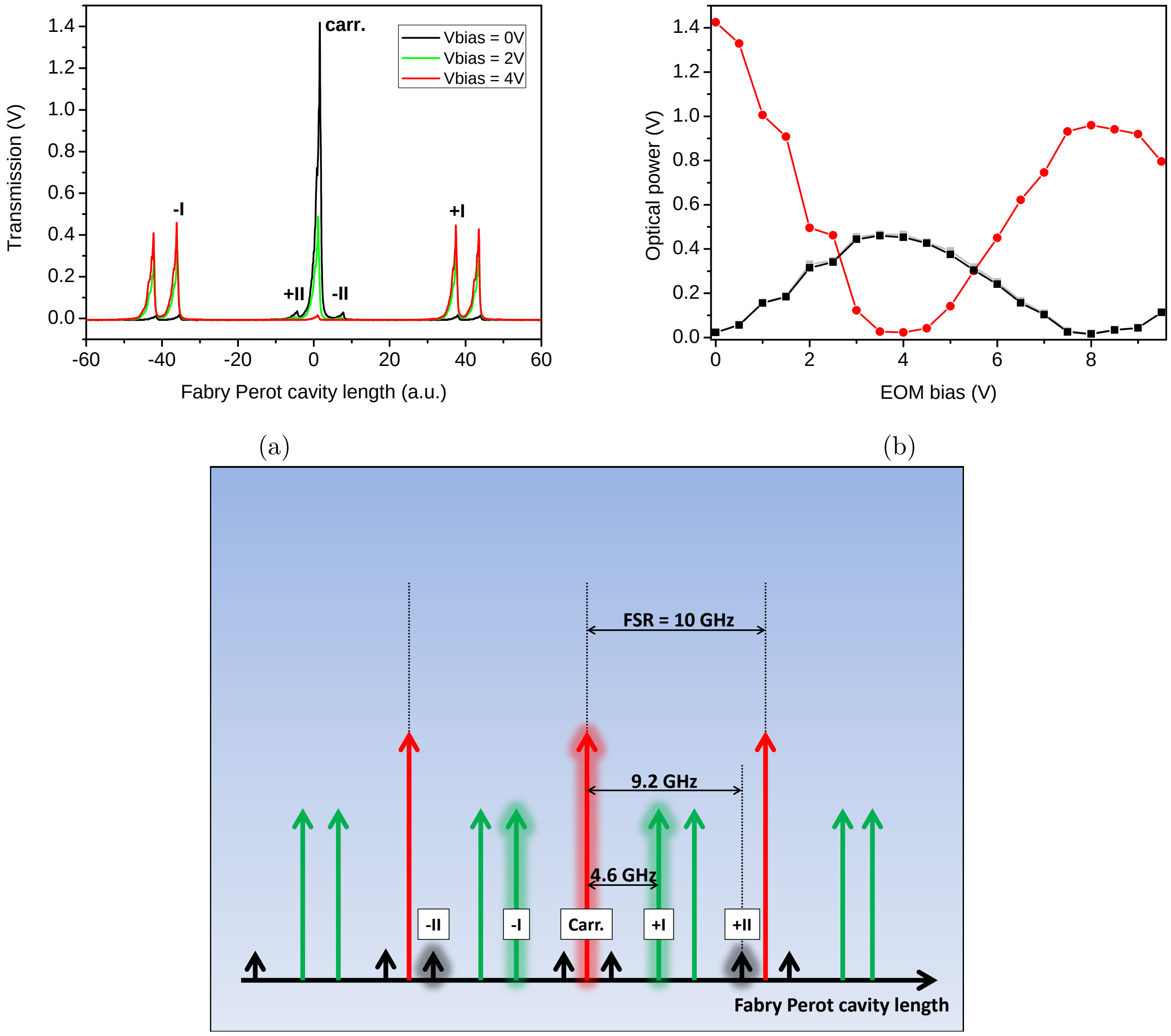

(a) (b)

(c)

Figure 3.12: (a) Typical spectra obtained with the Fabry Perot cavity for different bias voltages applied on the EOM. Red line: carrier minimized: black line: carrier maximized; green line: intermediary working point. (b) Repartition of the optical power over the carrier and the first order sidebands as a function of the bias voltage. Red circles: carrier; black squares: +I order sideband; grey squares: -I order sideband. (c) Representation of the FP output spectrum. Only the carrier and orders ±I and ±II sidebands are taken into account. The highlighted bands belong to the same reflection order in the FP cavity.

We observe that the optical power is maximum in the first order sidebands when it is minimum in the carrier. This is in good agreement with the expected behavior of the Mach-Zehnder interferometer. We set the EOM bias such that the carrier power is minimum. However we are not able to explain the difference in the maximal values of the carrier power obtained for bias voltages separated by $2V_\pi$.

3.3.2.2 Temperature behaviour

We measured the EOM transmission as a function of its temperature. The microwave signal driving the EOM is on. The result is shown in Fig. 3.13.

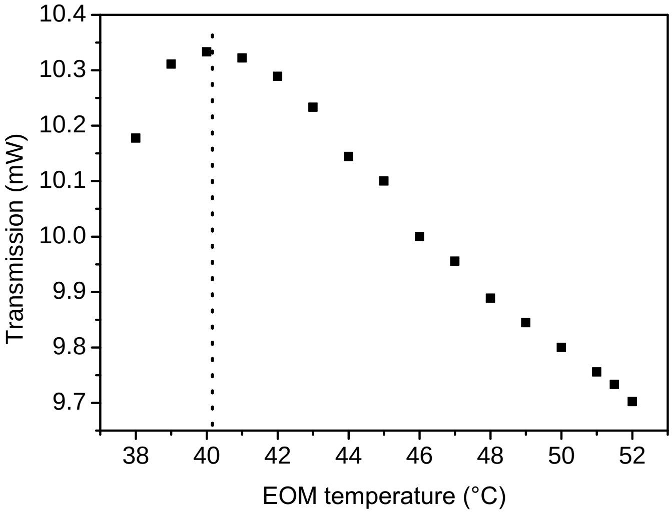

Figure 3.13: Transmitted power at the output of the EOM as a function of its working temperature. A turnover is found for T = 40.2 °C.

We observe that the transmission reaches a maximum value at a temperature inversion point of 40.2 °C. It is convenient to work at this point since sensitivity of the EOM output power to temperature is canceled at first order. We can locally fit the data by a quadratic function around the turnover such that the second order coefficient is $-13.9\,\mu\mathrm{W/K}^2$. The EOM module and its input and output fibers are thermally isolated in a dedicated box filled with insulating foam, shown in Fig. 3.7a. The temperature is monitored with a negative temperature coefficient (NTC) thermistor in thermal contact with the EOM package, and is actively stabilized with a temperature controller whose diagram is shown in appendix Fig. D.2. The controller drives the current flowing through a heating resistor placed on the EOM module and stabilizes the temperature at the inversion point. We monitored the temperature fluctuations of the EOM, measured with a different thermistor present inside the EOM module. The EOM package was placed on the optical bench during the measurement, in closed environment. The logged data points are presented in Fig. 3.14a. The Allan deviation of the EOM temperature fluctuations is computed from the data file and is shown in Fig. 3.14b.

The reached temperature stability is around 12 µK at 1 s and around 300 µK at 10 000 s. The thermal gain coefficient of the structure is around 200 at 1 s. If we suppose the EOM is stabilized at the temperature-insensitive point with an error of 0.1 K, the expected fractional power fluctuations at the EOM output due to temperature are less than $3.3\ 10^{-9}$ at 1 s averaging time.

3.3.2.3 Effect on the laser RIN

We studied the change in laser RIN after crossing the EOM. The photodiode was placed on the laser path before and after the EOM. The incident laser power on the photodiode is set at 900 µW. The PSD of the output voltage is measured with the FFT analyser. Figure 3.15 shows the laser RIN before the EOM and after for different values of the repartition of optical power between the carrier and the first order lateral bands. The RIN is obtained using Eq (3.1).

We observe a degradation of the laser RIN after crossing the EOM. At the moment, the reasons for such a behavior are not determined yet. The noise level is found to be dependent on the DC bias control. It reaches a minimal value when the total power is approximately equally distributed over the carrier and the lateral bands. It is around 3 dB higher than before the EOM. The noise is much higher at the carrier suppression point, which is the desired working point. In this case, the RIN is

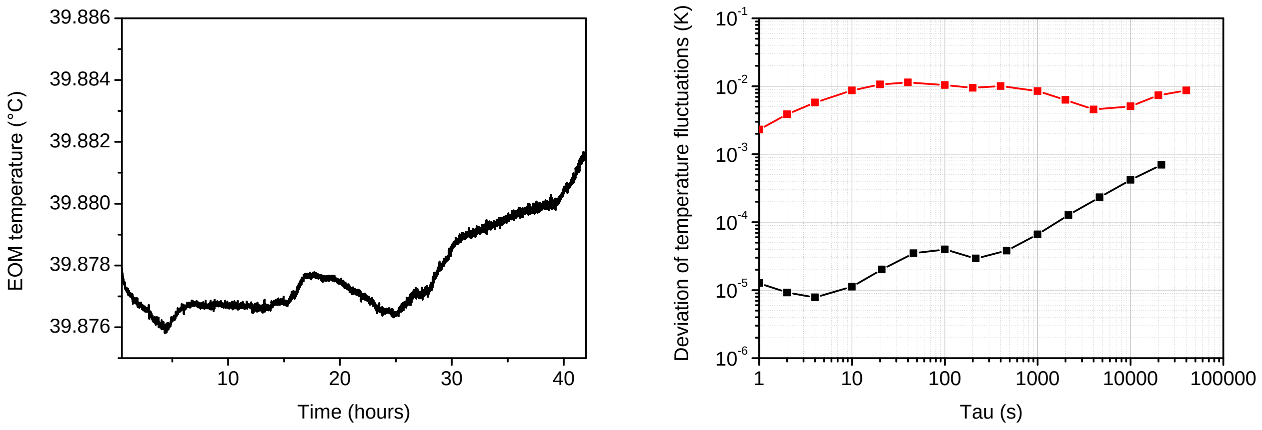

(a) (b)

Figure 3.14: (a) Typical temperature fluctuations of the EOM and (b) associated deviation. Black: EOM. Red: optical bench.

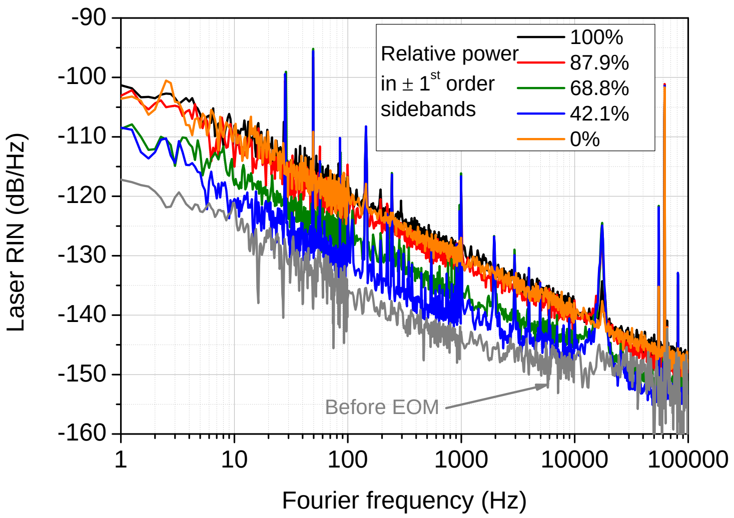

Figure 3.15: Laser RIN at the output of the EOM for several optical power distributions over the carrier and the first order bands. The percentages represent the ratio of the power contained in first order bands over the total power contained in the carrier and the first order.

approximately 15 dB higher than at the direct laser output. Furthermore, a long-term drift of the laser power has been observed at the EOM output, attributed to thermal effects. It is then necessary to lock the laser intensity at the EOM output with a large servo bandwidth to reduce the power noise level, especially close to the LO modulation frequency.

3.3.2.4 Microwave power

The microwave signal is released by a local oscillator, whose architecture is described in section 3.5. The signal is split in a 4-channels splitter. One arm is driven to the mixer for carrier suppression stabilization. We measured with the FP mentionned above the optical power contained in the carrier and first order lateral bands as a function of the microwave power driving the EOM. During the experiment, the EOM bias was stabilized on the carrier minimization point. The ratio between the optical powers contained in the first order bands and the carrier is reported in Fig. 3.16 as a function of the microwave power injected in the EOM.

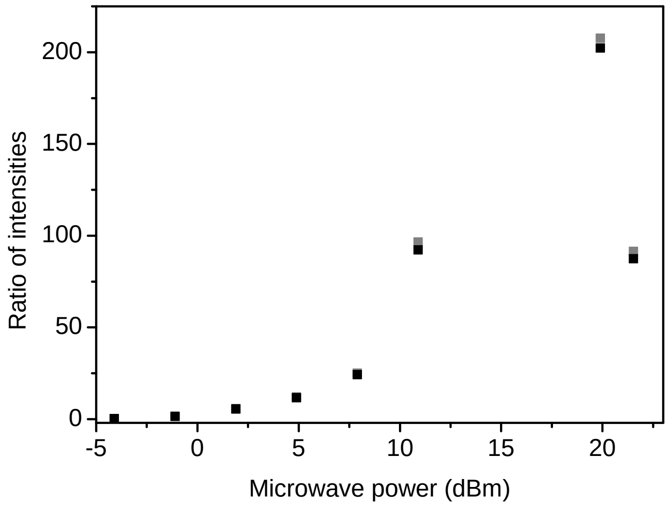

Figure 3.16: Ratio of intensities contained in the first order bands and in the carrier (black squares: +1 / carrier; grey squares: -1 / carrier) as a function of the EOM input microwave power. Between 13 dBm and 20 dBm, the carrier intensity was too low to be measurable with the oscilloscope.

We adjust the microwave power on the EOM such that the proportion of optical power is minimum in the carrier to approach an ideal bichromatic laser field. Between 13 dBm and 20 dBm, the carrier intensity is close to zero and was not measurable with the oscilloscope. We choose to inject a microwave power of about 20 dBm.

3.4 Laser frequency stabilization

3.4.1 Doppler-free spectroscopy

It is of critical importance for the laser frequency to be stabilized in order to achieve a high performance CPT clock. Laser frequency noise can indeed induce an increase of the AM noise on the photodetector via PM-AM conversion, leading to a degradation of vapor cell atomic clocks short-term stability[163]. Moreover the atomic levels are shifted via the AC Stark effect [164] when the detuning from atomic resonance is finite. The laser frequency can either be stabilized on an external cavity transmission mode or on an atomic resonance line. We use here the second technique.

In gas cell experiments, saturated absorption spectroscopy or Doppler-free spectroscopy [165, 166] is an elegant technique to circumvent Doppler broadening and to allow the detection of natural-linewidth resonance dips in the bottom of absorption profiles. This method, frequently used to stabilize the frequency of a laser to a particular atomic line, is applied in atomic frequency standards [40], magnetometers [167], laser-cooling experiments [5] or atom interferometry.

In a common saturated absorption scheme, two counter-propagating laser beams of same frequency, a pump-beam and a probe beam, derived from a single laser beam, overlap one another in an atomic vapor cell. Since both beams have the same frequency, the Doppler effect brings different velocity groups into resonance with each beam. On resonance, only atoms presenting zero velocity along the light propagation axis actually experience the two beams with the same laser frequency. If the pump-beam intensity is high enough, the ground state is depleted and therefore the absorption of the probe beam is reduced compared to the case without pump beam. In this case, a so-called Lamb dip, with lorentzian profile, appears at the resonance frequency of the atomic transition in the bottom of a gaussian Doppler-broadened absorption profile. The full-width at half maximum (FWHM) of the Doppler-free Lamb dip can be at low laser intensity as small as the natural linewidth of the atomic transition (4.6 MHz for the Cs D_1 line). This process is relatively easy to understand in the case of a simple two-level atom with a single-frequency laser system. In real experience, alkali atoms exhibit a complex multi-level energy structure with hyperfine structure splitting and numerous Zeeman sublevels, especially in the Cs case (see Fig. 2.7). Such multi-level structures can lead, under appropriate conditions, to a sign reversal of saturation resonances [168–170]

In many Cs CPT clocks, including chip-scale atomic clocks (CSAC)[98] and ours, the laser is modulated at 4.596 GHz (half of the Cs atom clock frequency). In this configuration, both first-order optical sidebands induce the CPT process and the laser carrier frequency needs to be frequency-stabilized 4.596 GHz away from Cs resonance transition. In CSACs, the laser frequency is currently stabilized onto the bottom of a homogeneously broadened optical line detected in the buffer-gas filled CPT cell, leading to modest laser frequency stabilization.

In a first step, with the initial objective to construct a clock architecture as simple as possible, the laser of our CPT clock was frequency stabilized using this method, i.e. on the bottom of the homogeneously broadened optical line (a few hundred MHz linewidth) of the buffer gas-filled CPT cell. Figure 3.17 represents the typical fluctuations observed on the laser and the clock frequencies in this case. For this purpose, we measured the beatnote frequency between this laser and a reference DFB laser frequency-stabilized using saturated absorption technique.

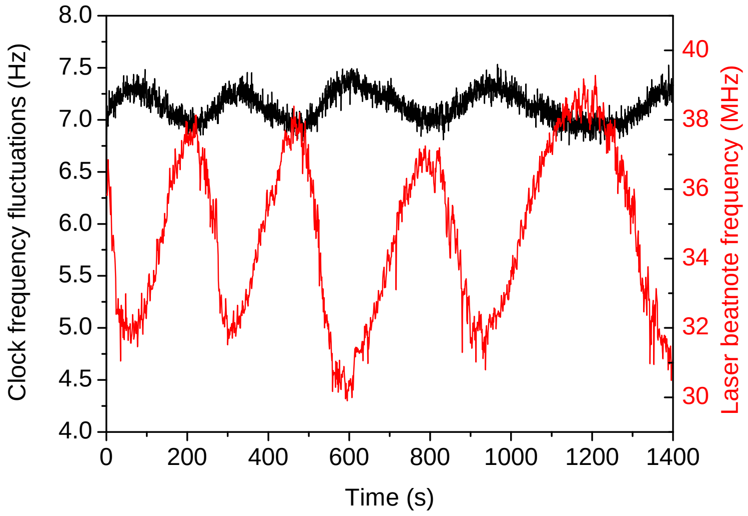

Figure 3.17: Correlations between the laser and the CPT clock frequency stabilities when the laser frequency is locked to the bottom of an optical buffer gas broadened absorption line. Red: laser beatnote frequency. Black: clock frequency.

Figure 3.17 highlights the direct correlation between the clock and the laser frequency fluctuations. They both oscillate in the experiment with a period of around 350 s. The cause has been identified as laser feedback effects and has been fixed by implementing a second optical isolation stage at the DFB laser output. Nevertheless, in this configuration, the clock frequency stability, from 1 to 10 s averaging time, was limited as a plateau at the level of 3-4 10^{-13}. In a high-performance CPT clock, enhanced stabilization of the laser frequency is then required. In that sense, we investigated the possibility to perform Doppler-free spectroscopy in a Cs vapor cell with a dual-frequency laser field originating from the EOM output. Here, in this two-frequency configuration, two different transitions are involved in the saturated absorption scheme, $|F=3\rangle \rightarrow |F'=4\rangle$ and $|F=4\rangle \rightarrow |F'=4\rangle$, where $F(F')$ are the hyperfine quantum numbers of the ground (excited) states, respectively.

3.4.2 Description of the set-up

Figure 3.18 shows the experimental set-up. The bichromatic laser beam is sent and reflected back in a 2-cm-diameter and 2-cm long Cs vapor cell. A quarter wave plate can be adjusted such that propagating and counter-propagating beams are linearly and parallel or mutually orthogonally polarized. The power of the reflected beam is measured by a photodiode. All tests were performed at ambient temperature (about 22.5 °C). The cell is surrounded by a mu-metal magnetic shield. No

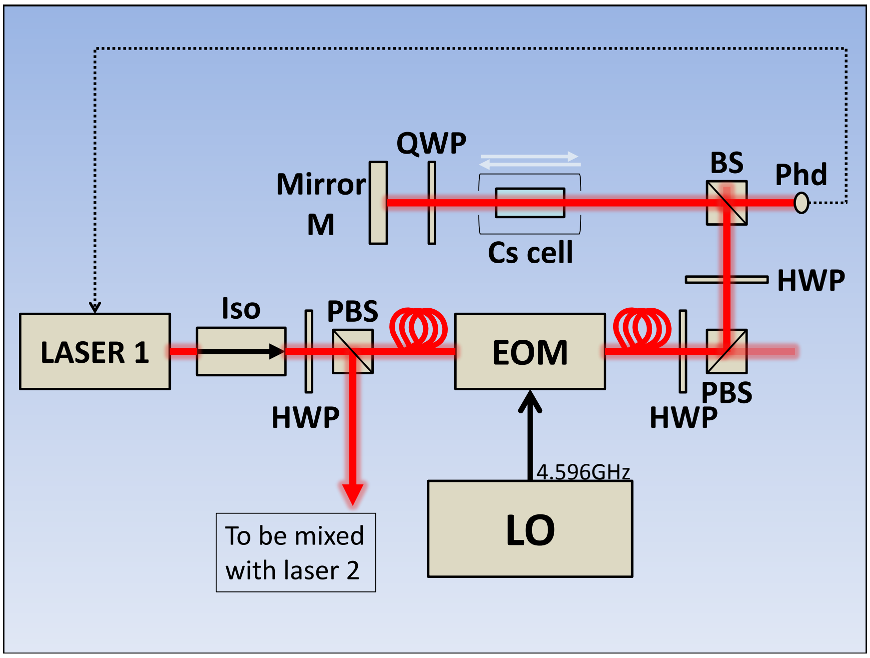

Figure 3.18: Saturated absorption set-up. The LO output is switched on or off to set respectively a single or a dual saturated absorption configuration. Iso: optical isolator. HWP: half-wave plate. BS: beam-splitter cube. PBS: polarizing beam-splitter cube. Phd: photodiode.

static magnetic field is applied. The laser modulation frequency is about 70 kHz. The servo bandwidth is 1 kHz.

3.4.3 Comparison between single- and dual-frequency resonances

Figure 3.19 shows typical transmission signals detected by the photodiode (Phd in Fig. 3.18) in the single-frequency configuration (microwave driving the EOM off) and the dual-frequency regime (microwave on).

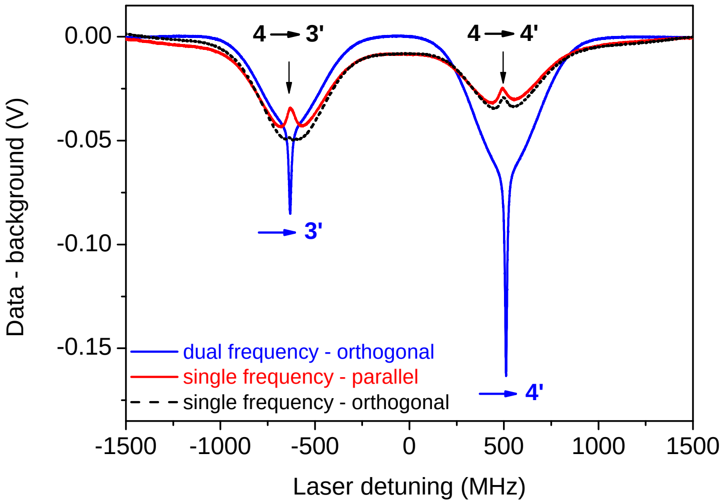

Figure 3.19: Spectroscopy signals detected in the Cs vapor cell in single-frequency (co-polarized or orthogonally polarized counterpropagating beams) and dual-frequency (crossed polarizations) regimes. For clarification of the figure, a background value of 0.45 V was subtracted to each curve. 3, 4, 3' and 4' stand for $|F=3\rangle$, $|F=4\rangle$, $|F'=3\rangle$ and $|F'=4\rangle$ respectively.

The total laser power incident in the cell is 400 µW in all cases. In the single-frequency case, the transition doublet $|F=4\rangle \rightarrow |F'=4\rangle$ and $|F=4\rangle \rightarrow |F'=3\rangle$ is shown. With parallel polarizations, the usual narrow Lamb dip, with Lorentzian profile, appears in the bottom of both Doppler-broadened absorption gaussian-profile lines. With crossed polarizations, the dip is totally vanished in the bottom of the $|F=4\rangle \rightarrow |F'=3\rangle$ transition [171]. This will be described in detail in section A. In the dual-frequency regime, with crossed polarizations, a significant sign-reversal of the dip and large increase in Doppler-free atomic absorption is observed for both atomic lines, especially at high laser power. It appeared to us that we could take advantage of the resulting high frequency discriminator to improve the efficiency of our laser frequency stabilization.

3.4.4 Theory

The dip reversal can be explained by CPT effects which are cancelled for counter-propagating waves. Here is a simple qualitative explanation. A more detailed study of these aspects, relying on the combination of Zeeman and hyperfine coherences, is given in section A. A complete theoretical investigation should take into account all the 25 involved Zeeman sublevels and can be only numerically computed. This work, in collaboration with D. Brazhnikov et al. (Institute of Laser Physics, Novosibirsk), is planned for a close future.

A linearly polarized monochromatic wave propagating along the quantification z-axis is σ polarized. In null magnetic field and at optical resonance, a Zeeman sublevel of the excited state $|e,m\rangle$ will then be linked to two sublevels of the ground state $|g,m-1\rangle$ and $|g,m+1\rangle$. These conditions allow the existence of a dark state that will disappear for increasing magnetic field, as soon as the Zeeman splitting is larger than the CPT resonance linewidth. This effect is known as the non-linear Hanle effect [172]. An example of full density matrix numerical calculation is reported in [173]. According to the linear polarization along the x-axis or y-axis, the dark state is given by:

$$\begin{aligned} |ds_x\rangle &= d_{e,m;g,m+1}\,|g,m-1\rangle + d_{e,m;g,m-1}\,|g,m+1\rangle\,, \\ |ds_y\rangle &= d_{e,m;g,m+1}\,|g,m-1\rangle - d_{e,m;g,m-1}\,|g,m+1\rangle\,, \end{aligned} \tag{3.10}$$

where $d_{e,m;g,m\pm1}$ are the dipole moments of the involved transitions. Equal field amplitudes are assumed. Note that both dark states are orthogonal. This means that the atoms driven in a dark state by a polarized wave will absorb the perpendicularly polarized wave (bright state).

Consider now atoms of a gas irradiated by this wave and the reflected counterpropagating wave. At non-zero values of the optical detuning Δ, because of the Doppler shift, one travelling wave is resonant for atoms of the axial velocity class $v=\Delta/k$ (k is the wave number) while the reflected wave is resonant for atoms of the velocity class $-v$. In that way, a fraction of atoms interacting with only one of the two waves is trapped in a dark state whatever the polarization of the other wave. At optical resonance the atoms of velocity class $v=0$ are resonant for both counter-propagating waves. When the polarization of the two fields is the same, dark states are common, less atoms can absorb the probe wave and the expected saturated absorption dip is observed. According to (3.10), when the polarization vectors are orthogonal, atoms in the dark states of the pump beam become bright and absorbing for the probe, and vice-versa. In this case, the absorption of both beams is increased and the Lamb dip is reversed. A similar effect has already been investigated for linear and elliptical polarizations in the Hanle configuration [171, 174]. In these articles, the monochromatic laser was tuned at resonance and the probe beam power was recorded versus the magnetic field. In Hanle configuration, the linewidth is limited by the CPT resonance width, inversely proportional to the Zeeman coherence lifetime.

In the present experiment, the magnetic field is kept null. Then, the sub-Doppler resonance cancels when no more atoms interact with both waves simultaneously, i. e. when $\Delta > \Gamma^*$, with Γ^* the linewidth of the optical transition. It can be shown that this CPT effect occurs when $F'=F-1$ [175]. It explains why we observe this phenomenon, for the monochromatic case, only on the ($|F=4\rangle \rightarrow |F'=3\rangle$) transition (see Fig. 3.19).

The same effect occurs with a bichromatic beam carrying two optical frequencies frequency-split by the hyperfine-transition frequency. Since the Doppler-shift difference related to both frequencies is negligible in this case, hyperfine coherences between Zeeman sublevels of both hyperfine states are also built. The previous argument is still valid. If the pump and probe beams have the same linear polarization, dark states are dark for both beams and the saturated absorption dip is observed. If pump and probe beams are orthogonally polarized, dark states are no more identical. For example, at $\Delta = 0$, assuming an optically thin medium and equal field amplitudes, the low-frequency σ^+ component of pump beam (polarized along the x-axis) and high frequency σ^- component of probe beam (polarized along the y-axis) induce the dark states:

$$\begin{aligned} |DS_x\rangle &= d_{e,m;\,4,m-1}\,|3, m+1\rangle + d_{e,m;\,3,m+1}\,|4, m-1\rangle\,, \\ |DS_y\rangle &= d_{e,m;\,4,m-1}\,|3, m+1\rangle - d_{e,m;\,3,m+1}\,|4, m-1\rangle\,, \end{aligned} \tag{3.11}$$

where 3(4) holds for $F = 3\,(F = 4)$, respectively, and e for $F' = 3$ or $F' = 4$ (see Fig. 3.20).

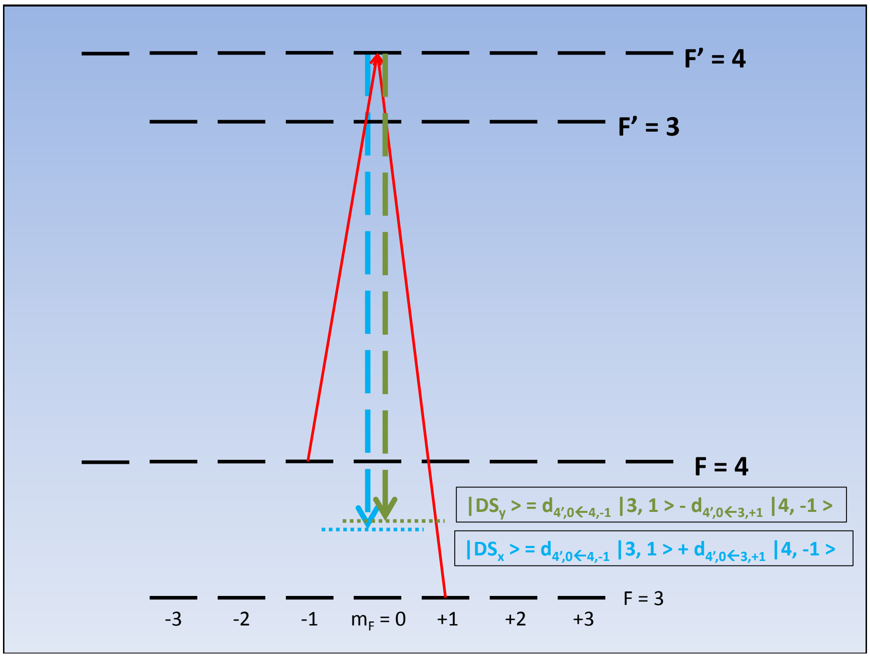

Figure 3.20: Example of a pair of orthogonal dark states $|DS_x\rangle$ and $|DS_y\rangle$. These are superpositions of states $|4', 0\rangle$, $|3, 1\rangle$ and $|4, -1\rangle$

Dark states of Eq. (3.11) are orthogonal. A higher absorption is expected at optical resonance. This occurs for Zeeman dark states and ($|\Delta F| = 1$, $|\Delta m| = 2$) dark states, but not for ($|\Delta F| = 1$, $|\Delta m| = 0$) dark states. In monochromatic and bichromatic cases, several state linear superpositions with $|\Delta m| = 2n$, $n \in \mathbb{N}^*$, can coexist. However, since the atomic transit time across the beam is short, the steady-state is not reached and these dark states should be poorly populated.

In Appendix A, we report detailed experimental investigations of the dual-frequency sub-Doppler spectroscopy phenomenon reported in this section, together with a full in-depth theoretical description. It is shown that several physical effects can contribute or oppose to the formation of the high-contrast central spike in the absorption profile. These effects are the creation or destruction of dark states in the ground state and velocity-selective optical pumping effects. Beyond their theoretical interest, results obtained in this study are of great interest for laser spectroscopy, laser frequency stabilization purpose, with applications in laser cooling, matter-wave sensors, atomic clocks or quantum optics.

3.4.5 Figure of merit

In the case of crossed polarizations, we measured the evolution of the lorentzian dip versus the total laser power incident in the cell for both single-frequency and dual-frequency regimes. For each laser power, the absorption profiles of the Cs D_1 line spectrum are each fitted by the sum of a Gaussian (Doppler broadened profile) and a Lorentzian function (Doppler-free dip). Figures 3.21a, 3.21b and 3.21c report the amplitude, FWHM and amplitude/FWHM ratio of the Lorentzian dip signal detected in the bottom of the Doppler-broadened profile versus the total laser power incident in the cell.

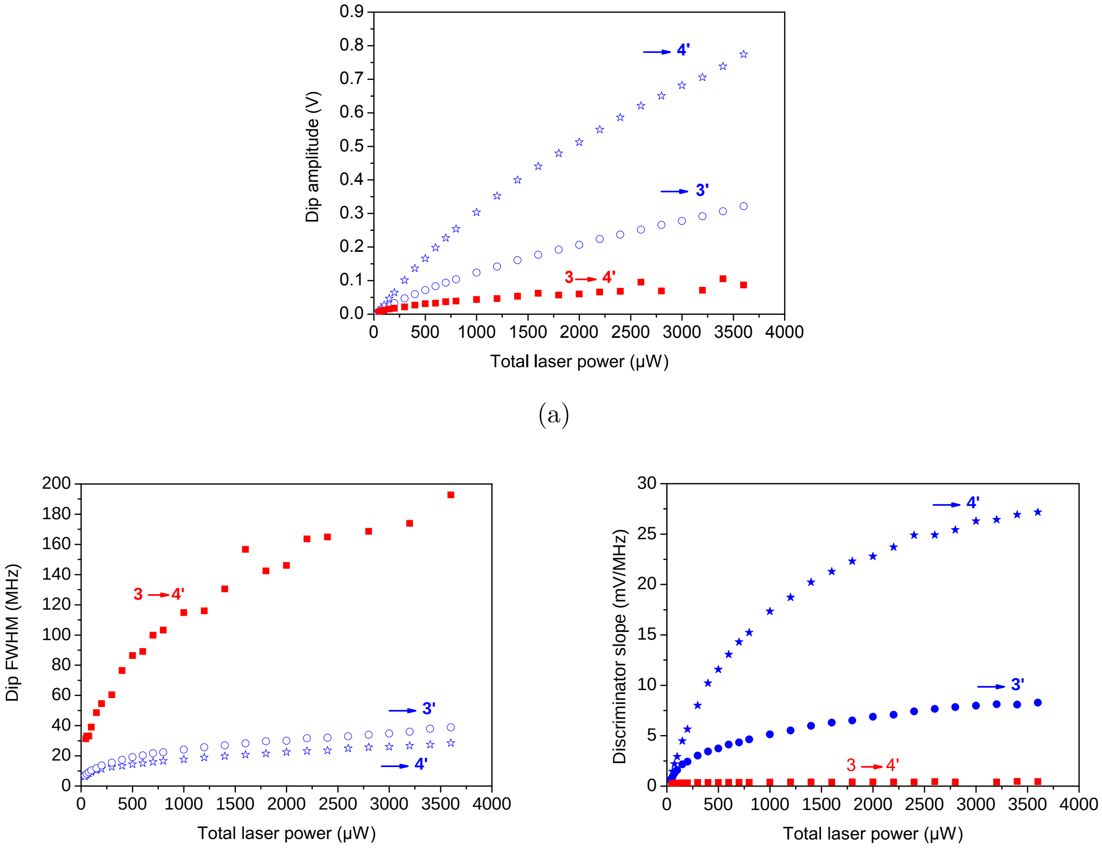

(a)

(b)

(c)

Figure 3.21: (a) Amplitude, (b) full-width at half maximum and (c) amplitude/FWHM ratio of the Lorentzian dip signal detected in the bottom of the Doppler-broadened profile versus the total laser power at the cell input. Black squares: single-frequency regime (3 → 4'). Blue: dual-frequency regime (Circles: → F' = 3, Stars: → F' = 4)

We observe in Fig. 3.21b that the power broadening of the one-frequency dip is larger than in the two-frequency case. Simultaneously, the amplitude of the dip is dramatically increased in the dual-frequency case (see Fig. 3.21a). These observations are attributed to optical pumping effects. In the single-frequency case, the atomic system is an open system, causing the atoms to be pumped into the other hyperfine ground state and leading to a higher effective saturation parameter [176]. At the opposite, in the dual-frequency regime, the atomic system is closed, avoiding the loss of atoms. In the latter regime, a significant result is the important increase of the dip apmplitude with laser power, particularly for transitions connecting the $(F' = 4)$ excited level. In Fig. 3.21c, we observe that the ratio signal/FWHM of the dip (slope of the frequency discriminator for laser frequency stabilization) is significantly increased in the dual-frequency regime. For a laser power of 500 µW, in the case of the transition to $F' = 4$, the dip-based frequency discriminator slope is about an order of magnitude higher than in the single-frequency case.

3.4.6 Frequency stability

Laser frequency stabilization experiments were performed to compare single and dual-frequency regimes. For this purpose, two laser systems, named LS1 and LS2, were implemented. Both systems are mounted on distinct optical tables separated by about 2 m and linked by an optical fiber. LS1 is similar to the system described in Fig. 3.18. LS2 uses a Distributed Bragg Resonator (DBR) laser and a phase EOM (PEOM) driven at 9.192 GHz. In this case, hyperfine CPT is induced by the carrier and one of the first-order sideband. The second first-order sideband is 9.192 GHz out of resonance and its interaction with the atomic system is neglected here. The microwave signal at 4.596 GHz is generated with a frequency synthesizor like described in subsection 3.5.2. The 9.192 GHz signal is generated with a commercial frequency synthesizor. Both are referenced to an active hygrogen maser from T4Science [79]. We note that the gain on the frequency discriminator slope in the dual-frequency regime compared to the standard single frequency regime was found to be about the same for MZ EOM and PEOM-based set-ups. Different tests were performed.

- In test 1, each laser is in the free-running regime.
- In test 2, LS1 operates in the dual-frequency stabilization regime (DFSR) whereas LS2 is in the single-frequency stabilization regime (SFSR). For LS1, the MZ EOM is driven at 4.596 GHz with carrier suppression. The laser direct output (carrier) is shifted 4.596 GHz away from Cs resonance and the dual-frequency MZ EOM output beam is sent into the cell for laser stabilization. For LS2, the PEOM microwave modulation is turned off and the PEOM output beam is sent into the cell for laser stabilization onto a Cs transition.
- In test 3, both laser systems operate in the DFSR. LS1 is configured as in test 2 and the PEOM of LS2 is driven at 9.192 GHz.

In all tests, the single-frequency direct output of each laser (before EOMs) is sent into a beam splitter cube. A laser beat-note at 4.596 GHz is detected by a fast photodiode, amplified and band-pass filtered. This signal is compared to a 4.621 GHz signal from a high-performance microwave synthesizer driven by a hydrogen maser. A final beat-note at 25 MHz is low-pass filtered and counted by a frequency counter (HP 53132A). The laser frequency is stabilized by modulating the laser injection current and demodulating it synchronously with a lock-in amplifier at the output of the photodiode. The bandwidth of the laser frequency servos is about 1 kHz. Figure 3.22 reports the laser beat-note stability for each test.

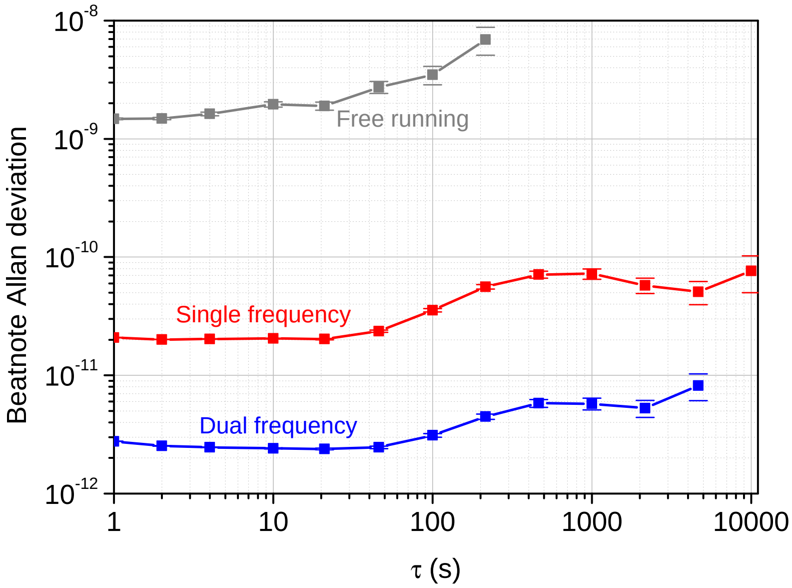

Figure 3.22: Allan deviation of the beatnote between two lasers in free regime or frequency locked using single or dual saturated absorption configuration. Grey: free-running. Red: dual frequency vs single frequency. Blue: dual frequency vs dual frequency.

In the free-running regime, the laser beat-note fractional frequency stability is 1.5 10^{-9} at 1 s averaging time, in good agreement with the estimated stability from the laser frequency noise performed in subsection 3.2.2.3. In test 2 where one of the laser is stabilized through a standard single-frequency saturated absorption scheme, results are similar to those reported in [159] and improved at the level of 2 10^{-11} at 1 s and 3.5 10^{-11} at 100 s. In test 3, where both lasers are stabilized through a dual-frequency Doppler-free spectroscopy set-up, the laser beat-note frequency stability is improved by almost 10 yielding 3 10^{-12} at 1 s and 5 10^{-12} at 1000 s. For a laser power of 500 µW, this improvement is in correct agreement with the increased frequency discriminator slope reported in Fig. 3.21c. The bump at 500 s on the Allan deviation plots is suspected to come from the room air conditioning cycle period. Degradation of the frequency stability at higher time scales could be explained by temperature variations, fiber perturbations or laser amplitude variations along time.
Since the use of the $F' = 4$ excited state led to a higher CPT contrast as compared to the $F' = 3$ state, we chose to stabilize the laser frequency on the $F' = 4$ transitions for all the following experiments.

3.5 Local oscillator

3.5.1 Motivations

One of the main contributions to the short-term frequency stability of high performance vapor cell atomic clocks is the LO phase noise through the so-called intermodulation effect in continuous regime clocks [177] or Dick effect in pulsed clocks [178, 179]. Indeed, the short-term frequency stability of an atomic clock can be degraded by down conversion of the LO frequency noise at even multiples of the cycle rate into the frequency band of the selective resonator response.
In an atomic clock working in continuous regime, with resonance frequency ν_0, operating at a LO modulation frequency F_M, the frequency stability limitation $\sigma_{y_{LO}}(\tau)$ due to this aliasing effect is such that [177]:

$$\sigma^2_{y_{LO}}(\tau) = \frac{1}{4\tau}\left(\frac{F_M}{\nu_0}\right)^2 S_\varphi(2F_M) = \frac{1}{4\tau} S_y(2F_M) \tag{3.12}$$

where $S_\varphi(2F_M)$ is the PSD of the LO phase fluctuations in the free-running regime at Fourier frequency $f = 2F_M$ and $S_y(f) = \frac{f^2}{\nu_0^2} S_\varphi(f)$ is the PSD of the LO fractional frequency fluctuations at offset frequency f. According to this relation, the developement of a Cs atomic clock with a fractional frequency stability of 10^{-13} at 1 s, operating at a LO modulation frequency $F_M = 125$ Hz, requires a local oscillator with a phase noise at $2F_M = 250$ Hz lower than -97 dBrad^2/Hz.
In a pulsed clock, the effect of the LO frequency noise has been characterized by the sensitivity function $g(t)$ [179] which is the response of the atomic signal to a phase step of the interrogation oscillator at time t. The shape of $g(t)$ depends on the atomic system and on the kind of interrogation used. The frequency stability limitation of a pulsed atomic clock due to the Dick effect is given from [179]:

$$\sigma^2_{y_{LO}}(\tau) = \frac{1}{\tau}\sum_{i=1}^{\infty}\frac{g_i^2}{g_0^2} S_y\left(\frac{i}{T_c}\right) = \frac{1}{\tau}\sum_{i=1}^{\infty}\frac{g_i^2}{g_0^2} S_y\left(2iF_M\right) \tag{3.13}$$

The parameters g_i and g_0 are defined from the sensitivity function g [179]. T_c is the clock cycle time and $\frac{i}{T_c}$ are the harmonics of the interrogation frequency. Additionally, compared to classical clocks based on a two-level atomic system, it has been recently demonstrated that the Allan deviation of pulsed CPT clocks exhibit a higher sensitivity to high frequency components of the LO noise [25]. The authors reported that the development of an atomic vapor-cell frequency standard of typical cycle time $T_c = 6$ ms with a fractional frequency stability better than 10^{-13} at 1 s requires a local oscillator with an absolute phase noise $S_\varphi(f)$ lower than -105 dBrad^2/Hz at $f = 2f_c = 2/T_c = 330$ Hz.
Reducing the intermodulation effect contribution requires the development of ultra-stable and low phase noise local oscillators. The purest microwave signals are nowadays obtained through optical-microwave frequency division with optical frequency combs [180, 181] or the use of cryogenic sapphire oscillators [182, 183] and associated frequency synthesis [184]. Nevertheless, these systems remain complex, voluminous, and are not compatible with compactness requirements of vapor cell atomic

clocks. In this domain, the generation of microwave signals referenced to an ultra-low noise quartz crystal oscillator remains a well-adapted solution [89, 90, 185–187]. In that sense, in the frame of my thesis and of the project MClocks, relying on the work of B. François (FEMTO-ST) and C. Calosso (INRIM), we engaged the development of ultra-low phase noise microwave frequency synthesis. Two different synthesis architectures were proposed. The first one is based on the frequency multiplication of a low-noise 100 MHz OCXO with non-linear transmission lines (NLTL). The second one, designed to be adaptable to Cs and Rb, uses a module containing a 100 MHz OCXO and a key-step frequency-multiplication stage to 1.6 GHz.

3.5.2 Architecture 1: NLTL-based frequency synthesis

Description Figure 3.23 shows a detailed scheme of the microwave frequency synthesizer architecture.

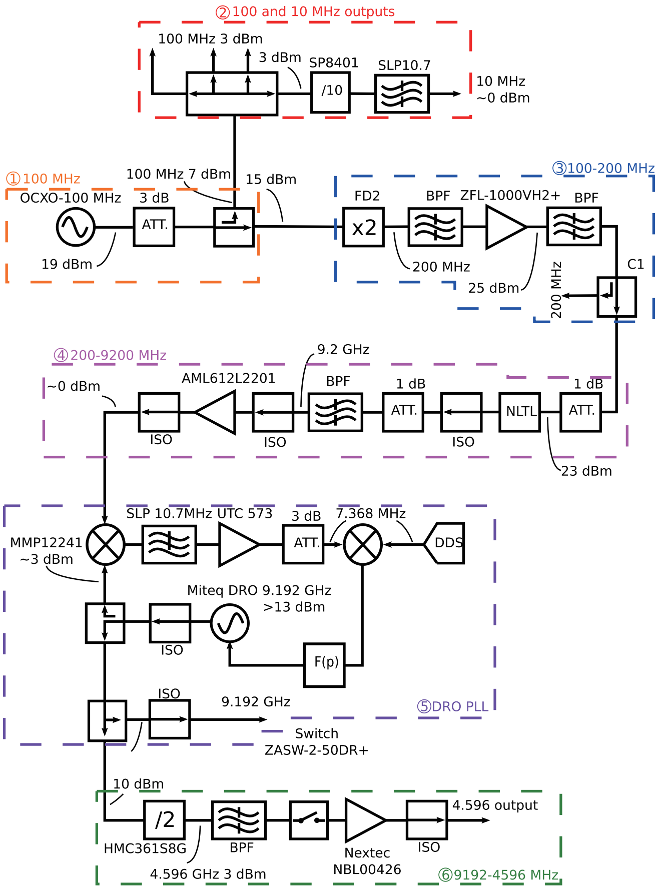

Figure 3.23: Architecture of the frequency synthesis chain based on an NLTL.

The pilot and key element of the synthesis chain is a 100 MHz oven-controlled quartz crystal oscillator (Pascall OCXOF-E-100) [188]. This source exhibits ultra-low phase noise in the 1 Hz - 1 MHz Fourier frequency range and is of relevant interest for compact vapor cell atomic clocks applications. The output power of the OCXO is 19 dBm. Its tuning voltage-frequency sensitivity was measured to be 500 Hz/V. Its tuning voltage - output power dependence was measured to be cancelled to first order around a tuning voltage of 5 V. The OCXO output frequency can be compared and stabilized, if needed, to a 100 MHz signal coming from a state-of-the-art reference active hydrogen maser from T4Science [79].

The output 100 MHz signal is split into two arms. In the first arm, reference signals at 100 MHz and 10 MHz using a digital frequency divider (Zarlink SP8401) are generated. In the second and main arm, the output 100 MHz signal is frequency-doubled to 200 MHz using a passive frequency-doubler (Mini-Circuits FD2). The output 200 MHz signal is bandpass filtered and amplified to a power of 23 dBm with a low noise amplifier (Minicircuits ZFL-1000VH2+). The 200 MHz signal is used to drive a Non-Linear Transmission Line (NLTL) comb generator device (Picosecond Model 7110) that generates harmonics up to about 20 GHz. The 9.2 GHz harmonic output is bandpass-filtered with a 50 MHz-bandwidth bandpass filter and amplified to a power of about 0 dBm with a low noise microwave amplifier (AML612L2201). Microwave isolators and attenuators are added at the output of the NLTL to help for impedance matching, optimization of the phase noise performances and to prevent undesired feedack. The NLTL component was found to be a critical element. Setting the optimal configuration that optimizes phase noise performances of this synthesis chain section can require patience and numerous experimental tests. Microwave isolators were selected for their high isolation properties. Optimization of impedance matching of NLTL input and output was found to be important. Once the best configuration is found, we observed excellent repeatability and stability of performances along time. The output 9.2 GHz is mixed with the 9.192 GHz signal coming from a dielectric resonator oscillator (DRO MITEQ - DRO-G-09192-MT±140), to produce a frequency beatnote at 7.368 MHz. The latter is low-pass filtered, amplified with a high-isolation radiofrequency amplifier (Avantek UTC-573) and compared to the 7.368 MHz signal from a direct digital synthesis (DDS Agilent 33220A). The DDS is referenced by a 10 MHz signal generated from the initial 100 MHz OCXO. The DRO is phase-locked to the frequency-multiplied 100 MHz signal with a bandwidth of about 1 MHz. Both input signals are mixed with a double balanced mixer (Mini-Circuits TFM-3MH) with a sensitivity of 0.225 V/rad. The resulting error signal is filtered, processed in a proportional-integral (PI) controller, summed with an offset voltage to fix the OCXO bias point and eventually used to phase-lock the DRO. High speed operational amplifiers (THS4011) are used to ensure proper and high-bandwidth lock of the DRO. An additional OP27 amplifier is used to monitor the error signal. A low phase noise 9.192 GHz signal with a microwave power of about 13 dBm is then obtained at the output of the DRO. This signal is split into two different arms. In the first arm, the 9.192 GHz arm is ready to use. In the other arm, the 9.192 GHz signal is frequency-divided by 2 with a low noise microwave frequency divider (Hittite HMC36158G). The 4.596 GHz output microwave signal is bandpass filtered and amplified with a 4-12 GHz bandwidth high-power amplifier (Nextec NBL-00426) to produce a microwave power of about 20-22 dBm driving the EOM in our clock experiment.

Absolute phase noise measurements Measurements are performed with a signal source analyzer (Agilent E5052B) using cross-correlation techniques for enhanced sensitivity [189–191]. The phase noise uncertainty at effective offset frequencies from 1 Hz to 100 MHz is given to be about ±5 dB [191]. Figure 3.24 plots absolute phase noise performances of key signals of the synthesis chain at 100, 200, 9200 and 9192 MHz (free-running or locked DRO).

The phase noise spectrum of the free-running 100 MHz Pascall OCXO is given in dBrad^2/Hz by the power law $S_\varphi(f) = \sum_{i=0}^{-4} b_i f^i$ with $b_0 = -182$, $b_{-1} = -130$ and $b_{-3} = -82$. These performances are excellent and are found to be in the $f = 1$ Hz - 10 kHz frequency range significantly better than other OCXOs we tested. For $f < 10$ kHz, the phase noise of the 200 MHz output signal is measured to be as expected 6 dB higher than the 100 MHz signal phase noise. For $f > 10$ kHz, the phase noise of the output 200 MHz signal is degraded compared to the ideally-multiplied 100 MHz signal. The white phase noise floor of the 200 MHz signal is measured to be -168 dBrad^2/Hz and is limited by the input power of the ZFL-1000VH2+ amplifier [192]. The 9200 MHz signal phase noise is -42, -100, -130 and -135 dBrad^2/Hz at 1 Hz, 100 Hz, 10 kHz and 1 MHz offset respectively. Except for the 200 Hz - 1 kHz region where an excess noise degradation of about 3 dB attributed to the NLTL residual phase noise is observed, the signal frequency multiplication from 200 MHz to 9200 MHz causes a 33 dB ($= 10 \log 46^2$, where 46 is the multiplication factor) increase of the noise as expected.

In the free-running regime, the DRO exhibits a phase noise of -112 dBrad^2/Hz at $f = 100$ kHz. Its phase noise floor for $f > 10$ MHz is -172 dBrad^2/Hz (not shown here). In the locked regime, the 9.192 GHz output signal exhibits phase noise performances of -42, -100, -129 and -130 dBrad^2/Hz at $f=$ 1 Hz, 100 Hz, 10 kHz and 1 MHz respectively. The peak at 7.3 MHz is the signal frequency generated by the DDS included in the DRO PLL. While not reported for clarity of the figure, phase noise performances of the 4.596 GHz signal were measured to be in good agreement with performances obtained at 9.192 GHz (6 dB reduction of the noise). The phase noise floor of the 4.596 GHz signal is limited for $f > 1$ MHz by the frequency divider residual noise at a level of -146 dBrad^2/Hz.

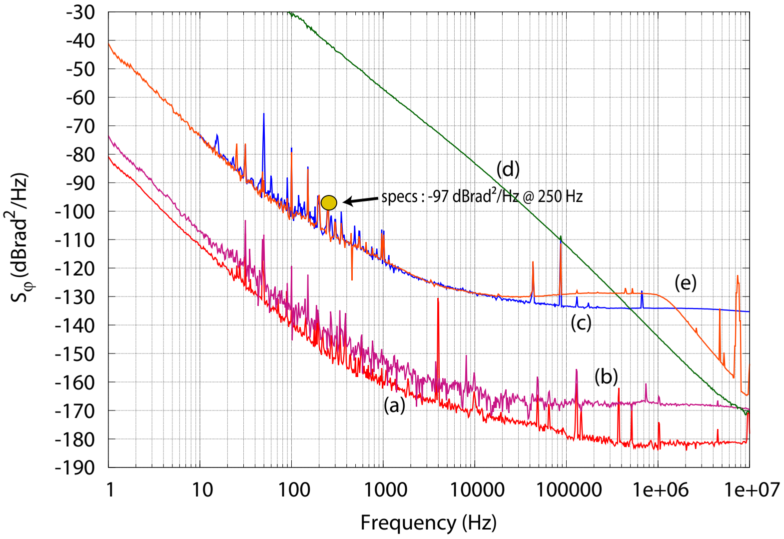

Figure 3.24: Absolute phase noise performances of key signals of the synthesis chain. (a) 100 MHz OCXO, (b) 200 MHz signal at the output of the ZFL-1000VH2+ amplifier (not connected to NLTL chain), (c) 9200 MHz signal at the output of the NLTL-based chain, (d) free-running DRO at 9.192 GHz, and (e) locked DRO at 9.192 GHz.

Optically carried microwave signal In atomic clocks based on CPT physics, the microwave interrogation signal of the LO is optically carried. Consequently, it has to be checked that there is no phase noise degradation between the microwave synthesis output and the optical beatnote that actually interrogates the atoms. Figure 3.25 reports absolute phase noise at 9.192 GHz in different cases noted (a) - (c).

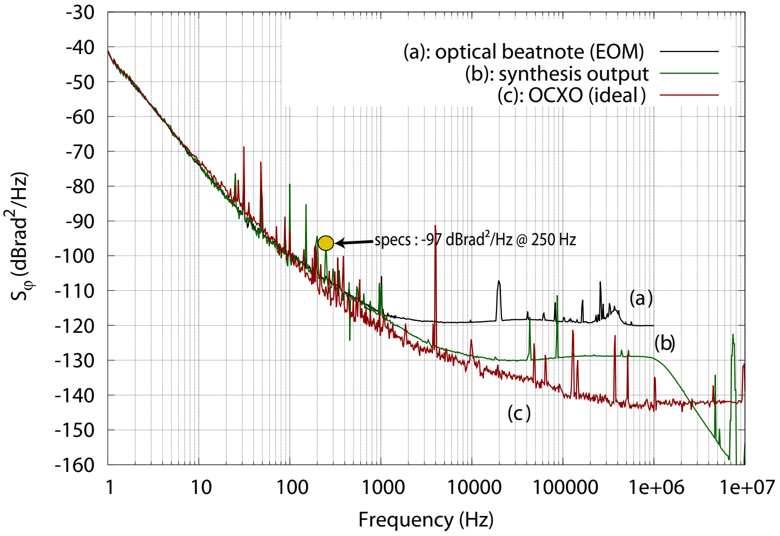

Figure 3.25: Absolute phase noise at 9.192 GHz of (a) the optical beatnote out of the fast photodiode (noise floor limitation due to the measurement setup), (b) the output of the present synthesis chain, and (c) the OCXO ideally multiplied.

Case (a) is the phase noise of the 9.192 GHz optical beatnote at the output of the EOM measured with the fast photodiode of Fig. 3.10, after amplification by 50 dB. Case (b) is the phase noise of the 9.192 GHz signal at the direct synthesis output. In this system, no phase noise degradation is observed between the 9.192 GHz optical beatnote and the direct synthesis output for $f < 1$ kHz. For $f > 1$ kHz, the phase noise floor of the 9.192 GHz optical beatnote is limited at a level of -118 dBrad^2/Hz. We checked that this limit was intrinsically due to the phase noise measurement set-up, more precisely by the low input power ($\sim -54\,$dBm) of the microwave amplifier placed at the output of the fast photodiode used to detect the optical beatnote.

The architecture described above has been proven to be suitable with the desired specifications for the CPT clock and was the architecture used during my PhD thesis. However, it was found to present several drawbacks. The NLTL comb generator requires high input driving power (up to 27 dBm for current generations) that imposes the use of high power consumption and bulky driving amplifiers. Their input frequency range is limited to a few hundreds of MHz. Their residual phase noise performances were shown to be highly sensitive to input and output impedance matching conditions and to depend strongly on the signal input power [89, 186]. Additionally, these components are expensive (about 3 k€ for a single unit). In the present architecture, absolute phase noise performances of the synthesis chain output were mainly limited in the 100 Hz - 1 kHz offset frequency range (3 dB degradation) by the NLTL-based chain excess residual noise while the white noise floor was greatly degraded by the 100 - 200 MHz frequency doubling stage residual noise (6 dB degradation).

3.5.3 Architecture 2: XM-16 Pascall module-based frequency synthesis

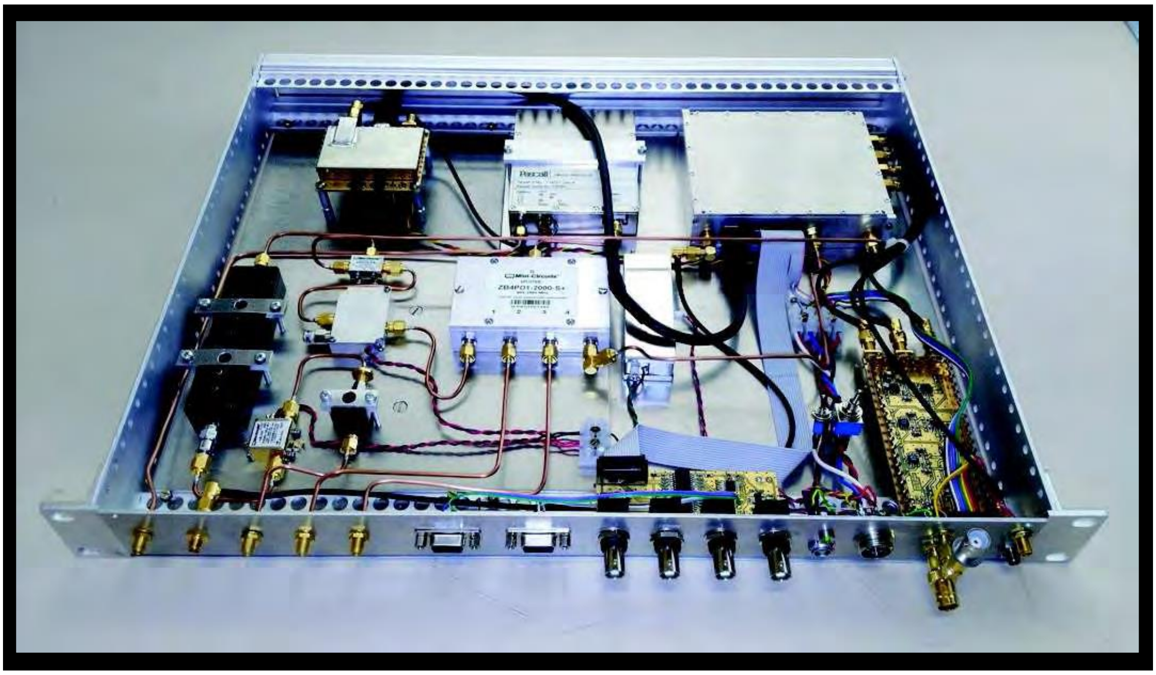

Figure 3.26: Photography of the frequency synthesis based on a Pascall module.

Motivations In the frame of the EURAMET MClocks project, and from the continuation of the collaboration between FEMTO-ST and INRIM, has been developed a novel simple-architecture microwave frequency synthesis chain with significant improved phase noise performances. The total price of a synthesizer is about 6 - 7 k€. The total volume of the synthesis chain is 13 dm^3 and its total power consumption is about 16 W. A picture of the ensemble is shown in Fig. 3.26.
The key element of these synthesizers is a custom-designed frequency multiplication input module that transfers the spectral purity of an ultra-low phase noise 100 MHz OCXO to 1.6 GHz with minor degradation. Other useful signal frequencies are generated from this 1.6 GHz signal using commercially available low residual phase noise frequency multipliers and dividers. It is important to note that the design of this simple architecture synthesis, with the presence of a key step at the frequency of 1.6 GHz, is well-adapted to be customized for the generation of either 4.596 GHz or 6.834 GHz signals, making it suitable simultaneously for ^{133}Cs clocks and ^{87}Rb clocks. These improvements have been made possible thanks to the progress in the direct digital synthesizer (DDS) technology in terms of

residual noise and spurs (higher resolution/frequency clock) while generating higher output frequency signals.

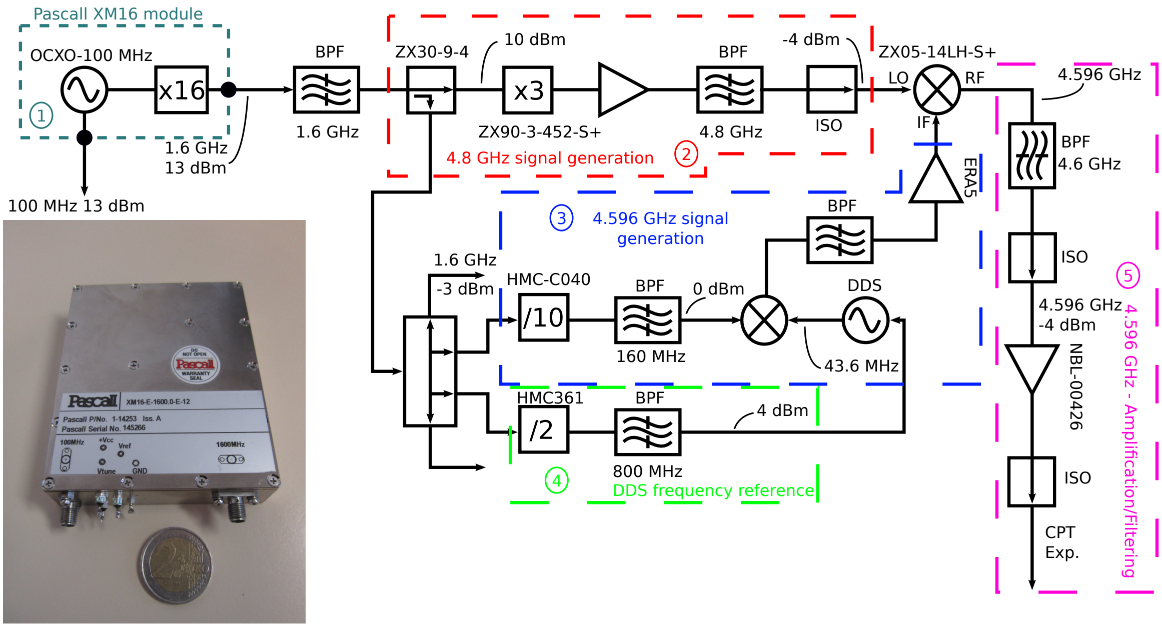

Figure 3.27: Architecture of the frequency synthesis chain for the Cs cell clock. 5 main blocks are indicated on the diagram for better understanding. 1: the XM16 Pascall module that integrates a high-performance OCXO and a 100 MHz - 1.6 GHz frequency multiplication module, 2: generation of a 4.8 GHz signal through frequency multiplication by 3 of the 1.6 GHz signal, 3: generation of a 4.596 GHz signal, 4: generation of a 800 MHz signal reference for a DDS, 5: amplification and filtering of the output 4.596 GHz signal. BPF: bandpass filter. ISO: isolator. CPT Exp: CPT experiment. In inset is a photography of a 100 MHz - 1.6 GHz XM16 Pascall frequency multiplication module.

Architecture Figure 3.27 shows a detailed scheme of the microwave frequency synthesizer architecture.The pilot and key element of the synthesis chain is a custom-designed XM16 Pascall module [193], shown in inset of Fig. 3.27. It integrates an ultra-low phase noise 100 MHz OCXO (Pascall OCXOF-E-100) and a frequency multiplication stage to produce a low noise 1.6 GHz output signal with a power of 13 dBm. Multiplication to 1.6 GHz is performed thanks to three multiplication stages, with bandpass filtering and amplification at each step to maintain low noise floor and to keep a low level of spurious 100 MHz harmonics. Heterojunction bipolar transistors-based amplifiers are used to minimize excess flicker noise. Multipliers are based on passive doublers using Schottky diodes in order to minimize conversion losses and to maximize the power into the following amplifier. This allows to reduce the noise figure of each new amplification stage. The module is designed in order to minimize leakages between sections and to achieve extremely low sub-harmonics spurious levels. Each stage uses its local voltage regulation, with particular attention paid to minimize low frequency noise on the oscillator supply. Three XM16 modules, named XM16-264, XM16-265, XM16-266, expected to be identical, were bought, tested and compared. As reported later, we observed that the XM16-265 module exhibits significantly better performances, mainly in the 500 Hz - 30 kHz range. The output 1.6 GHz signal is bandpass-filtered with a 50 MHz-bandwidth bandpass filter and power-split into different arms. In the first arm, the 1.6 GHz signal is frequency multiplied to 4.8 GHz with a low noise passive frequency multiplier (Minicircuits ZX90-3-452-S+). The output signal is amplified with a 13 dB-gain microwave amplifier (Hittite HMC606), bandpass filtered and isolated with a microwave isolator to prevent feedback. In a second arm, the 1.6 GHz signal is frequency-divided by 9 with a low noise programmable frequency divider (Hittite HMC705) to produce a 177.8 MHz signal that is later bandpass filtered. In the third arm, the 1.6 GHz signal is frequency-divided by 2 (Hittite HMC361) to an output frequency of 800 MHz. The 800 MHz signal is used to drive a DDS (AD9910) that generates an output frequency of 25.9 MHz. This signal is mixed with the 177.8 MHz output signal in a double-balanced mixer (Minicircuits ZFM-2-S+) in order to generate a 203.7 MHz signal, again filtered. The latter is sent into the IF port of a microwave double-balanced mixer (Minicircuits ZX05-14LH-S+) to be mixed with the 4.8 GHz signal and to ensure the generation of the final 4.596 GHz signal. The 203.7 MHz signal is kept below 0 dBm in order to stay in the microwave mixer linear behavior range. The purpose is then to control the output power of the synthesis chain by tuning the DDS amplitude. The 4.596 GHz signal is bandpass filtered, isolated, amplified with a microwave amplifier (Nextec NBL-00426). This signal is later used to drive the pigtailed intensity Mach-Zehnder electro-optic modulator devoted to generate two optical sidebands frequency-separated by 9.192 GHz in CPT-based clock set-ups.

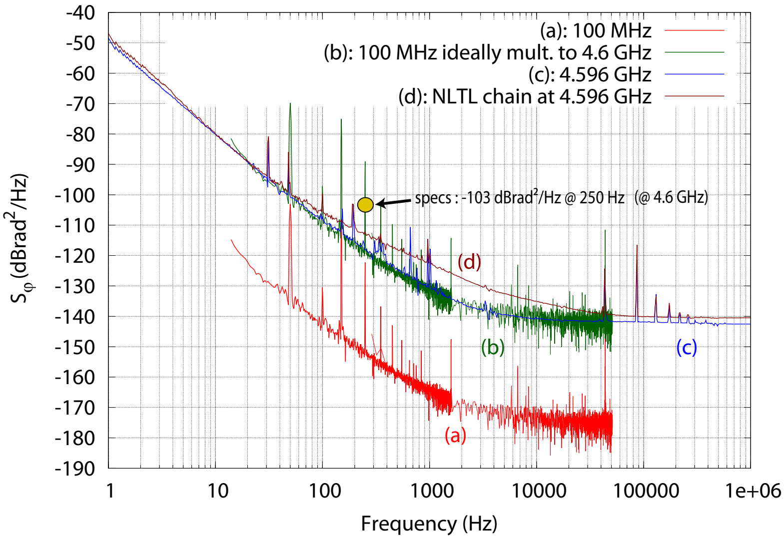

Figure 3.28: Absolute phase noise performances of key signals of the Cs clock synthesis chai. (a) 100 MHz OCXO, (b) 100 MHz OCXO ideally multiplied to 4.6 GHz, (c) 4.596 GHz, and (d) 4.596 GHz signal extracted from the 9.192 GHz signal from the NLTL-based synthesis chain.

Phase noise measurements Figure 3.28 plots absolute phase noise performances of key signals of the synthesis chain at 100 MHz and 4.596 GHz. In addition, it shows the absolute phase noise of the 9.192 GHz signal measured from the 9.192 GHz signal of the NLTL-based synthesis chain, reported at 4.596 GHz (-6 dB), for comparison.

The absolute phase noise of the 100 MHz OCXO ideally multiplied to 4.6 GHz is also plotted for information. The phase noise spectrum of the free-running 100 MHz Pascall OCXO has been measured at the level of -143, -167 and -175 dBrad^2/Hz at 100 Hz, 1 kHz and 50 kHz offset frequencies, respectively. The 4.596 GHz signal phase noise is measured to be -109, -131, -141 and -142 dBrad^2/Hz at 100 Hz, 1 kHz and 10 kHz and 100 kHz, respectively. These results are in good agreement with perfect frequency multiplication of the initial OCXO 100 MHz signal. For offset frequencies from 100 Hz to 100 kHz, a critical region to be optimized in order to reduce the Dick effect contribution in vapor cell atomic clocks, phase noise performances of the 4.596 GHz output signal are 2 - 8 dB better than performances measured with the NLTL-based architecture reported at the same carrier frequency. Additionally, the white noise floor is also improved by about 2 dB. For information, additional residual phase noise measurements of key components of the synthesis chain are reported in [90].

Residual frequency stability The experimental setup shown on Fig. 3.29a was implemented to measure the residual frequency stability of 1.6 - 4.596 GHz frequency multiplication chains. A common 1.6 GHz signal from the XM16-265 module is split into two arms and sent in two identical

1.6 - 4.596 GHz chains. Output signal frequencies at 4.5959 GHz and 4.5975 GHz are mixed to generate a beatnote at 1.6 MHz that is low-pass filtered and counted with a Symmetricom 5125A phase meter. The latter is driven by the 100 MHz signal of the XM16-265 module. Figure 3.29b reports the measured fractional frequency stability of the beatnote and the expected computed residual frequency stability of a single synthesis chain using a formula converting flicker phase noise into Allan deviation [44].

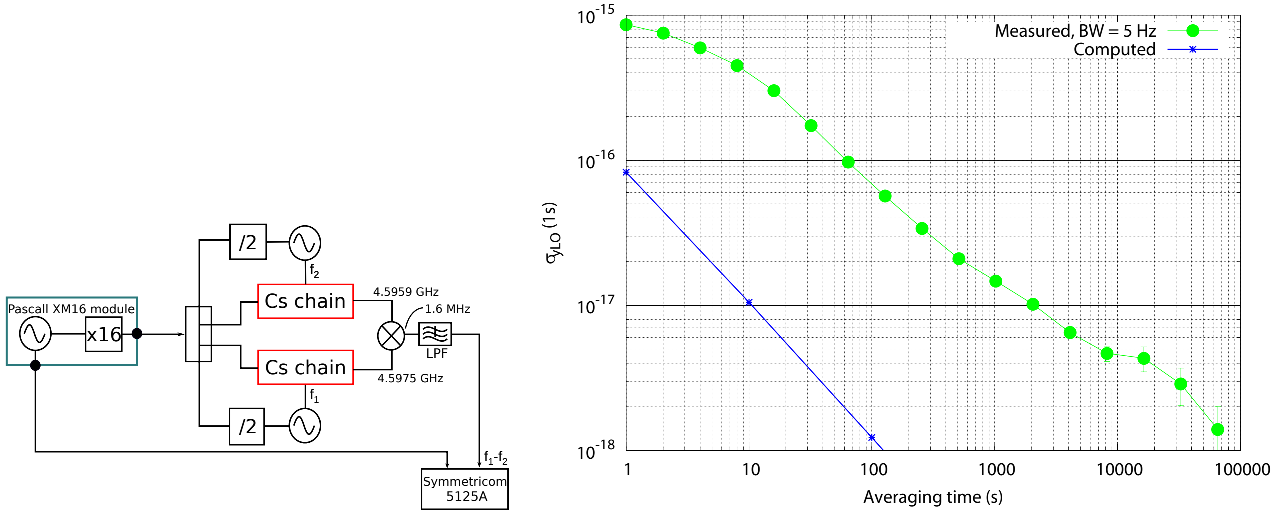

(a) (b)

Figure 3.29: (a) Experimental set-up used for measurement of the Cs clock synthesis chain residual frequency stability and (b) fractional frequency stability of the 1.6 MHz beatnote between two 1.6 - 4.8 GHz synthesis chains. The measurement bandwidth is 5 Hz. The phase noise of a single synthesis chain has been taken into account for the computed fractional frequency stability.

The residual frequency stability is measured to be 8 10^{-16} and 4.5 10^{-18} at 1 s and 10 000 s averaging time, respectively, with a measurement bandwidth of 5 Hz. As shown in Ref. [194], the PSD of phase fluctuations of a signal can be expressed by the power law model $S_\varphi(f) = \sum_{i=-4}^{0} b_i f^i$. The residual flicker noise is measured at the level of $b_{-1} = -123\,\mathrm{dBrad}^2$, yielding a computed stability of 8 10^{-17} τ^{-1} at 1 s with a measurement bandwidth of 5 Hz. These performances can be considered as the ultimate performances achievable by the synthesis chain. The differences we observe between this value and the measured residual frequency stability are probably related to environmental parameters (mainly temperature and humidity) that degrade the performances. In our application, the control of these parameters is not required since the measured performances are already one order of magnitude below the Dick effect contribution.

3.5.4 Dick effect contribution

The Dick effect contribution is calculated for a pulsed CPT clock using Eq. (3.13). Operating parameters and conditions of the Ramsey pulsed sequence in the present study are a pumping time τ_p of 2 ms and a free-evolution time T_R of 4 ms, i.e. a clock cycle time $T_c = \tau_p + T_R$ of 6 ms, or a clock cycle frequency $f_c = 1/T_c = 166$ Hz. The Dick effect contribution is reported (see Table 3.1) at the level of 3.1 10^{-14} at 1 s, close to the shot noise limit, while this limitation is estimated at 6.2 10^{-14} for the NLTL-based architecture. During my thesis, I worked with the latter kind of synthesis, but we expect the new architecture to be implemented soon. This architecture has already been succesfully implemented in the POP clock at INRIM and in the double-modulation clock at LNE-SYRTE, in the frame of the MClocks project.

Table 3.1 summarizes expected performances for each configuration. The computation has been performed by fitting each phase noise spectrum data set by a power-law function such that $S_\varphi(f) = \sum_{i=0}^{-4} b_i f^i$. All values are well below the aimed specifications.

Table 3.1: Dick effect contribution $\sigma_y, LO\,(1\,\mathrm{s})$ of synthesis chains to the clock short-term frequency stability.

Architecture	XM16-265-based	NLTL-based
Results for fitted data	$3.1\ 10^{-14}$	$6.2\ 10^{-14}$

3.6 AOM

The AOM plays several major roles: compensation of buffer gas optical shift, laser power stabilization and eventually generation of light pulses. These functions will be described in this section.

3.6.1 Buffer gas shift compensation

The first role of the AOM is to frequency-shift the EOM output spectrum to match the CPT cell optical resonances. The cell is filled with an N_2-Ar buffer gas mixture with total pressure $P = 15\,\mathrm{Torr}$ and a ratio $r(Ar/N_2) = 0.4$.

The use of buffer gas allows to obtain narrow Doppler-free CPT resonances through the Dicke regime [96, 129, 195]. Nevertheless, one drawback is that it also broadens and shifts the optical lines due to collisions of Cs atoms with buffer gas atoms. Optical shift and broadening coefficients have been studied for the Cs D_1 line in [88, 139, 196–198]. The article [88] reports the frequency shift dependence with pressure at a given temperature. It is measured at $\delta_{N_2}(318\,\mathrm{K}) = -7.69(1)\,\mathrm{MHz/Torr}$ for N_2 at $T = 318\,\mathrm{K}$ and $\delta_{Ar}(318\,\mathrm{K}) = -6.47(3)\,\mathrm{MHz/Torr}$ for Ar at $T = 313\,\mathrm{K}$.

The total expected optical shift can then be obtained from this equation:

$$\delta(308\,\mathrm{K}) = p_{N_2}(308\,\mathrm{K})\delta_{N_2}(308\,\mathrm{K}) + p_{Ar}(308\,\mathrm{K})\delta_{Ar}(308\,\mathrm{K}) \tag{3.14}$$

where $p_i(T)$ is the partial pressure of vapor i at temperature T.

The nominal total buffer gas pressure in the cell at 273 K is 15 Torr. Assuming $r = 0.4$, we thus have $p_{Ar}(273\,\mathrm{K}) = 4.29\,\mathrm{Torr}$ and $p_{N_2}(273\,\mathrm{K}) = 10.7\,\mathrm{Torr}$. The corresponding pressures at 308 K are found using the ideal gas law:

$$\frac{p_i(T_1)}{T_1} = \frac{p_i(T_2)}{T_2} \tag{3.15}$$

We find $p_{Ar}(308\,\mathrm{K}) = 4.84\,\mathrm{Torr}$ and $p_{N_2}(308\,\mathrm{K}) = 12.1\,\mathrm{Torr}$. The $\delta_i(T)$ dependences with temperature are given by [139]:

$$\frac{\delta_i(T_1)}{\delta_i(T_2)} = \left(\frac{T_1}{T_2}\right)^{n_i-1} \tag{3.16}$$

with $n_{Ar} = 0.56$ and $n_{N_2} = 0.18$. Finally, at 308 K the pressure shift coefficients are $\delta_{N_2}(308\,\mathrm{K}) = -7.89(1)\,\mathrm{MHz/Torr}$ and $\delta_{Ar}(308\,\mathrm{K}) = -6.56(3)\,\mathrm{MHz/Torr}$. The expected total pressure shift is $\delta(308\,\mathrm{K}) = -127\,\mathrm{MHz}$, in correct agreement with the measured shift. The difference between measured and the expected values of pressure shift can be explained by the errors in the nominal pressure of buffer gas and in the reading of the linear absorption resonances central frequencies.

Figure 3.30 shows the frequency shift of the optical resonances in the CPT cell containing Cs and an N_2-Ar (with $r = 0.4$ and $P = 15\,\mathrm{Torr}$) mixture from an evacuated Cs cell, used for laser frequency stabilization.

If the laser intensity is small enough, the cell absorption follows a Beer-Lambert law[144]. The transmitted light intensity is expressed as:

$$I\left(\nu_L\right) = I_0 e^{-\alpha(\nu_L)L} \tag{3.17}$$

where I_0 is the incident light intensity, ν_L is the laser frequency, α is the cell absorption coefficient and L its length. In order to access the absorption coefficient, the logarithm of the absorption spectrum from the evacuated cell (blue line in Fig. 3.30) is fitted by the sum of two Gaussian and two Lorentzian functions. The laser frequency is swept by scanning its injection current. We assume that the laser current-frequency conversion is linear. The x-axis scale is calibrated with the difference between the

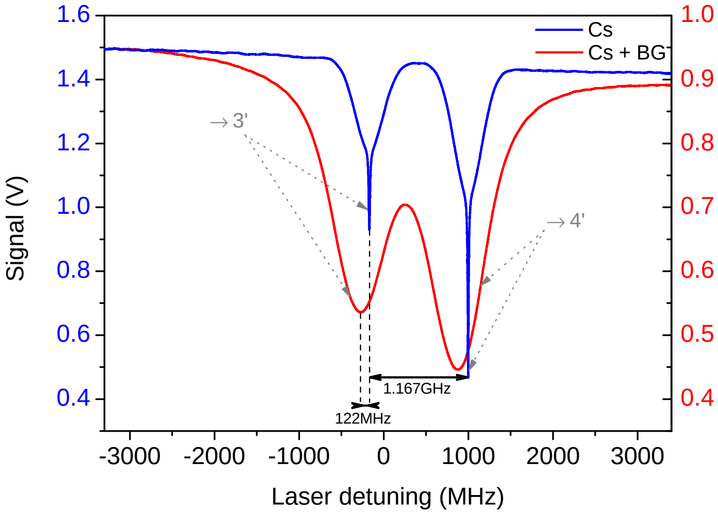

Figure 3.30: Absorption spectra from the evacuated cell in the dual-frequency Doppler-free spectroscopy set-up (blue line) and from the CPT cell with buffer gas (red line). The linear decrease of the background is due to the diminution of the laser output power with increasing injection current. The spectra are divided by a linear function before fitting.

center of the Lorentzian dips (1.167 68 GHz). The logarithm of the spectrum from the CPT cell (red line in Fig. 3.30) is fitted by the sum of two Gaussian functions (we neglected the Lorentzian component, otherwise we should have used a Voigt profile). We find the frequency shift due to the buffer gas to be −122 MHz, in correct agreement with the expected value of −127 MHz.
The AOM is driven by a frequency synthesizer at 122 MHz and it is optically injected so that the -1 diffraction order output is maximized. 46 % of the input optical power is typically transfered into the -1 order.

3.6.2 Laser power stabilization

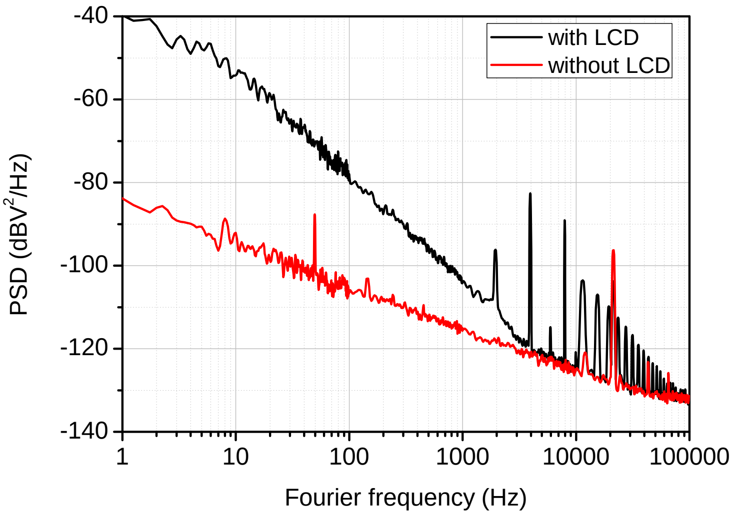

Figure 3.31: Effect of the liquid crystal attenuator on the laser amplitude noise.

In a first step, the laser power stabilization system was tried with a liquid crystal variable attenuator (LCA). The device transmission is a function of the amplitude of a square-shaped signal at 2 kHz applied on the modulation input. Figure 3.31 shows the PSD out of a photodiode placed on the laser beam path after crossing or not the LCA. We set for both cases the laser power on the photodiode at 370 µW.
We observe that the LCA increases significantly the noise by about 25 dB at $f = 100$ Hz and more than 45 dB at 1 Hz. In addition, it adds noise spikes at 2 kHz (operation modulation frequency) and respective harmonics. This excess noise induced by the LCA was not satisfying. Consequently, we decided to implement an AOM-based laser power stabilization system (LPSS).
Figure 3.32 shows the AOM LPSS principle. A fraction of the -1 order laser beam out of the AOM is extracted with a 50/50 transmission over reflection ratio beam splitter. The transmitted beam power is measured with a photodiode. The output voltage is compared with a DC voltage derived from a reference source (LM399). The difference signal is actively set to zero by a servo that delivers a correction signal to the AM modulation input of the synthesizer (Rohde & Schwarz SMB100A, or later SMC100A) that drives the AOM. Attention has to be paid on the RF power level out of the commercial synthesizers. The output noise level strongly depends on the output power range. For example, the noise of the RF signal is strongly increased for the SMB100A, for power levels higher than -4 dBm. The same happens for the SMC100A for power levels lower than -5.7 dBm. Figure 3.33 and appendix Fig. D.3 show a picture and a diagram of the electronic board for power stabilization.

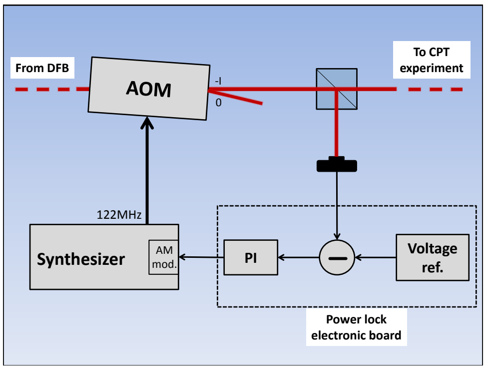

Figure 3.32: Simplified representation of the laser power stabilization set-up. Note that the directions of the output beams from different orders are not respected.

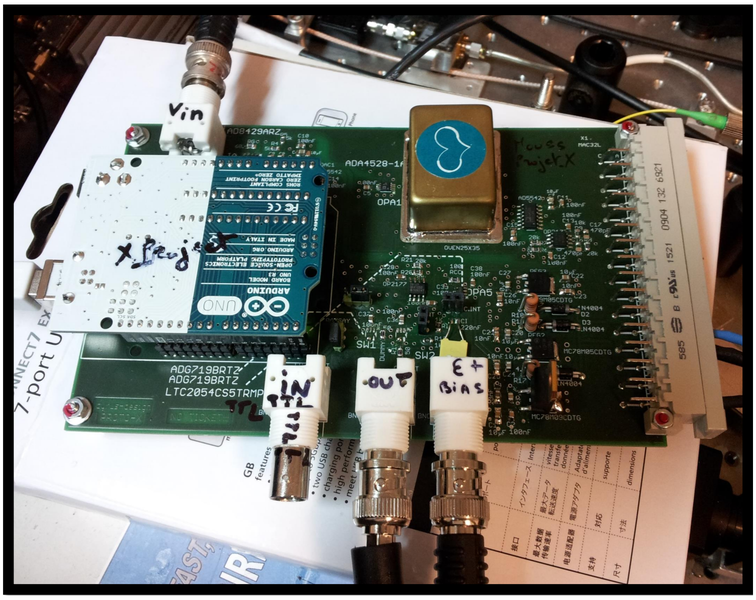

Figure 3.33: Picture of the LPSS electronic board. Developed by C. Rocher (FEMTO-ST).

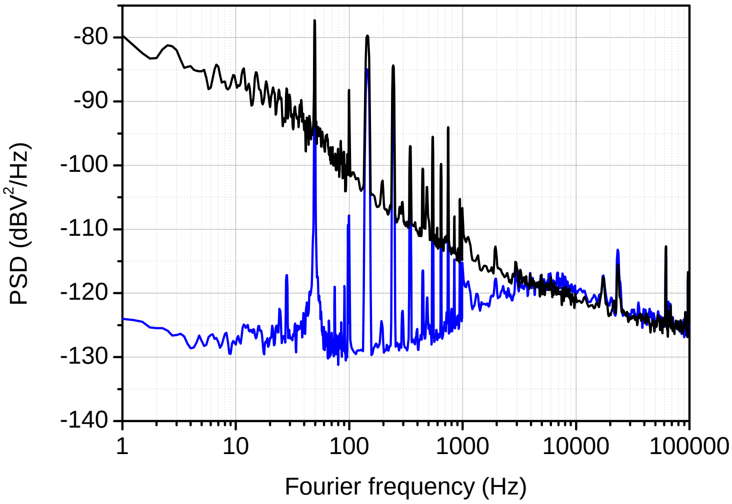

Figure 3.34: PSD of the error signal from the laser power stabilization servo. Black: open loop. Blue: closed loop.

Figure 3.34 shows the noise spectrum of the error signal generated by the servo in free mode (black curve) and in locked mode (blue curve). The noise level is reduced by about 12 dB at 1000 Hz and about 27 dB at 100 Hz. The servo loop bandwidth is around 8 kHz.

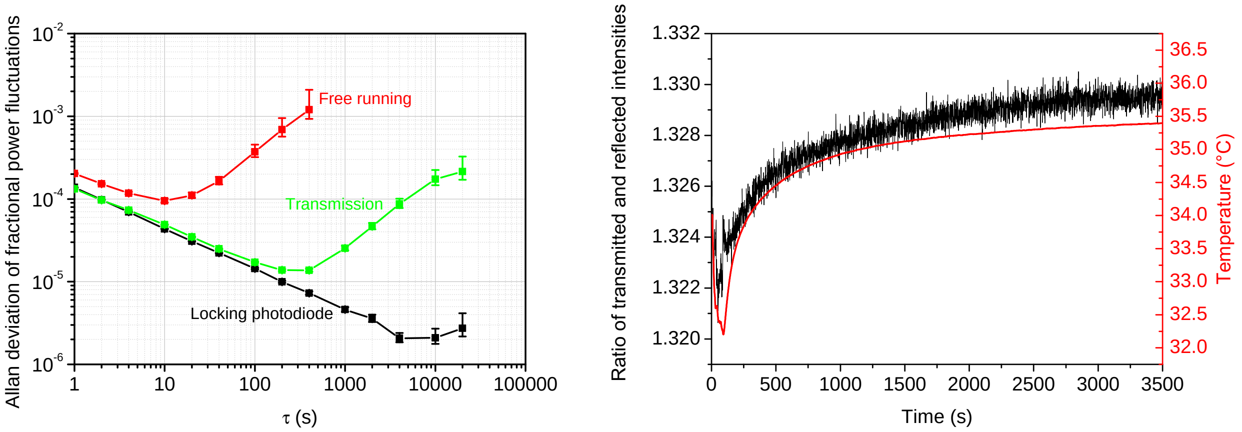

(a) (b)

Figure 3.35: (a) Allan deviation of fractional power fluctuations of (black) the beam used for power locking in closed loop, (green) the BS transmitted beam in closed loop, (red) the transmitted beam in free mode. (b) Effect of temperature on the BS reflectivity. Black: ratio between the BS transmitted and reflected powers. Red: temperature over the experimental bench.

Figure 3.35a shows the laser power stability gained thanks to the LPSS. The light intensities measured by the photodiode shown in Fig. 3.32 and by an additional photodiode placed on the BS transmitted beam path are monitored. The red curve is running in free mode. The laser fractional power fluctuations level is 2 10^{-4} at 1 s averaging time, 9.5 10^{-5} at 10 s and 3.7 10^{-4} at 100 s. Green curve and black curve stand for the BS transmitted and reflected beams, respectively, when the servo is on. For the directly stabilized arm (black curve) the fractional stability is 1.4 10^{-4} $\tau^{-1/2}$ until several thousands of seconds averaging time. It reaches a plateau at 2 10^{-6}. The transmitted arm (green curve), which is intended to make CPT interaction, presents the same intensity stability level (1.4 10^{-4}) at 1 s. The latter is slightly higher than for the reflected beam until several hundreds of seconds and reaches a floor at the level of 1.4 10^{-5}. At higher averaging times, we observe a drift of the power in this arm. The origin of this behavior is highlighted in Fig. 3.35b. The ratio of the photodiodes voltages is plotted as a function of time, as well as the surrounding temperature, in open loop mode. The acquisition is done just after closing the protection box surrounding the bench. The temperature of the set-up is progressively tending to steady state. We observe that the BS reflectivity depends on temperature. Then, even if the reflected arm power of the LPSS is stabilized, changes in temperature may cause the power in the transmitted beam to fluctuate. During acquisition the temperature changed by about 3 K and the BS reflectivity about 0.6 %. The sensitivity is then around 0.2 %/K. To reach the 10^{-14} level in clock frequency stability, the reflecty fluctuations have to be no more than 10^{-5}, meaning a control of the box temperature at the level of about 10 mK, which is not achievable without active temperature stabilization.

3.6.3 Generation of light pulses

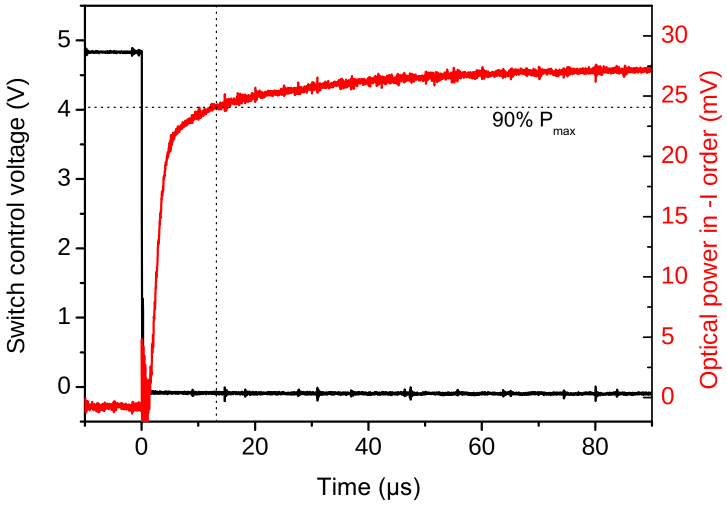

Figure 3.36: AOM output response to a pulse on the switch control voltage. Black: control voltage. Red: power in order -1 output of the AOM. The negative power observed at the beginning of the experiment is due to a negative offset in the photodiode output voltage measured with the oscilloscope.

By introducing an RF switch (Mini-Circuits ZASW-2-50DR+) between the frequency synthesizer and the AOM, we are able to switch on and off the light arriving to the cell. The switch state is controlled by an input TTL voltage (0 - 5 V). The power contained in the -1 order output of the AOM is set to zero when the control voltage goes from 0 V to 5 V. The attenuation coefficient is measured to be approximately 30 dB. Figure 3.36 shows the AOM output response to a pulse on the control voltage. The rise time of the laser (value taken at 90 % of the maximum) is 13 µs. This is satisfactory since the typical durations in the patterns used for Ramsey interrogation are of the order of a ms.

3.7 Push-pull scheme generation

In section 1.2.2, it was recalled that the CPT clock short-term frequency stability depends, among others, on the CPT resonance amplitude. In our CPT clock set-up, we use the PPOP scheme, produced by the Michelson interferometer-like system already represented in Fig. 2.12, to maximize the atomic population in the $m = 0$ Zeeman sublevels such that the 0-0 CPT resonance contrast is increased. The importance of the path length difference between the two arms of the Michelson set-up is highlighted in Fig. 3.37. The transmitted power through the CPT cell is measured as a function of the mobile mirror position.

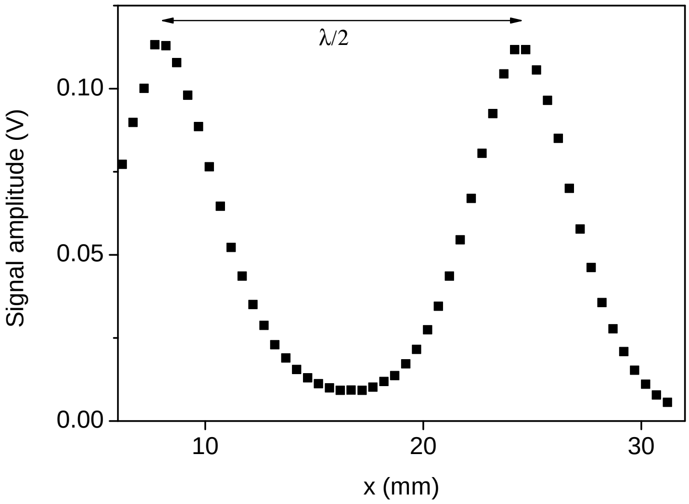

Figure 3.37: Cell transmission as a function of the Michelson set-up mobile mirror position.

The cell transmission periodically alternates between maxima and minima with a period $\Delta L = 16\,\text{mm}$, in agreement with Eq. (2.36). From this figure we conclude that we should set the mirror position at $x \approx 8\,\text{mm}$. Note that to date, no particular precaution is taken in our setup to stabilize ΔL, which proves that it is not of critical importance in order to reach the aimed specifications for the clock stability. This aspect will be detailed in subsection 4.3.5.

3.8 Physics package and vapor cell

3.8.1 Description of the physics package

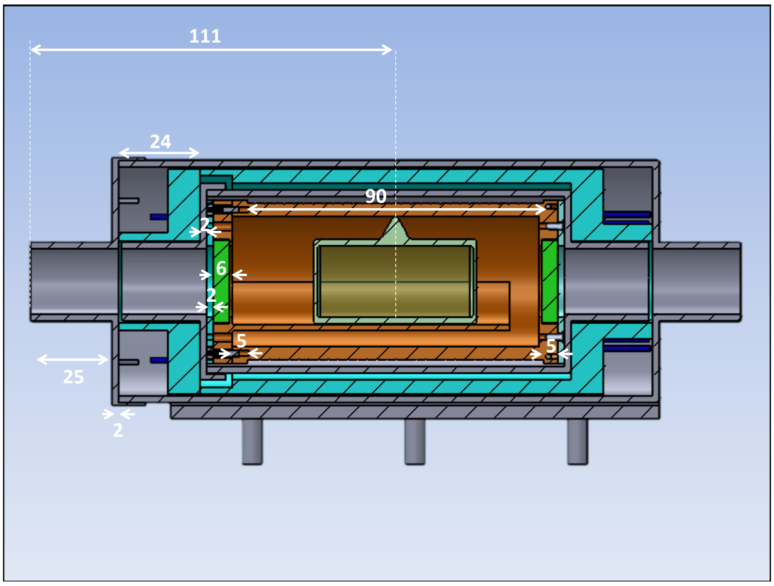

Figure 3.38: Drawing of the physics package. Designed and realized by P. Yun (LNE-SYRTE). Dimensions are given in mm.

A scheme of the physics package is shown in Fig. 3.38. The design of the physics package was performed by P. Yun (LNE-SYRTE) in the frame of the MClocks project. Pictures showing the different layers are shown in Fig. 3.39. The cells we used during my PhD thesis were filled at LNE-SYRTE by P. Bonnay. The empty cells are from Hellma, and the Cs bulbs are from Aldrich. The filling process is detailed in [122].

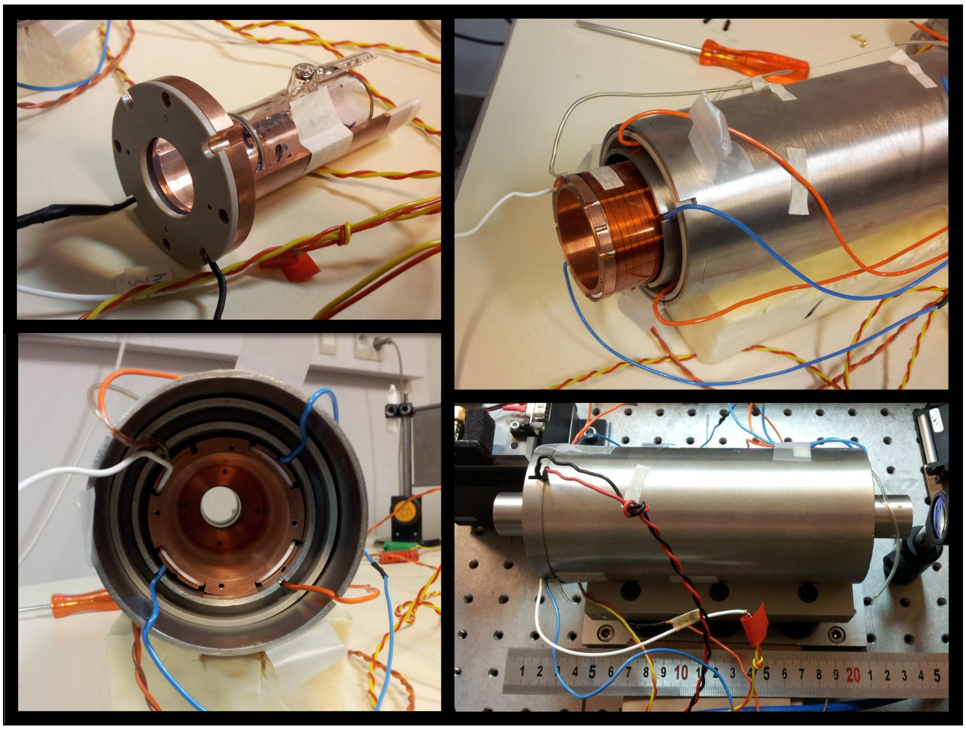

Figure 3.39: Pictures of the physics package.

The heart of the clock is a borosilicate glass cell containing the ^{133}Cs atoms and a N_2-Ar vapor mixture, like shown in Fig. 3.40. Several cells filled with a N_2/Ar buffer gas mixture were used during my thesis:

- cell "G", a 5 cm-long and 2 cm-diameter cell with total pressure 15 Torr and $r(Ar/N_2) = 0.4$.
- cell "C1B", a 5 cm-long and 2 cm-diameter cell with total pressure 15 Torr and $r(Ar/N_2) = 0.6$.
- cell "2-20", a 2 cm-long and 2 cm-diameter cell with total pressure 20 Torr and $r(Ar/N_2) = 0.6$.

The cell is placed inside a temperature-stabilized copper oven. Two additional glass windows are placed at each side of the cell to prevent thermal convection by air while allowing the laser beam to cross the package. The ensemble is isolated from the external magnetic field by a set of two mu-metal shields. A static magnetic field is also imposed by a DC current supplying a coil surrounding the cell, in order to lift the Zeeman degeneracy.

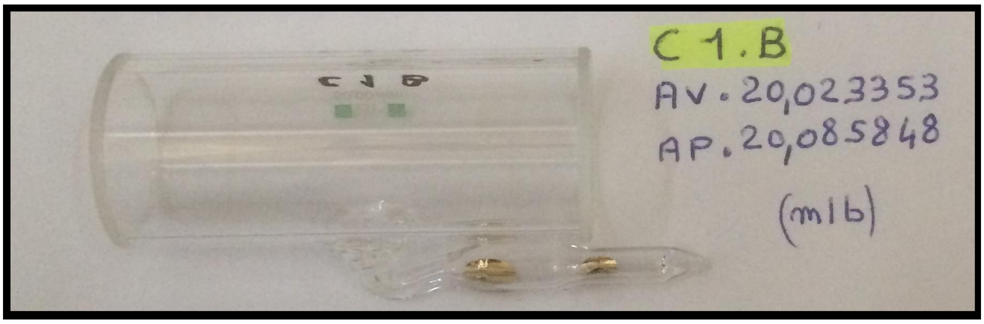

Figure 3.40: Photography of a Cs cell ("C1B") filled at LNE-SYRTE by P. Bonnay.

3.8.2 Magnetic field

3.8.2.1 Magnetic field homogeneity

Figure 3.41 shows the mapping of the axial static magnetic field along the physics package revolution axis. A Gaussmeter probe is moved along the revolution axis of the package and the axial field is measured. The coil intensity current in this experiment is 20 mA.

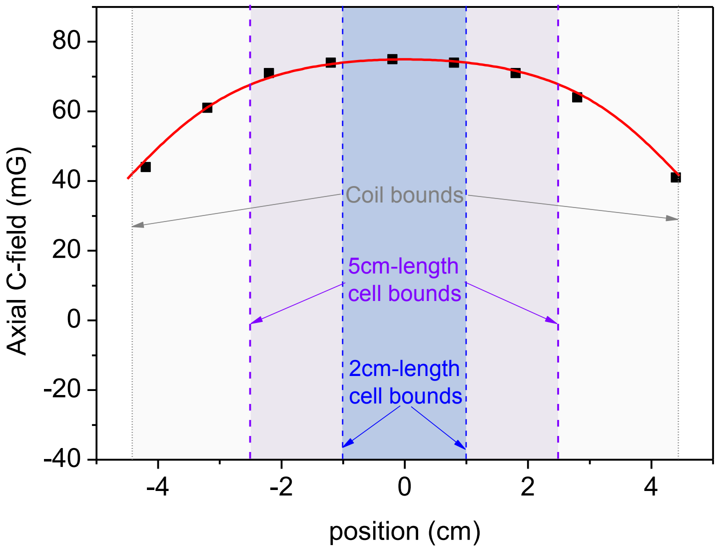

Figure 3.41: Measurement of the axial static magnetic field along the physics package revolution axis (black squares), and theoretical axial field computed from 3.18 (red line). The 0 position coincides with the coil center.

The axial magnetic field B_0 along the revolution axis of a finite solenoid can be derived from the Biot-Savart law and is expressed as:

$$B_0\left(z\right) = \frac{\mu_0 n I}{2}\left(\frac{a+z}{\sqrt{\left(a+z\right)^2+R^2}} + \frac{a-z}{\sqrt{\left(a-z\right)^2+R^2}}\right) \tag{3.18}$$

where z is the axial coordinate if $z = 0$ is the coil center position, $\mu_0 = 4\pi 10^{-7}$ is the permeability of free space, $n = 333\,\mathrm{m}^{-1}$ is the coil number of loops per unit length, $2a = 9\,\mathrm{cm}$ is its length, $R = 4.5\,\mathrm{cm}$ is its radius, and $I = 20\,\mathrm{mA}$ is the intensity current flowing through the coil. The measured data is in correct agreement with the expected magnetic field map. Figure 3.41 reveals the inhomogeneity of the static magnetic field inside the vapor cell. For a 5 cm-length cell, the maximum magnetic gradient felt inside the vapor is $\Delta B = 7\,\mathrm{mG}$. We neglected here any radial inhomogeneity. Atoms positioned in the gradient extrema experience a clock frequency shift difference due to magnetic field (it will be detailed in subsection 4.3.1) of around 0.4 Hz. This effect contributes to the broadening of the overall 0-0 resonance which can also be assessed as approximately 0.4 Hz. This value is very small compared to the typical CPT linewidths observed with this experiment (several hundreds of Hz). The maximum field amplitude difference in a 2 cm-long cell is only 1 mG, so the effect is even smaller. We can then state that the values of lengths of the coil and of the cell are sufficiently distant to allow us to neglect the effect of magnetic inhomogeneity in the cell on the 0-0 resonance width, and consequently on the clock short-term stability. However the other Zeeman resonances are expected to be much more impacted by these inhomogeneities. Figure 3.42 shows the effect of the cell length on the observed Zeeman spectrum in PPOP configuration. In this experiment a Zeeman spectrum is achieved in the same experimental conditions using two different cells. The black line is for a 2 cm-long cell (cell "2-20") and the red line for a 5 cm-long one (cell "G"). The cells also have different buffer gas ratios but since they do not impact the clock frequency dependence to magnetic field, it is not relevant here. The applied magnetic field is 24.4 mG. We observe that for the longer cell, the non 0-0 resonances

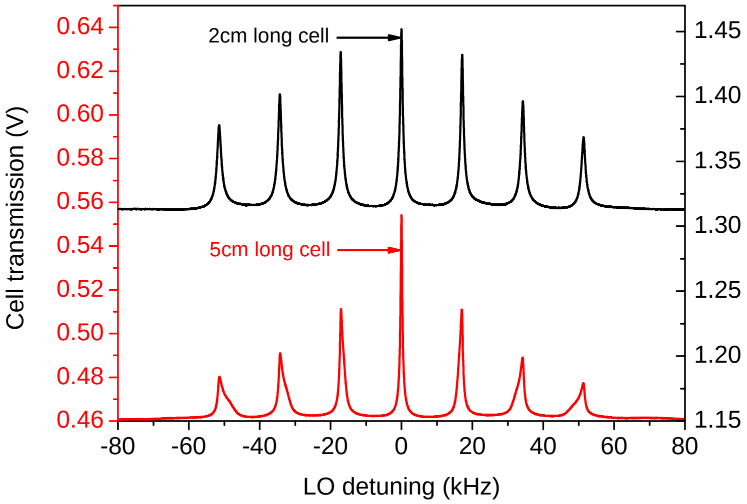

Figure 3.42: CPT spectra showing the Zeeman degeneracy lifting for a 2 cm-long cell ($r(Ar/N_2) = 0.6$, dark) and a 5 cm-long one ($r(Ar/N_2) = 0.4$, red). The static magnetic field inhomogeneity is well revealed on the non-{0-0} transitions when the cell length approaches the coil one. Left y-axis: 5 cm-long cell. Right y-axis: 2 cm-long cell.

are broadened and asymmetric. It is not noticeable on the 0-0 resonances for both cells. The Zeeman resonances are much less distorted for the shorter cell at this magnetic field level.

3.8.3 Temperature stabilization

The cell is positioned inside a copper cylinder, closed at its edges by two glass windows as already shown in Fig. 3.38. The cylinder is surrounded by a coaxial cable with high electrical resistance arranged in a serpentine pattern to heat the oven while canceling the produced magnetic fields in the cell. A NTC thermistor is in thermal contact with the oven and is used for the temperature regulation system. The latter relies on a controller similar to the one represented in Fig. D.2. Another NTC thermistor is disposed in close contact with the cell window to monitor as closely as possible the atomic vapor temperature fluctuations. Figure 3.43a shows typical fluctuations of the temperature sensed by the monitoring thermistor. The associated Allan deviation is plotted in Fig. 3.43b.

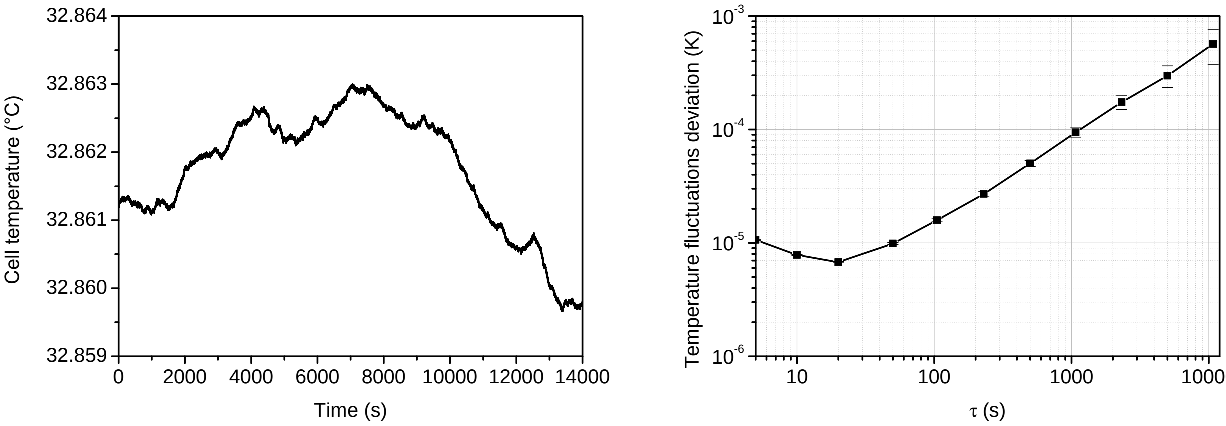

(a) (b)

Figure 3.43: (a) Cell temperature fluctuations and (b) associated deviation.

Typical temperature fluctuations are measured at the level of 21 µK at 1 s, 8 µK at 10 s and 90 µK at

1000 s.

3.9 Light detection

The photodiode used to detect the CPT cell transmission (Hamamatsu S1337-66BR) is implemented in a transimpedance amplifier circuit shown in Fig. 3.44a. Figure 3.44b is a picture of the photodiode package.

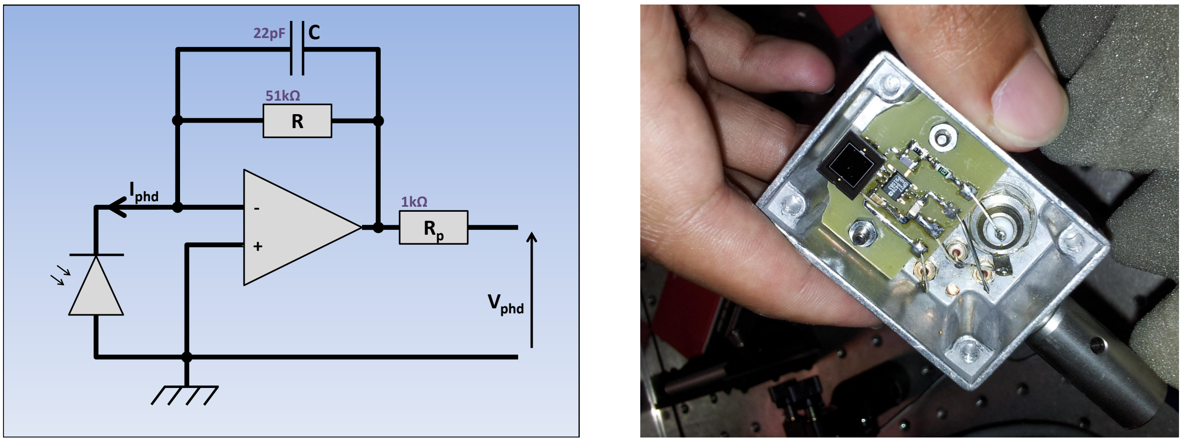

(a)

(b)

Figure 3.44: (a) Electrical diagram of the transimpedance amplifier circuit with gain R. (b) Photography of the CPT photodiode and the circuit.

For a DC photocurrent I_{phd} in the photodiode, the transimpedance circuit output signal is $V_{phd} = RI_{phd}$, where R is the transimpedance resistance. In our case, the feedback resistance is 51 kΩ and the feedback capacitor is 22 pF. This yields a bandwidth of 140 kHz.
Figure 3.45 shows typical absorption spectra obtained when scanning the laser frequency around the Cs D_1 line. The cell transmission is measured with the photodiode described above after the CPT cell (containing Cs and buffer gas).

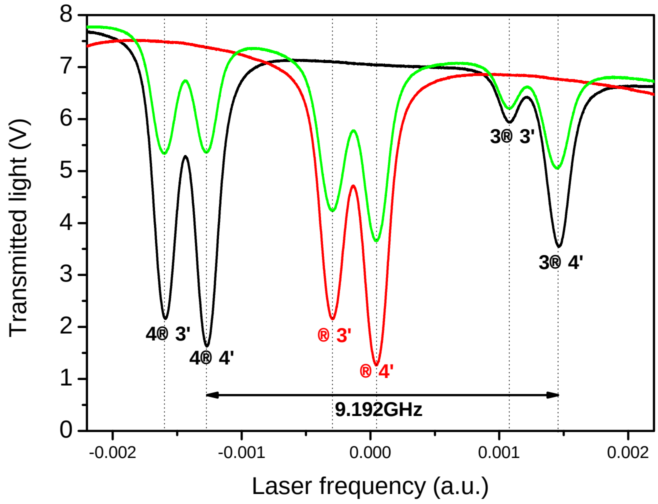

Figure 3.45: Cs D_1 optical lines. The x axis origin is arbitrary. Black: the laser is not modulated. Red: the laser is modulated at 4.596 GHz with suppressed carrier. Green: the laser is modulated with residual carrier power. The lateral pairs of absorption lines (3 → 3’, 3 → 4’, 4 → 3’, 4 → 4’) correspond to unique resonances. The central one (→ 3’, → 4’) is the sum of two pairs of resonances.

The laser frequency is controlled by the current supply intensity. The slope observed in the background is due to the change of laser power during the frequency scan. The black curve is collected when the laser is not microwave modulated. We observe 4 distinguishable absorption valleys corresponding to the Doppler broadened Cs D1 optical transitions. There are two doublets of valleys separated by 1.167 GHz, the excited state hyperfine frequency. Both doublets are separated by 9.192 GHz, the ground state hyperfine frequency. When the EOM is modulated at 4.596 GHz, an additional doublet appears in the middle of the original ones (see the green curve). Two extra doublets (not shown in the figure) also appear around the original ones. All doublets are now separated by 4.596 GHz. From left to right, they correspond to:

- EOM output order +1 exciting $F = 4$ transitions.
- EOM output carrier exciting $F = 4$ transitions.
- EOM output order +1 exciting $F = 3$ transitions and EOM output order -1 exciting $F = 4$ transitions.
- EOM output carrier exciting $F = 3$ transitions.
- EOM output order -1 exciting $F = 3$ transitions.

When setting the EOM input bias voltage at the carrier suppression point (see the red curve), the original doublets disappear, and the remaining ones are all separated by 9.192 GHz. The central doublet is deeper because both ground state hyperfine levels are involved, resulting in a cancellation of optical pumping effects in one of the latters. CPT occurs in the bottom of one of these central dips. The $F' = 4$ excited-state transitions are chosen since the CPT contrast for these transitions was found to be higher.

3.10 Servo system

The principle for locking the LO frequency (or the laser frequency) is the one described in [199]. Here, a square-wave modulation signal is generated by a multifunction data acquisition (DAQ) module (NI USB-6259-BNC) driven by a personal computer (PC). This signal modulates the DDS (see subsection 3.5.2) frequency so that the microwave frequency is modulated around the clock resonance. The photodetector signal is measured, digitized and averaged with the DAQ. The PC handles the signal demodulation and correction of the DDS output frequency. The modulation/demodulation technique allows to detect the CPT signal in a Fourier frequency band where the laser frequency flicker noise level is lower than in DC. At the same time it generates an error signal that zeroes when at exact microwave resonance, making possible the generation of a correction signal to stabilize the LO frequency on the center of the CPT resonance. Note that the modulation of the microwave phase can also be used instead of the microwave frequency.

A Python based software has been developed by V. Maurice (FEMTO-ST) and myself to manage the spectroscopic acquisition, the LO frequency locking, as well as the control of main electrical devices and the monitoring of crucial experimental quantities. Thousands of code lines have been written in the programme. The software manages:

- CPT spectroscopy in continuous or pulsed regime.
- LO frequency stabilization on the CPT resonance in continuous and pulsed regime.
- fit extraction of CPT resonances with main characteristics (contrast, linewidth, ...).
- scanning of the Fabry Perot cavity.
- monitoring of photodiode outputs and many other voltage signals.

- GPIB/USB interface for communication with devices (synthesizers, digital multimeters, FFT analyzer, ...).
- computation and display of Allan deviations.

A typical "user-interface", in CPT spectroscopy mode and in frequency-stability measurement mode, is shown in Fig. 3.46.

3.11 Passive protection from environment

On top of the optical bench is arranged a wooden box covered with an isolating foam layer as shown on the photography of Fig. 3.47a. This box is mainly intended for isolating the set-up from vibrations, spurious light and external temperature fuctuations, which could induce additional noise to the photodetector signal or clock frequency shifts. The effect of spurious light is represented in Fig. 3.47b. It is clear that the box allows to reduce the number and levels of 50 Hz harmonics (from ambient light) parasitic spurs.

We determined the efficiency of the box in passively filtering the external temperature fluctuations. The temperature is monitored with two NTC thermistors. One is placed inside the box and the other one outside the box in the laboratory room. The temperature in the room is stabilized around 22 °C with an air conditioning system. Inside the box the temperature is usually higher because of heating of the the cell and of the EOM module. Figure 3.48a reports the fluctuations of the temperatures measured by the two probes. The associated Allan deviations are plotted in Fig. 3.48b. The bench box was closed long before the beginning of the measurement to ensure a steady state has been established.

The mean temperature inside the box is measured to be around 26 °C and around 23.2 °C outside. The levels of inner temperature fluctuations are 2.2 mK at 1 s averaging time, 8.5 mK at 10 s and at 1000 s. We estimate that the box thermal insulation coefficient is around 6 until 1000 s averaging time. For longer durations, the box ability to filter thermal variations blurs.

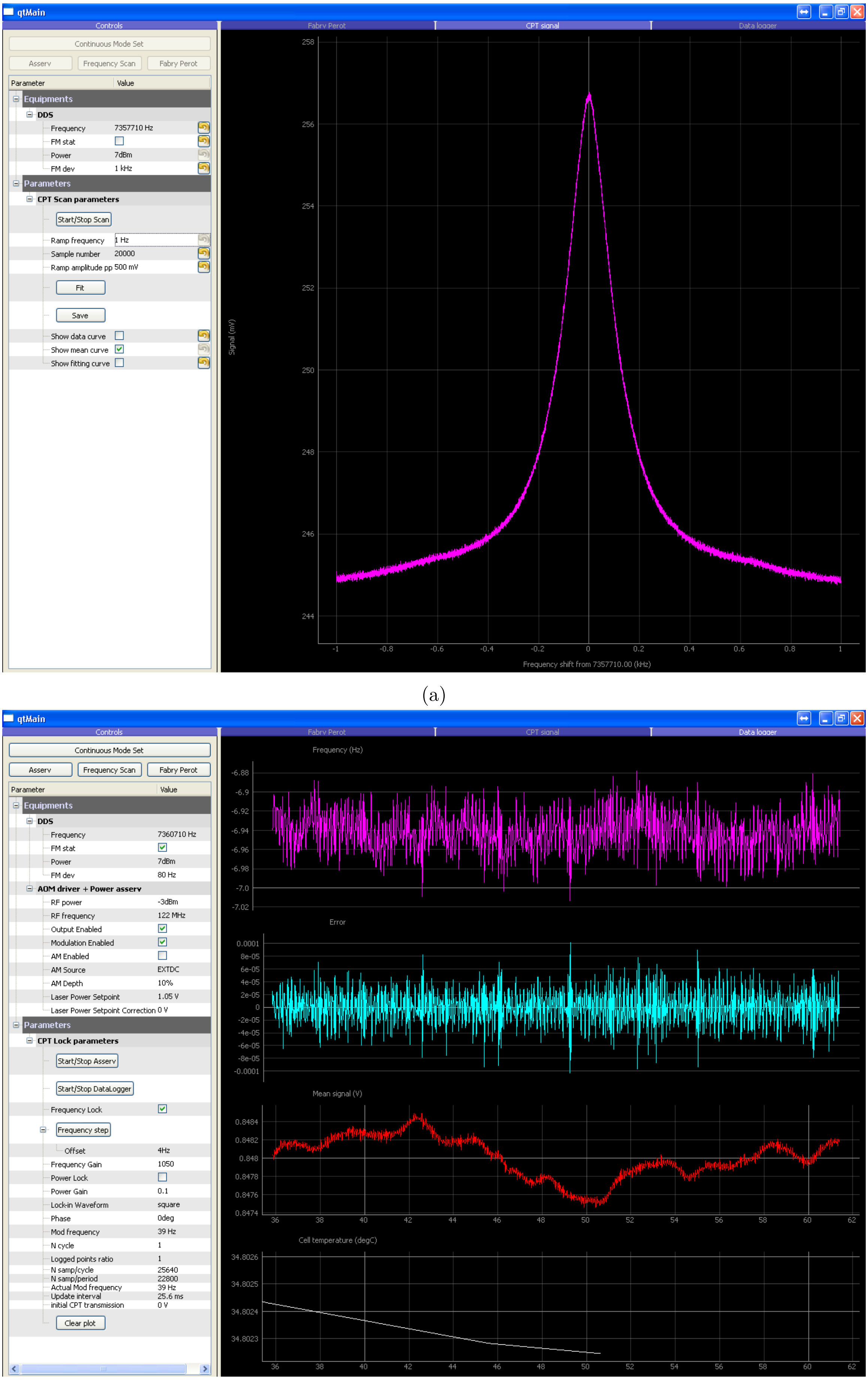

Parameter	Value
Equipments	
DDS	
Frequency	7357710 Hz
FM stat	☐
Power	7dBm
FM dev	1 kHz
Parameters	
CPT Scan parameters	
Ramp frequency	1 Hz
Sample number	20000
Ramp amplitude pp	500 mV
Show data curve	☐
Show mean curve	☑
Show fitting curve	☐

(a)

Parameter	Value
Equipments	
DDS	
Frequency	7360710 Hz
FM stat	☑
Power	7dBm
FM dev	80 Hz
AOM driver + Power asserv	
RF power	-3dBm
RF frequency	122 MHz
Output Enabled	☑
Modulation Enabled	☑
AM Enabled	☐
AM Source	EXTDC
AM Depth	10%
Laser Power Setpoint	1.05 V
Laser Power Setpoint Correction	0 V
Parameters	
CPT Lock parameters	
Frequency Lock	☑
Offset	4Hz
Frequency Gain	1050
Power Lock	☐
Power Gain	0.1
Lock-in Waveform	square
Phase	0deg
Mod frequency	39 Hz
N cycle	1
Logged points ratio	1
N samp/cycle	25640
N samp/period	22800
Actual Mod frequency	39 Hz
Update interval	25.6 ms
initial CPT transmission	0 V

(b)

Figure 3.46: Screenshot showing the python software graphic interface (a) in spectroscopy mode and (b) in clock-locked regime. Pink: Clock frequency fluctuations. Blue: error signal. Red: mean photodetector signal. White: cell temperature.

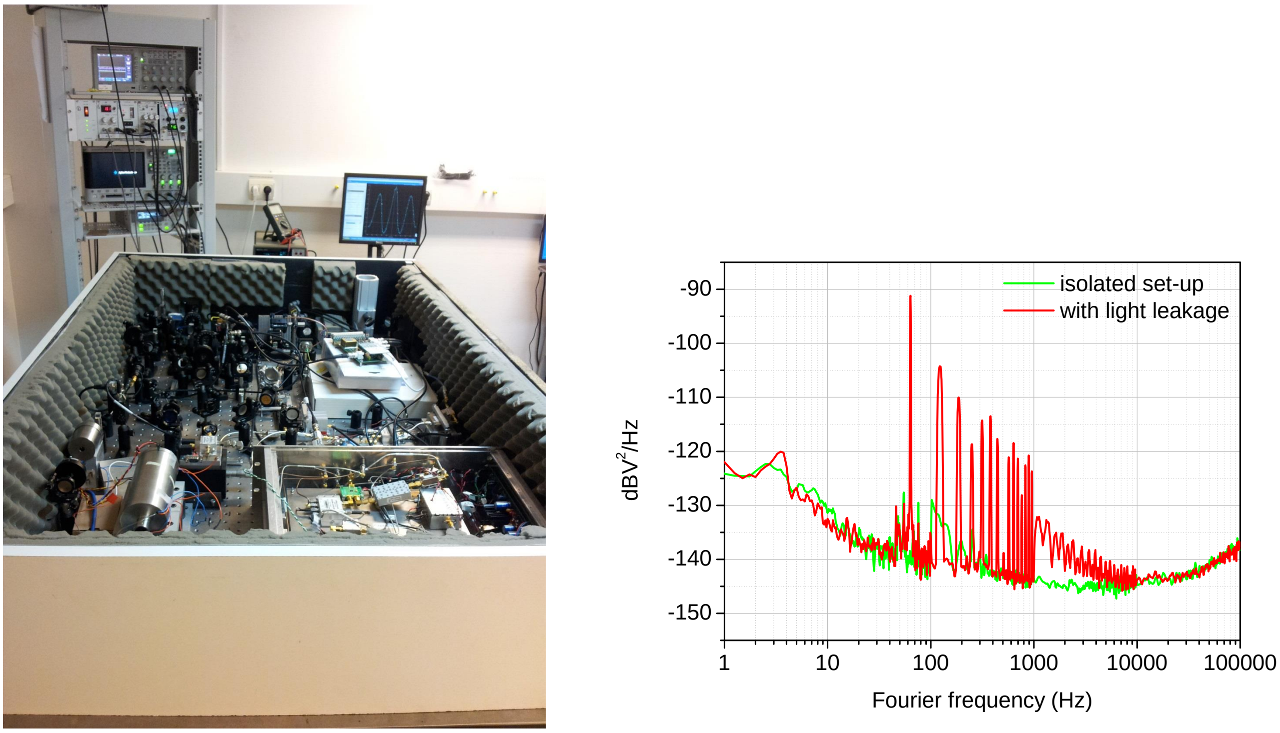

(a) (b)

Figure 3.47: (a) Photography of the set-up inside its protection box. (b) Effect of spurious light from the environment on the detected amplitude noise. The red curve is observed in the presence of a hole in the protection box. The hole is closed for the green curve.

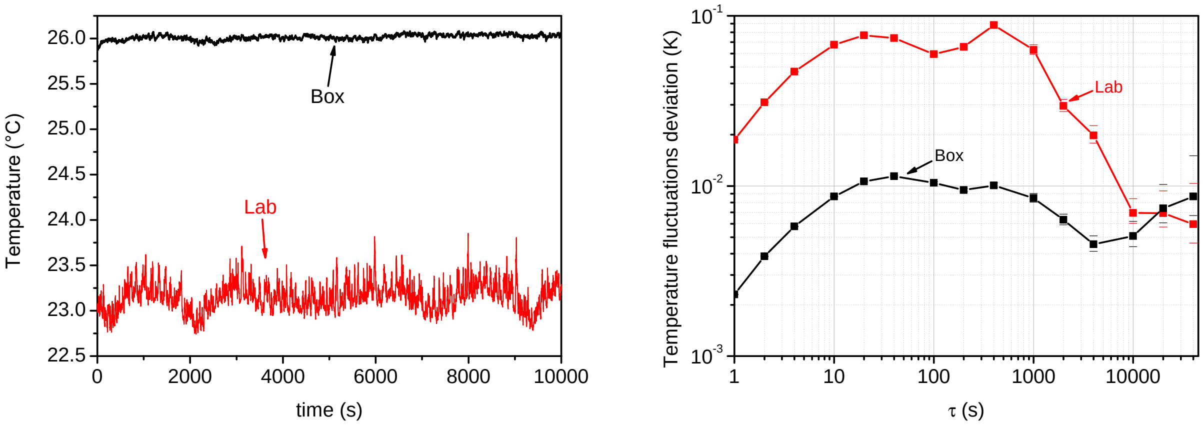

(a) (b)

Figure 3.48: (a) Typical fluctuations and (b) associated deviation of the temperature inside the protection box (dark) and out of it in the labroom (red).

Chapter 4

Continuous-mode CPT clock

This chapter reports metrological characterization and fractional frequency stability performances of the CPT clock operating in the CW regime, using the set up described in chapter 3.
I will describe first the operation sequence principle to stabilize the local oscillator frequency onto the CPT resonance.
In a second part, the study is focused on the clock short-term frequency stability. Starting from first encouraging stability results obtained in 2015, the clock performances were later improved. For this purpose, the impact of several experimental parameters, such as the laser power, the cell temperature or the EOM bias voltage, on the clock resonance properties was measured. This optimization, combined with several advanced steps to reinforce the setup, has allowed to demonstrate a clock frequency stability at the level of 2 10^{-13} $\tau^{-1/2}$ up to 100 s averaging time in the CW regime. A detailed noise budget is reported, highlighting the dominant contribution of laser effects.
In a third part, the clock mid-term frequency stability is studied and characterized in detail by evaluating mainly contributions from the Zeeman shift, the buffer-gas induced collisional frequency shift and light shift effects. The contribution from the Michelson system and the EOM are also reported. A detailed stability budget, for an averaging time of 1000 s, is extracted, highlighting major contributions from laser power and cell temperature effects. In the end of this chapter, a relevant number of further tests were performed in order to try to reduce power-induced light shift effects in the clock. For this purpose, the impact of numerous experimental parameters on the power-induced light-shift coefficient was investigated, trying to find a solution to cancel or reduce the light-shift slope. Moreover, a novel double-stage laser power stabilization electronics was developed to improve the laser power stabilization for mid- and long-term averaging times. Preliminary tests with the latter are reported. We'll show that we have not succeeded to improve the clock mid-term stability in the CW regime, limited to date at a record level of 2-3 10^{-14}. Nevertheless, these significant efforts and studies will constitute precious information for future activities on this CPT clock.

4.1 Operation sequence

The experimental set-up is the one described in chapter 3. In the continuous regime, light is continuously shining the vapor. The transmitted power is detected with a photodiode. The sequence used for frequency stabilization of the LO on the atomic resonance is shown in Fig. 4.1.

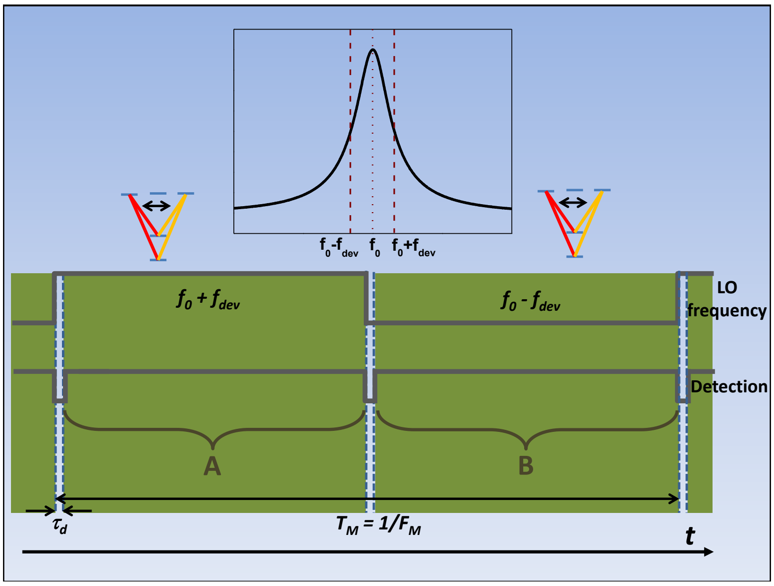

Figure 4.1: Sequence used for stabilizing the LO frequency on the CPT resonance. f_0 is the CPT resonance central frequency. f_{dev} is the depth of the LO frequency modulation. F_M is the LO modulation frequency, T_M the associated period. A and B are the averaged photodetector signal values over the detection windows for two successive half-periods. τ_d is a dead time during which the signal is not averaged.

The local oscillator frequency is modulated around the CPT resonance, at frequency F_M and amplitude f_{dev}. The detected signal is synchronously demodulated and filtered. For each period, the mean value B of the signal detected during the second half-period is substracted to the mean value A obtained in the first half-period. We obtain an error signal with shape similar to the one reported in [199] which cancels exactly at microwave resonance. A servo is assigned to generate and to send a correction signal to the local oscillator. At the beginning of each half-period is implemented a dead time τ_d, during which the signal data is not averaged, to take into account the transient regime appearing each time the LO frequency is sharply changed. A reduction of the error signal amplitude is observed when τ_d is too small.
If not mentionned, results exposed in this chapter have been obtained with a 5 cm-long and 2 cm-diameter Cs cell, filled with 15 Torr N_2-Ar buffer gas mixture with $r(Ar/N_2) = 0.4$ ("cell G").

4.2 Short-term frequency stability

4.2.1 Definitions

The short-term frequency stability of an atomic clock is usually limited by a white frequency noise that appears as a $\tau^{-1/2}$ slope in the Allan deviation. More particularly, in vapor cell atomic clocks, where the interrogation is all-optical, the photodiode detection noise dominates.
The PSD of frequency fluctuations, when it is white, can be written:

$$S_y(f) = h_0 \tag{4.1}$$

where h_0 is a positive constant. According to Table 1.1, it is possible to estimate the Allan deviation associated to the detection noise:

$$\sigma_y(\tau) = \left(\frac{S_y}{2}\tau\right)^{-1/2} \tag{4.2}$$

It is convenient to express it in term of the photodiode voltage noise, since this quantity is easily accessible. We have:

$$S_y = \frac{S_V}{\left(S_l\,\nu_0\right)^2} \tag{4.3}$$

where S_l is the resonance signal frequency discriminator, S_V the PSD of the photodiode output voltage fluctuations and ν_0 the central frequency. We will assume the approximation $S_l = \frac{A}{\Delta\nu}$, where A is the resonance signal amplitude and $\Delta\nu$ the linewidth. The Allan deviation is then:

$$\sigma_y(\tau) = \sqrt{\frac{S_V}{2}}\frac{\Delta\nu}{A\nu_0}\tau^{-1/2} \tag{4.4}$$

In the following, we will omit the factor 2 in the denominator inside the square root, because one-sided PSD is used. In the case where the dominating noise is not white ($S_V(f)$ is not constant), we will use the more general expression:

$$\sigma_y(\tau) = \left(\sigma_V\right)_{1\,\mathrm{Hz}}\frac{\Delta\nu}{A\nu_0}\tau^{-1/2} \tag{4.5}$$

where $(\sigma_V)_{1\,\mathrm{Hz}}$ is the deviation of the photodiode output voltage fluctuations in a 1 Hz-bandwidth measured at the modulation frequency F_M. We will assume $(\sigma_V)_{1\,\mathrm{Hz}} = S_V\,(F_M)$.
From Eqs. (4.4) and (4.5), we can easily understand that improving the clock performances implies to act on two fronts: the first one is to optimize the resonance amplitude over linewidth ratio, and the second one is to reduce the detected signal noise.

4.2.2 Resonance characteristics and noise measurements

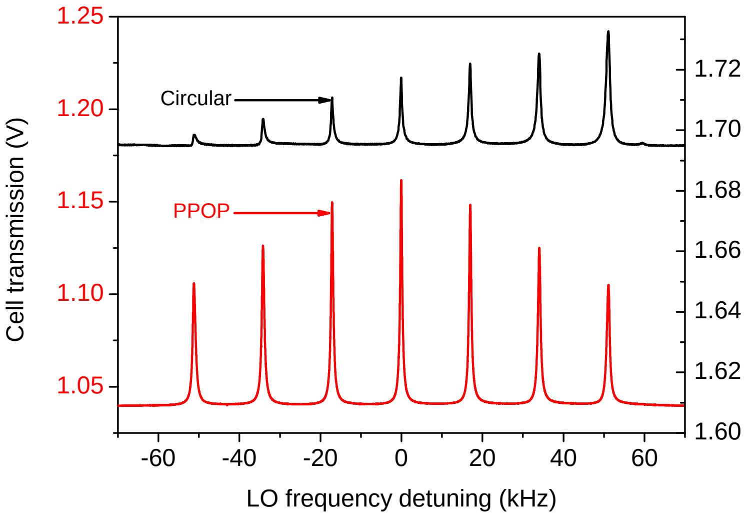

Figure 4.2: CPT spectra showing the Zeeman degeneracy lifting in single circular pumping and in PPOP schemes obtained with cell "2-20". The total input laser power is 400 µW (0.13 mW/cm^2), the static axial magnetic field is 24.5 mG and the cell temperature is 38 °C.

Figure 4.2 shows the impact on the Zeeman CPT spectrum of PPOP-type interrogation. When the gas cell is illuminated with a single circularly polarized light (black curve), one of the extreme Zeeman CPT resonance is favored with respect to other resonances. For a laser input intensity of 0.13 mW/cm^2 and a cell temperature of 38 °C, the 3-3 resonance ($m_{F=3} = 3, m_{F=4} = 3$) amplitude is 38 mV whereas the 0-0 resonance ($m_{F=3} = 0, m_{F=4} = 0$) amplitude is 22 mV, i.e. the amplitude ratio is 0.6. When using the PPOP scheme, the central 0-0 resonance is favored. In the same experimental conditions, the 3-3 resonance amplitude is 66 mV whereas the 0-0 resonance amplitude is 122 mV, i.e.

the amplitude ratio is 1.6. Comparing the 0-0 peaks contrasts in both configurations, we find 1.3 % for a circular polarization, and 11.7 % for PPOP. The contrast is raised by a factor of 9 using the PPOP scheme.

Figure 4.3a shows a typical CPT resonance signal obtained in clock configuration. The CPT signal amplitude is 104 mV, the signal level off resonance is 393 mV, the contrast is 26.4 % and the linewidth is 454 Hz. The discriminator slope, approximated by $S_l = \frac{A}{\Delta\nu}$, is 2.3 10^{-4} V/Hz. The noise spectrum recorded from the photodiode output signal for different experimental configurations: in the dark (a), without any stabilization and in presence of the CPT cell (b), with both laser frequency and AOM-based laser power servo active but without the CPT cell (c), with both laser frequency and AOM-based laser power servo active in presence of the CPT cell (d). For the latter (curve d), the detection noise is measured at half-height of the CPT resonance.

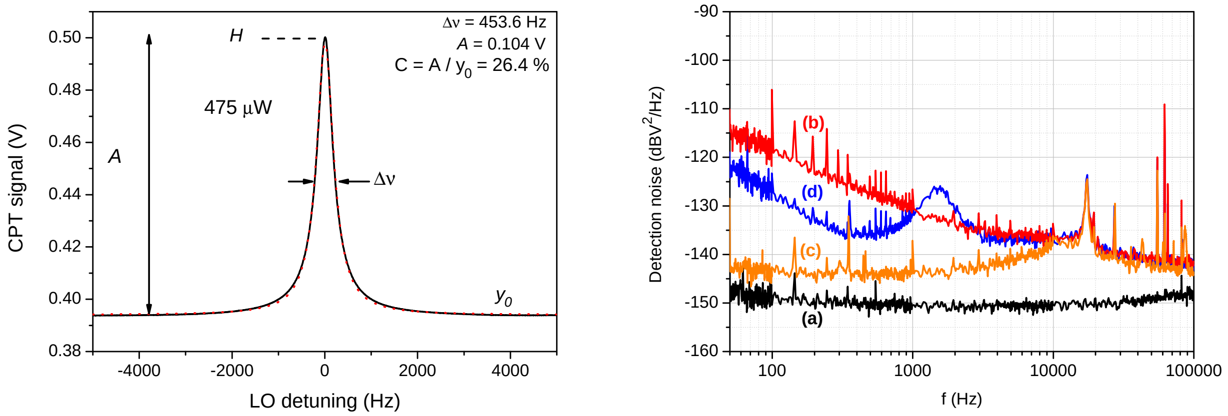

(a) (b)

Figure 4.3: (a) Black line: typical CPT resonance spectrum obtained for P = 475 µW. Red dotted line: Lorentzian fit. (b) Total detected noise at the output of the photodiode in different configurations. (a) In the dark, (b) with neather laser frequency stabilization, nor laser power stabilization, (c) with laser power and frequency stabilization and without the CPT cell, (d) with laser power and frequency stabilization in presence of the CPT cell.

4.2.3 Noise budget

The Allan variance is additive. Then, the clock allan deviation $\sigma_y(\tau)$ is the quadratic sum of all its contributions. If we name $\sigma_{y,i}(\tau)$ the contribution from parameter i to the clock stability, we can write:

$$\sigma_y(\tau) = \sqrt{\sum_i \sigma_{y,i}^2(\tau)} \tag{4.6}$$

In the following are listed the main expected sources of noise that can affect the short-term fractional frequency stability of the CPT clock. An estimation on their contribution is given using Eq. (4.4).

4.2.3.1 Shot noise

The shot-noise limited clock frequency stability $\sigma_{y,shot}(\tau)$ is calculated in the CW regime by [124]:

$$\sigma_{y,shot}(\tau) \simeq \sqrt{\left(\frac{\Delta\nu}{\nu_0}\right)^2 \frac{2h\nu_L}{C^2 P_o} \frac{1}{\tau}} \tag{4.7}$$

with h the Planck constant, ν_L the optical frequency (3.35 10^{14} Hz for the Cs D_1 line), C the resonance contrast and P_o the cell output power. In our case, according to the resonance characteristics, and $P_o = 17$ µW, we obtain $\sigma_{y,shot}$ (1 s) = 3.0 10^{-14}.

4.2.3.2 Photodetector intrinsic noise

Resistor thermal noise The resistor thermal noise, generated by the thermal motion of carriers in the component, is given by:

$$S_{V,R} = 4k_BTR \tag{4.8}$$

where $k_B = 1.38\ 10^{-23}$ J/K is the Boltzmann constant, T the resistor temperature in K and R the electric resistance. For a resistance of 51 kΩ and a temperature of 300 K, we obtain $S_{V,R} = 8.4\ 10^{-16}\ \mathrm{V}^2/\mathrm{Hz}$.

Operational amplifier (op-amp) voltage and current noise The op-amp used in the transimpedance circuit is an OP27G. The datasheet [200] indicates the op-amp voltage noise to be $1.4\ 10^{-17}\ \mathrm{V}^2/\mathrm{Hz}$ at 10 Hz (lower at higher Fourier frequencies) and the op-amp current noise is $1.0\,\mathrm{pA}/\sqrt{\mathrm{Hz}}$ at 30 Hz (also lower at higher Fourier frequencies), yielding an additional noise on the amplifier output signal of $2.6\ 10^{-15}\ \mathrm{V}^2/\mathrm{Hz}$. The total transimpedance noise is then lower than $2.6\ 10^{-15}\ \mathrm{V}^2/\mathrm{Hz}$ at 125 Hz.

Dark current noise The dark current is the residual current flowing through the photodiode when the latter is not illuminated. It is less than 100 pA for the Hamamatsu S1337-66BR [201]. The shot noise $S_{I,dark}$ associated with this additional I_{dark} current is

$$S_{I,dark} = 2eI_{dark} \tag{4.9}$$

It converts at the transimpedance output into a voltage noise $S_{V,dark} = S_{I,dark}R^2$, where R is the transimpedance circuit resistance. We find $S_{V,dark} = 8.3\ 10^{-20}\ \mathrm{V}^2/\mathrm{Hz}$.

Total photodetector noise The dominant noise is the op-amp current noise. We find $\sigma_{y,PD} < 2.4\ 10^{-14}\tau^{-1/2}$. Another way to get the contribution $\sigma_{y,PD}(\tau)$ of the detector noise is given by:

$$\sigma_{y,PD}(\tau) \simeq \sqrt{\left(\frac{1}{\nu_0}\right)^2 \frac{S_{V,dark}}{S_l^2}\frac{1}{\tau}} \tag{4.10}$$

with $S_{V,dark}$ the power spectral density of voltage noise at the output of the photodetector in the dark measured at $f = F_M$ and S_l the signal amplitude/linewidth ratio. In our case, as shown in Fig. 4.3b, the measured value of $S_{V,dark}$ is $1.3\ 10^{-15}\ \mathrm{V}/\sqrt{\mathrm{Hz}}$ at $f = F_M = 125$ Hz. This yields $\sigma_{y,PD}\ (\tau) = 1.7\ 10^{-14}\ \tau^{-1/2}$, in correct agreement with the previous calculated value.

4.2.3.3 Laser noise

The laser contributes to the detection noise by two mechanisms, which are direct laser amplitude noise, and frequency noise converted to amplitude noise after crossing the CPT cell [163, 202]. In curve (c) of Fig. 4.3b, the CPT cell is removed and the laser power impinging on the photodetector is adjusted to be similar to the one in clock operation, in the presence of the CPT cell. In this case, FM-AM conversion is canceled and the measured noise results mainly from the pure laser AM noise. In this configuration we observe that the total detection noise is largely smaller than in the presence of the CPT cell. In the CW regime, the contribution $\sigma_{y,AM-AM}(\tau)$ of the laser AM noise to the clock short-term frequency stability is given by:

$$\sigma_{y,AM-AM}(\tau) \simeq \sqrt{\left(\frac{1}{\nu_0}\right)^2 \frac{S_{V,AM-AM}}{S_l^2}\frac{1}{\tau}} \tag{4.11}$$

where $S_{V,AM-AM}$ is the PSD of the photodetector voltage in the conditions described above, in V^2/Hz, at $f = F_M$. In our conditions, at $f = 125$ Hz, in locked power conditions and for a laser power $P_o = 17$ µW impacting the photodetector, we measure $S_{V,AM-AM} = 5.0\ 10^{-15}\ \mathrm{V}^2/\mathrm{Hz}$, and then we find $\sigma_{y,AM-AM}$ (1 s) = $3.4\ 10^{-14}$.

The total contribution from the laser noise (AM-AM and FM-AM) is given by Eq. (4.11) by replacing

$S_{V,AM-AM}$ by S_V, measured in presence of the cell, and the laser power is adjusted to 475 µW at the cell input (curve (d) of Fig. 4.3b). We suppose the photodetector intrinsic noise is negligible (cf. subsection 4.2.3.2) and the dominating noise is white. We measure $S_V(125\,\mathrm{Hz}) = 1.6\ 10^{-13}\,\mathrm{V}^2/\mathrm{Hz}$ and we deduce $\sigma_{y,laser}\,(1\,\mathrm{s}) = 1.9\ 10^{-13}$.
Considering that the total photodetector noise is the sum of the contributions of FM-AM and AM-AM, then the contribution of laser frequency fluctuations to the clock short-term stability is $\sigma_{y,FM-AM} = \sqrt{\sigma^2_{y,laser} - \sigma^2_{y,AM-AM}}$. We thus have $\sigma_{y,FM-AM} = 1.9\ 10^{-13}$.

4.2.3.4 Intermodulation induced noise

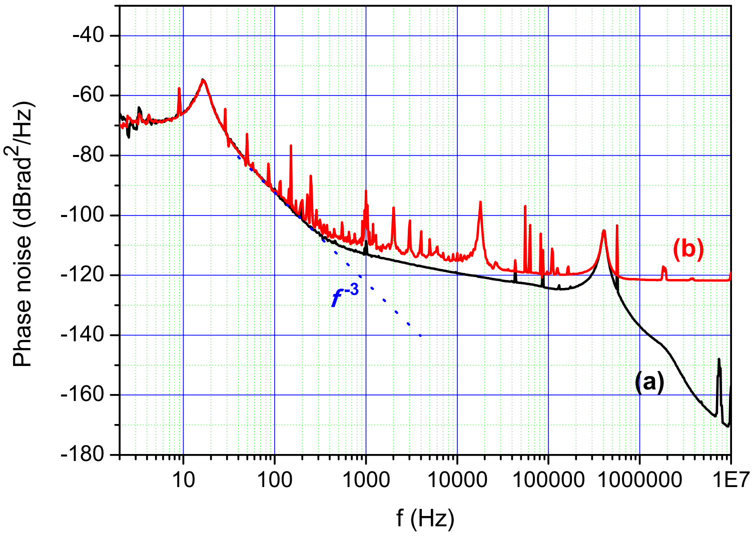

Figure 4.4: Absolute phase noise of the 9.192 GHz signal from the synthesis used in this experiment (different from the ones described in section 3.5). (a) Direct synthesis output, (b) 9.192 GHz optical beatnote at the EOM output. For information, the part of the spectrum with a f^{-3} slope is shown.

The contribution $\sigma_{y,LO}(\tau)$ of the LO phase noise to the clock short-term frequency stability is approximated in the CW regime by Eq. (3.12). Figure 4.4 shows an absolute phase noise measurement of the frequency synthesis used at the time of the experiment. The latter is different from the frequency synthesis presented in 3.5. It is an older version of the NLTL-based architecture, presenting higher phase noise than the one described in 3.5. We measured a phase noise $S_\varphi(2F_M) = S_\varphi(f = 250\,\mathrm{Hz}) = -101\,\mathrm{dBrad}^2/\mathrm{Hz}$, yielding $\sigma_{y,LO}\,(1\,\mathrm{s}) = 6.1\ 10^{-14}$.

4.2.3.5 Summary

Table 4.1 resumes the main contributions to the clock short-term frequency at 1 s averaging time. The main limitations are FM-AM conversion process in the cell, laser AM noise and the LO phase noise through the intermodulation effect. Other contributions are much lower and negligible at the moment.

4.2.4 Clock short-term frequency stability

Figure 4.5 reports first encouraging short-term fractional frequency stability results of the CPT clock, obtained in March 2015. In normal operation (curve (b)), the latter is measured to be 3 10^{-13} $\tau^{-1/2}$ up to about 100 s averaging time, in correct agreement with SNR measurements.
In these measurements, the bump between 1 s and 10 s was attributed to the EOM bias voltage servo loop gain. For confirmation, we performed during a shorter time a measurement of the clock frequency

Table 4.1: Summary of the different noise sources and their contributions to the clock short-term stability at 1 s averaging time.

Noise source	$\sigma_{\mathbf{y}}(1\,\mathrm{s})$
Shot noise	$3.0\ 10^{-14}$
Detector intrinsic noise	$1.7\ 10^{-14}$
Local oscillator phase noise	$6.1\ 10^{-14}$
Total laser noise (AM and FM-AM)	$1.9\ 10^{-13}$
Total	$2.0\ 10^{-13}$

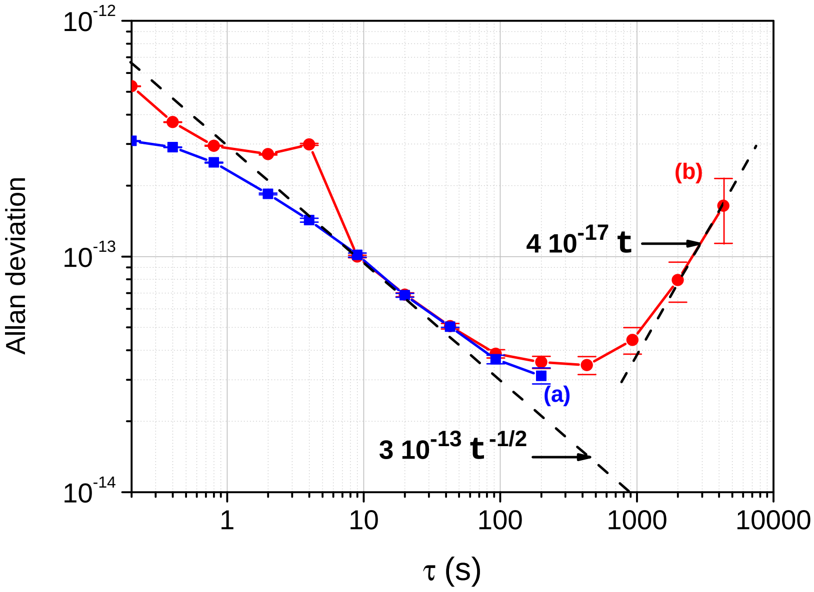

Figure 4.5: Allan deviation of the clock frequency. The laser power incident to the cell is 475 µW. The static magnetic field is 89 mG. (a) EOM bias servo loop off and (b) EOM bias servo loop activated. Two dashed lines with slopes $3\ 10^{-13}\ \tau^{-1/2}$ and $4\ 10^{-17}\ \tau$ are also represented.

stability when turning off the EOM bias servo loop (see Fig. 4.5, curve (a)). In this case, the bump between 1 s and 10 s averaging time clearly disappeared. The presence of this bump was fixed later by adjusting the servo gain. The measured short-term frequency stability level is a little higher than the expected value given in Table 4.1. As it will be shown in subsection 4.3.3, this could be explained by the fact that laser power fluctuations already contribute to the clock frequency stability at short averaging times via intensity light-shift effects (AM-FM).

4.2.5 CPT resonance spectroscopy: signal/linewidth optimisation

In order to optimize the clock short-term frequency stability, we investigated in detail the evolution of the CPT resonance with numerous experimental parameters. The cell temperature is 35 °C. Figure 4.6 details the behavior of the clock CPT resonance characteristics with light power at the cell input. The background level is proportional to the input power. This behavior is expected as long as the optical absorption follows the Beer-Lambert law, i.e. the laser intensity is below the saturation intensity. The signal amplitude A is given by Eq. (2.7). Ω_R is proportional to the light intensity squared. For small powers ($\Omega_R^2 << \gamma_{12}\Gamma^*$), the CPT amplitude depends quadratically on laser power. This is observed for $P < 100\,\mu\mathrm{W}$. For high powers ($\Omega_R^2 >> \gamma_{12}\Gamma^*$), the dependence is linear. This is observed for $P > 400\,\mu\mathrm{W}$ (see Fig. 4.6b).

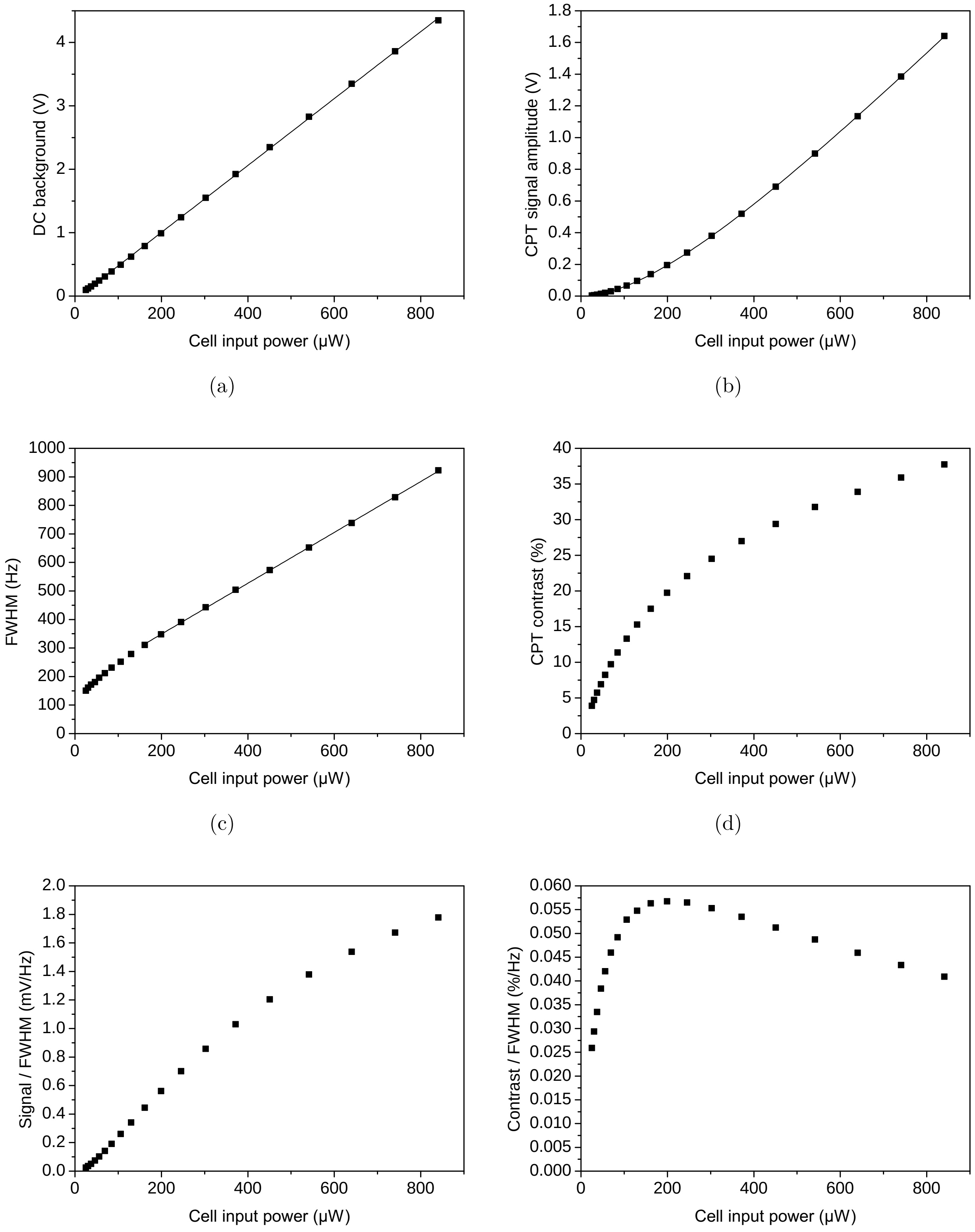

(a) (b)

(c) (d)

(e) (f)

Figure 4.6: CPT resonance spectroscopy versus the cell input optical power in CW regime. Cell temperature = 35 °C. Magnetic field = 89 mG.

According to Eq. (2.9), the CPT linewidth $\Delta\nu = FWHM$ is expected to be linearly dependent with the input power. We observe a linear behavior ($\Delta\nu[\text{Hz}] = 170 + 0.89P[\mu\text{W}]$) at high intensities but the slope seems to change at very low input powers ($P < 100\,\mu\text{W}$). We do not explain this behavior at this time, but an investigation is currently performed in the frame of G. Coget's thesis at FEMTO-ST, with our colleagues from Institute of Laser Physics (Novosibirsk). The CPT contrast and the ratio $A/\Delta\nu$ seem to increase monotonically with laser intensity in the range studied. The contrast reaches a value of 20 % and 35 % at 200 µW and 800 µW, respectively. We expect the detector output noise PSD to increase quadratically with laser power. In order to take it into account, we define a figure of merit as the CPT contrast/linewidth ratio. We observe in Fig. 4.6f that this quantity is maximized for an input laser power of around 200 µW. The laser power should be adjusted in this power range to optimize the clock short-term frequency stability.

Figure 4.7 presents a similar study versus the cell temperature. The laser input power is 200 µW. When increasing the temperature, the atomic density in the cell increases. The effect is to increase the atomic absorption and the CPT resonance amplitude. Due to atomic absorption, the light intensity at the entrance of the cell is usually higher than close to the cell output. This intensity decrease along the cell length is more brutal when increasing the temperature. The CPT linewidth resulting from the zone closer to the cell output is expected to be smaller than at the cell entrance, yielding a narrowing of the overall resonance with increasing temperature. On the other hand, inelastic collisions with the buffer gas are more frequent at higher temperatures. The ground hyperfine coherence lifetime decreases. This is expected to diminish the signal amplitude and to increase the linewidth. This is well observed in Fig. 4.7: the background level goes down when the temperature increases, the CPT signal amplitude reaches a maximum at around 29.5 °C before decreasing, and the linewidth decreases until 44 °C, before it increases again. The signal amplitude/linewidth ratio is maximized for a cell temperature of around 33 °C. The contrast/linewidth ratio is maximized in the 38-40 °C range.

A last comparable study has been performed versus the EOM bias voltage (see Fig. 4.8) and the static magnetic field amplitude (not shown). We will retain that the experience confirmed that the figures of merit defined before are maximized at the carrier suppression setpoint (EOM bias = 1.8 V in Fig. 4.8), and that it is almost independent from the applied magnetic field, as long as the latter is high enough to resolve the Zeeman CPT resonances.

In summary, we found from this CPT spectroscopy study that experimental conditions allowing to optimize the clock short-term frequency stability are a cell input power of about 200 µW, a cell temperature around 33 °C, and an EOM bias at carrier suppression setpoint. We will see in section 4.4.1 that setting these parameters allowed us to improve the short-term frequency stability at the level of $2\ 10^{-13}$ at 1 s averaging time.

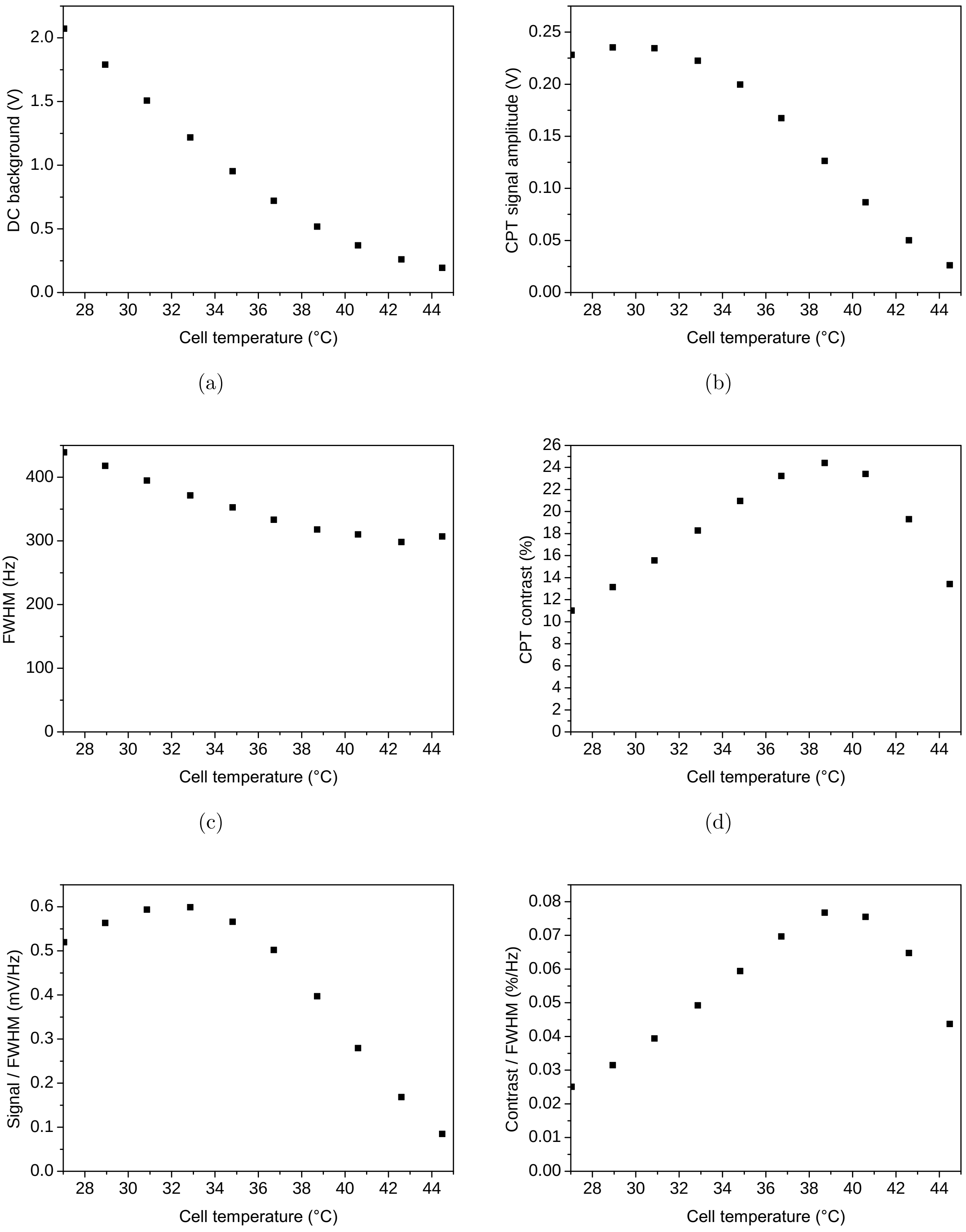

(a) (b)

(c) (d)

(e) (f)

Figure 4.7: CPT resonance spectroscopy versus the cell temperature in continuous regime. Input laser power = 200 µW. Magnetic field = 89 mG.

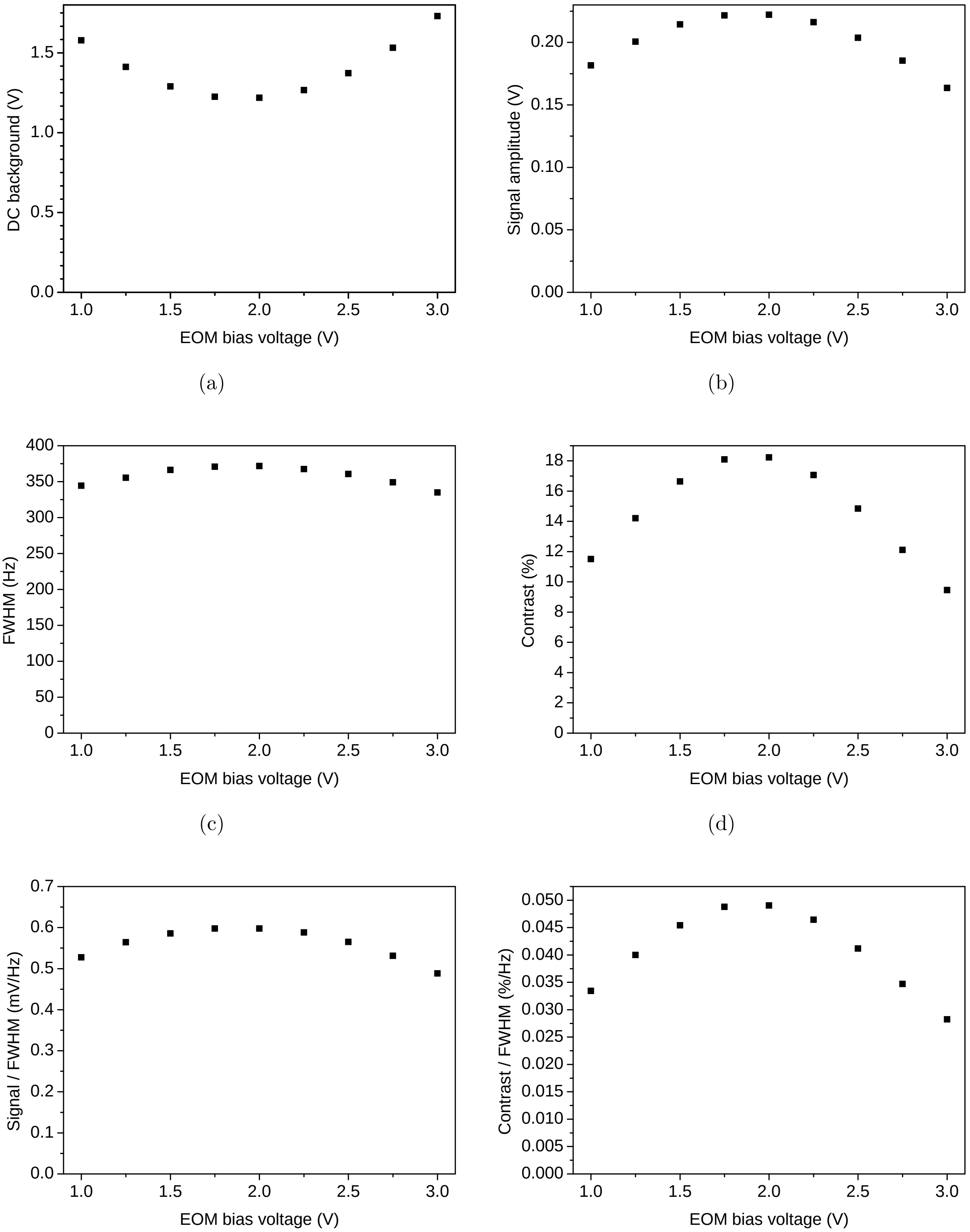

(a) (b)

(c) (d)

(e) (f)

Figure 4.8: CPT resonance spectroscopy versus the EOM bias voltage in CW regime. Input laser power = 275 µW. Cell temperature = 35 °C. Magnetic field = 89 mG.

4.3 Mid-term frequency stability

In this section, we characterize how experimental parameters impact the clock mid-term stability. The sensitivity of the clock frequency to the main experimental parameters is measured. Recording the typical fluctuations of these parameters allow us to extract their respective contributions to the clock mid-term stability. In this study, in agreement with the clock signal allan deviation of Fig. 4.5, evaluations are reported for an averaging time of 1000 s.

4.3.1 Magnetic field

4.3.1.1 Introduction

The Zeeman sublevels energies depend on the surrounding magnetic field. The transition energy between two Zeeman sublevels can be calculated from the Breit-Rabi formula (Eq. (2.14)). In particular, one can infer from Eq. (2.14) the relative displacement of neighbouring ground hyperfine transitions ν_{mm} and ν_{-m-m} (where m is 1, 2 or 3):

$$\nu_{mm} - \nu_{-m-m}(x) = m\nu_0\frac{x}{2} \tag{4.12}$$

For Cs we can directly write:

$$\nu_{mm} - \nu_{-m-m}(B) = m\ 1.401\,681\,3\ 10^6 B \tag{4.13}$$

We notice from Eq. (4.13) that the non-0-0 CPT transitions frequencies are excellent indicators of the actual axial static magnetic field experienced by the Cs atoms in the cell. In that sense, we decided to measure the fluctuations of the 1-1 resonance central frequency to determine the magnetic field fluctuations in the vapor.

4.3.1.2 Current intensity-magnetic field calibration

In a first step, in order to calibrate the coil current to magnetic field conversion, we measure the frequency of the neighbouring resonances from the 0-0 peak as a function of the magnetic field. The LO frequency is initially locked on the $|3,1\rangle \to |4,1\rangle$ resonance. The Cs cell used for this experiment (cell "2-20") was 2 cm long and is filled with 20 Torr of a N_2-Ar mixture with ratio $r(Ar/N_2) = 0.6$. This avoids broadening and distortion of the Zeeman CPT peaks as shown in Fig. 3.42 when using a longer cell. The static magnetic field is generated by injecting a current in the coil surrounding the CPT cell. The current driver is from Thorlabs (LDC202C). We measured the frequency displacement of the LO stabilized on the 1-1 transition when rising the coil current intensity. A similar experiment was performed with the LO locked on the $|3,-1\rangle \to |4,-1\rangle$ resonance. The frequency difference $\nu_{11} - \nu_{-1-1}$ between these two resonances is plotted in Fig. 4.9.
The data is fitted by a linear curve with slope 5.73 kHz/mA. Using Eq. (4.13) with $m = 1$, we conclude that the current to magnetic field conversion coefficient is 4.09 G/A.

4.3.1.3 Clock frequency sensitivity to magnetic field

The LO frequency is stabilized again on the magnetic field-insensitive 0-0 clock CPT resonance. Figure 4.10 shows the measured clock frequency as a function of the static magnetic field, using the coefficient found above. The clock frequency increases quadratically with the magnetic field, and the second order coefficient extracted from fitted data is 427 Hz/G^2, in excellent agreement with Eq. (2.17). Note that the same experiment has been done using a 5-cm long cell (cell "G") and the measured quadratic coefficient was rather 391 Hz/G^2. This gap between the observed and the expected values is attributed to the distorsion and spreading of the Zeeman CPT peaks due to magnetic inhomogeneities in the long cell (see section 3.8.2.1). Assuming a static magnetic field of 50 mG, the clock frequency sensitivity to magnetic field is 4.6 10^{-9} G^{-1}.
At high enough magnetic fields, we can resolve two resonance peaks at each side of the clock resonance. These are $\Delta m = 2$ CPT resonances, as it was shown in Fig. 2.10. They have weak amplitudes ($\sim 6\,\%$

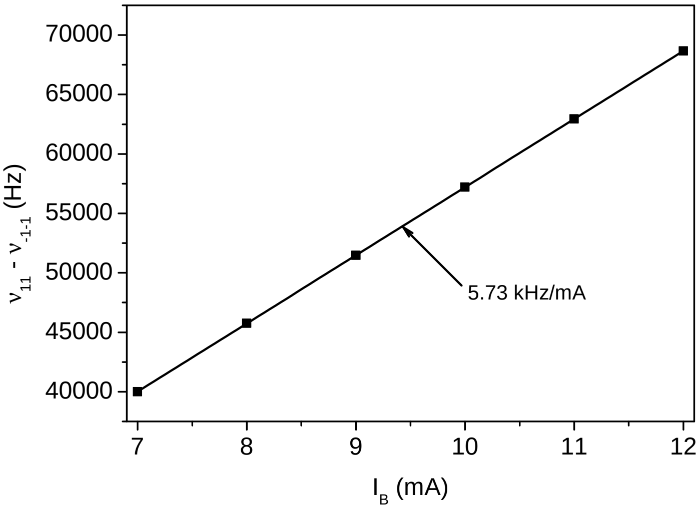

Figure 4.9: Frequency difference between $|3,1\rangle \rightarrow |4,1\rangle$ and $|3,-1\rangle \rightarrow |4,-1\rangle$ resonances, plotted as a function of the coil current intensity. Black squares: experimental data. Black line: linear fit. Cell = "2-20". Input laser power = 275 µW. Cell temperature = 35 °C.

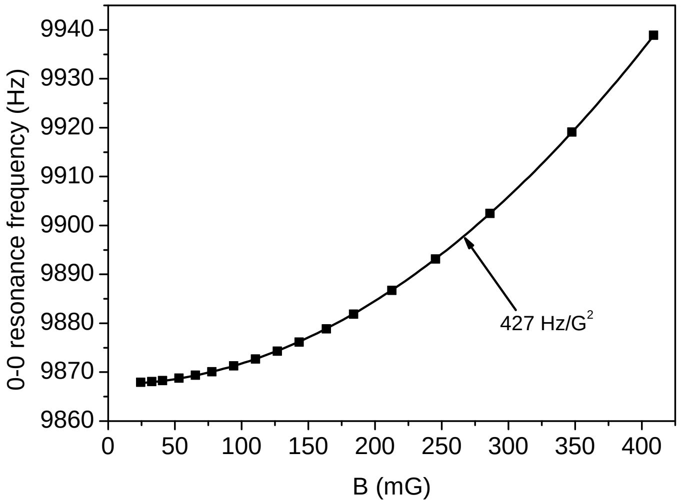

Figure 4.10: Clock frequency versus the static magnetic field. Black squares: experimental data. Black line: quadratic fit. The y-axis is relative to the Cs natural ground hyperfine frequency (9 192 631 770 Hz). Cell = "2-20". Input laser power = 275 µW. Cell temperature = 35 °C.

of the 0-0 resonance amplitude) and their shift from the central resonance is given by Eq. (2.33). For a static magnetic field of 50 mG, the frequency shift of the $\Delta m = 2$ transitions is about ±56 Hz, far lower than typical CPT resonances linewidths in clock condition. Furthermore, Fig. 4.10 shows that even in presence of these sideways resonances, the measured central frequency shift still follows the one of the 0-0 theory. Thus, we will neglect their effect in the rest of the manuscript.

4.3.1.4 Contribution to the clock frequency stability

In order to estimate the contribution of the magnetic field fluctuations on the clock mid-term stability, the local oscillator frequency was locked on the $|3,1\rangle \rightarrow |4,1\rangle$ CPT peak. We measured the fluctuations $\delta\nu_{11}$ of the LO frequency in these conditions. From Eq. (2.14), we get that the

$|3,1\rangle \to |4,1\rangle$ transition frequency ν_{11}, for Cs and at first order, is such that:

$$\nu_{11}(B)[\text{Hz}] = 9\,192\,631\,770 + 700\,840.64\,B[\text{G}] \tag{4.14}$$

Derivation of this equation gives:

$$d\nu_{11}(B)[\text{Hz}] = 700\,840.64\,dB[\text{G}] \tag{4.15}$$

In parallel, from Eq. (2.17), one finds:

$$d\nu_{00}[\text{Hz}] = 854.906\,60\,B[\text{G}]\,dB[\text{G}] \tag{4.16}$$

If we consider small fluctuations, the contribution of the magnetic field to the clock frequency stability can then be derived from the monitored fluctuations $\delta\nu_{11}$ of the $|3,1\rangle \to |4,1\rangle$ transition frequency and is given by:

$$\frac{\delta\nu_{00}}{\nu_0} = \frac{854.906\,60}{\nu_0[\text{Hz}]}B[\text{G}]\,\delta B[\text{G}] = \frac{854.906\,60}{700\,840.639\,\nu_0}B[\text{G}]\,\delta\nu_{11}[\text{Hz}] \tag{4.17}$$

where $\delta\nu_{00}$ and δB are the fluctuations of the clock resonance frequency and of the magnetic field, respectively. This contribution is reported in Fig. 4.11 for $B = 50$ mG. The measured contribution of the magnetic field to the clock frequency stability is 4.1 10^{-16}, 1.2 10^{-15} and 2.3 10^{-15} at 1 s, 100 s and 10 000 s averaging times, respectively. We conclude that, presently, the magnetic field fluctuations are not a limitation for the desired specifications until 10 000 s. This contribution could be reduced even further with a lower static magnetic field or using a current source with lower intensity noise.

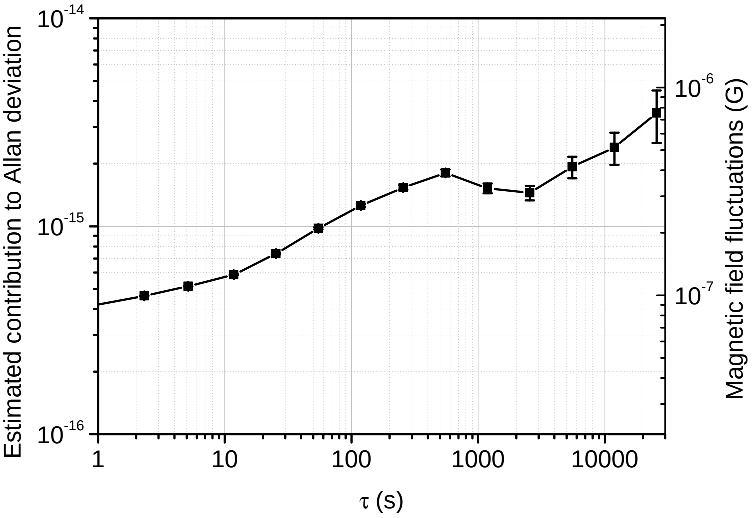

Figure 4.11: Estimated contribution of the static magnetic field fluctuations to the clock frequency stability $\frac{\delta\nu_{00}}{\nu_0}$ (for $B = 50$ mG) according to Eq. 4.17.

4.3.2 Cell temperature

4.3.2.1 Collisional frequency shift measurements

We remind that the presence of a buffer gas causes a frequency shift $\Delta\nu_{bg}$ of the clock frequency that can be written, for a mixture of two buffer gas and in a limited temperature range (see Eq. (2.19)). Using the coefficients reported in [139], we can write for $r(Ar/N_2) = 0.4$:

$$\Delta\nu_{bg} = P_0\left[603.1 + 0.2629T - 0.001792T^2\right] \tag{4.18}$$

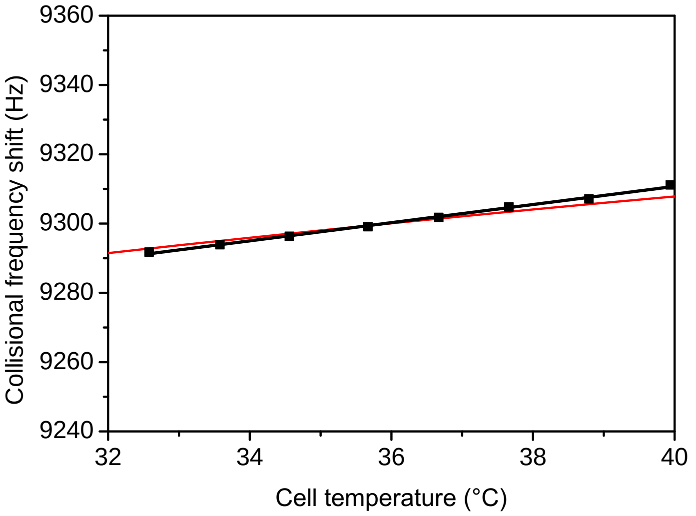

Figure 4.12: Experimental (black squares) and theoretical (red line) collisional frequency shift. The black line is a local linear fit of experimental data, with slope 2.6 Hz/K. Magnetic field = 24 mG.

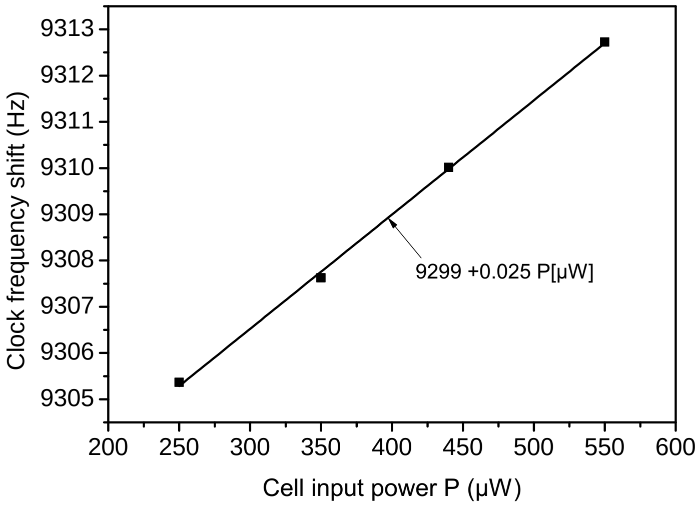

Figure 4.13: Black squares: light shift measurement for a cell temperature of 35.67 °C Magnetic field = 24 mG. Black line: linear fit of experimental data.

where T in °C. At a given cell temperature, the measured clock frequency ν_0 is given by:

$$\nu_0 = \nu_{00} + \Delta\nu_Z + \Delta\nu_{bg} + \Delta\nu_{ls} \tag{4.19}$$

where ν_{00} is the Cs reference frequency (9 192 631 770 Hz) , $\Delta\nu_Z$ is the Zeeman frequency shift and $\Delta\nu_{ls}$ is the light shift.

In Fig. 4.12 is plotted the measured collisional frequency shift $\Delta\nu_{bg}$ of the clock transition versus the cell temperature. The magnetic field is 24.4 mG during the whole experiment. To extract the value of $\Delta\nu_{bg}$, the used protocol is as following. At a given cell temperature, the local oscillator is locked on the clock resonance. The clock frequency is measured for several cell laser input powers. In order to isolate the value of the temperature-dependent collisional frequency shift, the Zeeman contribution ($\Delta\nu_Z = 391B^2 = 0.23$ Hz) is substracted from data, as well as the Cs natural hyperfine frequency (9 192 631 770 Hz). Resulting data for a given cell temperature is fitted by a linear function (see an example in Fig. 4.13). The slope of the fitting function gives the light-shift coefficient (2.7 10^{-12} μW^{-1}

at 35.67 °C) and the intercept (frequency shift at null intensity) gives the collisional shift $\Delta\nu_{bg}$ of the clock resonance (9299 Hz at 35.67 °C). The experiment was repeated for several cell temperature values, ranging from 32 °C to 39 °C. The result is given by the black-squared data in Fig. 4.12. These data are fitted by a linear function giving the local dependence of the collisional shift with temperature. The value extracted from the fit is $2.8\ 10^{-10}\,\mathrm{K}^{-1}$. Experimental data in this range remain in correct agreement with the expected dependence, calculated from Eq. (4.18) and shown as a solid line in Fig. 4.12.

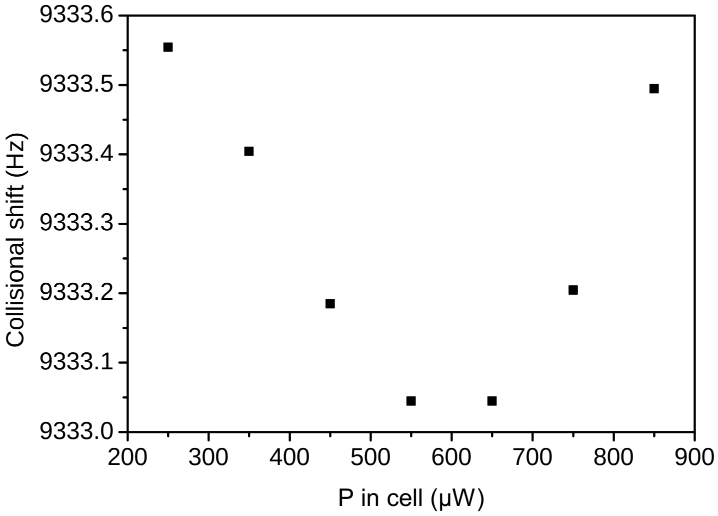

Figure 4.14: Light shift measurement for a cell temperature of 45.03 °C. Magnetic field = 24 mG

We tried to repeat the experiment at higher temperature values. We note that, at high intensities, the data were well-fitted by a linear function. However, at low laser powers, we observed a strong non-linearity in the light shift coefficient, resulting even in a sign reversal at high temperatures. For example, Fig. 4.14 shows the clock frequency shift versus the light intensity at the cell input for a temperature of 45.03 °C. A turnover is clearly seen around P = 600 µW, corresponding to a cancellation of the light-shift slope at first order. However, the CPT signal is very low at these high temperatures (see Fig. 4.7b). It appears not to be interesting to work at these temperatures because the short-term stability of the clock is dramatically degraded. We have not investigated these effects in further details yet, but this study would be interesting to be pursued in the future. Note that similar reversals have been observed in previous studies. The reader can refer to [114, 203].

4.3.2.2 Contribution to the clock frequency stability

The cell temperature fluctuations have been monitored as described in subsection 3.8.3. Temperature fluctuations are converted to clock frequency fluctuations using the coefficient found above ($2.8\ 10^{-10}$ Hz/K). Figure 4.15 shows the contribution of the cell temperature fluctuations to the clock frequency Allan deviation. The latter is measured at the level of $7\ 10^{-15}$, $4.3\ 10^{-15}$ and $1.5\ 10^{-14}$ at 1 s, 100 s and 10 000 s averaging times, respectively. We conclude that the cell temperature fluctuations could be a limiting factor for the clock stability, at averaging times higher than a few hundreds of seconds. According to Fig. 2.6, we note that the use of a N_2-Ar buffer gas mixture with a pressure ratio $r(Ar/N_2) = 0.57$ would allow to cancel the temperature dependence of the Cs clock frequency around the present operating temperature of about 35 °C [139] and to reduce further the cell temperature dependence of the clock frequency.

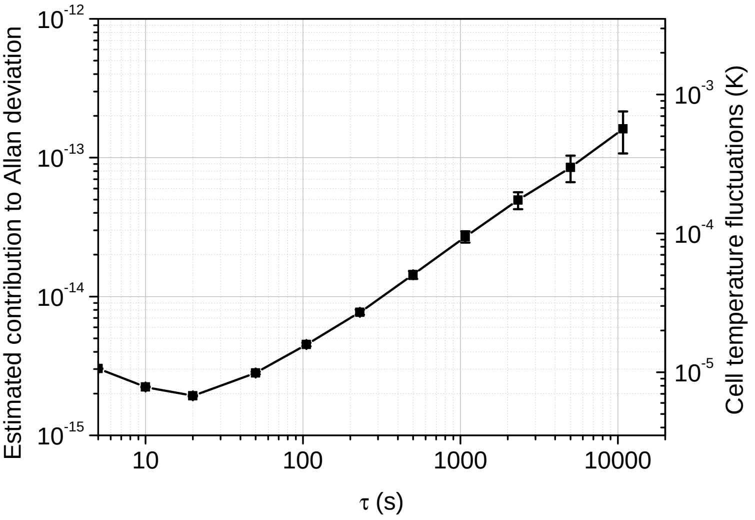

Figure 4.15: Estimated contribution of the cell temperature fluctuations on the clock stability. Cell temperature = 35 °C. Magnetic field = 24 mG.

4.3.2.3 Shape of the cell

In Ref. [83], a simple model of the ideal gas law suggests that temperature gradients between the cell stem and the cell active volume result in buffer gas density redistribution between both cell parts and can lead to a dramatic enhanced temperature sensitivity (ETS) of the clock frequency. This geometrical effect is increased with an increased ratio $v = V_s/V_c$ between the stem volume and the cell active volume. It is also enhanced for higher temperature gradients between the stem temperature T_s and the cell temperature T_c. In Refs [26, 83], the stem of the cell is outside of a microwave cavity and the ratio v is about 0.03 or even higher. Up to date, we did not investigate experimentally this effect in our experiment. However, we note that in our apparatus, the cell active volume is 5 cm long and 2 cm diameter while the cell stem is 3.5 cm long and has an internal diameter of 1 mm. This yields a ratio $v = 0.0017$, a factor 18 lower than in the configuration reported in [26] where a factor of 10 has been measured between the clock frequency sensitivity to the cell stem temperature and the cell volume temperature. Additionally, in our experiment, the entire volume of the cell, including the stem, is inserted in a cylindrical copper cavity surrounded by a coaxial heating wire for thermal control. In permanent thermal regime, we can then think that temperature gradients between the cell volume and the stem volume are extremely small, limiting gas exchanges between both volumes. In [83], it is suggested theoretically that the ETS effect becomes negligible when the physics package is designed in such a way that T_s and T_c are correlated. Accordingly, we expect that this ETS effect should be greatly minimized in our experimental configuration and should not limit our performances presently.

4.3.3 Light-shift effects

4.3.3.1 Laser power-induced frequency shift

In Fig. 4.13 is shown a typical light shift measurement for a cell temperature of 35.67 °C. Experimental data are fitted by a linear function with a slope of 25 mHz/µW, yielding a sensitivity of the clock frequency of 2.8 10^{-12} μW^{-1}.

We recorded the voltage level at the output of a photodiode placed at the cell entrance. In Fig. 4.16, we show the fractional fluctuations of the laser power crossing the vapor cell while the LPSS is on and the estimated contribution to the clock frequency stability when applying the power-induced light-shift coefficient. The graph is plotted for a total input power of 475 µW. This contribution is estimated at 5.1 10^{-14} at 1000 s averaging time. To achieve a clock frequency stability of 5 10^{-15}, we should reduce the laser power fluctuations by a factor of 10, yielding a fractional laser power stability

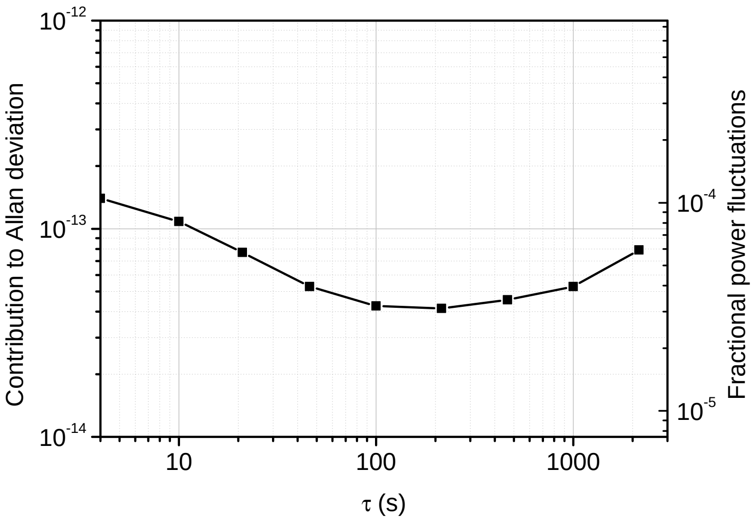

Figure 4.16: Contribution of the laser intensity fluctuations to the clock frequency stability. Given for a total power crossing the cell of 475 µW.

of 3 10^{-6}. Reaching this level of stability seems to be a complicated task, although several paths could be envisaged, involving the sensitivity to temperature of the beam splitter (used for LPSS) reflectivity, or even the choice of the reference voltage source. Note that light-shift effects already contribute to the clock frequency stability at a level above 10^{-13}, before 10 s averaging time. They are clearly a limiting factor even for the clock short-term frequency stability. Indeed, we can see a strong similarity between Fig. 4.16 and Fig. 4.5 showing the clock frequency Allan deviation. In that sense, we have performed a study in the CW regime to try to find a way for reducing the clock frequency sensitivity to the light power. Corresponding results are reported in detail in subsection 4.3.8.

4.3.4 Laser frequency-induced frequency shift

We have measured the clock frequency sensitivity to the laser frequency variations. For this purpose, we first calibrated the sensitivity of the laser frequency to the applied voltage on the laser controller modulation input. A DDS (Agilent 33220A) is used as a DC voltage generator. We observe on an oscilloscope the transmitted signal out of the cell from the laser frequency stabilization set-up cell (see Fig. 3.1). The laser frequency is first roughly adjusted around the dual-frequency resonance involving excited state $F = 4'$ (dip on the right in blue curve of Fig. 3.19). Then a DC voltage is applied on the modulation input such that the laser is exactly at resonance. The corresponding value of the voltage $V_{4'}$ is recorded. We then set it such that the laser frequencies are exactly resonant with the $F = 3'$ transitions (dip on the left in blue curve of Fig. 3.19). We call $V_{3'}$ the corresponding DC voltage value. The voltage difference $\Delta V = V_{3'} - V_{4'}$ is 1.01 V. Assuming the laser frequency is a linear function of the applied voltage, we estimate the sensitivity of the laser at 1.156 GHz/V.

In a second step, we measured the clock central frequency as a function of the applied voltage value, when the CPT bands frequencies are initially tuned around the $F = 4'$ resonances. The result is given in Fig. 4.17, after conversion of the x-axis quantity into laser frequency. In the laser detuning range studied, experimental data are well fitted by a linear function with a coefficient of −39 mHz/MHz, yielding a coefficient of −4.2 10^{-12} MHz^{-1} in terms of clock fractional frequency.

We measured the typical laser frequency fluctuations in clock operation by beating the laser signal with the one from another DFB laser frequency-stabilized by saturated absorption. In Fig. 4.18 is plotted the laser beatnote frequency fluctuations versus averaging time, and the corresponding contribution to the clock frequency Allan deviation using the coefficient found above. At 1 s and 1000 s, the laser beatnote frequency fluctuations are 900 Hz and 1.9 kHz respectively. Assuming that both lasers contribute equally to these fluctuations, this yields a limitation to the clock fractional frequency stability at the level of 2.7 10^{-15} at $\tau = 1$ s and 5.5 10^{-15} at $\tau = 1000$ s.

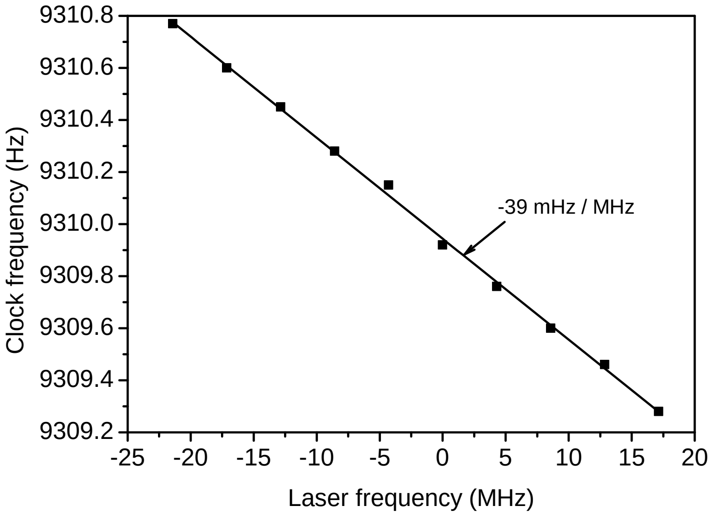

Figure 4.17: Clock frequency variations with laser frequency. Black squares are experimental data. The black solid line is a linear fit. input laser power = 450 µW. Cell temperature = 35 °C. Magnetic field = 89 mG.

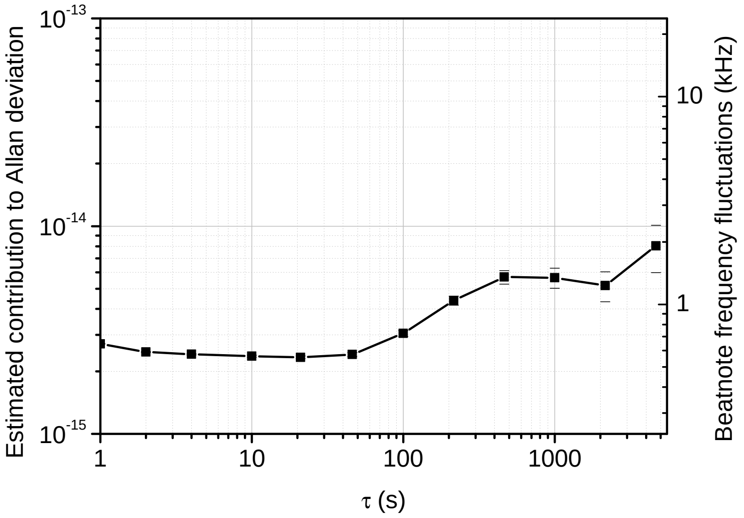

Figure 4.18: Estimated contribution of laser frequency fluctuations on the clock stability.

4.3.5 PPOP delay fluctuations

It was of critical importance to determine the impact of the length difference between the paths of the two arms of the Michelson interferometer-like system. One arm of the Michelson system is fixed. In the second arm, the mirror is placed on a linear translation stage to evaluate the sensitivity of the clock frequency to variations of the optical path difference between the two arms of the set-up. Figure 4.19 shows the evolution of the clock frequency versus the mobile mirror position x. Experimental data are locally well fitted by a second-order polynomial function, such that $\nu_c - \nu_0[\text{Hz}] = 9109 + 12.2x - 0.35x^2$. The clock frequency sensitivity to the mirror translation is canceled at first order for $x_i = 24.3\,\text{mm}$ ($\approx \frac{3}{4}\lambda_{Cs}$), where the CPT signal is maximized. For a mirror with average position $x \sim x_i$ and experiencing position fluctuations Δx, the contribution of the position fluctuations of the mirror to the clock short-term stability is $\sigma_{y,mirror} = \frac{1}{\nu_0} 0.70\,(x - x_i)\,\Delta x$, where x is expressed in mm. We estimate the error on the mean position of the mirror to be less than 200 µm, and we put upper

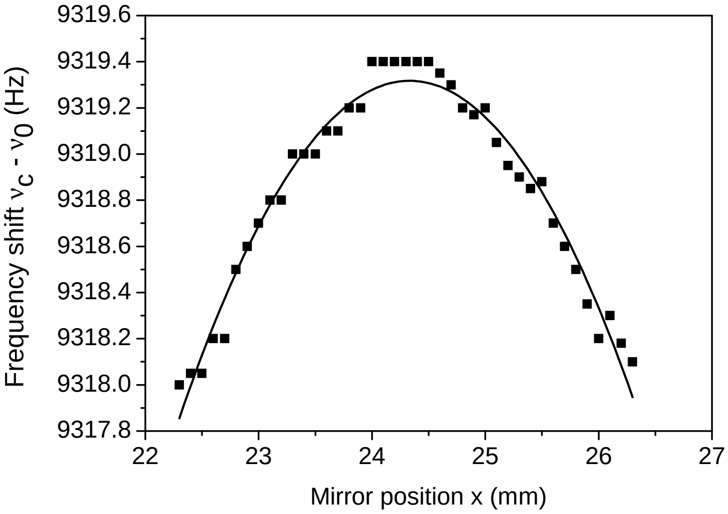

Figure 4.19: Clock frequency versus the mobile mirror position. The x axis indicates the length difference difference between both arms of the Michelson system. Squares: experimental data. Solid line: scond-order polynomial fit. Input laser power = 475 µW. Cell temperature = 35 °C.

bounds on a single mirror position typical fluctuations. We assume the latter to be mainly due to thermal expansion of the 1 cm-depth glass cylinder supporting the mirror. Considering a coefficient of thermal expansion for glass of 9 10^{-6} K^{-1}, and considering the ambient air temperature fluctuates no more than 100 mK (see Fig. 3.14b), we estimate the maximal mirror position fluctuations to be of the order of 10 nm. Thus, we expect the contribution of this effect to the clock fractional frequency stability to be lower than 1.5 10^{-16}.

4.3.6 Contribution from the EOM

A similar study has been performed to isolate the contributions from the EOM to the clock frequency stability. Figures 4.20a and 4.20b plots the CPT resonance frequency versus the EOM temperature and of EOM bias voltage setpoint, respectively.

The clock frequency - EOM temperature dependence is well fitted by a second-order polynomial function such that $\nu_c - \nu_0$ [Hz] $= 9328 + 4.1\ T_{EOM} - 0.05\ T_{EOM}^2$. The clock frequency sensitivity to EOM temperature variations is canceled at first order around $T_i = 41$ °C, close to the point where the EOM transmission is maximized (see Fig. 3.13). The curvature C around T_i of the clock frequency-EOM temperature characteristic defined as $C = \left|\frac{1}{\nu_c}\frac{\partial^2\nu_c}{\partial T_{EOM}^2}\right| = \frac{2\ 0.05}{\nu_c}$ is 1.1 10^{-11} K^{-2}. Typical EOM temperature fluctuations around the setpoint were measured to be 70 µK for $\tau = 1000$ s (see Fig. 3.14b). Assuming that the temperature control system allows to set the EOM temperature at $T_i \pm 1$ K, the contribution to the clock frequency stability would be 7.7 10^{-16} at $\tau = 1000$ s.

The clock frequency dependence to the EOM bias voltage is well fitted by a sine function with equation $\nu_c - \nu_0$ [Hz] $= 9359.4 + 45.5 \sin\left(\pi\frac{Vbias+1.75}{2.74}\right)$. The curvature C around the inversion bias voltage value V_i (which is also the carrier suppression point) of this function, defined as $C = \left|\frac{1}{\nu_c}\frac{\partial^2\nu_c}{\partial V_{bias}^2}\right| = 45.5\left(\frac{\pi}{2.74}\right)^2$ is 6.5 10^{-9} V^{-2}. If we consider the servo stabilizes the EOM bias voltage around V_i with a static error less than 1 mV and that the typical fluctuations are of the order of 100 µV, then the contribution to the clock frequency stability would be 6.5 10^{-16} at $\tau = 1000$ s.

We can definitely conclude that the total contribution of the MZ-EOM to the long-term frequency stability of the CPT clock is negligible in these conditions.

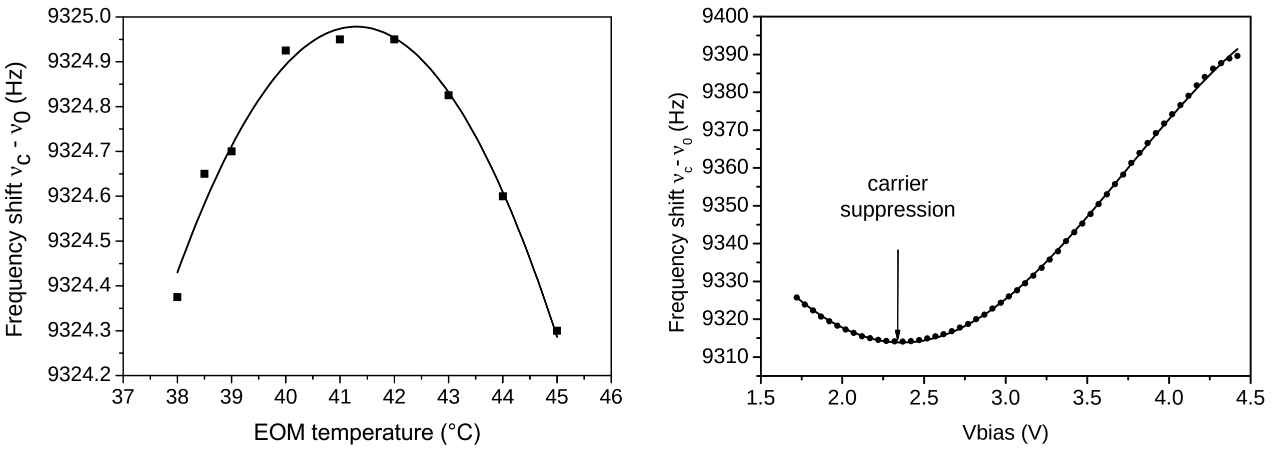

(a) (b)

Figure 4.20: Clock frequency versus (a) the EOM temperature and (b) the EOM bias voltage. Squares and dots are experimental data. Data are fitted (black lines) by a second-order polynomial function in (a) and by a sine function in (b). Cell temperature = 35 °C. Magnetic field = 89 mG.

4.3.7 Summary

Table 4.2 summarizes the contributions from the main experimental parameters to the clock mid-term frequency stability. The clock frequency stability at 1000 s is expected to be 5.7 10^{-14}, in excellent agreement with the value measured in Fig. 4.5 (4.6 10^{-14}). The main limitations are identified to be the power fluctuations (intensity light shift), followed by the cell temperature fluctuations (collisional shift).

Table 4.2: Main contributions to the clock mid-term frequency stability at τ = 1000 s.

Parameter	Value	Fluctuations @1000 s	Clock sensitivity	Contribution @1000 s
Magnetic field	50 mG	0.32 µG	4.6 10^{-9} G^{-1}	1.5 10^{-15}
Cell temperature	35 °C	80 µK	2.8 10^{-10} K^{-1}	2.5 10^{-14}
Laser power	475 µW	19 nW	2.8 10^{-12} μW^{-1}	5.1 10^{-14}
Laser frequency	-	1.4 kHz	-4.2 10^{-12} MHz^{-1}	5.8 10^{-15}
$\Delta L_{Michelson}$	$<$ 0.2 mm	$<$ 10 nm	1.5 10^{-11} mm^{-1}	$<$ 1.5 10^{-16}
EOM temperature *	40.2 °C	70 µK	$<$ 1.1 10^{-11} K^{-1}	$<$ 7.7 10^{-16}
EOM bias *	- ±1 mV	0.1 mV	$<$ 6.5 10^{-15} V^{-1}	$<$ 6.5 10^{-16}
Total	-	-	-	5.7 10^{-14}

* Given only for information. Not included in the computation of the total estimation of the frequency stability.

In order to push the stability limits in the mid term imposed by these effects, we investigated several solutions, the results of which are exposed in the following. We tried to reduce the sensitivity of the clock frequency to laser intensity fluctuations (subsection 4.3.8). In the opposite direction, we also tried to increase the laser power stability limited by the beam-splitter sensitivity to temperature by implementing a second stage of laser power stabilization with narrow bandwidth (subsection 4.3.9). Finally, we investigated the possibility to reduce the collisional shift by replacing the cell with one filled with a buffer gas ratio expected to present an inversion temperature at the cell operating temperature (seen in chapter 5).

4.3.8 Impact of experimental parameters on the light shift coefficient

Since we pointed out that laser power fluctuations through the light-shift effect were the main limitation to the clock mid-term frequency stability, we have decided to investigate the impact of several experimental parameters onto the light-shift slope in CW-regime. For each parameter, the clock frequency is measured for several values of laser power. Experimental data are fitted by a linear function and a power light-shift coefficient (in μW^{-1}), expressed in fraction of the clock frequency, is extracted.

Microwave power Various articles in the literature [203–206] report the possibility to cancel the power light shift slope by adjusting the power of the microwave signal driving the optical system. In these articles, optical sidebands generation is performed by directly modulating a diode laser through its injection current or by using an external phase electro-optic modulator. In our Mach-Zehnder intensity EOM-based system, as reported in Fig. 4.21 for a cell temperature of 35 °C, no significant variation of the light shift slope was found by tuning the 4.596 GHz signal power driving the EOM. This coul be possibly explained by the fact that, in our MZ EOM-based system, the optical carrier and even-order harmonics are actively rejected and changing the microwave power does not change significantly the amplitude symmetry between both first-order optical lines that participate to the CPT interaction.

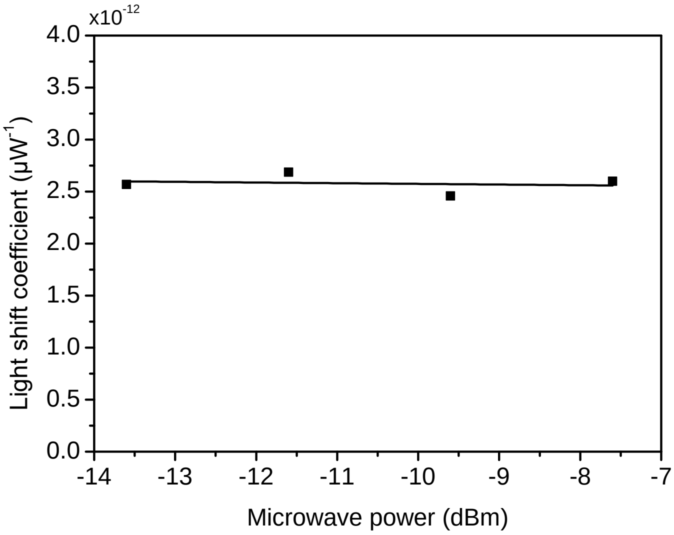

Figure 4.21: Effect of the microwave modulation index on the light shift coefficient. Cell temperature = 35 °C. Magnetic field = 24 mG.

Cell temperature From the results of subsection 4.3.2.1, we measured the evolution of the light shift coefficient versus the cell temperature. Results are reported in Fig. 4.22.

In this experiment, the light shift slope was found to decrease from about 3.2 $10^{-12}\,\mu W^{-1}$ to about 1.6 $10^{-12}\,\mu W^{-1}$ in the 32-40 °C range. The impact of the cell temperature on intensity-light shift has already been reported in [114, 203], with even a possible change in the sign of the light shift slope at a given temperature. The evolution of intensity light shift with temperature can be explained by different mechanisms. First, increasing the cell temperature induces a broadening of optical lines (increase of the Doppler width), increasing the mixing between excited states. This mixing can induce a temperature-dependent asymetry of the CPT resonance, explaining that laser intensity light shift can change with temperature. Second, the shift of optical lines is known to depend on the cell temperature [139], yielding a change of the optical detuning with the cell temperature and potentially a change of the intensity light shift. Third, the absorption of the vapor is increased with temperature. This yields to a reduction of the "effective" light seen by atoms, possibly explaining a reduction of the intensity light shift. Simultaneously, the increase of the cell absorption causes enhanced intensity gradients

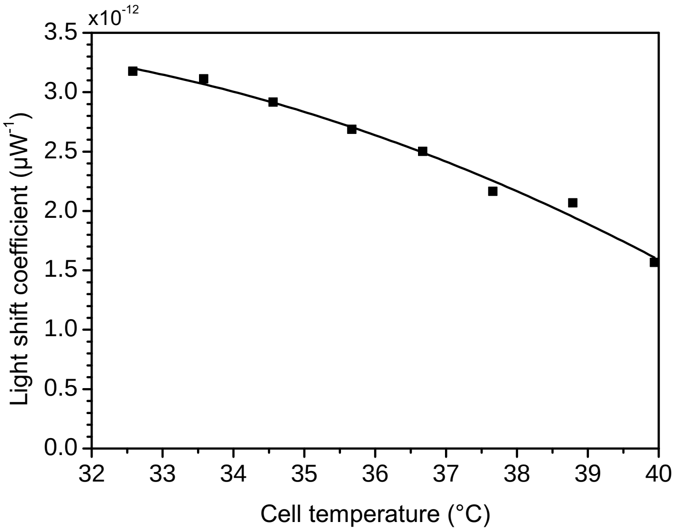

Figure 4.22: Light shift coefficient as a function of the CPT cell temperature. Black squares: data. Black line: quadratic fit. Magnetic field = 24 mG

along the cell length. The resulting asymmetry of the CPT resonance, changing with temperature, could explain a change with temperature of the intensity light shift coefficient. A detailed study would be necessary to quantify clearly the contribution of these different mechanisms. We fitted the data of Fig. 4.22 with a second-order polynomial with expression $(-6.9 + 0.74\,T - 0.013\,T^2)10^{-12}$. This expression cancels at a temperature of 45.2 °C (see Fig. 4.14). Nevertheless, at this temperature, the CPT signal and consequently the short-term frequency stability was degraded by at least one order of magnitude. Furthermore, as seen in subsection 4.3.2.1, non-linearities in the light shift coefficient occur at these high values of the cell temperature.

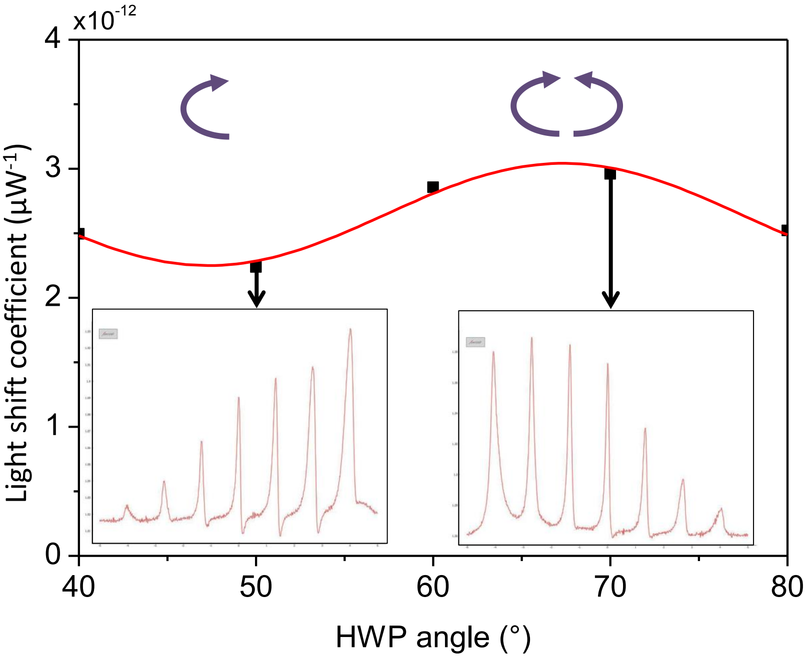

Figure 4.23: Light shift coefficient versus the PPOP scheme asymmetry. Cell temperature = 35 °C. Magnetic field = 24 mG.

Push pull polarization unbalance Figure 4.23 shows the evolution of the light-shift coefficient as a function of the power asymmetry in the arms of the Michelson set-up. The studied experimental parameter is the half-wave plate angle at the entrance of the Michelson system. For each HWP position, the clock frequency is measured at different input laser powers. The data is fitted by a line and its slope is measured. The given angle is read on the HWP mount, and no particular attention has been taken to make the mount reference axis (0°) coincide with the incoming light polarization axis. In insets are shown the Zeeman CPT spectrum at two measurement points. The optical power is balanced between the two arms when the angle is about $68° + m \times 45°$, where m is a relative integer. The incident light is linearly polarized with an angle of 45° with the HWP slow axis. PPOP is established. The power is fully redirected in a single arm when the angle is about $46° + m \times 45°$. The incident light is linearly polarized either along or orthogonal to the HWP slow axis. The interrogating light is circularly polarized. The light shift coefficient oscillates between $2.2\ 10^{-12}/\mu W$ when the asymmetry is maximum, and $3.0\ 10^{-12}/\mu W$ when both paths are well-balanced. We conclude that the power unbalance between the arms of the Michelson-like system has poor influence on the light shift coefficient.

LO frequency modulation depth If there is any asymmetry in the CPT resonance, we can expect that the LO is frequency stabilized with an offset with respect to the resonance central frequency. Eventually, this asymmetry could lead to a reduction of the light shift coefficient for a proper modulation index of the LO frequency. The light shift coefficient is measured versus the amplitude F_M of the LO frequency modulation. F_M is changed within a range from 60 Hz to 180 Hz in the experiment. The results are reported in Fig. 4.24.

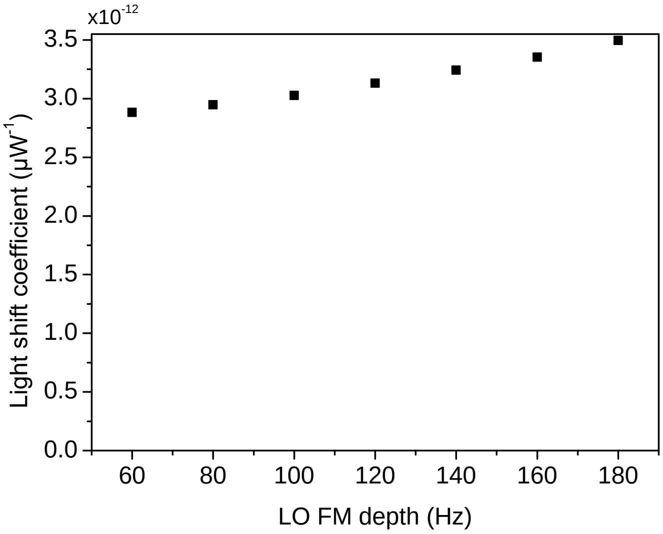

Figure 4.24: Light shift coefficient versus the local oscillator modulation depth. Cell temperature = 35 °C. Magnetic field = 24 mG.

The light shift coefficient increases linearly with the modulation depth in the studied interval. However it is far from being cancelled. The minimum is $2.8\ 10^{-12}/\mu W$ for $F_M = 60\,\text{Hz}$. Worse, at low modulation depths, the clock frequency discriminator slope is strongly degraded and the clock short-term stability is affected.

Carrier suppression Figure 4.25 shows the evolution of the light shift coefficient with the intensity repartition between the carrier and the first order bands.

The EOM DC voltage is varied. For each point we measured the light shift coefficient and the power ratio between the carrier and the +I order band. The carrier minimization point is at 8.6 V in this experiment. It also corresponds to the minimum light shift slope measured ($3.4\ 10^{-12}/\mu W$). This

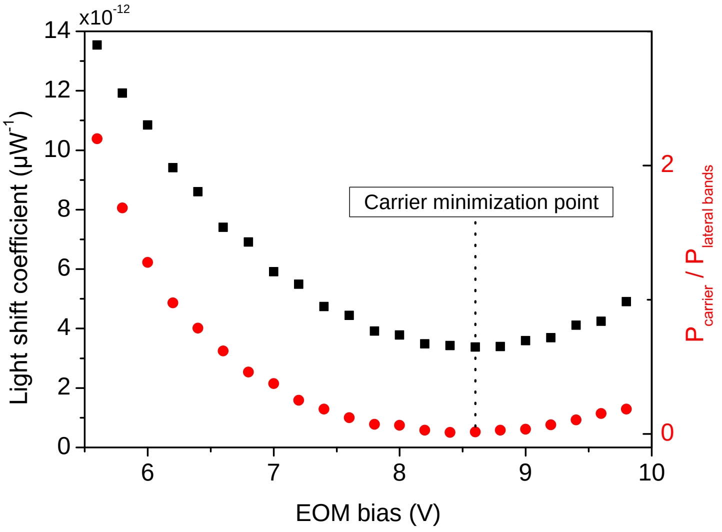

Figure 4.25: Black squares: light shift coefficient versus the EOM bias. Red squares: optical power repartition between the carrier and the first order lateral band. Cell temperature = 35 °C. Magnetic field = 24 mG.

measurement confirms the necessity to operate the EOM bias voltage as close as possible to the setpoint that minimizes the carrier intensity and "cleans" the optical spectrum for CPT interaction.

Magnetic field Figure 4.26 shows the evolution of the light shift coefficient versus the static magnetic field. Since the push-pull interaction scheme induces $\Delta m = 2$ transitions in the neighbouring of the clock transition, we wondered if the magnetic field intensity could somehow affect the light shift coefficient, as it was observed at LNE-SYRTE [207] in the pulsed CPT clock experiment. However, we measured that the latter was not changed significantly. It increases slightly from 3.2 $10^{-12}\,\mu W^{-1}$ to 3.5 $10^{-12}\,\mu W^{-1}$ for magnetic fields ranging from 0 to 800 mG.

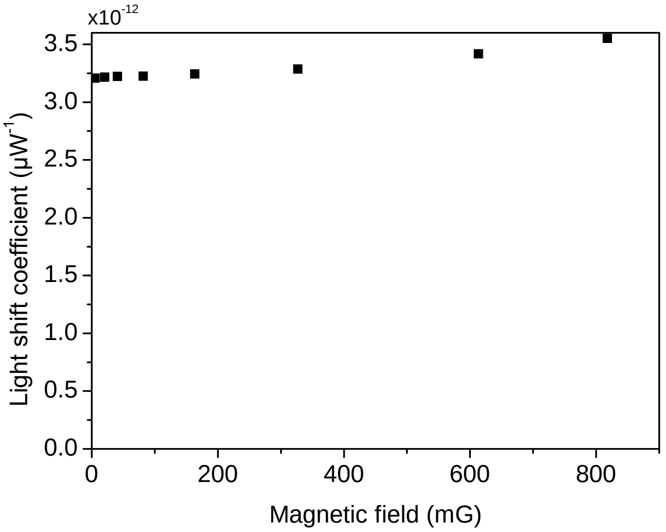

Figure 4.26: Light shift coefficient versus the static magnetic field. Cell temperature = 35 °C.

Other parameters The experiment is repeated for several experimental parameters that are likely to have an impact on the intensity light shift coefficient. Figure 4.27 is the measurement of the light shift coefficient versus the LO detuning from CPT resonance. The LO frequency is stabilized while keeping a constant offset in the servo error signal. The light shift coefficient is measured and reported in the figure for different offset values. On one side of the resonance, the minimum value of the light shift obtained is 2.7 $10^{-12}\,\mu\mathrm{W}^{-1}$, when the LO frequency is close to the CPT resonance half maximum. Of course, the frequency discriminator in this region is dramatically reduced in this region and the clock short-term stability is strongly affected. On the other side of the resonance, the light shift coefficient continuously increased with increasing offsets from resonance.

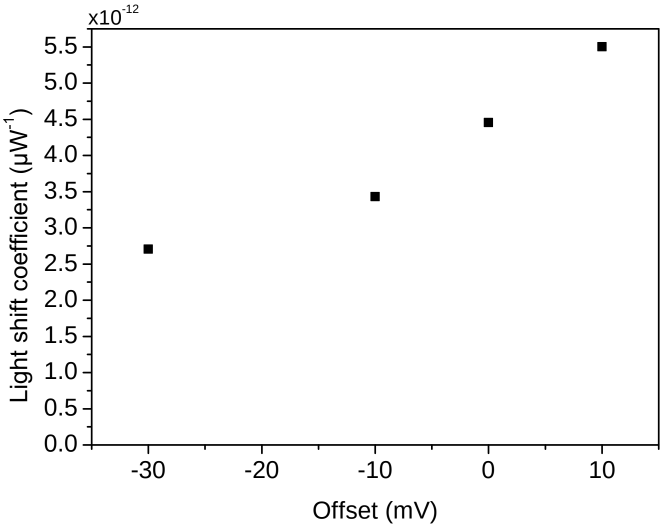

Figure 4.27: Light shift coefficient versus the local oscillator detuning. Cell temperature = 35 °C. Magnetic field = 24 mG.

Figure 4.28 shows the evolution of the light shift coefficient versus the laser carrier frequency in a range of −40 MHz to 40 MHz around optical resonance. The intensity light shift coefficient does not change significantly with laser optical detuning. The variation is only 0.1 $10^{-12}\,\mu\mathrm{W}^{-1}$ in the studied laser frequency range.

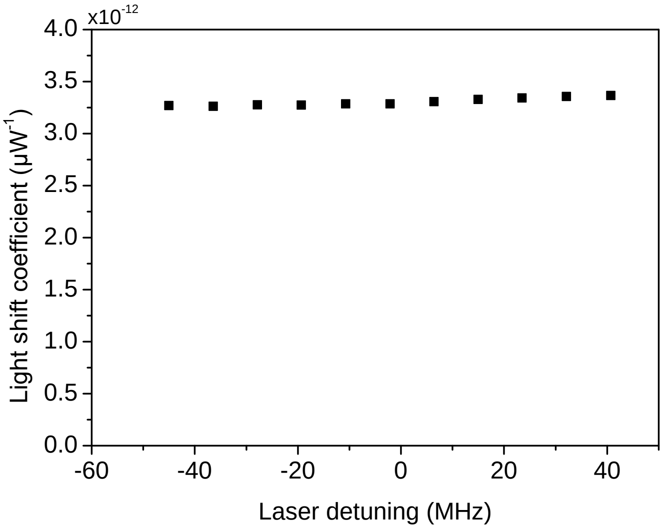

Figure 4.28: Light shift coefficient versus the laser detuning. Cell temperature = 35 °C. Magnetic field = 24 mG.

Finally, we studied the impact of the LO modulation signal pattern on the light shift coefficient. Instead of sending a square-wave modulation signal on the LO with amplitude $\frac{\Delta\nu}{2}$, the pattern is customized. The LO frequency spends 30 % of the upper-state duration in value a and 30 % of the lower-state duration in value b. Detection of the CPT transmission is performed only in the remaining 70 % of the time. The modulation signal is sketched in Fig. 4.29a. The light shift coefficient is measured for different values of the couple "$a; b$". Results are reported in Fig. 4.29b.

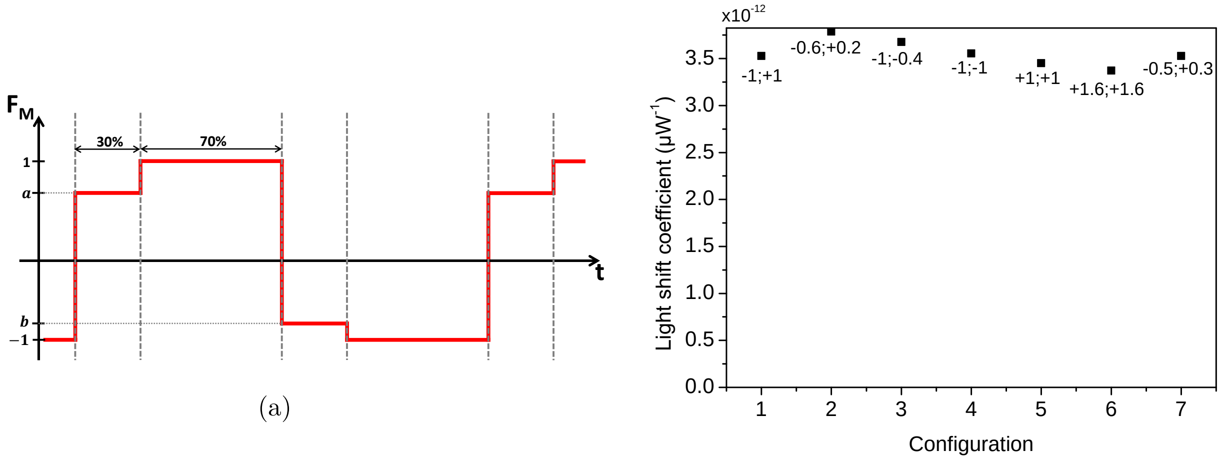

(a)

(b)

Figure 4.29: (a) Schema of the LO modulation signal pattern. F_M is normalized to $\Delta\nu/2$. (b) Light shift coefficient versus modulation pattern. Values of a and b are given for each configuration in the form "$a; b$". Cell temperature = 35 °C. Magnetic field = 24 mG.

Again, whatever the modulation pattern, the light shift coefficient is not impacted.

As a conclusion, despite the wide range of experimental parameters covered in this study, to date, we have not found any relevant way to reduce the sensitivity of the clock frequency to laser power variations in the CW regime. We believe that this light shift coefficient could be reduced or even cancelled using a phase EOM [203] instead of a Mach-Zehnder EOM, but at the expense of the clock short-term stability. Another solution to reduce laser intensity effects is to use a Ramsey-type temporal pulsed interrogation [208]. It has been demonstrated that pulsed interaction reduces strongly the intensity light shift sensitivity [24, 209], prevents the CPT line broadening and allows the detection of narrow and high-contrast Ramsey fringes if combined with optimized CPT pumping schemes [103, 113, 208, 210]. This approach is explored in chapter 5. Additionally, we think that, in the pulsed regime, extensions of hyper-Ramsey spectroscopy [211–214] or original synthetic frequency protocol [215] applied to 3-level schemes could be implemented for further suppression of this predominant effect.

4.3.9 Dual-stage LPSS

We tried to implement a second stage of laser power stabilization to the set-up. The goal is to compensate for the slow laser intensity fluctuations at the output of the beam splitter used in the LPSS shown in Fig. 3.10, due to the latter's sensitivity to temperature. We did as represented in Fig. 4.30a. The set-up origins from the LPSS of Fig.3.10. This fast servo has a 10 kHz-bandwidth. On top of it is implemented a second servo system. The observable is the laser power transmitted through the CPT cell, and measured with photodiode PD2. A correction signal is applied on the setpoint of the fast laser power stabilization stage to maintain the signal of PD2 constant. The second servo is slower. It has a time constant of a few seconds.

Figure 4.30b shows the effect of this two-level LPSS on the clock frequency stability. The latter reaches a level of 2 10^{-14} at 100 s averaging time. We gain a factor of 2 with respect to the case with only one stage of LPSS at 100 s and we reach the limitation due to collisional shift. However, we expect this method to have a limited benefit on the laser power stabilisation, since the observable (laser power at

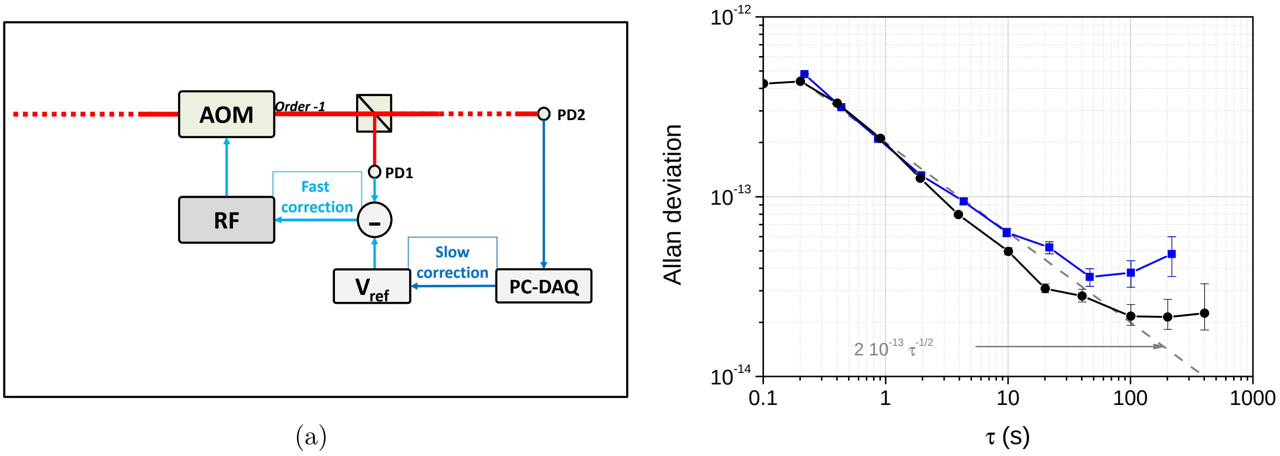

(a)

(b)

Figure 4.30: (a) Functional diagram of the two-level LPSS. (b) Effect of the second stage of laser power stabilization on the clock frequency stability. Blue squares: with one-level LPSS. Black circles: with two-level LPSS. Laser input power = 200 µW. Cell temperature = 33 °C. Magnetic field = 24 mG.

the cell output) depends on the absorption from the vapor, which also depends in particular on the cell temperature and on the laser frequency. Consequently, it is not such a good indicator of the laser intensity incoming to the CPT cell.

4.4 Conclusion

4.4.1 Chronology of the CPT clock frequency stability level

Figure 4.31 resumes the evolution of the CPT clock Allan deviation in continuous regime since the first measurements in 2014.

During my thesis, the stability level at 1 s averaging time has been improved by more than one order of magnitude. For the first measurement in 05/2014, a clock frequency stability of 4.5 10^{-12} $\tau^{-1/2}$ up to only 2 s was achieved. Since the end of 2016, it has reached 2 10^{-13} at 1 s averaging time and 2.1 10^{-14} at 100 s.

For the first clock frequency stability measurements performed in 05/2014 (pink curve), the clock performances were limited by laser feedback effects on the laser frequency and intensity, due to reflections at the fibered EOM input. We implemented an additional optical isolation stage (35 dB) to reach 70 dB isolation between the laser output and the EOM input. This allowed us to reach the stability level of the purple curve (07/2014). Next, we implemented the AOM-based laser intensity stabilization system. This allowed to reduce considerably the detection noise at the modulation frequency (−15 dB). The achieved stability at 1 s averaging time was 4.5 10^{-13}, shown in the red curve (09/2014). To this date, the laser frequency was still stabilized on the bottom of a CPT cell buffer gas-broadened absorption valley. The introduction of the dual-frequency laser frequency stabilization technique, described in subsection 3.4.2, helped us to improve further the short-term stability to 3 10^{-13} at 1 s averaging time, and above all, allowed us to observe the expected $\tau^{-1/2}$ dependence over almost two decades, signature of a white frequency noise (green curve of 03/2015). Optimization of the modulation, servo and experimental parameters (P_i = 200 µW, T_{cell} = 35 °C), allowed to demonstrate a record stability of 2 10^{-13} $\tau^{-1/2}$ up to 100 s averaging time (orange, blue and black curves).

Currently, the clock short-term frequency stability in the CW regime is 2 10^{-13} $\tau^{-1/2}$ until 100 s, limited by laser power effects. This level was achieved thanks to the implementation of a Doppler-free spectroscopy-based laser frequency stabilization set-up and of a laser power stabilization system. After τ =100 s, the clock stability reaches a flicker floor at the level of 2-3 10^{-14}. In the mid term,

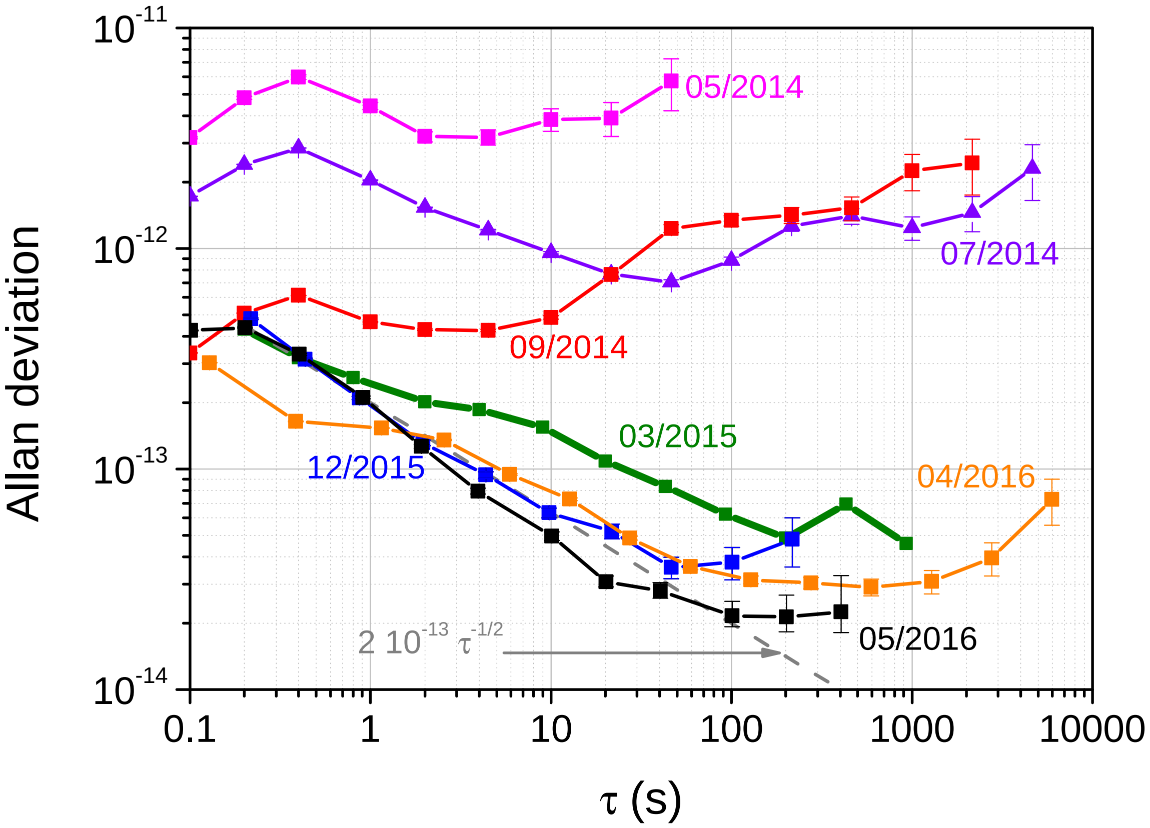

Figure 4.31: Evolution of the clock stability during the thesis.

the limiting factors are mainly intensity light shift and collisional shift effects.

The motivation for pulsing the laser field comes essentially from two major issues encountered in the continuous regime. In the latter regime, the CPT resonance contrast increases with input laser intensity at the expense of power broadening. In the pulsed regime, as long as the dark pulse duration is much larger than the pumping duration, the Ramsey-CPT fringe width depends only on the dark time between the interrogating and the probing pulses, independently of the laser intensity. Secondly, the use of light pulses reduces the interaction time between the optical fields and atoms. We thus expect the light-induced clock frequency shifts to be much less important than with a continuous interrogation of atoms.

Chapter 5

Pulsed-mode CPT clock

In this chapter, the clock setup is studied using a Ramsey-like pulsed interrogation technique. In this regime, atoms interact with a sequence of optical CPT pulses where each pulse can be used for CPT pumping and detection of the signal. This technique allows to detect high-contrast narrow Ramsey-CPT fringes whose linewidth is expected to depend only on the free-evolution time between two light pulses. Moreover, light shift effects are expected to be reduced in this regime. First, I will describe the different CPT pulse sequences used for Ramsey-CPT spectroscopy (scan of the Ramsey-CPT fringes) and for actual stabilization of the local oscillator. The impact of several experimental parameters onto the clock resonance and short-term fractional frequency stability, including the laser power, the cell temperature and the Ramsey sequence parameters, has been investigated. Short-term fractional frequency stability results at the level of 2.3 10^{-13} $\tau^{-1/2}$ are obtained in the pulsed regime (without laser power stabilisation), comparable to those obtained in the CW regime. Preliminary investigations on light-shift effects are also reported in the pulsed regime and compared to the CW regime case.

5.1 CPT pulse sequence

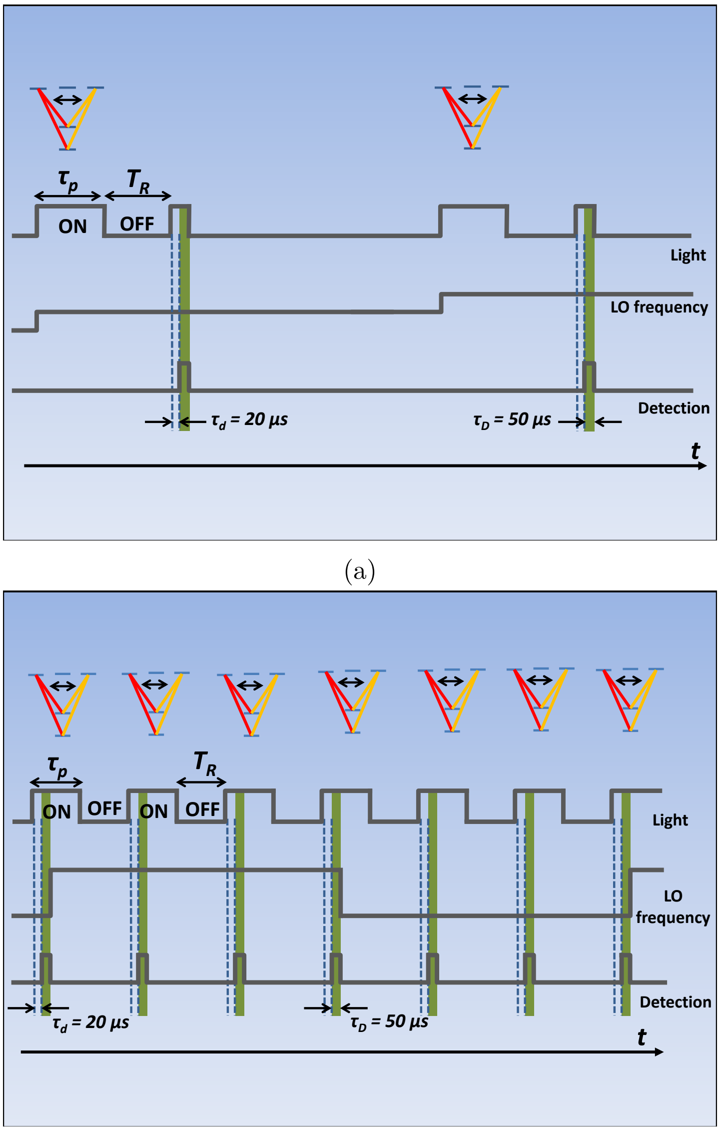

(a)

(b)

Figure 5.1: CPT pulse sequence in (a) spectroscopy mode and (b) closed loop mode.

We use a Ramsey-like laser pulse sequence [216], which consists of two interaction time intervals, separated by a dark time where atoms are isolated from light. The CPT pulse sequence slightly differs from the original Ramsey sequence. In the latter, used for example in Cs beam standards (see Figs. 1.6 and 1.7), the vapor is first prepared in one of the ground states, either by magnetic selection or by optical pumping. Then, a first microwave pulse pumps the atoms in a coherent superposition of both ground states. After the first pulse, atoms evolve freely during the Ramsey time T_R close to the ground hyhperfine relaxation time. The second pulse, when at microwave resonance, brings the atoms back to their initial ground level. The atomic population in this level is detected either with magnetic deflection or with optical detection. At microwave resonance, the detected signal is maximum.
I will now describe the CPT variant of the pulse sequence, implemented in our set-up. Two different pulse sequences were used during my thesis. The first one, shown in Fig. 5.1a, is used for spectroscopic measurements. The second one, shown in Fig. 5.1b, is used for LO frequency stabilization. In the sequence used for spectroscopy, a first pulse of length τ_p allows to pump the atoms into the CPT state. Atoms then evolve freely in the dark during a time T_R. A second pulse is used for CPT signal detection. A delay τ_d of 20 µs is taken before opening a detection window with a length τ_D. The clock

signal is averaged over the detection window with a rate of 1 Msamples/s. A significant dead-time of 35 ms ($\sim 10\ T_2$, with T_2 the hyperfine coherence relaxation time) is applied between each data point measurement to ensure that most of the atoms relaxed from the CPT state before entering in the next cycle. In the sequence used in clock closed loop operation, atoms interact with a CPT pulse sequence where each pulse is used both for CPT pumping and CPT detection. The sequence cycle duration is noted $T_c = \tau_p + T_R$. The associated cycle frequency is noted $f_c = 1/T_c$. The local oscillator (LO) frequency is changed and corrected every 3 cycles just after the detection window. The clock output signal is compared to the signal of a state-of-the-art reference active hydrogen maser with a fractional frequency stability of $8\ 10^{-14}$ and $3\ 10^{-15}$ at $\tau = 1$ s and 100 s respectively [79].

5.2 Ramsey-CPT spectroscopy

5.2.1 Ramsey-CPT fringes

In the present study, no laser power stabilization was applied in the pulsed regime. The cell is replaced by a new one with 15.3 Torr total pressure and a buffer gas ratio $r(Ar/N_2) = 0.6$ (cell C1B). For most of the results reported, the cell temperature T_{cell} is 35°C. A static magnetic field ($B = 4.5$ μT) is applied parallel to the laser beam propagation. Figure 5.2 shows typical Ramsey-CPT fringes, detected in the CPT cell for a total input laser power P_i of 850 µW and a free-evolution time T_R of 3.5 ms, with different span windows. The central fringe linewidth is about 134 Hz. The CPT contrast, defined as the ratio between the central fringe peak-peak amplitude ($A = 0.48$ V) and the dc level at half-height of the central fringe ($y_0 = 2.85$ V), is about 17 %.

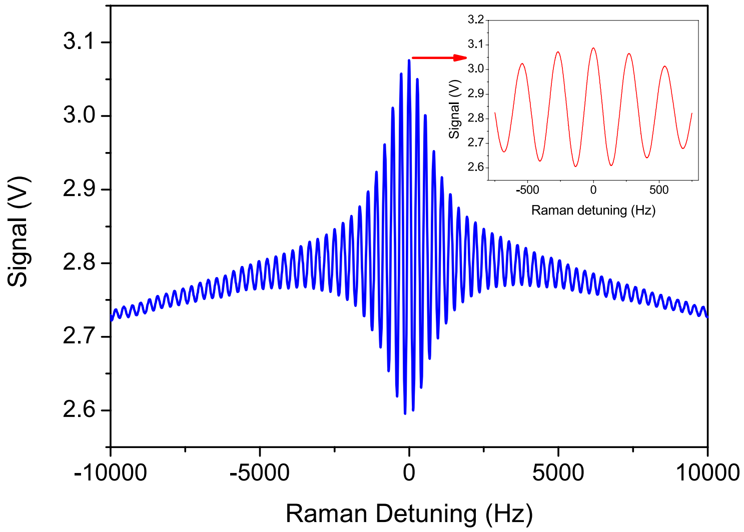

Figure 5.2: Typical Ramsey-CPT fringes. Experimental parameters are T_R = 3.5 ms, τ_D = 50 µs, τ_p = 1.1 ms, P_i = 850 µW, T_{cell} = 35 °C. The inset shows a zoom on Ramsey-CPT fringes with a total span of 1.5 kHz.

5.2.2 Central fringe linewidth

Figure 5.3 shows the linewidth of the central fringe versus the total laser power P_i incident to the cell for different values of the free-evolution time T_R. For comparison, CPT linewidth measurements obtained in the continuous regime are reported.

In the pulsed case, the central fringe linewidth is mostly measured narrower than the expected Ramsey linewidth given by $1/(2T_R)$, especially for low values of T_R and at low laser power, and tends to $1/(2T_R)$ at high power. In the power range studied here, for T_R = 1 ms, a non-negligible power

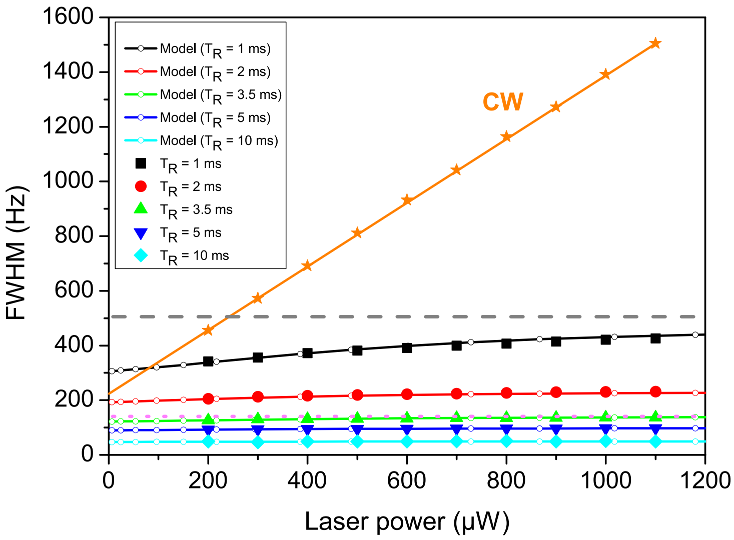

Figure 5.3: Central fringe linewidth versus the laser power P_i incident in the cell for several values of T_R (1 ,2, 3.5, 5 and 10 ms). Experimental parameters are: T_{cell} = 35 °C, τ_D = 50 µs, τ_p = 1.1 ms. Experimental data are compared with a numerical model based on optical Bloch equations. For information, the grey dashed and the pink dotted lilnes show the expected $1/(2T_R)$ linewidth for $T_R = 1$ or 3.5 ms, respectively. Results obtained in the pulsed regime are compared to the CPT linewidth measured in the same cell in the continuous regime. Experimental data in the continuous case are fitted by a linear function. Symbols: experimental data. Solid lines: fit by E. de Clercq (LNE-SYRTE).

broadening of the CPT Ramsey fringe is observed, yielding 341 Hz at 200 µW and about 426 Hz at 1100 µW, i.e. an increase of 20 % of the fringe linewidth. This effect is less visible for higher values of T_R. This behaviour is not so surprising. In a two-level atom [40], the $1/(2T_R)$ linewidth of the central Ramsey fringe is known to be a valid approximation only if $T_R \gg \tau_p$, where τ_p is the length of each pulse. Otherwise, the width is narrower than $1/(2T_R)$, it depends on the pulses durations and on the Rabi frequency. In a three-level system, like in CPT, the same behaviour is expected. In this configuration, the resonance signal can be considered as the product of a broad Lorentzian resonance, whose width is driven by the first pulse length and the Rabi frequency, multiplied by a fast oscillating function of width $1/(2T_R)$. In the case where the $1/(2T_R)$ width can not be assumed to be small compared to the broad resonance linewidth, the observed linewidth of the central fringe is a complicated function of all the parameters [127] but the effect of the broad resonance is to reduce the apparent fringe width. Since the broad resonance widens with the laser power, its effect on the fast oscillation is reduced with increased power and the observed fringe width then increases towards the $1/(2T_R)$ limit. Since we do not know exact analytical expression to describe this behaviour in the CPT case, a numerical simulation based on optical Bloch equations has been performed by E. de Clercq (LNE-SYRTE), applied to a three-level atom in presence of two resonant light fields. Parameters of the simulation are the Rabi frequencies ω_R of both optical transitions (assumed equal if use of equal laser intensities on the Cs D_1 line, $\omega_R = 2.3\ 10^6\sqrt{P_i/S_c}$ in rad/s with P_i the total laser power and S_c the laser beam section area), the experimental Ramsey-CPT sequence parameters τ_p, T_R, τ_D, the spontaneous relaxation rate Γ (such that $\Gamma/(2\pi)$ = 4.6 MHz corresponding to the excited state natural linewidth), the relaxation rate of the excited state $\Gamma^\star$ taking into account the buffer-gas induced optical broadening [88] (such that $\Gamma^\star/2\pi$ = 333 MHz), the relaxation of optical coherences ($\gamma_o = \Gamma^\star/2$), and the relaxation rate of hyperfine coherence and ground-state populations ($\gamma_{12} = 1/T_2$, with $T_2 \sim 3$ ms). Calculation results of this very simplified model, reported in Fig. 5.3 for several values of T_R, are in correct agreement with experimental data. Despite the power broadening in the pulsed regime (especially for low values of T_R), we note that the resonance linewidth and the power broadening are significantly reduced in the pulsed regime compared to the continuous interrogation case. In the latter regime, as shown on Fig. 5.3, experimental data of the linewidth $\Delta\nu$ are well-fitted by a linear function such as $\Delta\nu$ [Hz] $= 225 + 1.16\ P_i$ with P_i in µW.

5.2.3 Contrast

Figure 5.4 shows the contrast of the Ramsey-CPT central fringe versus the laser power for several values of T_R.

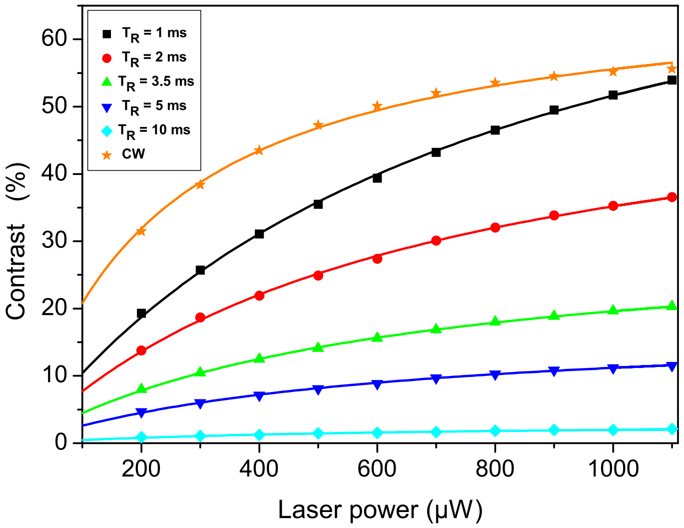

Figure 5.4: Central fringe contrast versus the laser power incident to the cell for several values of T_R. Results in the continuous regime are reported. Symbols: experimental data. Solid lines: fit.

The CPT contrast obtained in the continuous regime is also given for comparison. In the CW regime, the contrast is increased from 31 to about 53 % in the studied laser power range. A saturation plateau seems to be reached for laser powers higher than 900 µW. In the pulsed case, the fringe contrast is reduced with increased values of T_R because of relaxation of the hyperfine coherence. For $T_R =$ 3.5 ms, the fringe contrast is increased from 8 to 17 % in the 200-1100 µW range. We can assume that the fringe amplitude scales as the resonance amplitude obtained in the CW interrogation case. From [126], we deduce that the resonance amplitude A, for a three-level atom at steady state, is such that:

$$A \simeq \frac{\omega_R^4/\Gamma^{*2}}{\gamma 12 + \omega_R^2/\Gamma^*}, \tag{5.1}$$

ω_R^2 is proportional to the laser power. As the background level scales as the laser power P_i, we can fit the experimental contrast data by $C = aP_i/(225 + bP_i)$, where a and b are the free parameters and 225 is the relaxation term given by the fit of the CW linewidth versus the laser power. The agreement with the experimental data is satisfactory. From results obtained in Figs 5.3 and 5.4, we note that the fringe contrast/FWHM ratio is increased with laser power by a factor 2.5 from 200 to 1100 µW for $T_R = 3.5$ ms.

5.2.4 Cell temperature

Figure 5.5 reports the central fringe contrast, linewidth and contrast/linewidth ratio versus the cell temperature. The laser power is 863 µW while $T_R = 2.7$ ms and $\tau_p = 1.1$ ms. The fringe contrast is found to be maximized for a temperature of about 38 °C. The fringe linewidth is slightly decreased with increased cell temperature. The ratio contrast/linewidth is optimized for a temperature of about

38 °C. Nevertheless, we note that the variation of this ratio is quite modest (less than a factor 2) in the studied temperature range. We report in Fig. 5.6 the clock Allan deviation at 1 s averaging time for different laser power values at several cell temperatures. In the temperature range studied here, the short-term frequency stability is optimized in the pulsed case for laser powers higher than about 700-800 µW and reaches after a plateau where no further improvement is achieved. Similar optimal stabilities of about 2-3 10^{-13} at 1 s averaging are demonstrated in the 33-42 °C temperature range.

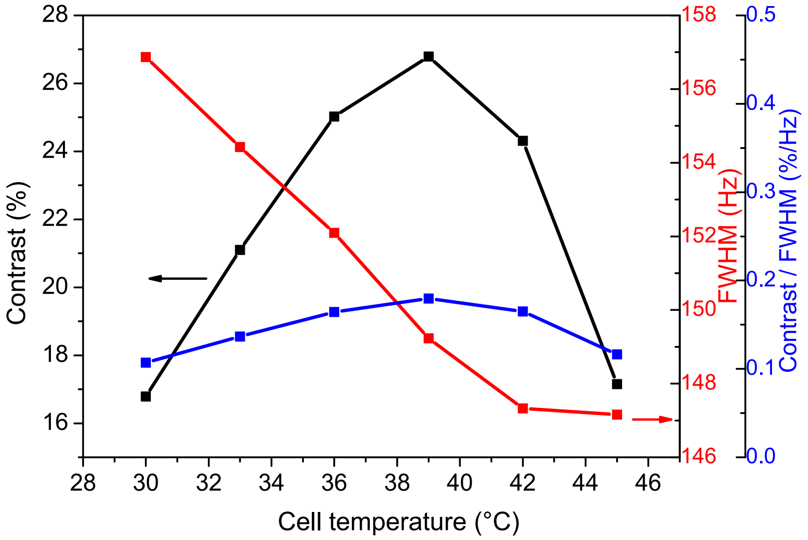

Figure 5.5: Central fringe contrast, linewidth and contrast/linewidth ratio versus the cell temperature. Experimental parameters are $P_i = 863\,\mu\text{W}$, $T_R = 2.7\,\text{ms}$, $\tau_D = 50\,\mu\text{s}$, $\tau_p = 1.1\,\text{ms}$.

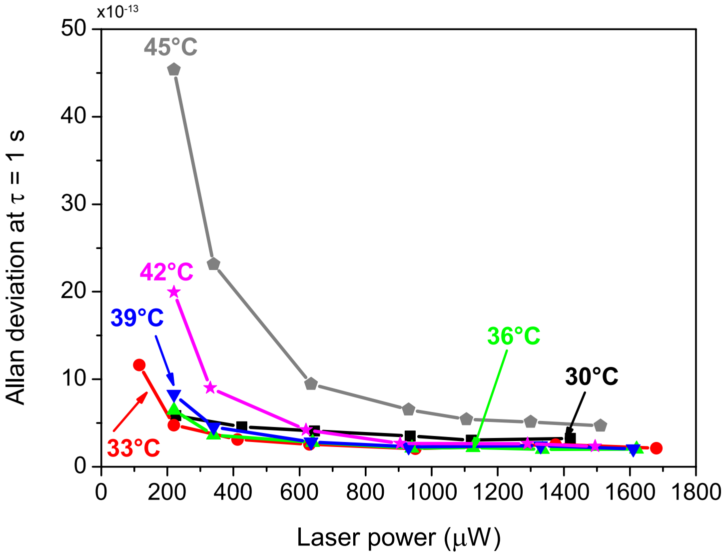

Figure 5.6: Clock Allan deviation at 1 s averaging time versus the laser power for several cell temperature values. Experimental parameters are $T_R = 2.7\,\text{ms}$, $\tau_D = 50\,\mu\text{s}$, $\tau_p = 1.1\,\text{ms}$. For each temperature, the microwave frequency modulation depth and loop gain were optimized.

5.2.5 Optimization of the pulse sequence

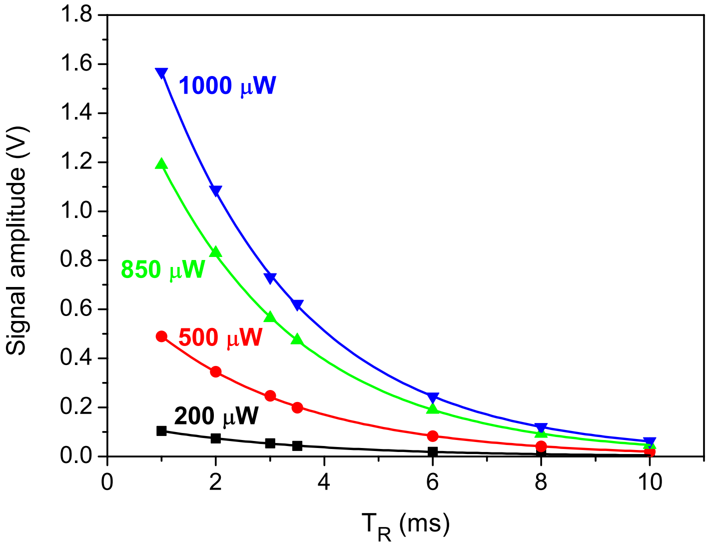

Figure 5.7: Fringe amplitude versus the free-evolution time T_R for several values of the laser power (200, 500, 850, 1000 µW). Experimental data are fitted by an exponential decay function.

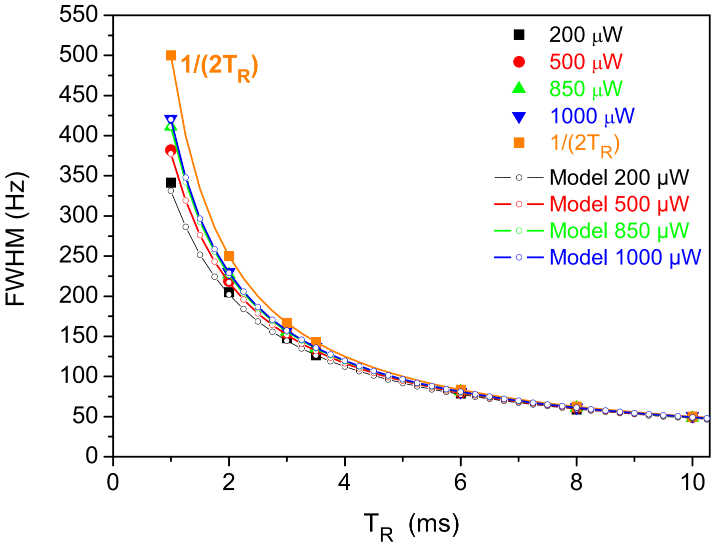

Figure 5.8: Fringe amplitude versus the free-evolution time T_R for several values of the laser power (200, 500, 850, 1000 µW). Experimental data are compared to the $1/(2T_R)$ linewidth. The data are in correct agreement with a 3-level atom model calculation [118].

Figures 5.7 and 5.8 report the central fringe amplitude and linewidth versus the free-evolution time T_R for several values of the laser power. The pumping time is 1.1 ms and the detection window is 50 µs. On Fig. 5.7, experimental data of the fringe amplitude are well-fitted by an exponential decay function, with a time constant of about 2.8 ms. The latter can be interpreted as an estimation of the CPT coherence lifetime T_2 in the cell. On Fig. 5.8, we observe again for low values of T_R that the central fringe linewidth can be narrower than the expected linewidth given by $1/(2T_R)$ (see orange squares on Fig. 5.8). This effect is the same than the one explained previously. Our numerical simulations based on a density-matrix calculation for a three-level atom are in good agreement with experimental data. Figure 5.9 reports the clock short-term fractional frequency stability at 1 s averaging time versus the free-evolution time T_R. The clock frequency stability is optimized for a plateau with $2.8\,\text{ms} < T_R < 3.5\,\text{ms}$, i.e. for $T_R \sim T_2$. This behaviour has been already reported in numerous articles [24, 110, 217].

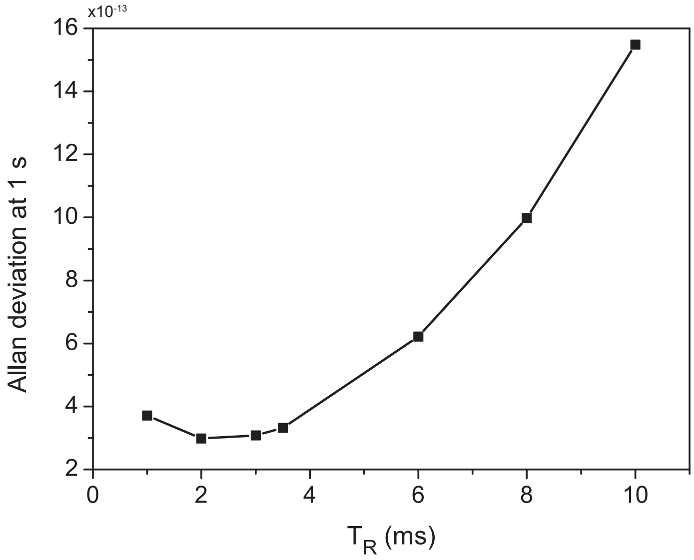

Figure 5.9: Clock short-term fractional frequency stability at 1 s averaging time versus T_R. The laser power P_i is 850 µW.

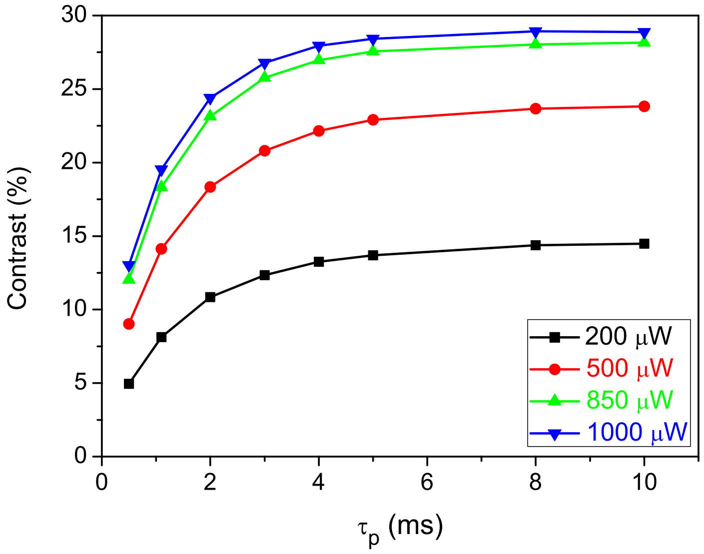

Figure 5.10: Central fringe contrast versus the pumping time τ_p for several values of the laser power (200, 500, 850, 1000 µW). $T_R = 3.5\,\text{ms}$. A dead time of 35 ms is applied between each acquisition point.

Figures 5.10 and 5.11 show respectively the central fringe contrast and linewidth versus the pumping time for several values of the laser power P_i. Experimental parameters are $T_R = 3.5\,\text{ms}$ and $\tau_D = 50\,\mu\text{s}$. The contrast is increased with the pumping time and reaches a plateau for $\tau_p \sim 4\,\text{ms}$. Simultaneously, the fringe linewidth is decreased when the pumping time increases to reach progressively a minimum value. This minimum value is reached for higher pumping time values when the laser power is reduced.

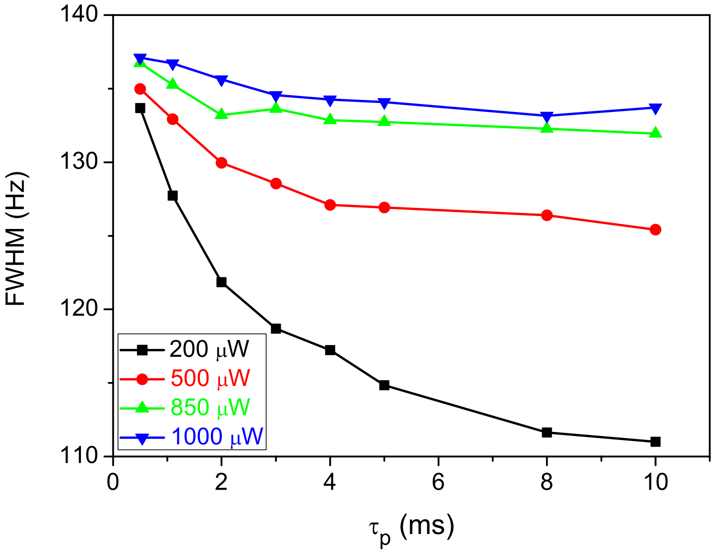

Figure 5.11: FWHM versus the pumping time τ_p for several values of the laser power (200, 500, 850, 1000 µW). T_R = 3.5 ms. A dead time of 35 ms is applied between each acquisition point.

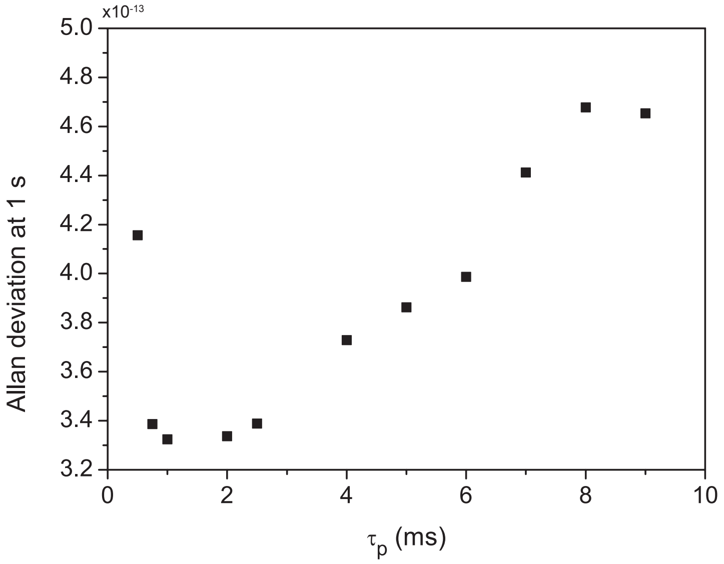

Figure 5.12: Clock short-term frequency stability at 1 s averaging time versus τ_p. The laser power P_i is 850 µW.

Looking at Figs 5.10 and 5.11, we could expect that the clock Allan deviation is optimized for pumping times higher than 4-5 ms. However, as shown on Fig. 5.12, we found that the clock short-term frequency stability is optimized for pumping times in the 1-2 ms range. For clarification, we report on Fig. 5.13 the evolution of the central fringe linewidth with the pumping time in two different sequence parameters conditions. In the first case, during the Ramsey-CPT fringe spectroscopy, a dead time of 35 ms (~ 10 - 12 T_2) is applied between each acquisition point. In the second case, the sequence is closer to the one used in clock locked configuration (see Fig. 5.1). The dead time is suppressed, the LO frequency is swept more rapidly and the transmitted power through the CPT cell is measured every clock cycle, i.e. every 4.6 ms. For both tests, the Ramsey time T_R is 3.5 ms and the laser power P_i is 850 µW. With a slow scan of the LO frequency, the fringe linewidth is reduced with increased pumping time for low values of the pumping time. The behaviour is totally opposite when lecture of the transmitted power is performed every clock cycle, without any dead time between two acquisition points. For low values of τ_p, it is worth to note that the steady state is not reached at the end of the first pulse. Consequently, when the Ramsey-fringes scan is fast and that no dead time is applied between two acquisition points, the hyperfine coherence is not fully relaxed at the end of the free-evolution time and the new coherence builds up from the previous one. This is equivalent to a longer pumping time yielding a still narrower recorded fringe. For $\tau_p > 5$ ms, both configurations give the same fringe linewidth value because the steady state is reached at the end of each pulse.

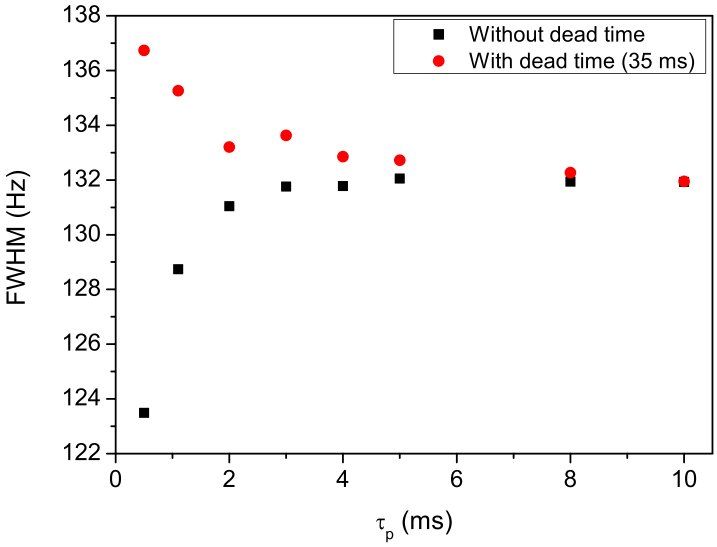

Figure 5.13: Central fringe linewidth versus the pumlping time τ_p in two different conditions. In the first case, a dead time of 35 ms is applied between each acquisition point. In the second case, the transmitted power through the cell is recorded every clock cycle, i.e. every 4.6 ms. Experimental parameters are $T_{cell} = 35\,°C$, $P_i = 850\,\mu W$, $T_R = 3.5$ ms.

Figure 5.14 shows the impact of the detection window length on the clock short-term frequency stability. T_c is the same in each experiment. The clock Allan deviation is optimized for a detection time window ranging from 50 μs to about 200 μs.

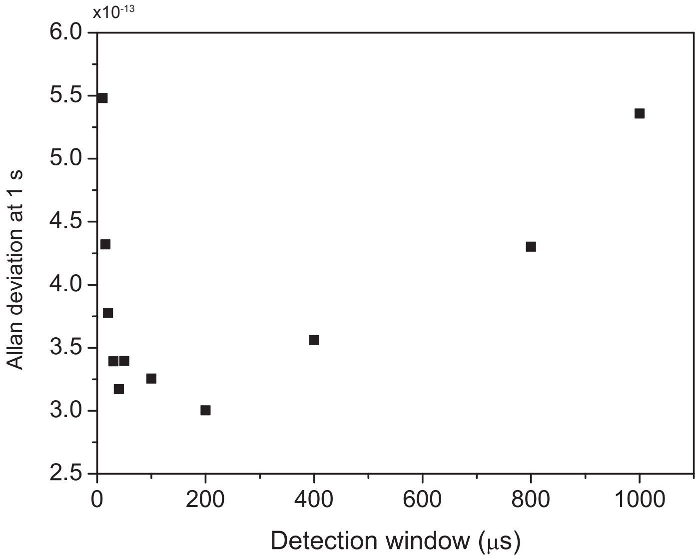

Figure 5.14: Clock Allan deviation at 1 s averaging time versus the detection window length. Experimental parameters are T_{cell} = 35 °C, P_i = 850 µW, τ_p = 1.1 ms, T_R = 3.5 ms, τ_D = 50 µs.

5.3 Short-term stability - comparison with the continuous regime

5.3.1 Short-term stability

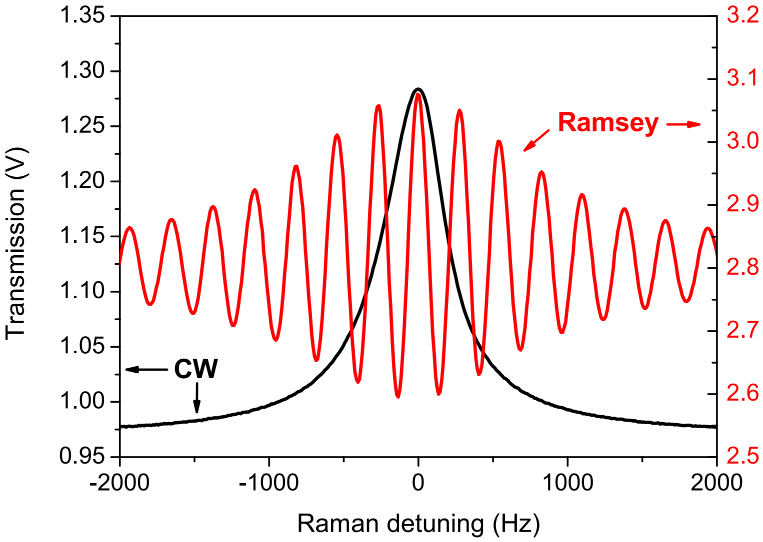

Figure 5.15: Typical clock signals in CW and pulsed regimes. In the CW regime, the laser power is 270 µW. In the pulsed regime, parameters are: P_i = 850 µW, T_R = 3.5 ms, τ_p = 1.1 ms, τ_D = 50 µs.

Measurements of the clock short-term fractional frequency stability were performed for comparison in both CW and pulsed regimes, with the parameter values optimizing the stability in respective cases. In the CW regime the AOM-based laser power stabilization system, as described in section 3.6.2 was implemented. In clock closed-loop operation, the LO modulation frequency F_M is 125 Hz, the modulation depth is ±80 Hz, the cell input laser power P_i is 270 µW and the cell temperature T_{cell} is 35 °C. In the pulsed regime, no laser power stabilization is applied to date. Experimental parameters are $T_c = 4.6\,\text{ms}$, $T_R = 3.5\,\text{ms}$, $\tau_p = 1.1\,\text{ms}$, $\tau_D = 50\,\mu\text{s}$, $P_i = 850\,\mu\text{W}$ and $T_{cell} = 35\,°\text{C}$. Figure 5.15 shows typical recorded clock signals in both CW and pulsed regimes. In the CW regime, the signal amplitude is $A = 0.31\,\text{V}$, the resonance linewidth is $\Delta\nu \sim 538\,\text{Hz}$, yielding a frequency discriminator slope roughly estimated by $S_l = A/\Delta\nu = 5.7\ 10^{-4}\,\text{V/Hz}$ and the resonance contrast is $C = 31.8\,\%$. In the pulsed regime, we obtain a central fringe with an amplitude $A = 0.48\,\text{V}$, a linewidth $\Delta\nu = 134\,\text{Hz}$, yielding $S_l = 3.6\ 10^{-3}\,\text{V/Hz}$ and a contrast C of 17 %. These characteristics in both regimes are resumed in Table 5.1.

Table 5.1: Main characteristics of the clock resonance and contributions to the clock short-term frequency stability at $\tau = 1\,\text{s}$. The noise sources contributions are named and calculated as described in [153]. The local oscillator phase noise item describes the contribution of the LO phase noise to the clock Allan deviation through the intermodulation (CW case) or Dick effect (pulsed case). The laser AM-AM noise is the amplitude noise induced by the laser intensity noise. The laser FM-AM noise is the amplitude noise induced by the laser carrier frequency noise. The $P_{\mu w}$ item stands for contributions of the microwave power fluctuations to the clock Allan deviation. Laser AM-FM and FM-FM are laser-induced frequency-shift effects from laser power or laser frequency variations respectively. Other contributions, from the cell temperature (item T_{cell}) and magnetic field (item B), are much lower. In the CW regime, the laser power is stabilized whereas it is not in the pulsed case.

Regime	CW	Pulsed
A (V)	0.31	0.48
$\Delta\nu$ (Hz)	538	134
$S_l = A/\Delta\nu$ (V/Hz)	5.7×10^{-4}	3.6×10^{-3}
C (%)	31.8	17
CS_l	1.8×10^{-4}	6.1×10^{-4}
P_i (μW)	270	850
P_o (μW)	56	205
T_{cell} (°C)	35	35
F_M or f_c	125	217
Noise Source	σ (1 s) $\times 10^{13}$	σ (1 s) $\times 10^{13}$
Shot noise	0.16	0.27
Detector noise	0.11	0.10
LO phase noise	0.5	0.6
Laser AM-AM	0.6	2.7
Laser FM-AM	0.39	0.49
$P_{\mu w}$	5×10^{-2}	5.7×10^{-2}
Laser AM-FM	2.16	0.49
Laser FM-FM	2.7×10^{-2}	2.9×10^{-2}
T_{cell}	8×10^{-3}	2.4×10^{-3}
B	3.8×10^{-3}	3.8×10^{-3}
Total (expected)	2.4	2.9
Measured	2.1	2.3

Figure 5.16 shows the Allan deviation of the clock frequency in both CW and pulsed regimes (performed in cell "C1B"). The clock short-term fractional frequency stability is measured to be $2.1\ 10^{-13}\ \tau^{-1/2}$ and $2.3\ 10^{-13}\tau^{-1/2}$ for averaging times up to 100 s in the CW regime (with laser power servo) and pulsed case respectively. These performances are comparable to those reported in chapter 4 and close to those of best vapor cell atomic frequency standards [24, 91]. In the present study, comparable performances are obtained in the CW and the pulsed regime. Such conclusions were also reported in [218, 219].

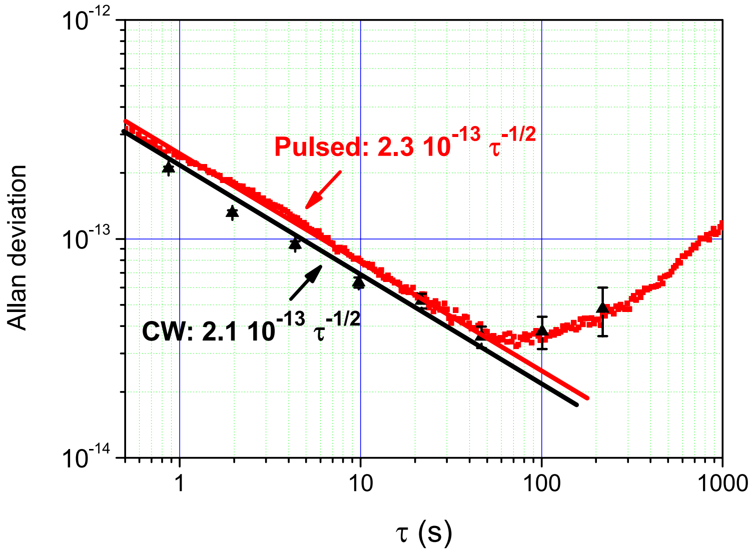

Figure 5.16: Typical clock signals in CW and pulsed regimes. In the CW regime, the laser power is 270 µW. The experimental spectrum is fitted by a Lorentzian function (blue dashed curve). In the pulsed regime, parameters are: $P_i = 850\,\mu\mathrm{W}$, $T_R = 3.5\,\mathrm{ms}$, $\tau_p = 1.1\,\mathrm{ms}$, $\tau_D = 50\,\mu\mathrm{s}$.

5.3.2 Noise budget

The short-term frequency stability of an atomic clock results from a trade-off between the resonance-based frequency discriminator slope S_l and the detection noise. In the pulsed case, the sequence parameters have also to be taken into account. Table 5.1 resumes and compares main experimental conditions, clock resonance characteristics and noise contributions to the clock short-term fractional frequency stability, in both CW and pulsed regimes. The definition and estimation of noise sources contributions, supported by experimental measurements, were performed following the methodology described in [153]. For sake of simplicity, we consider only white noise sources and we assume that the different noise contributions can independently add up. The total expected Allan variance $\sigma_y^2(\tau)$ is computed as the sum of $\sigma_{y,LO}^2$ (contribution due to the phase noise of the local oscillator) and $\sum_i \sigma_{y,p_i}^2$, with σ_{y,p_i}^2 the Allan variance of the clock frequency induced by the fluctuations of the parameter p_i [153].

A correct agreement is found between measurements and calculations. In the CW regime, the main limitation of the clock short-term frequency stability is the laser-induced amplitude modulation to frequency modulation (AM-FM) effect, caused by the sensitivity of the clock frequency to laser power variations. Following contributions are the laser amplitude modulation to amplitude modulation (AM-AM) noise (detection signal AM noise induced by the laser AM noise) and the LO phase noise. We note that, without laser power stabilization, the laser AM-FM noise contribution is increased by a factor 2-3 while the AM-AM noise contribution is increased at the level of 1.9 10^{-13}. In this case, the clock short-term fractional frequency stability was found to be degraded by a factor of 2-3, yielding 4-6 10^{-13} at 1 s. In the pulsed case, the main contribution to the noise budget is to date the laser AM-AM noise process at the level of 2.7 10^{-13}, followed by the laser FM-AM conversion process (detection signal AM noise induced by the laser carrier frequency noise), the LO phase noise and the laser AM-FM process. Other contributions are well below and negligible at the moment. With laser power stabilization, assuming a gain on the detection noise similar to the one obtained in the CW regime, the laser AM-AM contribution could be reduced in the pulsed case at the level of 4.8 10^{-14} instead of 2.7 10^{-13} presently. This would lead in the pulsed case to an overall fractional frequency stability at the level of 1 10^{-13} at 1 s averaging time. In the present configuration, pulsed and continuous regimes show similar short-term stability levels. Indeed, according to Table 5.1, we notice that the contribution to the clock stability of the laser AM-FM noise is 4.4 times lower in the pulsed case than in the CW case, due to a larger light shift coefficient in the latter case. This improvement in pulsed regime is compensated by the laser AM-AM noise contribution, which is 4.5 times larger in the pulsed case. This is due to a large extent to a higher AM-AM noise level (29 dB, or a factor of 28 with respect to the CW regime), because of the lack of power stabilisation and a higher incident power to the cell, counter-balanced by a larger frequency discriminator (6.3 times larger in pulsed regime).

5.4 Preliminar investigations on light-shift effects

A major and common issue in most vapor cell clocks is the degradation of their fractional frequency stability for averaging times typically higher than 100 s or 1000 s. This characteristic is a serious obstacle to their deployment in practical applications. This degradation is generally caused by laser intensity and frequency light-shift effects, cell temperature or pressure effects. In general, light shift is recognized as a major cause and is being studied with significant interest [114, 203, 210–215, 220, 221] for improvement of atomic frequency standards. As reported in previous literature [111, 209], the pulsed interaction presents the advantage to reduce significantly the sensitivity of the clock frequency to laser intensity variations.

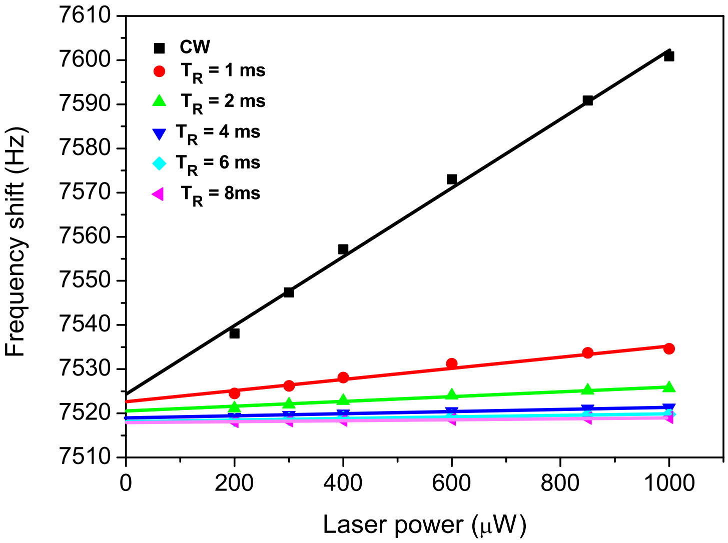

Figure 5.17: Clock frequency shift (from the unperturbed Cs atom frequency) versus the laser power P_i in the CW and pulsed regimes for several values of T_R. Experimental parameters are: $T_{cell} = 35\,°\mathrm{C}$, $\tau_p = 1.1\,\mathrm{ms}$ and $\tau_D = 50\,\mu\mathrm{s}$.

For this purpose, we decided to report a preliminary investigation of light-shift effects in this clock in the pulsed regime. Figure 5.17 plots the clock frequency (frequency shift from the unperturbed Cs atom frequency 9.192 631 770 GHz) versus the laser power for several values of T_R. Results obtained in the continuous regime are reported for comparison. Experimental parameters are: $T_{cell} = 35\,°\mathrm{C}$, $\tau_p = 1.1\,\mathrm{ms}$ and $\tau_D = 50\,\mu\mathrm{s}$. In the CW regime, the intensity light-shift coefficient is measured to be $8\ 10^{-12}\,\mu\mathrm{W}^{-1}$ (in fraction of the clock frequency). In the pulsed case, we observe a significant reduction of the light-shift slope with increased Ramsey time, resumed in Fig. 5.18. The light-shift slope is reduced to $6\ 10^{-13}\,\mu\mathrm{W}^{-1}$ and $3\ 10^{-13}\,\mu\mathrm{W}^{-1}$ for $T_R = 2\,\mathrm{ms}$ and 4 ms respectively. This behavior is qualitatively explained by the fact that with increased T_R, atoms spend a longer fraction of the clock cycle in the dark where they experience no or a greatly reduced light shift effect. In Ref. [222], C. Bordé reports for a 2-photon transition scheme that the light-shift slope in a pulsed Ramsey scheme should be reduced compared to the continuous regime case by a factor proportional to d/w_0 where d is the distance between both Ramsey cavity zones and w_0 the interaction length.

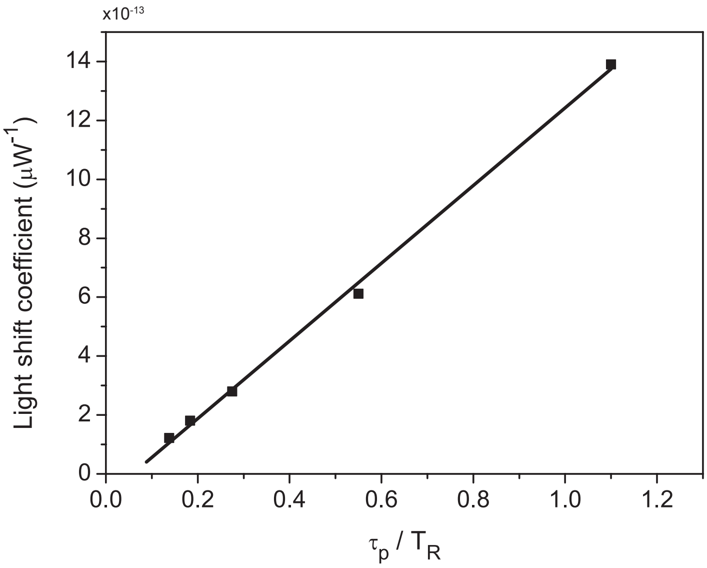

Figure 5.18: Light-shift slope versus the τ_p/T_R ratio.

In the present pulsed CPT clock experiment, the ratio d/w_0 is equivalent to the T_R/τ_p ratio. In our experimental case, with $\tau_p = 1.1\,\mathrm{ms}$ and $T_R = 3.5\,\mathrm{ms}$, we observe that the light-shift slope is reduced by a factor of about 26 in the pulsed regime, much greater than the expected factor $3.5/1.1 = 3.2$. In Ref. [220], the authors propose an estimation of the clock frequency light shift in the pulsed regime $\Delta\nu_{ls,pulsed}$ from the hyperfine coherence relaxation rate $\gamma_{12} = \pi\Delta\nu$ and the light-shift level in the CW regime $\Delta\nu_{ls,CW}$:

$$\Delta\nu_{ls,pulsed} = \Delta\nu_{ls,CW}\frac{\tau_{eff}}{\tau_{eff} + T_R\exp^{-\pi\Delta\nu\tau_D}} \tag{5.2}$$

$$\tau_{eff} = \frac{1-\exp^{-\pi\Delta\nu\tau_p}}{\pi\Delta\nu} \tag{5.3}$$

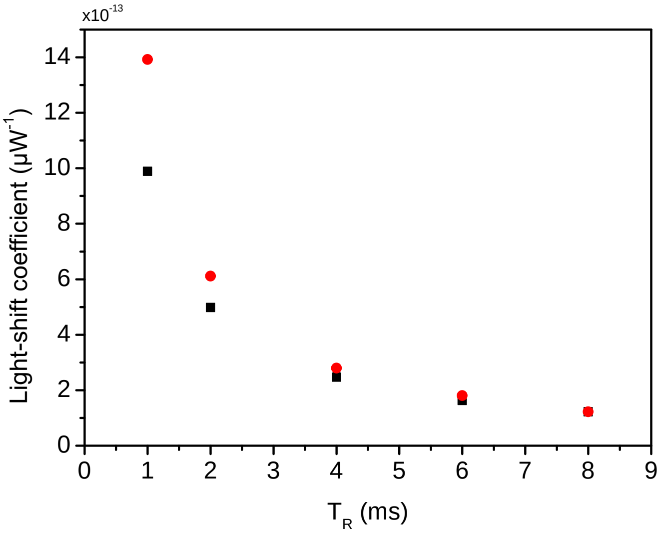

Figure 5.19: Light-shift slope versus the dark time. Red circles: data. Black squares: theoretical value using Eq. (5.3)

Figure 5.19 shows the measured light-shift coefficient in pulsed regime versus the Ramsey time and the prediction from Eq. (5.3). Theoretical and experimental values are in excellent agreement for high free-evolution times but the error is about 29 % for $T_R = 1$ ms. This disagreement will be studied in a near future.

In the present experiment, the sensitivity of the clock frequency to laser power variations is (in fractional value) at the level of $8\ 10^{-12}\,\mu\mathrm{W}^{-1}$ in the CW regime and reduced by a factor 26 to $3\ 10^{-13}\,\mu\mathrm{W}^{-1}$ in the pulsed case ($T_R = 3.5$ ms). Simultaneously, the typical laser power used in optimal clock operation is a factor 3.14 lower in the CW case ($P_i = 270\,\mu$W) than in the pulsed case ($P_i = 270\,\mu$W). In that sense, we can expect that the pulsed interaction, compared to the CW case, should relax the constraints on the required fractional laser power fluctuations by a factor of about $26/3.14 = 8.3$ (about one order of magnitude) to reach a given clock frequency stability level.

An ideal clock with a fractional frequency stability of $2\ 10^{-13}\ \tau^{-1/2}$ is expected to reach the 10^{-14} level after about 400 s averaging time. In the CW regime, from data given just above, this requires to demonstrate that laser power fluctuations σ_{P_i} at 400 s averaging time are lower than 1.25 nW, i.e. $\sigma_{P_i}/P_i = 4.6\ 10^{-6}$. In the pulsed case, this laser power control level would be reduced such that $\sigma_{P_i}/P_i = 3.8\ 10^{-5}$, which seems easier to achieve. In that sense, the pulsed interaction is expected to be the best solution for the demonstration of a clock with improved mid-term and long-term frequency stability. Note that the pulsed interaction involves a bit more complex digital electronics design for proper operation of all required servo loops of the clock and the addition of a fast optical switch to generate the light pulsed sequence. However, these functions remain accessible without any significant increase of the consumption and cost of the device. Detailed investigations will be pursued in the future in the laboratory to improve the mid-term and long-term frequency stability performances of the present clock.

Figure 5.20a resumes the clock frequency shift dependence with the laser input power and the cell temperature. Similarly to continuous regime, the light shift also presents non-linearities at high cell temperatures and low laser intensities.

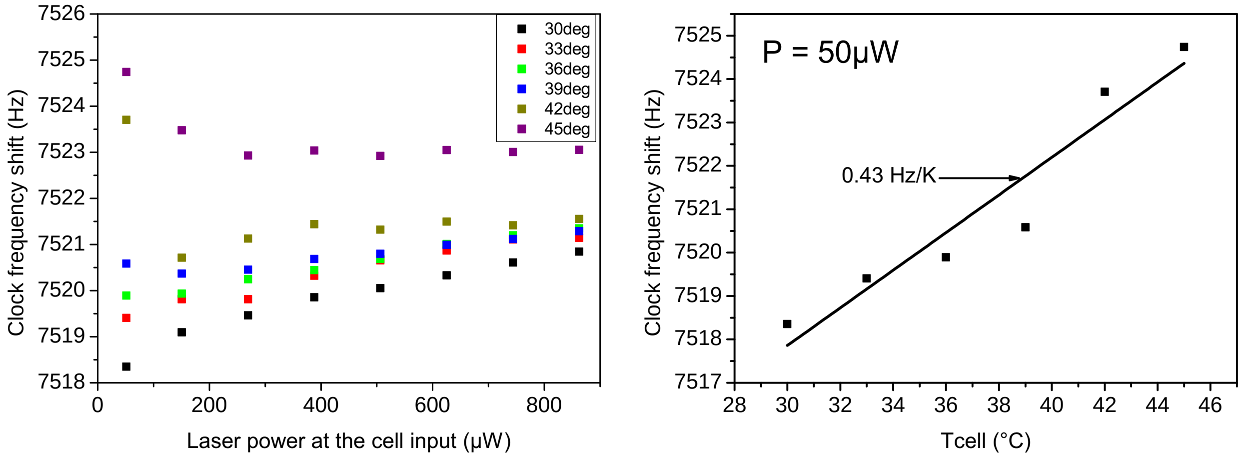

(a) (b)

Figure 5.20: (a) Light shift curves for several values of the cell temperature. (b) Buffer gas shift versus the cell temperature at 50 µW.

Figure 5.20b shows the evolution of the clock frequency with the cell temperature at the specific laser power of 50 µW. According to Fig. 2.6, we expect a cell filled with N_2 and Ar with a pressure ratio $r(Ar/N_2) = 0.6$ to present an inversion temperature $T_{inv} \approx 28\,^{\circ}$C. The dependence seems to be linear in the 30-45 °C range and no appreciable curvature in this temperature interval causes us to sense the presence of an inversion temperature of around 28 °C. Unfortunately, we could not go lower in temperature at the time the experiment was performed because of air conditioning issues in the lab. Instead a sensitivity of 0.43 Hz/K is measured, yielding $4.7\ 10^{-11}\ \mathrm{K}^{-1}$. Sensitivity to cell temperature is thus still close to an order of magnitude lower than for the cell with $r(Ar/N_2) = 0.4$, which allows to get closer to the desired clock specifications.

5.5 Conclusion

We have demonstrated a pulsed CPT-based Cs vapor cell atomic clock exhibiting a short-term fractional frequency stability of 2.3 10^{-13} $\tau^{-1/2}$ up to 100 seconds averaging time. These short-term stability performances are close to what is obtained in continuous regime and comparable to those of best vapor cell microwave frequency standards developed worldwide. The clock short-term frequency stability was optimized through the adjustment of key experimental parameters including the cell temperature, the laser power and the Ramsey-CPT sequence parameters. A dependence on laser power of the central fringe in the pulsed regime was reported. The central fringe linewidth was measured commonly narrower than the expected Ramsey linewidth $1/(2T_R)$ for short free-evolution times. A significant reduction of the clock frequency sensitivity to laser power variations was measured in the pulsed case, especially for high values of the free-evolution time T_R.

Chapter 6

Characterization of Cs vapor cell coated with OTS using CPT spectroscopy

The CPT clock developed during my thesis has become an attractive platform to perform original physical tests and to investigate novel techniques dedicated potentially to improve the frequency stability of next-generation vapor cell clocks.

This chapter reports the characterization of an octadecyltrichlorosilane (OTS) wall coated Cs vapor cell. Such wall coatings could represent an alternative or complementary solution to the conventional buffer gas filling technique to demonstrate the detection of long-lived relaxation time spin-polarized atoms in vapor cells.

It has to be noted that the CPT clock platform described in this manuscript has also been used to characterize Cs vapor micro-fabricated cells developed in FEMTO-ST. In particular, I have contributed to studies performed on collisional frequency shift measurements in micro-fabricated cells filled with He-Ne buffer gas mixture. Moreover, I have performed measurements, with my colleague V. Maurice, to characterize a novel and original micro-fabricated cell architecture named reflective cell. These two aspects are missing in this manuscript but the reader can refer to Refs. [223, 224] and in thesis manuscripts of E. Kroemer and V. Maurice for further information [122, 225].

6.1 Introduction

The detection of long-lived relaxation time spin-polarized atoms in alkali vapor cells is of critical importance in a relevant number of fundamental physics experiments and applications including optical magnetometry [167, 226], vapor cell atomic frequency standards [40], quantum information storage [227], quantum teleportation [228], slow-light applications [229, 230], investigation of atomic parity non conservation [231] or spin-squeezing [232]. In alkali vapor cells, two main techniques are used to slow down the fast wall-induced depolarization of the atoms. The first method is to dilute the alkali vapor in a buffer gas. In the so-called Dicke regime [129], slight and frequent alkali-buffer gas collisions result in a slow diffusive motion of atoms in the cells and contribute to increase the time for alkali atoms to collide against the cell walls. Nevertheless, the presence of a buffer gas induces a frequency shift and broadening of the optical resonance signal [88] that degrades the optical pumping efficiency and consequently the stability of atomic clocks and magnetometers but also a temperature-dependent frequency shift of the atomic clock hyperfine transition frequency [136, 138, 139]. These drawbacks are particularly critical in chip-scale atomic devices [98] where high buffer gas pressures (up to 700 Torr) are required in order to minimize the wall-induced relaxation.

The second method consists in coating the glass walls of the resonance cell with a chemically-inert anti-relaxation film material in order to make the atoms experience a significant number of bounces before complete destruction of the observed atomic population or coherence. Paraffin-coatings such as polyethylene, Paraflint [$CH_3(CH_2)_nCH_3$] or tetracontane [$CH_3(CH_2)_{38}CH_3$], formed by long-chain alkane molecules, were pioneerly proposed by Ramsey [233], first demonstrated by Robinson et al.[234], studied by Brewer [235] and later extensively by Bouchiat et Brossel [236]. These coatings have demonstrated to support up to 10^4 atom-wall collisions, leading to observed linewidths in centimeter-scale cells of a few Hertz on either Zeeman [237] or hyperfine transitions [238]. More recently, Balabas et al. reported exceptional anti-relaxation properties of alkene-based coatings (C_nH_{2n+1}) demonstrating polarized alkali-metal vapor with minute-long transverse Zeeman population and coherence lifetimes in a 3 cm diameter cell, which corresponds to about 10^6 polarization preserving bounces [239, 240]. For clock applications, it has to be noted that comparable microwave hyperfine frequency shift and linewidths have been recently measured between paraffin-coated and alkene-coated Rb cells [241, 242]. However, a drawback of paraffin and alkene-based coatings, recently studied and investigated in detail using surface science techniques by a large scientific community [243], is their relatively low-temperature melting point (about 85 °C and 35-100 °C [239, 240] respectively). This feature prevents them from being used in microfabricated vapor cells because of the high temperature of the anodic bonding process [244] In addition, cell temperatures higher than 80 °C are usually required in miniature atomic clocks. For this purpose, OTS layers, thermally stable up to 170 °C in presence of Rb vapor [245], are interesting candidates. Seltzer et al. reported the measurement of up to 2100 collisions before the population relaxes (T_1) in a K vapor cell with OTS multilayers [246] and typically 25 bounces with OTS monolayers in Rb vapor [247]. In the presence of Rb, multilayer and monolayer OTS were found to withstand 170 °C and 190 °C, respectively [245]. Through measurements of hyperfine resonance linewidths and frequency shifts, Yi et al. demonstrated in a 8 mm side cubic Rb vapor cell that Rb atoms collide up to 40 times with the cell walls before coherence relaxation and estimated their adsorption energy to be 0.065 eV [248]. From relaxation rate measurements in Rb vapor cells, Camparo et al. reported about 5 collisions with other silane materials [249]. More recently, a microfabricated vapor cell with OTS anti-relaxation coating was reported with the demonstration of 11 surviving wall collisions [250] in a double resonance Rb clock setup.

In FEMTO-ST, we proposed an original buffer-gas filled Cs vapor microcell fabrication and filling technology [251] that uses post-activation of Cs vapor in the hermetically-sealed cell through local laser heating of a Cs pill dispenser. Since no alkali vapor is present during the anodic bonding process, we can expect from the conclusions of [252] that the OTS coating should withstand the temperature of 350 °C. This procedure could be well-adapted for the development of OTS-coated microcells since anodic bonding process could be operated in optimal conditions at such elevated temperatures. In that sense, we investigate here the use of OTS coatings in Cs vapor cells for compact CPT-based atomic clocks applications and potentially later for miniature atomic clocks. Surprisingly, we found only one article in the literature where interactions between OTS coating and Cs atoms were studied

[253].

This section aims to report the detection, spectroscopy and hyperfine clock frequency shift measurements of coherent population trapping resonances in centimeter-scale OTS-coated Cs vapor cells. Subsection 6.2 describes the cell coating and filling procedure and the experimental set-up used to perform CPT spectroscopy. Subection 6.3 reports, using CPT spectroscopy, the characterization of a Cs-OTS cell through measurements of the CPT resonance linewidth, adsorption energy of the coating, T_1 and T_2 relaxation times. The detection of Ramsey fringes in the Cs-OTS cell is reported. The potential of the Cs-OTS cell in atomic clocks applications is finally discussed.

6.2 Experimental set-up

6.2.1 Wall coating and filling of Cs vapor cells

Figure 6.1: Photograph of the OTS-coated cell.

We produced and tested 3 different cylindrical vapor cells made of borosilicate glass (Borofloat®33, Schott). The first cell is a reference evacuated Cs cell with a diameter of 15 mm and a length of 15 mm. The second cell, named Cs-OTS, with the same dimensions than the evacuated Cs cell, is equipped with OTS anti-relaxation coating and does not contain any buffer gas. The last cell, named Cs-N_2-Ar, is a Cs vapor cell filled with a N_2-Ar buffer gas mixture of total pressure 15 Torr and pressure ratio $r(Ar/N_2) = 0.4$. Its dimensions are a diameter and a length of 10 mm. The coating and filling procedure for the Cs-OTS cell was performed as follows. First, the cell was cleaned with piranha solution (H_2SO_4/H_2O_2) and rinsed with de-ionized water. The cleaned cell was dried in an oven at 150 °C for 20 min. The cell was hermetically connected to a bottle containing a few microliters of OTS (from Sigma-Aldrich Inc.). This step was performed in a glovebox under a dry nitrogen (N_2) atmosphere to prevent OTS oxidation. Still connected to the bottle, the cell was baked in an oven at 150 °C for 4 h to let OTS evaporate and polymerize on the cell inner surface. The cell was later returned to the glovebox, disconnected from the bottle, rinsed with acetone and dried. Since the inner diameter of the capillary linking the cell to its sidearm is narrow (typically 600 µm), the introduction of any liquid inside the cell is impeded by capillary action. Consequently, the sidearm of the cell was immersed in the solution and the pressure in the glovebox was alternatively decreased and increased to allow the gas contained in the cell to be gradually replaced by the solution. Once coated, the cell was connected to a glass manifold evacuated with a turbomolecular pump below 10^{-7} mbar. Cesium (from Alfa Aesar Inc.) was distilled in the sidearms of the cells before being finally sealed off. Figure

6.1 shows a photograph of the OTS-coated cell. The presence of the coating material is confirmed by the existence of "milky" patches, layers or thin droplets on the cell inner walls.

6.2.2 Experimental set-up

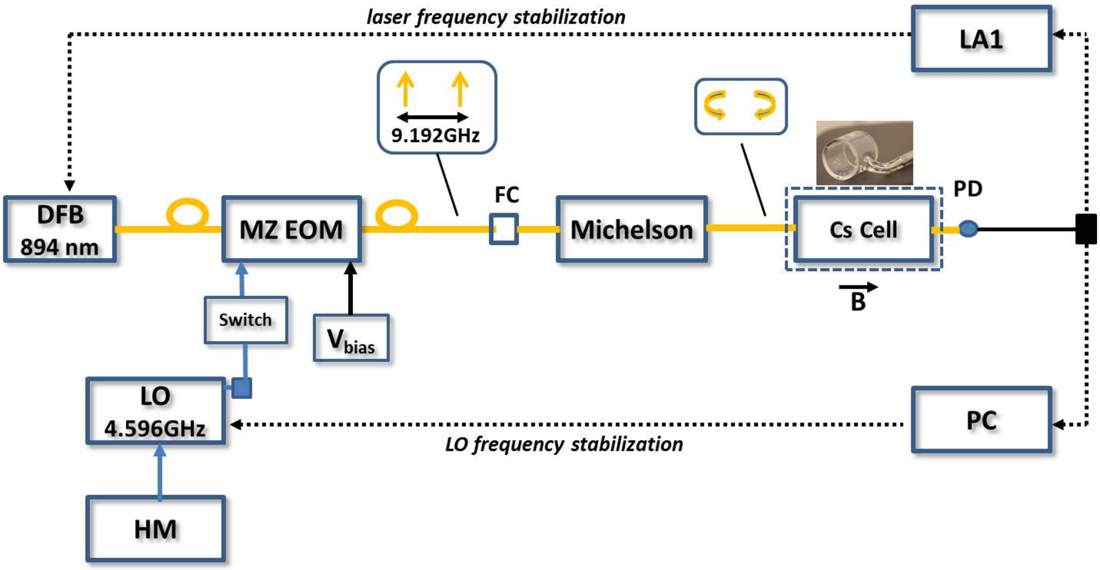

Figure 6.2: Experimental setup used to detect CPT resonances in Cs vapor cells. DFB: Distributed-Feedback diode laser, MZ EOM: Mach-Zehnder electro-optic modulator, Michelson: Michelson delay-line and polarization orthogonalizer system, V_{bias}: dc bias voltage applied onto the EOM to reject the optical carrier, LO: local oscillator, FC: fiber collimator, PD: photodiode, LA1: lock-in amplifier, PC: personal computer. A microwave switch can be used to turn on and off the 4.596 GHz signal in order to make the atoms interact with a sequence of optical pulse trains.

Figure 6.2 shows the experimental set-up used to perform coherent population trapping spectroscopy or relaxation time measurements in the Cs vapor cells. This setup is comparable to the one described in 3.4 with some differences to be noted.

In this experiment, performed in 2015, the laser frequency, when stabilized, was stabilized onto the bottom of the homogeneously broadened optical line of the CPT cell. The dual-frequency sub-Doppler laser frequency stabilization technique presented in section 3.4 was not implemented yet. The beam diameter was expanded to about 1.5 cm before entering the CPT cell. A variable neutral density filter was added to produce laser power variations and a diaphragm inserted in order to change the laser beam diameter.

The cell physics package was different from the one described in section 3.4. Here, we used the physics package used in the frame of my predecessor X. Liu PhD thesis [119].

A magnetic field flux density value of 1.55 G (for both the Cs cell and the Cs-OTS cell) and 100 mG (for the buffer-gas cell) was applied in order to separate and discriminate correctly Doppler-broadened ground state microwave Zeeman transitions. The assembly was surrounded by a double-layer mu-metal magnetic shield to protect atoms from environmental magnetic perturbations.

Eventually, in this experiment, no AOM was implemented. To produce pulsed light experiments, inspired by Ref. [208], the 4.596 GHz microwave signal power was switched on and off and the MZ EOM was used directly as a light switch. This technique was convenient to perform relaxation times measurements through the Franzen's technique of relaxation in the dark [254] or to produce a Ramsey-like pulsed interrogation.

6.3 Experimental results

6.3.1 Continuous regime CPT spectroscopy

Figure 6.3 reports, for identical experimental conditions, the CPT clock resonance in the Cs-OTS cell and in the evacuated Cs cell for a total incident laser power of 100 µW. Both cells exhibit about the same off-resonance background level, i.e. the same laser power absorption. The CPT resonance in the pure Cs cell is well approximated by a Lorentzian function. The dual-structure of the dark resonance, signature of the anti-relaxation effect, is obvious in the OTS-coated cell. The pedestal of the resonance is characterized by a Doppler-broadened structure whereas the top of the resonance is narrowed thanks to the coating material. As shown in the figure inset, the narrow structure is well approximated by a Lorentzian function with a linewidth of 1486 Hz.

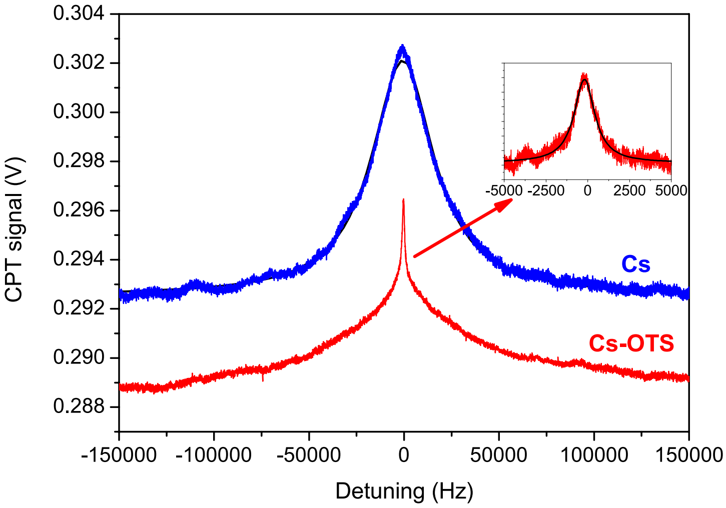

Figure 6.3: CPT clock resonance in the Cs-OTS cell compared to the one detected in the evacuated Cs cell. The laser power incident on the cell is 100 µW. The cell temperature is 35 °C. Experimental data for the evacuated Cs cell are approximated by a Lorentzian fit function. The narrow structure of the resonance in the Cs-OTS cell (figure inset) is approximated by a Lorentzian fit function. The laser beam diameter is 15 mm. For the Cs-OTS cell, the slight asymetry of the CPT resonance is attributed to a minor thermal transient of the clock set-up table during the scan of the CPT resonance.

Figure 6.4 shows the signal of the CPT resonance (narrow structure) in the Cs-OTS cell versus the cell temperature. The amplitude of the CPT signal is found to be maximized for a cell temperature of about 35 °C. The same behavior was observed for the broad structure signal. The contrast of the narrow structure was found to increase from 1.4 to 2.6 % from 29 to 42 °C. Note that the CPT linewidth of both narrow and broad structures were measured to be reduced very slightly with temperature in the 30 - 50 °C. The CPT signal-to-linewidth ratio is optimized at 35 °C, and most of the following results are obtained at this temperature.

For further investigation, Fig. 6.5 shows the linewidth of the CPT resonance in the three different Cs vapor cells versus the total laser power P for a cell temperature of 35 °C.

In an evacuated Cs cell, the main effects contributing to the CPT resonance linewidth are the Doppler broadening, the power broadening, the atom-light limited transit time and the Cs-Cs spin-exchange collisions. In a Doppler-broadened system, as explained in Ref. [255] for a similar experiment of electromagnetically induced transparency (EIT) and in Ref. [256] , it can be shown that the CPT linewidth is proportional to the square root of intensity for low laser intensity of the driving field and is independent of the Doppler width. This is an effect similar to the laser-induced line narrowing effect [257]. At higher laser intensities, the usual power broadening effect is recovered with a CPT linewidth proportional to the laser intensity. This behavior is clearly demonstrated in our measurement where the CPT linewidth - laser power dependence curve shows two distinct regimes with a sudden linewidth

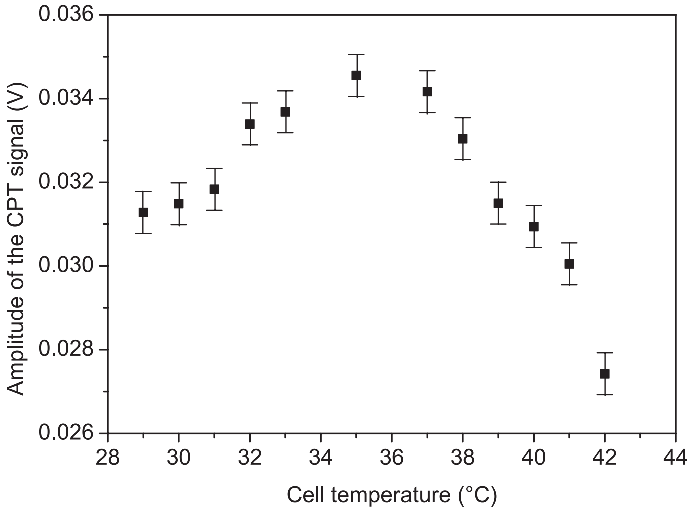

Figure 6.4: Amplitude of the CPT signal (narrow structure) in the Cs-OTS cell versus the cell temperature. The laser power is 600 µW. The static magnetic field is 892 mG.

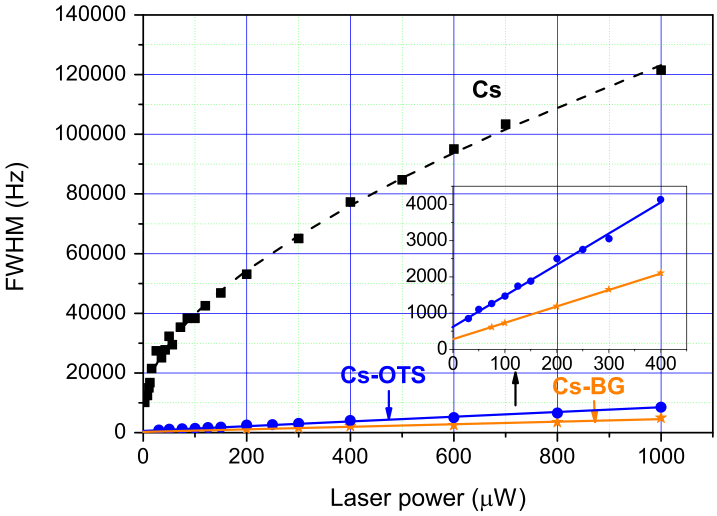

Figure 6.5: Linewidth of the CPT resonance in vapor cells versus the laser power for: evacuated Cs cell (black squares), Cs-OTS cell narrow structure (blue circles), Cs-N_2-Ar cell (orange stars). Error bars are covered by data points. The cell temperature is 35 °C. Data of the evacuated Cs cell are fitted by the function $a + b\sqrt{P} + cP$ (dashed line, P the laser power, a, b, and c are constants). Experimental data in the Cs-OTS cell and the buffer-gas filled cell are fitted by a linear function. The figure inset is a magnification for Cs-OTS and Cs-N_2-Ar cells.

decrease for laser powers lower than about 50 µW. In this laser power region, the contribution of the Doppler broadening is gradually reduced as the laser intensity is decreased. For a cell temperature of 35 °C, the CPT linewidth extrapolated at null laser power in the evacuated Cs cell is measured to be 7 kHz, in excellent agreement with theoretical calculations yielding a total linewidth of 7.07 kHz (sum of spin-exchange and transit-time contributions). The transit time contribution is given by $1/(\pi t_t)$ where t_t is the mean time of flight between two wall collisions. We note $t_t = \ell/v_m = 45\,\mu\text{s}$ with $v_m = \sqrt{8k_BT/(\pi m)} = 222\,\text{m/s}$ being the mean atomic velocity, T the cell temperature, k_B the Boltzmann constant and m the mass of the Cs atom. We note $\ell = 10\,\text{mm}$ the mean free path between two wall collisions in a cylindrical cell of radius R and length L such as $1/\ell = (1/R + 1/L)/2$ [40]. The transit time limited linewidth is 7.05 kHz. The spin exchange relaxation term is calculated at

35 °C following [126] as:

$$\Delta\nu_{se} = (11/16) n_{Cs} v_r \sigma_{se}/\pi. \tag{6.1}$$

Here n_{Cs} is the Cs density ($1.2\ 10^{11}$ atom/cm^3 [258]), v_r is the average relative velocity of Cs atoms, $v_r = \sqrt{2} v_m = 313\,\mathrm{m/s}$, and σ_{se} is the Cs spin-exchange cross-section ($2.18\ 10^{-14}\,\mathrm{cm}^2$ [40]), yielding $\Delta\nu_{se} = 18\,\mathrm{Hz}$. For the Cs-OTS cell and the buffer-gas filled Cs cell, experimental widths in Hz are well fitted by linear functions $634 + 8.6\ P$ and $268.9 + 4.6\ P$, respectively, with P in µW. The CPT linewidth extrapolated at null laser power is about 10 times narrower in the Cs-OTS cell compared to the pure Cs cell but 2.4 wider than in the buffer-gas filled Cs cell. In the Cs-OTS cell, the laser power broadening is about 13 times smaller than in the evacuated Cs cell and 2 times bigger than in the Cs-N$_2$-Ar cell.

In a cell coated with an anti-relaxation material, atoms collide with the surface, stick to it for a characteristic time τ_s and eventually return to the vapor. Attraction of the atom to the cell walls is mainly dominated by the long-range van der Walls force F that depends on the dielectric constant ε of the wall and the electric dipole operator D of the atom such as $F \propto (\varepsilon - 1)/(\varepsilon + 1) D^2$ [253]. The Cs energy levels are shifted during the atom-surface interaction, so that the phase of the hyperfine coherence of the escaping atom is shifted by a mean amount Φ at each collision, which depends on the surface characteristics. Reducing the wall surface attraction through the choice of a surface with low polarizability and choosing a coating material with low dielectric constant will help to reduce the atom-wall interaction time and to make the collision more elastic. This physisorption process can be characterized by an adsorption energy E_a, related to the sticking time τ_s, that traduces the kinetic energy an atom must have to escape the coating surface attraction and in turn the period the alkali atoms spend physically adsorbed on the wall of the cell. The adsorption energy can be estimated from the measurement of the clock frequency shift $\delta\nu$, defined as the difference between the actual clock frequency and the exact unperturbed Cs atom frequency (9.192 631 770 GHz), versus the cell temperature T as [259, 260]:

$$|\delta\nu| \propto E_a \exp[E_a/k_B T] \tag{6.2}$$

We measured the clock frequency versus the cell temperature (from 30 to 47 °C) to extract the value of E_a. The temperature of the Cs reservoir was kept slightly lower than the temperature of the cell wall to prevent deposition of Cs onto the wall coating. For each cell temperature, the clock frequency is measured for different values of laser intensity and extrapolation to null laser intensity is performed as shown on the inset of Fig. 6.6.

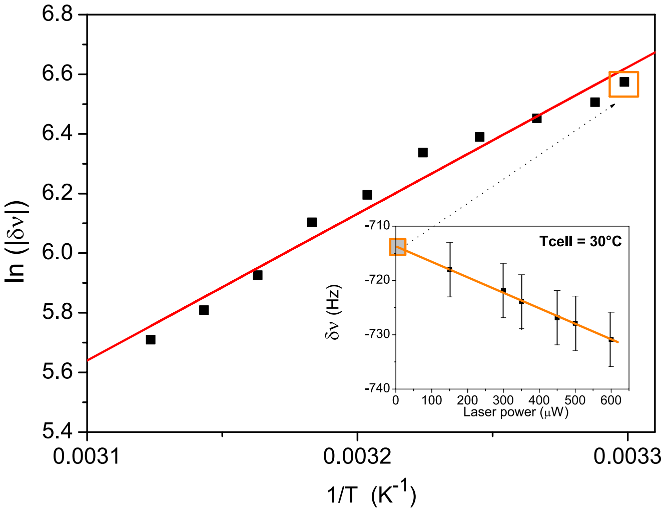

Figure 6.6: Logarithm of the frequency shift $|\delta\nu|$ versus the inverse of the cell temperature $1/T$ with T in K. Experimental data are fitted by a linear function from which is extracted the value of E_a. In the main figure, error bars are covered by data points. The inset shows an example for a cell temperature of30 °C of light shift measurement used to extract the temperature frequency shift at null laser power.

A negative frequency shift of a few hundreds of Hz is measured as usually observed on wall-coated cells [241, 248]. At high temperatures, an atom spends less time on the wall and is found to experience a smaller frequency shift magnitude. The shift rate is measured to be 24.6 Hz/K. According to Eq. (6.2), the plot of $\ln(|\delta\nu|)$ against $1/T$ (see Fig. 6.6) is a straight line of slope E_a/k_B. The fitting data of Fig. 6.6 leads to $E_a = 0.42\,\text{eV}$ with a statistical uncertainty of 0.03 eV. This value corresponds to a sticking time of the atom on the surface $\tau_s = \tau_0 \exp\frac{E_a}{k_BT} \sim 29\,\mu\text{s}$, where $\tau_0 \sim 10^{-12}\,\text{s}$ [253]. The value of E_a is in good agreement with the value ($0.40 \pm 0.03\,\text{eV}$) reported by Stephens et al. [253], the only one we found in the literature for Cs-Pyrex-OTS. It is worth to note that the measurement of [253] is based on a completely independent method, namely the atomic number density measurement. For Cs-Paraflint interaction, E_a was estimated to be 0.8 eV [259]. This value remains higher than the typical value of about 0.1 eV reported by other researchers in Rb vapor cells coated with paraffin [235, 236] or even 0.065 eV in OTS-coated Rb cells [248].
The frequency shift of the clock transition is related to the mean phase shift per wall collision Φ as [242, 259, 260]:

$$\delta\nu = \Phi/(2\pi t_t). \tag{6.3}$$

The phase shift values, computed from data of Fig. 6.6, are shown in Fig. 6.7 as a function of the cell temperature. On the limited experimental temperature range around 39°C the phase shift can be fitted by a straight line,

$$\Phi = -0.138(2) + 0.0074(3)(T_{cell} - 39), \tag{6.4}$$

with T_{cell} being the cell temperature in degree Celsius. $\Phi = -168(2)$ mrad/collision at 35 °C and $-94(2)$ mrad/collision at 45 °C. For comparison, Φ was measured to be 90(10) mrad/collision for Cs-Paraflint coating [259] at an unspecified temperature, -19 mrad/collision [250] and -65 mrad/collision [248] in Rb-OTS cells of smaller dimensions heated at 60 °C. Φ is proportional to $E_a \exp[E_a/k_BT]$ and E_a is proportional to the polarizability of the atom [259]. As cesium has the largest polarizability a larger phase shift is expected for cesium than for rubidium or potassium.

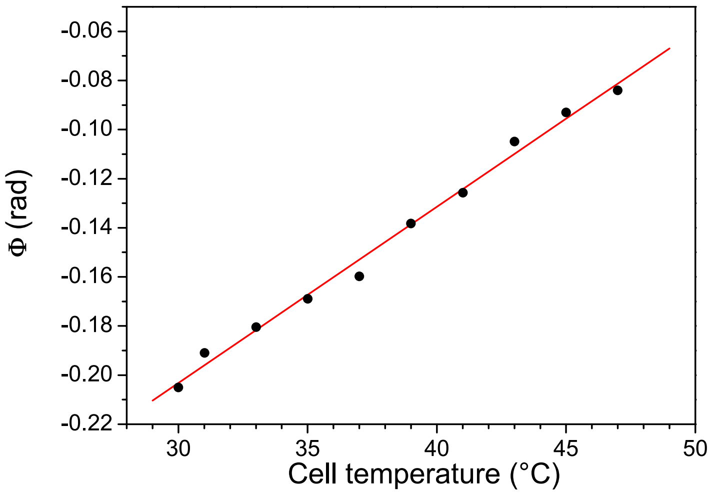

Figure 6.7: Phase shift per wall collision as a function of the cell temperature. The solid line is a linear fit. Error bars are covered by data points.

The actual phase shift experienced by an atom colliding the wall (adiabatic collision) is assumed to follow a Gaussian distribution of mean Φ and of variance Φ^2 [242, 259]. Here we do not take into account the atomic velocity distribution and t_t is considered as a constant. After n collisions the accumulated phase shift distribution $G(n, \varphi)$ is also Gaussian of mean $n\Phi$ and of variance $n\Phi^2$. The probability of experiencing n collisions during a time t is assumed to obey a Poisson distribution $p(n,t) = \frac{e^{-t/t_t}}{n!}(t/t_t)^n$ [242]. As a result, the mean and the variance of the phase shift after a time t

are:

$$\begin{aligned}\varphi_m &= \Sigma_{n=0}^{\infty} p(n,t) n\Phi = (t/t_t)\Phi, \\ \sigma_\varphi^2 &= <\varphi^2> - \varphi_m^2 = 2(t/t_t)\Phi^2.\end{aligned} \tag{6.5}$$

The lineshape L_S of the CPT resonance is given by the weighted sum of detuned Lorentzian profiles $L(\delta,\gamma)$:

$$L_S(\delta,\gamma) = \Sigma_{n=0}^{\infty}\left(p(n,t)\int_{-\infty}^{+\infty} L(\delta - \varphi/t_t, \gamma) G(n,\varphi) d\varphi\right), \tag{6.6}$$

with δ the angular frequency Raman detuning, and γ the half-width of the resonance. We have no analytical expression for L_S, which is a weighted sum of Voigt profiles. Nevertheless, as shown in Fig. 6.3 the lineshape is well fitted by a Lorentzian profile. Budker et al. [242] have shown that the contribution of the phase dispersion to the line width of a "classical" microwave transition is (in Hz) [242, 261]:

$$\Delta\nu_\Phi = \frac{\Phi^2}{\pi t_t}. \tag{6.7}$$

At null laser intensity the width of a CPT resonance or a "classical" resonance are given by the same coherence relaxation terms, thereby we can assume that Eq. (6.7) is valid in our case. The full resonance width (FWHM) $\Delta\nu$ can be written as the sum of different contributions:

$$\Delta\nu = \Delta\nu_w + \Delta\nu_\Phi + \Delta\nu_{se} + \Delta\nu_{st}. \tag{6.8}$$

Here, these terms are evaluated for a cell temperature of 35 °C. $\Delta\nu_{st}$ is the relaxation term due to atoms incoming in the stem. We assume that an atom impacting the stem region, of radius r, is lost and that this probability is proportional to the stem fractional area with respect to the whole cell area. It follows $\Delta\nu_{st} = \frac{1}{\pi t_t}\frac{r^2}{2R(R+L)}$. We estimate $r \simeq 0.8\,\mathrm{mm}$ and $\Delta\nu_{st} = 13\,\mathrm{Hz}$. The spin-exchange term $\Delta\nu_{se}$ is about 18 Hz. The dephasing term of Eq. (6.7) is 200 Hz. The $\Delta\nu_w$ term takes into account other relaxation contributions induced by wall collisions, e.g., population and hyperfine coherence relaxations or velocity changes such that the atoms go out of optical resonance by Doppler effect and are lost for the signal. As $\Delta\nu = 634\,\mathrm{Hz}$ at null laser intensity, $\Delta\nu_w$ is estimated to be about 400 Hz. The coating can be characterized by a mean number n of useful bounces before the loss of the atom or the loss of atomic phase memory. n is equal to the ratio of the relaxation term due to wall collisions in the coated cell, $n \approx \frac{1/t_t}{\pi(\Delta\nu_w + \Delta\nu_\Phi)}$. We get $n \approx 12$ bounces. This result is of the same order of magnitude as the one (11 bounces) reported by Straessle et al. in Rb-OTS cells [250] and as those (20-30 bounces) reported in Ref. [248], and much smaller than results obtained with paraffin or alkenes.

6.3.2 Measurements of population lifetime T_1

Additional characterization of the OTS-coated cell was realized through measurements of T_1 relaxation time in the dark using the Franzen's technique. Atoms interact with a sequence of optical pulse trains. The sequence is sketched in Fig. 6.8. Atoms are first optically pumped during a constant τ_p duration pulse ($\tau_p = 3\,\mathrm{ms}$) in the ($F = 4$) state with a single laser frequency. Then, light is switched off and atoms relax (($F = 4$) population) in the dark during a dark time T. Each cycle, the duration of the time T is slightly incremented. The next light pulse allows to detect the atomic signal by measuring the laser power transmitted through the cell. The signal is measured 20 µs after the beginning of the pulse. It is defined as the average value of 25 successive measurements realized in a 25 µs duration measurement window of the same light pulse. This study allows to measure how the atomic system, initially prepared in a determined initial state, evolves to the Boltzmann equilibrium. It is a measure of the hyperfine population relaxation performed on all Zeeman sublevels.

Figure 6.9 reports, for an incident laser power of 500 µW, the measurement of the relaxation time T_1 in the dark of the hyperfine level ($F = 4$) population.

A single laser frequency is obtained by detuning the carrier frequency of 9 GHz, tuning consequently a single sideband to the atomic resonance. For information, we noted that the polarization scheme

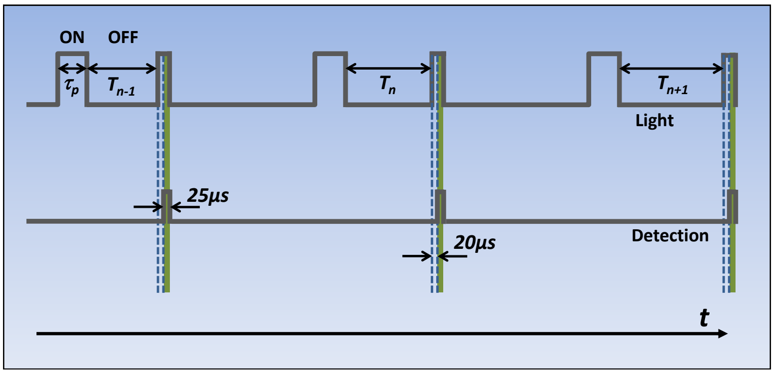

Figure 6.8: Representation of the Franzen sequence used to determine the hyperfine population relaxation time T_1.

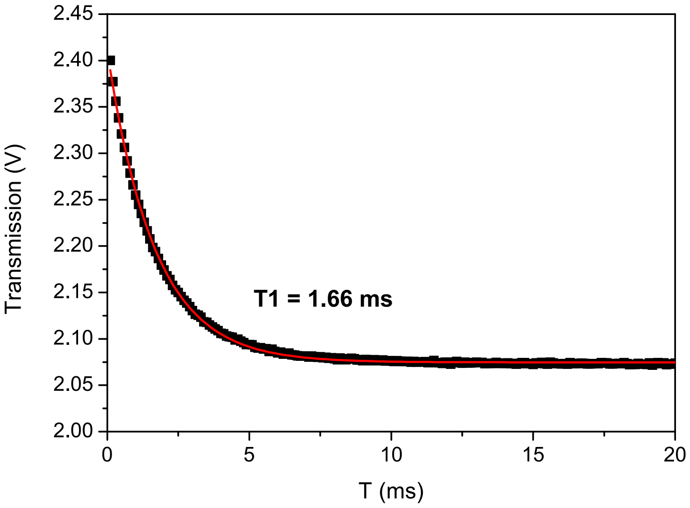

Figure 6.9: Measurement of the T_1 relaxation time in the Cs-OTS cell. The total laser power incident on the cell is 500 µW. The actual power seen by the atoms (power of one sideband) is about one half of the total laser power. The cell temperature is 35 °C. The static magnetic field is 900 mG. Squares: data, solid line: fitted exponential function.

(circularly polarized beam or push-pull optical pumping) and the static magnetic value had a negligible impact on the measured value of the T_1 relaxation time. Experimental data are well fitted by an exponential decay function with a time constant $T_1 = 1.660(7)$ ms. Such a time constant corresponds to about 37 useful bounces. Figure 6.10 shows the evolution of the measured T_1 value function of the laser power. For laser power higher than 300 µW, the value of T_1 is measured to increase slightly with the laser power before saturation above 1 mW. On the opposite, below 300 µW, the T_1 value increases for decreasing laser power. Clearly, there are two opposite phenomena that are not yet identified and need further investigations.

6.3.3 Motion-induced Ramsey narrowing and Ramsey spectroscopy in Cs-OTS cells

In a wall-coated cell without buffer gas, the ballistic transport mechanism is distinct from the diffusive behavior in buffer gas-filled cells. Atoms move randomly from wall to wall with constant velocity and direction. For small beam diameters compared to the cell diameter, repeated interactions of atoms with the light fields are equivalent to a sequence of randomly spaced Ramsey pulses in which the two optical fields are turned on and off. The free motion of the polarized atomic spins in and out of the optical interaction region before spin relaxation induces a well-known Ramsey narrowing of the CPT resonance, well studied and described in paraffin-coated cells [262, 263]. Additionally, it

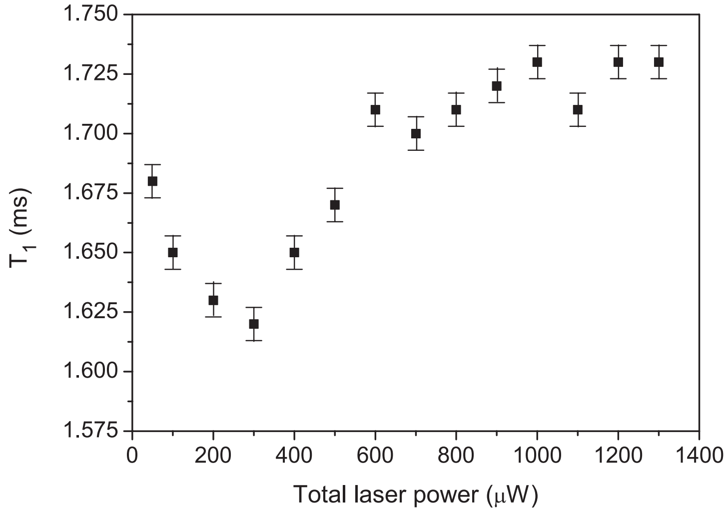

Figure 6.10: Measurement of the T_1 relaxation time in the Cs-OTS cell versus the total laser power incident on the cell. The actual power seen by the atoms is about one half of the total laser power. The cell temperature is 35 °C. The static magnetic field is 900 mG.

has to be noted that in our experiments, the residual Doppler effect on the clock transition is reduced by a Dicke-type narrowing because the cell characteristic length (1.5 cm) is smaller than the Cs atom ground-state microwave wavelength (3.2 cm).

We investigated in Cs-OTS cells the CPT resonance lineshape for different beam diameters. Figure 6.11 shows a CPT resonance in the Cs-OTS cell for a beam diameter of 8 mm and a laser power of 100 µW. The lineshape has a Doppler-broadened structure of linewidth 43 kHz, in correct agreement with the atom transit time through the interaction volume. The narrow central peak exhibits a width of 1924 Hz. Figure 6.12 shows the linewidth of the CPT resonance narrow structure versus the laser intensity for different laser beam diameters (8, 10 and 12 mm).

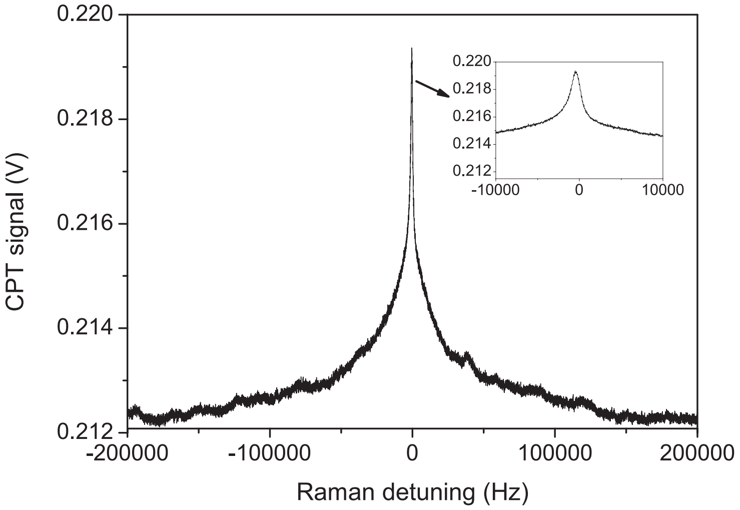

Figure 6.11: CPT resonance in the Cs-OTS cell for a beam diameter of 8 mm. The laser power is 100 µW.

For low laser intensities, which is the case for each experimental data point of the figure, the width of the narrow structure increases linearly with laser intensity. Most significantly, we observe a decrease of the linewidth with increase of the volume of the interaction region at constant optical intensity. Indeed, smaller beams allow longer phase evolution of atoms in the dark, making the CPT narrow structure lineshape narrower. Simultaneously, as observed in [262], we measured an increase of the CPT resonance amplitude with the laser beam radius. This can be explained qualitatively as an

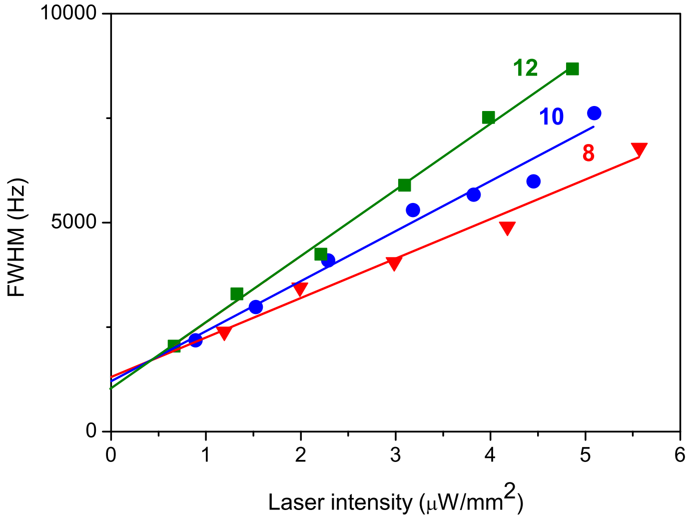

Figure 6.12: Linewidth of the CPT resonance narrow structure versus the laser intensity for different laser beam diameters (8, 10 and 12 mm). Error bars are covered by data points.

increase of the number of interacting atoms in the interrogation volume. On the contrary, we observed that the broad structure linewidth is increased with smaller beam diameter, which corresponds to a reduced atom-light interaction time. The Ramsey picture of bright and dark times also indicates that the narrow structure linewidth should saturate with increasing intensity, rather than continue power broadening as it would in most vapor-cell systems. This occurs because, for sufficient intensity, light fields optically pump atoms into the dark state in a single pass through the beam. This behavior was clearly observed in Ref. [263].

Additionally, the experimental set-up described above was used to detect CPT-Ramsey fringes in the Cs-OTS cell. Figure 6.13 shows a CPT-Ramsey fringe detected in the Cs-OTS cell. Atoms interact with light in a pulsed CPT sequence where the CPT pumping time τ_p is 3 ms and the free evolution time in the dark T_R is 0.2 ms. The laser power is 650 µW.

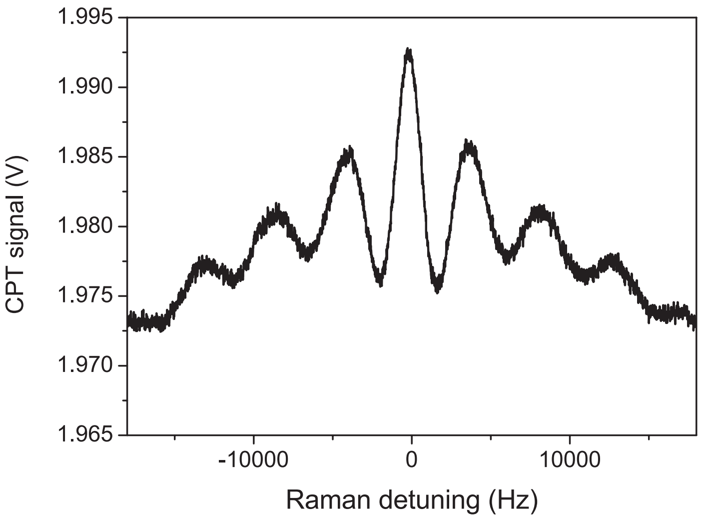

Figure 6.13: CPT-Ramsey fringe detected in a Cs-OTS cell. τ_p = 2 ms, T_R = 0.2 ms. The laser power is 650 μW. The cell temperature is 35°C. The beam diameter covers the whole cell diameter.

Figure 6.14 shows the evolution of the central Ramsey fringe amplitude versus the Ramsey time T_R. Experimental data are well fitted by an exponential decay function with a time constant of 0.46(5) ms. This value can be interpreted as an experimental estimation of the CPT hyperfine coherence lifetime

T_2. This value of T_2 is in correct agreement and slightly smaller than the one extracted from the zero-intensity CPT linewidth measurement of 634(50) Hz reported in Fig. 6.5, which yields a T_2 time of $T_2 = 1/(\pi\Delta\nu) = 0.50(4)$ ms.

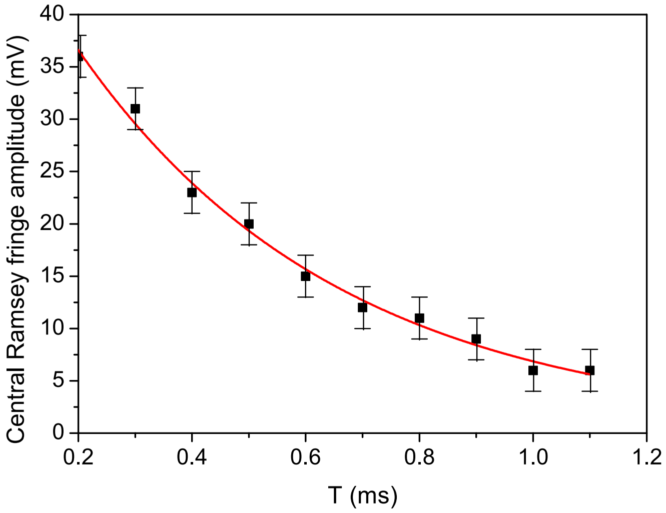

Figure 6.14: Amplitude of the central CPT-Ramsey fringe detected in a Cs-OTS cell versus the Ramsey time T_R. The laser power is 1.4 mW. Experimental data are fitted by an exponential decay function of time constant $T_2 = 0.46$ ms.

Note that the contribution of the phase shift dispersion term to the relaxation rate of the Ramsey fringes is the same as in the CW interrogation case. When the phase distribution is Gaussian of variance σ_φ^2, it can be shown that the fringe amplitude scales as $e^{-\sigma_\varphi^2/2}$. Here $\sigma_\varphi^2/2 = (t/t_t)\Phi^2$, see (6.5), which is equivalent to a time constant t_t/Φ^2 , i.e. the same as the one of the continuous measurement deduced from (6.7).

6.3.4 Applications to atomic clocks

Figures 6.15a and 6.15b show the signal and the contrast (defined as the ratio between the CPT signal amplitude and the off-resonance dc background) respectively of the CPT resonance in CW regime for different values of the laser power in the Cs-OTS cell, when the beam diameter covers the whole cell diameter.

The signal amplitude shows a quadratic dependence for laser power below 50 µW while the dependence is linear above this value. This behavior is in good agreement with the CPT signal expression derived in Ref. [126]. As observed in buffer-gas filled Cs vapor cells using push-pull optical pumping technique, the resonance contrast is measured to increase with the laser power while a saturation value is expected to be observed at higher intensities [120].

We remind that the short-term fractional frequency stability of an atomic clock, in terms of Allan deviation $\sigma_y(\tau)$, is given by:

$$\sigma_y(\tau) \approx \frac{\Delta\nu}{\nu_0}\frac{1}{SNR}\tau^{-1/2} \tag{6.9}$$

where ν_0 is the clock transition frequency (about 9.192 GHz for Cs atom), $\Delta\nu$ is the resonance full-width at half maximum, SNR is the signal-to-noise ratio of the detected resonance in a 1 Hz bandwidth and τ is the averaging time of the measurement. Assuming that detection is limited by photon shot noise, it can be written that [124]:

$$SNR = C\sqrt{\frac{P_l}{2h\nu_l}} \tag{6.10}$$

with P_l the laser power at the output of the cell and $h\nu_l$ the thermal energy of a single photon. From measurements of $\Delta\nu$ and C reported in Fig. 6.5, 6.15a and 6.15b, Fig. 6.15c shows the expected shot-noise limited clock frequency Allan deviation in CW regime versus the laser power. The best

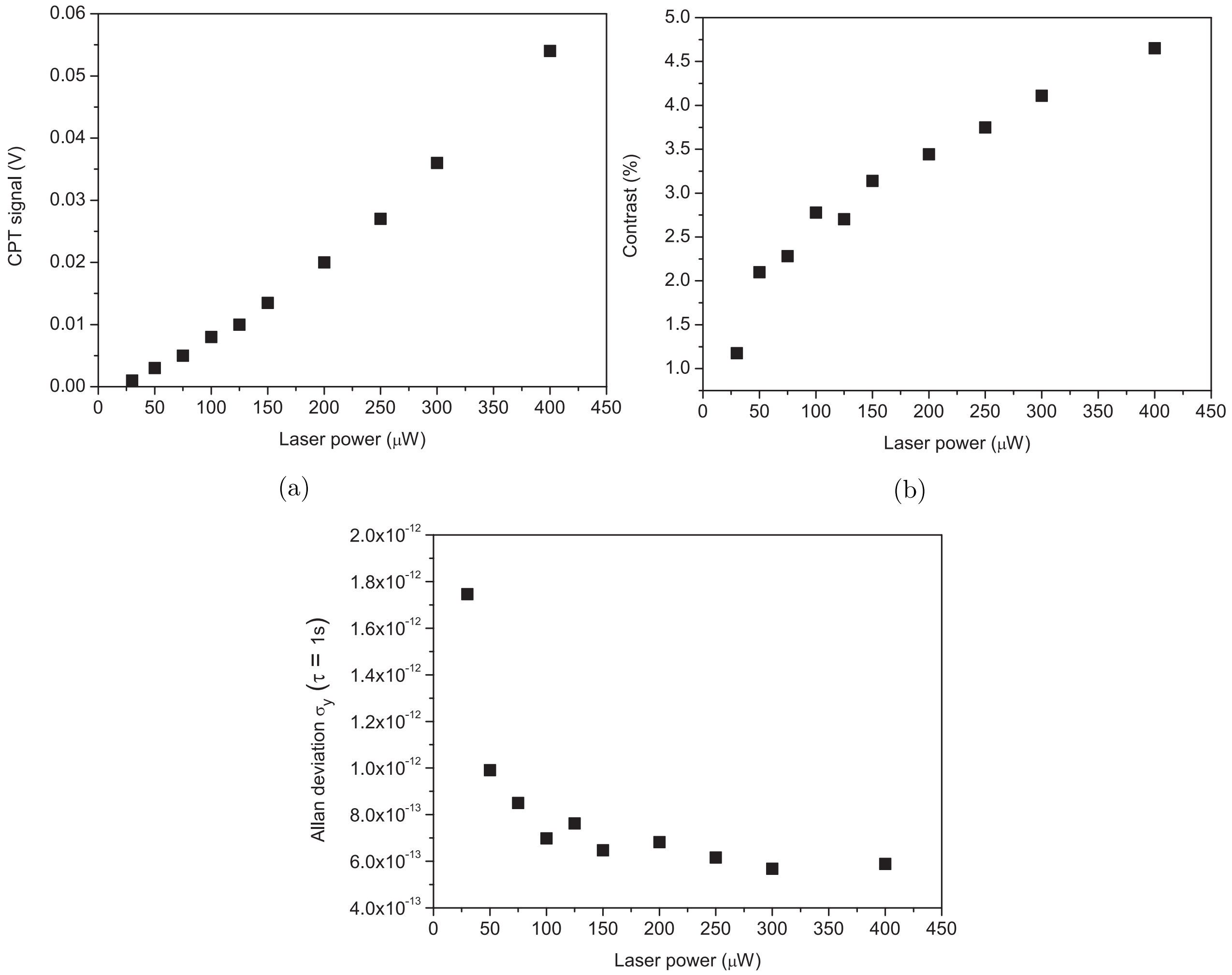

(a)

(b)

(c)

Figure 6.15: (a): CPT resonance signal, (b) CPT resonance contrast, (c) calculated shot-noise limited clock frequency Allan deviation versus the laser power incident on the cell. The cell temperature is 35 °C. The laser beam diameter equals the cell diameter. Error bars are covered by data points.

frequency stability result, at the level of 6 10^{-13} at 1 s, is obtained for a laser power of about 300 µW. This result is about 3 times worse than the expected fractional frequency stability of a clock using a buffer-gas filled Cs vapor cell of slightly smaller dimensions (10 mm-length and 10 mm diameter) [120].

Narrowing the linewidth through the motion-induced Ramsey narrowing process could improve the frequency stability, but Breschi et al. [262] have shown that the gain on the shot-noise limited frequency stability does not follow the gain on the resonance linewidth reduction. Actually, the same short-term fractional frequency stability can be obtained with a large beam diameter at small laser intensity and a smaller beam diameter at higher laser intensity (i. e. higher clock signal). With the Ramsey technique, the optimum clock short-term frequency stability is expected to be obtained when the free evolution time T_R equals the microwave coherence relaxation time T_2 [24, 110, 208]. In the present study, the free evolution time is limited to $T_2 \simeq 0.50\,\mathrm{ms}$, yielding a central fringe width of about 1 kHz. The shot-noise limited frequency stability is given by [208]:

$$\sigma_y(\tau) \approx \frac{\Delta\nu}{\nu_0}\frac{1}{C}\sqrt{\frac{h\nu_l}{P_l}}\sqrt{\frac{T_c}{t_m}}\tau^{-1/2}, \tag{6.11}$$

with T_c the length of an interrogation cycle, t_m the length of the signal measurement. The stability limit in our case is about 3.5 10^{-12} at 1 s, worse than a CW interrogation, showing that a Ramsey

interrogation is not the most appropriate in the case of a fast signal decay.
Eventually, from Fig. 6.6, we note that for a cell temperature of 30 °C, the light shift slope is measured to be $-0.029\,\mathrm{Hz/\mu W}$, i.e $-50.9\,\mathrm{Hz\,cm^2/mW}$, which yields relatively to the clock frequency $5.5\ 10^{-9}\,\mathrm{cm^2/mW}$. This value is of the same order of magnitude than light-shift coefficients measured in Ref. [262] in paraffin-coated cells. Moreover, we note in Fig. 6.6 that the temperature dependence of the clock transition in the Cs-OTS cell is roughly 24 Hz/°C, which yields relatively to the clock frequency $2.7\ 10^{-9}\,\mathrm{K^{-1}}$. This sensitivity is about 10 times higher than the one measured ($2.7\ 10^{-10}\,\mathrm{K^{-1}}$) in a laser-pumped paraffin-coated cell rubidium frequency standard [264] and huge compared to typical sensitivities that can be achieved in optimized buffer-gas filled vapor cells [136, 139, 203]. This high temperature sensitivity could be a serious drawback for the use of OTS-coatings towards the development of high-performance compact atomic clocks.

6.4 Conclusions

We reported the realization of a centimeter-scale Cs vapor cell wall-coated with octadecyltrichlorosilane (OTS) using a simple vapor phase deposition technique. The coating properties were characterized by means of CPT spectroscopy of the Cs ground state hyperfine transition, in view of application to vapor cell atomic clocks. The presence of a narrow peak Lorentzian structure on the top of a Doppler-broadened broad structure is a relevant signature of the OTS anti-relaxation coating. Experimental results are given for a cell temperature of 35 °C, which maximizes the CPT signal. Using clock frequency shift measurements, the adsorption energy of Cs atoms on OTS surface was measured to be $E_a = 0.42(3)\,\mathrm{eV}$, in agreement with the value reported in the literature for Cs-OTS-Pyrex [253] by a completely different method. A clock frequency shift rate of 24.6 Hz/°C was measured. The phase shift per collision with the OTS surface was estimated to $-168(2)$ mrad, with a shift rate of 7.4 mrad/°C.
Measurements of hyperfine population lifetime (T_1) and microwave coherence lifetime (T_2) of about 1.6 and 0.5 ms were reported, corresponding to about 37 and 12 useful bounces, respectively. For comparison, in [246], the reported number of bounces (for the lifetime T_1) for four OTS-coated K cells ranges from 20 to 2100. Using a Rb cell coated with an OTS monolayer, Ref. [248] reports 31 bounces (at 82 °C) and 41 bounces (at 102 °C) for Zeeman coherences, and 21 (at 102 °C) and 30 (at 170 °C) for hyperfine coherence. Ref. [250] reports for a Rb-OTS cell 11 bounces for the hyperfine coherence at a not clearly specified temperature, probably 60 °C. It appears that the number of useful bounces is smaller for hyperfine coherence than for Zeeman coherences, decreases at lower temperatures and decreases for atoms with higher polarizability. In that sense, the relatively low number of bounces (12) reported here for the hyperfine coherence of Cs at 35 °C is reasonable and give us confidence on the quality of the coating.
Motion-induced Ramsey narrowing [262, 263] where atoms alternately spend bright and dark time intervals inside and outside the laser beam was observed in the Cs-OTS cell in continuous interaction regime by reducing the laser beam diameter. Raman-Ramsey CPT fringes were detected in the Cs-OTS cell using a temporal Ramsey-like pulsed interrogation scheme. Applications to atomic clocks were discussed. The best calculated shot-noise limited frequency stability was obtained for a CW interrogation.
As a matter of fact, the high Cs-OTS adsorption energy leads to a large atom-wall collision induced phase shift, a high temperature sensitivity of the clock transition frequency, $2.7\ 10^{-9}\,\mathrm{K^{-1}}$ in fractional frequency, and a limited number (about 12) of bounces preserving the hyperfine coherence. We consider these aspects as serious drawbacks for the development of a high-performance Cs-OTS atomic clocks compared to the buffer gas technique. Nevertheless, OTS coatings could be of interest in microfabricated cells and miniature atomic clocks applications. Miniaturized cells usually work at higher temperature ($\sim 80 - 100\,^{\circ}\mathrm{C}$) than centimeter-sized cells in order to increase the Cs density and the signal. As shown in Fig. 6.7, the module of the phase shift per collision decreases when the temperature increases. If the microcell operates at a temperature where the phase shift value is reduced or canceled, the broadening term $\Delta\nu_{\Phi}$ can be reduced and consequently the number of useful bounces increased. On the other hand, the temperature-related shift will be certainly reduced but

not canceled. The use of OTS coatings will be compliant with miniature atomic clocks applications if both the sensitivity of the clock frequency to cell temperature variations and cell temperature control are compatible with typical clock fractional frequency stability performances objectives at the level of 10^{-11} at 1 hour and 1 day averaging time.

Conclusion and perspectives

In the manuscript, I reported my contribution to the development and metrological characterization of a high-performance Cs cell CPT clock, in the frame of the Mclocks project. This project aimed to initiate the transfer of high-performance vapor cell atomic clocks technologies to the industry.

The CPT clock architecture combines a single DFB laser emitting at the Cs D1 line, a pigtailed Mach-Zehnder EOM for the generation of a quasi-pure bi-chromatic CPT field, an AOM assuming several roles (compensation for the buffer gas-induced optical shift, stabilization of the laser power, eventually generation of Ramsey-CPT pulses), a Michelson system to generate the so-called PPOP pumping scheme, a cm-scale buffer gas-filled Cs cell and electronics. Each of these main functional blocks has been characterized. The PPOP technique has allowed the detection of high-contrast CPT resonances on the 0-0 magnetic-insensitive clock transition without the constraints brought by the use of two phase-locked lasers. The clock can operate in the CW and in the pulsed regimes. In the latter case, the Cs atoms interact with a sequence of optical CPT pulses separated by a free-evolution time T_R in which they evolve in the dark, conducting to the detection of high-contrast and narrow Ramsey-CPT fringes.

In each regime, a spectroscopic study versus the cell temperature, laser power and magnetic field was performed to find the optimal experimental parameters for the clock operation. In the pulsed mode, we looked for the pulses timing optimizing the clock short-term stability. In addition, a detailed noise budget and full characterization of the experimental parameters inducing clock frequency perturbations was performed. It was identified that laser power effects are currently the major limitations of the CPT clock frequency stability.

A clock fractional frequency stability of the order of $2\ 10^{-13}\ \tau^{-1/2}$ until 100 s averaging time has been demonstrated, both in the CW and in the pulsed regimes. These performances have been achieved in particular thanks to the use of an AOM-based laser power stabilization setup, and to an improvement of the laser frequency stability. The latter was achieved by implementing an important optical isolation stage to reduce laser feedback effects, and by using an original dual-frequency Doppler-free spectroscopy laser stabilization setup. An attempt to reduce the clock frequency sensitivity to laser power fluctuations in the CW regime has been made by looking for a proper set of experimental parameters. This trial remained unsuccessful without dramatically degrading the clock resonance signal and short-term stability. We showed an improvement of the laser power stability by implementing a second stage of laser power stabilization, but the effect was modest. In pulsed regime, a significant reduction of the clock frequency sensitivity to laser power fluctuations has been demonstrated, and the central fringe linewidth has been measured narrower than the expected Ramsey linewidth $1/(2T_R)$. However, as no arrangement has been done yet to stabilize the laser power in pulsed regime, and because the optimal laser input power is high in the pulsed regime compared to the CW case, no significant improvement of the clock frequency short-term and mid-term frequency stabilities have been observed to date in the pulsed regime.

An in-depth experimental and theoretical investigation was performed to describe underlying physical processes of the dual-frequency sub-Doppler scpectroscopy setup, highlighting the relevant contribution of Zeeman CPT, hyperfine-splitting (HFS) CPT states and velocity-selective optical pumping effects.

The clock "platform" has also been used to perform, using CPT spectroscopy, the characterization of a Cs vapor cell coated with octadecyltrichlorosilane (OTS). The spectroscopy has shown a narrow

Lorentzian peak on top of a Doppler-broadened structure, signature of anti-relaxation coatings. We measured a number of 12 useful bounces before microwave hyperfine coherence relaxation and a high sensitivity to temperature of $2.7\ 10^{-9}\,\mathrm{K}^{-1}$. These results obtained in a cm-scale Cs cell seem very constraining for metrological aspects, but they could become more interesting in micro-fabricated cells which work at higher temperatures.

The short-term frequency stability level of the CPT clock is to date among the best reported for vapor cell atomic clocks. However, it remains one order of magnitude worse than the fundamental shot noise-limitation and further progress is to be done. For improvement, several paths can be envisioned. In a first approach, it could be interesting to understand and to limit the excess noise added by the MZ-EOM in the specific carrier suppression set point. Additionally, we think that the use of the laser feedback spectroscopy technique proposed by V. I. Yudin et al. [157], combined with the push-pull optical pumping technique, could be a solution to increase further the CPT resonance signal at the expense of a slight complexification of our setup for detection of the atomic fluorescence. While this process is not the highest contribution to the clock frequency stability, an additional modification could be to replace the DFB laser by an extended cavity diode laser (ECDL) with narrower spectral linewidth in order to reduce the laser frequency noise. Such a laser has been recently ordered thanks to the support of Région Bourgogne Franche-Comté. In the pulsed regime, we expect important benefits on the clock short-term frequency stability from stabilization of the laser power. This aspect will be implemented as soon as possible in our next studies. Note also that the realization of vapor cells with increased hyperfine coherence relaxation times, for example by combining buffer gas and efficient anti-relaxation coatings, could be a solution to allow to operate the pulsed clock with increased free-evolution times, and consequently narrower Ramsey-CPT fringes linewidth. This would also benefit to the clock short-term fractional frequency stability.

While the improvement of the clock short-term frequency stability is a relevant challenge, we're convinced that the main issue to tackle to validate fully CPT clocks technology for industrial applications is to improve their mid-term and long-term frequency stability. This problem has remained a persistant issue over many years for vapor cell clocks and must be solved to make such systems fully attractive for real-life industrial applications.

In that sense, we think first that laser power stabilization in the pulsed regime should help. Moreover, this thesis work has highlighted that future works should target a better understanding of light-shift effects in CPT clocks (including non-linearities we observed) and finding a definitive solution to reduce their effects. In the literature [203–206], when direct laser modulation or external phase modulation is applied, an efficient technique to cancel power-induced light shift effects in CPT clocks is to adjust the microwave power. Indeed, by modifying the relative amplitudes of CPT optical sidebands, there exists a so-called magic microwave power set point allowing to cancel at the first-order the light shift slope. This technique has been efficiently implemented in several CPT clocks systems, including recently in FEMTO-ST for microcell-based CPT atomic clocks. In our setup, this solution is difficult to implement due to the use of a Mach-Zehnder electro-optic modulator. A solution could be to evaluate and to control the sidebands asymmetry at the output of the MZ EOM by using a temperature-controlled Fabry-Perot cavity playing the role of a tunable filter. Nevertheless, this solution would increase the complexity of the clock.

At the opposite, in the pulsed regime, we think that solutions inspired from hyper-Ramsey spectroscopy techniques [211, 213, 214, 265, 266] applied to CPT should lead to a cancellation of light shift. We expect to test such solutions in the future, by collaborating with several partners known for their expertise in this domain.

Another contribution to be reduced will be also the effect of the cell temperature collisional frequency shift. Working with a cell exhibiting an inversion temperature [40, 136, 139] seems a key requirement to fit with the clock long-term stability specifications.

Note also that advanced engineering and integration of such a clock setup should allow to reduce greatly environmental effects such as temperature effects and should really help to improve the mid and long-term stability of high-performance CPT clocks. We recently observed in the lab that such

efforts are about crucial to demonstrate state-of-the art mid- and long-term frequency stabilities in microcell-based CPT clocks.
All these studies will be performed in a near future with the CPT clock in FEMTO-ST.

Once mid-/ long-term stabilities at the level of 10^{-14} at 1 day integration time will have been demonstrated with such vapor cell CPT clocks, we believe that such a clock technology, with high potential for integration and simplicity, could be attractive candidates for industrial applications. Next efforts will be later focused on the development of next-generation ultra-compact microwave or optical atomic clocks, using cold-atom or trapped-ion technologies. This approach has been recently proposed in the FEMTO-ST by C. Lacroûte, aiming to develop a compact single-Yb+ ion optical clock.

Appendix A

Dual-frequency Doppler-free Spectroscopy

A.1 Introduction

In section 3.4, we described our laser frequency stabilization set-up using Doppler-free spectroscopy in Cs vapor cells using a dual-frequency laser system tuned on the Cs D_1 line. In the dual-frequency configuration, two different transitions are involved in the single saturated absorption scheme ($|F=3\rangle \rightarrow |F'=4\rangle$ and $|F=4\rangle \rightarrow |F'=4\rangle$) where F (F') are the hyperfine (HF) quantum numbers of the ground (excited) states, respectively. In this configuration, using counter-propagating beams with crossed linear polarizations, an original sign-reversal of the dip and large increase in Doppler-free atomic absorption were observed. This high-contrast resonance allowed to demonstrate a relevant improvement of the laser frequency stabilization compared to a standard single-frequency saturated absorption scheme setup. In this study, the amplitude of the central spike was very high relatively to the Doppler background and much higher than those observed earlier for such kind of signals in the literature [168–170, 267–270]. In section 3.4, the dip reversal and enhanced absorption in the dual-frequency regime was briefly explained by the existence of dark states canceling each other for incident and reflected beams for atoms of null velocity. The dark states are non-coupled (NC) to the light and are induced by the coherent population trapping phenomenon [123] when a common excited state is shared between two optical transitions. Nevertheless, no extensive theoretical explanations were reported and only a few specific optical configurations were investigated.
Supported by E. de Clercq (LNE-SYRTE, Paris) and D. Brazhnikov (IPL, Novosibirsk), this appendix aims to fill this gap and to report a detailed theoretical and experimental investigation on Cs D_1 line Doppler-free spectroscopy with a dual-frequency laser field in a wide variety of experimental configurations. Subsections A.2 and A.3 reports a wide variety of experimental results obtained using a single laser source-based experimental setup. Tests are performed in the single-frequency and dual-frequency regimes. The shape of Doppler-free absorption profiles is studied under various configurations, investigating the impact of polarization conditions, static magnetic field, Raman detuning and involved Cs D_1 line transitions. In the dual-frequency regime, the detection of CPT resonances under appropriate conditions in the bottom of the enhanced-absorption reversed spike is clearly reported. Subsection A.8 describes the theoretical formalism, based on the density matrix approach, of main processes involved in the reported experiments. A three-level atomic Λ-scheme is proposed to understand the physical nature of spectra observed under various conditions. Three main nonlinear optical effects are identified to contribute potentially to the formation of the central absorption spike. They are: coherent population trapping between levels of the ground-state hyperfine splitting (HFS-CPT), CPT between Zeeman sublevels in each ground-state HF level (Zeeman-CPT) and optical pumping effects. The complementary action of these different effects can lead to a significant increase of the contrast of the nonlinear resonance. A discussion is reported in the end of the manuscript to provide a clear and rigorous link between experimental tests and the theoretical section, highlighting for main experimental figures which of these three processes dominantly contribute to the experimental observation. The experimental set-up is the same as described in subsection 3.4.2 (see Fig. 3.18).

A.2 Single frequency regime: Zeeman CPT

In this subection, the microwave power driving the EOM is turned off. The usual single laser frequency Doppler-free spectroscopy is performed. Here and in the following, the optical transitions will be denoted only by the HF numbers $F - F'$ of the involved levels. Figures A.1a and A.1b show the 4-4' and 4-3' transitions for counter-propagating parallel or crossed polarizations respectively, with two different static magnetic field values of 0 or 490 mG.

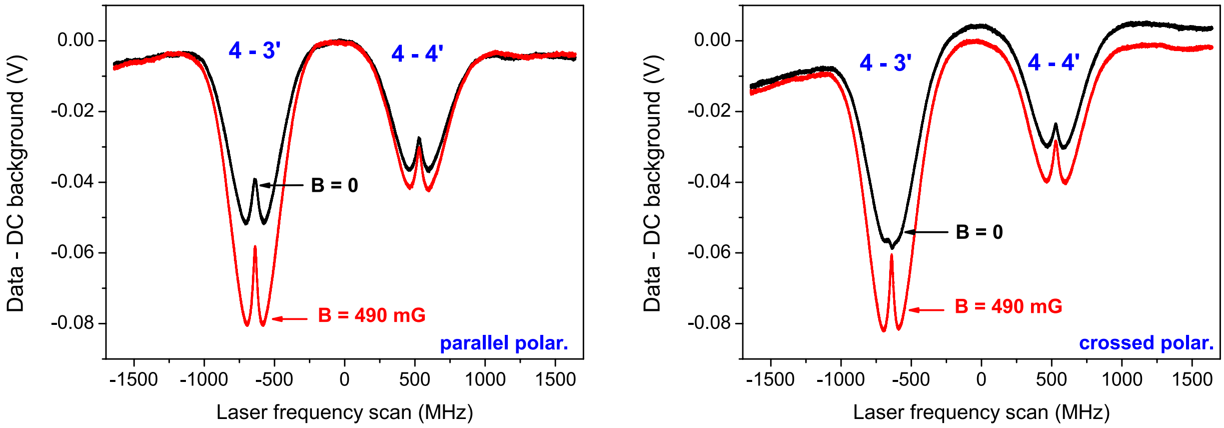

(a)

(b)

Figure A.1: Absorption profiles in the single-frequency laser regime. The laser power incident in the cell is 200 µW. (a): Parallel linear polarizations, (b): Crossed linearly polarized beams are used. For (a) and (b), the static magnetic field is 0 or 490 mG. For (b), an offset of 5 mV is added to the data for $B = 0$ in order to distinguish correctly the orientation of the dip. The frequency axis origin is arbitrarily chosen.

For parallel polarizations, the usual Doppler-free dip is observed. The presence of a static magnetic field tends to increase the depth of the Doppler-broadened absorption profile for the 4-3' transition. This is also observed on the 4-4' transition but with a reduced strength. For orthogonally polarized counter-propagating beams, at null magnetic field, we clearly observe that the 4-3' dip is cancelled or even slightly reversed. Note that at "high" magnetic field, there is no significant difference between absorption profiles of both polarization schemes. This behavior will be theoretically explained in section A.10. Briefly, at low magnetic field, a linearly polarized wave, traveling along the quantization axis $\hat{z}$, pumps atoms in a state superposition of m_F Zeeman sublevels, such as Δm_F, the difference of m_F, is even. These states, so-called “dark” or (NC) states [175], are uncoupled from light, explaining the low absorption. This is the CPT phenomenon.

When the magnetic field strength increases, the Zeeman sublevels of the ground state are frequency-split and become out of the two-photon resonance. The creation of dark states does not occur for any one-photon detuning δ and the transparency of the vapor cell decreases. This explains why the Doppler absorption profiles of the 4-3' as well as 4-4' transitions are shifted down when the magnetic field is on (compare black and red curves in Fig. A.1). This effect is lower on the 4-4' transition for two main reasons. Firstly, the 4-4' transition probability is weaker than for the 4-3' transition (the ratio between both spectral line strengths is 7/5 in favor of the 4-3' transition). Secondly, the branching ratio for the 4-4' transition is smaller than for the 4-3'. The latter leads to a considerable optical pumping of atoms to the non-resonant ground level F=3 when the 4-4' transition is being excited.

It should be also noted that the central resonance structure is very sensitive to the light waves polarizations but also to the branching ratio of the certain atomic transition (these features will be considered further in the theoretical section). In particular, one can observe an increase of the transparency at the center of the resonance for parallel light polarizations for the 4-3' transition (Fig.

A.1a, left black resonance) and a slight increase of absorption under the crossed polarizations (Fig. A.1b, left black resonance). At the same time, the central resonance for the weak 4-4' transition (right black resonances in Fig. A.1a and A.1b) is almost insensitive to the light polarizations and always appears as a peak in transparency. At optical resonance, at low magnetic field, only the atoms of axial velocity close to zero can absorb the light field. These atoms are resonant with both travelling and counter-propagating waves. As explained in section A.10, in the parallel polarization scheme, dark states are common to both fields and no change occurs: the regular saturated absorption dip is observed. On the contrary, in the case of crossed polarizations, the respective dark states are mutually orthogonal and cancel each other (see section A.10). In this case, the absorption increases, counterbalancing the regular dip.
The last interpretation is sustained by transmission curves as a function of the magnetic field. We have recorded absorption spectra (4-4' and 4-3' transitions) versus the static magnetic field. Parallel or orthogonally linearly polarized counter-propagating beams were tested. The total laser power incident in the cell is 200 µW for each configuration test. The solenoid current direction was changed to apply "negative-sign" magnetic fields. The reported spectra represent the regular magneto-optical Hanle resonances observed under counter-propagating light waves [171].

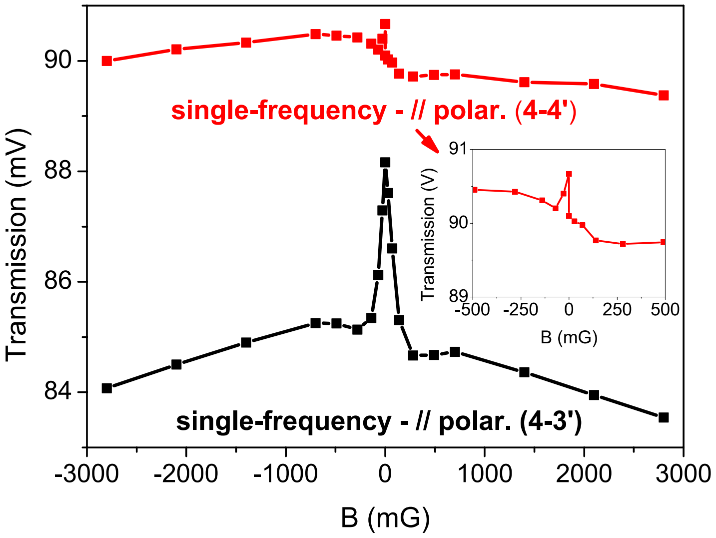

Figure A.2: Lorentzian dip transmission peak value (for 4-4' and 4-3' transitions) versus the magnetic field in the single-frequency regime and parallel linear polarizations. The figure inset is a zoom of the 4-4' transition case for magnetic field values ranging from −500 to 500 mG.

Figure A.2 shows, for parallel-polarization counter-propagating beams, the transmission signal when the laser frequency is tuned on the 4-4' or 4-3' transition for different values of the static magnetic field B. The maximum transmission level of the transitions' dip is increased around the null magnetic field value. As explained later in section A.10, this resonance peak is due to the existence of atoms in dark states which vanish at higher magnetic field strength. The weakness of the transition 4-4' explains why the amplitude and linewidth of the central peak is smaller for this transition. The openness of the transition 4-4' contributes also to reduce the amplitude of the central peak compared to the 4-3'. The background resonance (pedestal of the central narrow peak) is due to the velocity-selective saturation effect which regularly takes place in a gas of atoms under interaction with resonant light waves. This resonance structure can be attributed to the regular saturated-absorption resonance whose width is of the order of 10 G. Increasing more the scanning window (up to 200-250 G) should allow to observe an outer wider profile (not shown in the figure), the Doppler profile, with a width equal to several hundreds of Gauss, resulting from the Maxwellian velocity distribution and peculiarities of the optical pumping process.

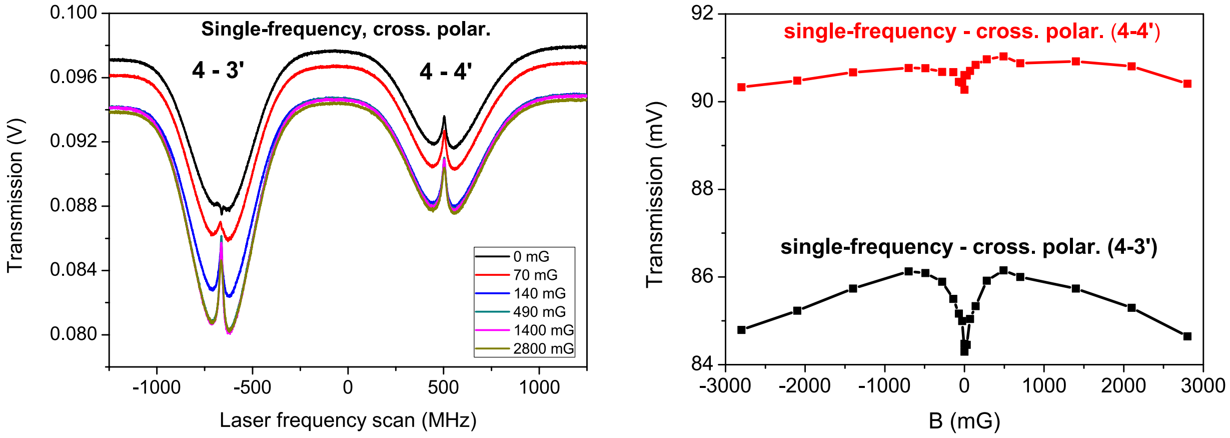

(a) (b)

Figure A.3: (a): Absorption spectra (4-3' and 4-4' transitions) for several magnetic field values in the single-frequency regime and crossed linear polarizations. An offset of 3 mV and2 mV was added to experimental data for $B = 0$ and $B = 70$ mG cases, respectively. This helps to distinguish well the dip sign for each case. The frequency axis origin is arbitrarily chosen. (b): From (a), Lorentzian dip transmission peak value (for 4-3' and 4-4' transitions) versus the magnetic field.

We did similar tests with crossed linear polarizations. Recorded absorption spectra for several values of the static magnetic field are reported in Fig. A.3a. Figure A.3b resumes, for crossed polarizations, the same experiment than the one reported on Fig. A.2 for parallel polarizations. The decrease of transmission observed at null magnetic field for both transitions is explained by the absence of a common dark state to both counter-propagating waves. The dark states built by a light wave are destroyed by the reflected wave. The number of absorbed photons is increased (increase of absorption), counterbalancing the saturated dip. With increasing B values, most of the CPT resonances become out of resonance. The usual saturated absorption scheme is observed again and the absorption peak becomes a regular saturated dip (see Fig. A.1). Here again, the effect is reduced for the 4-4' transition. In this case, the decrease of transmission at null magnetic field value in Fig. A.3b is difficult to observe. This situation could be changed significantly if an additional resonant laser radiation acting on the 3-4' transition was used as a repumper for atoms. This kind of situation can be realized in the dual-frequency regime and will be discussed later in details.

Using a repumping radiation, one can expect that both 4-3' and 4-4' transitions will exhibit a noticeable narrow dip at the center of transmission curves. Nevertheless, this additional coherent radiation in the dual-frequency regime does not act only as a repumping field. Indeed, if we have two mutually coherent waves driving adjacent optical transitions (for instance, 3-4' and 4-4'), other types of dark states can be created, involving magnetic sublevels of different hyperfine levels of the ground state $6^2S_{1/2}$. These dark states can also lead to observation of a high-contrast absorption peak at the center or the profile, as well as CPT states involving magnetic sublevels of one single hyperfine level. Corresponding details will be considered in the theory section.

A.3 Dual-frequency regime: Zeeman and hyperfine HFS-CPT

A.4 Basic approach

In this section, the EOM is driven at half the ground state splitting $\nu_g/2$. A dual-frequency Doppler-free spectroscopy is performed. In a first approach, Figs. A.4a and A.4b compare typical Doppler-free spectra observed in the Cs cell at null magnetic field in respective cases where a single-frequency laser field (parallel linear polarizations) or a dual-frequency laser field (crossed linear polarizations) is used.

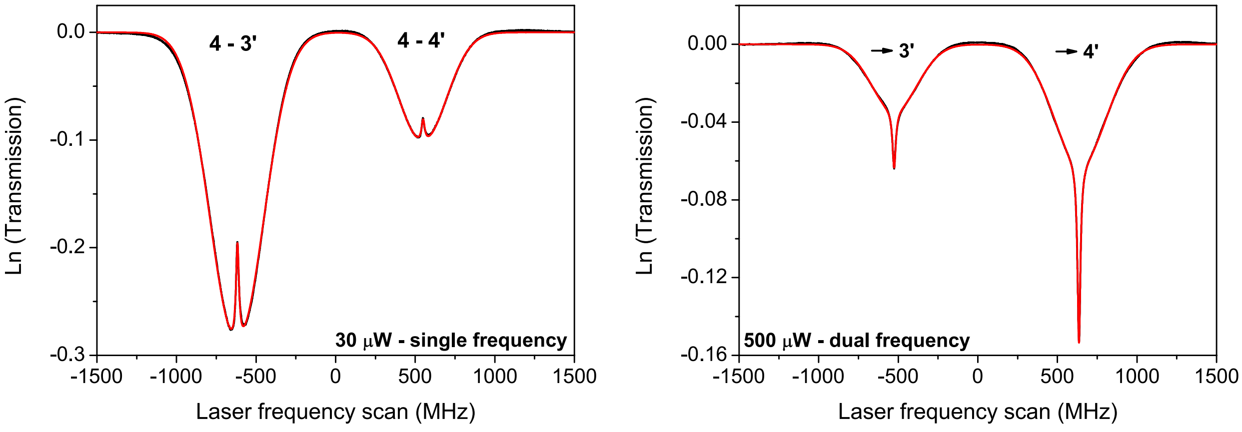

(a) (b)

Figure A.4: Doppler-free spectra. (a): single-frequency (usual saturated absorption spectroscopy), parallel case, B=0 (b): dual-frequency laser field (a single-modulated DFB laser source), perpendicular case, B=0. For (a), the total laser power is 30 µW. For (b), it is 500 µW. Both curves are fitted by the sum of Gaussian Doppler-broadened profiles and narrow Doppler-free Lorentzian dips. The black lines are the experimental data. The red lines are the fitting curves.

For the dual-frequency case, transitions are only labelled by F' the HF number of the common excited state.
In the single frequency regime, using parallel polarizations, the usual narrow Lamb dip, with Lorentzian profile, appears in the bottom of both Doppler-broadened absorption gaussian-profile lines. With crossed polarizations, the dip is totally vanished in the bottom of the 4-3' transition as reported above on A.1. In the dual-frequency regime, with crossed polarizations, a significant sign-reversal of the dip and large increase in Doppler-free atomic absorption is observed, especially at high laser power. As in the previous section, Zeeman coherences are built but now in each HF level. Moreover, microwave hyperfine coherences are also built as reported in section A.9. At resonance (null detuning of both optical transitions), atoms of null axial velocity are resonant with both counter-propagating beams. In the crossed polarization case, Zeeman CPT states built by a beam are destroyed by the reversed beam, as the HFS-CPT states, leading to a Doppler-free enhancement of the absorption. This observation is in good agreement with theoretical explanations reported in section A.9. In section 3.4, we studied the FWHM, signal (amplitude) and amplitude/FWHM ratio of the Doppler-free lorentzian dip versus the laser power. We observed that the power broadening of the one-frequency dip is larger than in the dual-frequency case. Simultaneously, the amplitude of the dip is dramatically increased in the dual-frequency case, especially when the F'=4 excited state is connected. In the single-frequency case, the atomic system is an open system, causing the atoms to be pumped into the other hyperfine ground state and leading to a higher effective saturation parameter. At the opposite, in the dual-frequency regime, the atomic system is closed, avoiding the loss of atoms. In the latter regime, a significant result is the important increase of the dip amplitude with laser power, particularly for transitions connecting the F' = 4 excited level. These aspects were exploited in our CPT clock to demonstrate a significantly improved laser frequency stabilization using the dual-frequency regime.

A.5 Impact of the static magnetic field

Figure A.5a shows the transitions to 3' and 4' excited states, in dual-frequency regime, with orthogonally polarized counter-propagating beams, for different values of the static magnetic field. We observe that the dip is reversed at null magnetic field. Increasing the magnetic field, the dip is progressively

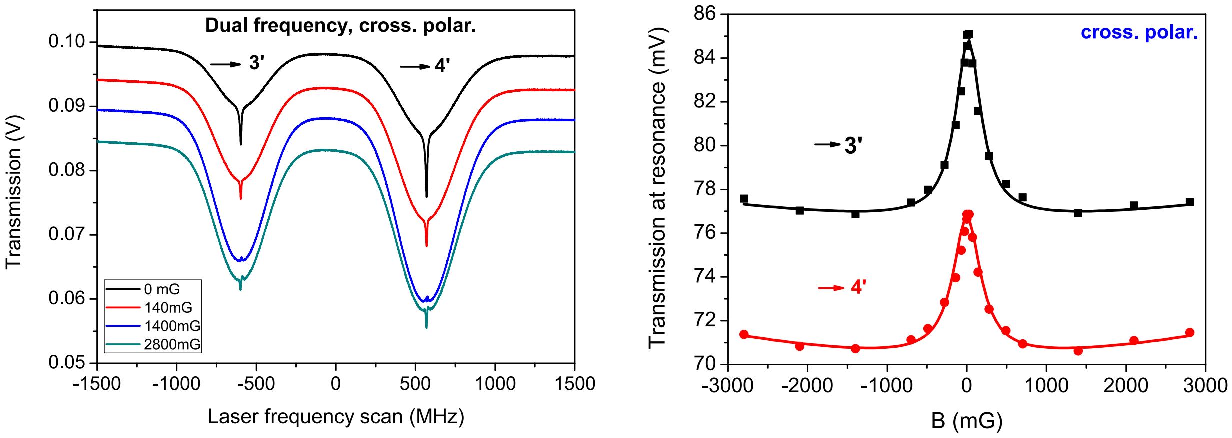

(a)

(b)

Figure A.5: (a): Doppler-free spectra in the dual-frequency regime with crossed linear polarizations for several values of the static magnetic field. For clarity of the figure, an offset of $-50\,\text{mV}$, $-100\,\text{mV}$ and $-150\,\text{mV}$ was added to the data for $B = 140$, 1400 and 2800 mG cases respectively. (b): From data shown in (a), transmission peak value of the Doppler-free Lorentzian dip versus the static magnetic field (for transitions to 3' or 4' excited states). The total laser power is 187 µW. Experimental data are fitted by a sum of two Lorentzian functions with opposite signs.

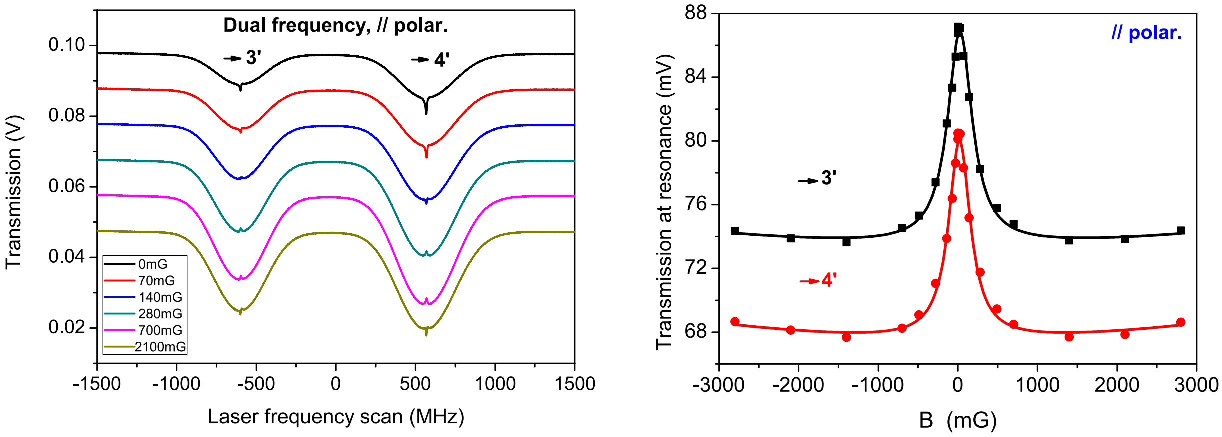

(a)

(b)

Figure A.6: (a): Doppler-free spectra in the dual frequency regime with parallel linear polarizations for several values of the static magnetic field. For clarity of the figure, an offset of $-10\,\text{mVV}$, $-20\,\text{mV}$, $-30\,\text{mV}$, $-40\,\text{mV}$ and $-50\,\text{mV}$ was added to the data for $B = 70$, 140, 280, 700 and 2100 mG cases respectively. (b): From data shown in (a), transmission peak value of the Doppler-free Lorentzian dip versus the static magnetic field (for transitions to 3' or 4' excited states). The total laser power is 187 µW. Experimental data are fitted by a sum of two Lorentzian functions with opposite signs.

appearing as an increase of the transmitted light. For large magnetic fields, the dip becomes reversed again. Nevertheless, in terms of transmission at exact resonance, we observe a reduction of the transmission with increased magnetic field up to about 1 G and then again a very slight increase. The depth of the Doppler broadened profile is increased with the magnetic field, because of the suppression of CPT states (see section A.8).

Figure A.5b resumes, for transitions to 3' and 4' excited states, the transmission value at the summit of the Lorentzian dip versus the static magnetic field for crossed polarizations conditions. For both transitions, experimental data are fitted by two Lorentzian functions with opposite signs. The central transmission peak is the Hanle resonance due to the creation of the Zeeman and HFS coherences. This resonance can be significantly narrower than the homogeneous linewidth. The wide background dip is the manifestation of saturation and optical pumping effects. When the level $F' = 3$ is the shared level, the FWHM of the central peak is about 390 mG. This magnetic field corresponds to a Raman detuning for ($\Delta m_F = 2$) Zeeman coherences of about 272 kHz. The Raman detuning δ_R is equal to the frequency difference between both components of the laser beam and the splitting of both ground-state sublevels involved. For the 4' transition, the FWHM of the central Lorentzian function is about 420 mG, yielding a Raman detuning for ($\Delta m_F = 2$) Zeeman coherences of about 294 kHz. As reported in the next section, we were able to detect CPT resonances in the bottom of enhanced absorption dips by scanning the microwave frequency driving the EOM around $\nu_g/2$. At null magnetic field and null optical detuning (see black curve of Fig. A.7), working with the 4' excited state, the detected CPT resonance exhibits a full-width at half maximum of about 382 kHz, a value comparable to the value of 294 kHz extracted from Fig. A.5b, taking into account the large uncertainty on the fit parameters due to the little number of points delimiting the broad Lorentzian curve.

We performed a similar study in the dual-frequency regime using counter-propagating linear parallel polarizations. Figures A.6a and A.6b resume these results. As shown on Fig. A.6a, the depth of the Doppler-broadened Gaussian line is enhanced with increased static magnetic field up to about 1.5 G. The dip is first reversed at low magnetic field, then regular for magnetic field values up to about 1 G and reversed again after. For parallel polarizations, at null magnetic field and if only Zeeman CPT was involved, we expected the dip to be regular (increased transmission). This behaviour was observed experimentally at low laser power. At higher laser power (as in Fig. A.6a), the Doppler-free dip was experimentally observed to be reversed (increased absorption) at null magnetic field. The change of orientation of the dip with some experimental conditions (such as the laser power here, or the magnetic field) is not so surprising. Indeed, it is important to note again that the Doppler-free dip observed in the center of the absorption profile results from the competition of Zeeman-CPT states (see section A.10) and HFS-CPT states (see section A.9). Thus, the main orientation of the dip will result in real experimental conditions depending on respective strengths and sum of these contributions. In Fig. A.6b, the fit of the central Lorentzian profile yields a Raman detuning for ($\Delta m_F = 2$) Zeeman coherences of about 261 and 231 kHz for 3' and 4' connected states, respectively.

A.6 Coherent population trapping spectroscopy in the reversed dip

We have performed microwave hyperfine CPT spectroscopy in the bottom of the reversed dip in order to demonstrate the HFS-CPT resonances. Tests were performed using the transition to the 4' excited state. For this purpose, the laser frequency is tuned either on the extremum of the reversed dip (null optical detuning, $\delta = 0$) or is slightly shifted from optical resonance ($\delta \neq 0$). More precisely, the laser carrier frequency ν_L (before the EOPM) is tuned between the middle of the ground-state HFS and the F'=4 level. The optical detuning is then defined as $\delta = \nu_L - \frac{\nu_{4'3}+\nu_{4'4}}{2}$, with ν_{ji} the frequency of the optical transition $F = i \rightarrow F' = j$. For these different laser frequency detuning operation points, the laser is not frequency-stabilized and the microwave signal that drives the EOM is swept around $\nu_g/2$. These tests were performed in different configurations including null or fixed values of the static magnetic field in crossed polarizations.

A typical spectrum detected in the bottom of the reversed dip at null magnetic field is shown in Fig. A.7 for crossed polarizations. In this experiment, the laser power is 187 µW. Note also that in this test, the beam splitter (BS) cube of Fig. 3.18 was replaced by a polarizing beam splitter cube. Consequently, the laser power interacting with atoms in the cell is the same but the laser power detected by the photodiode (i.e. the photodiode output voltage) is about two times higher than in Fig. A.5a.

We observe that the amplitude of the CPT resonance is considerably reduced under the exact optical resonance condition ($\delta = 0$). When the one-photon detuning is sufficiently far from zero ($\delta \gg \gamma$,

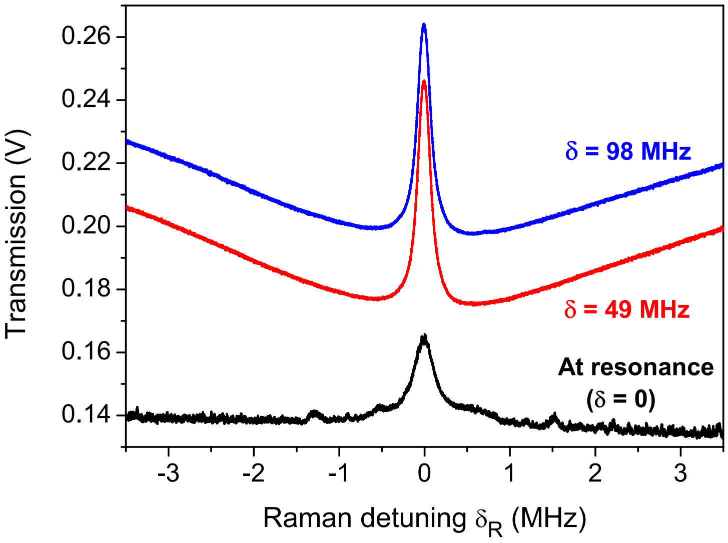

Figure A.7: CPT spectroscopy in the reversed dip for several values of the optical detuning (δ = 0, 49 and 98 MHz). The static magnetic field is null. Crossed polarizations are used. The laser power is 187 µW. For the black curve ($\delta = 0$), the central CPT peak can be fitted by a Lorentzian function with a FWHM of 382 kHz.

with γ the half natural linewidth of the optical transition, about 2.3 MHz for the Cs D_1 line), we detect in Fig. A.7 transparency peaks with a large amplitude. The amplitude of these peaks is first increased with increase of the optical detuning and reduced again if the optical detuning is further increased. The behavior of the resonance curve is quite clear. For $\delta \gg \gamma$, the counter-propagating laser beams are resonant for atoms of two separate velocity groups having axial velocities $\nu = -2\pi\delta/k$ and $\nu = +2\pi\delta/k$ (≈ 40 m/s for $\delta = 49$ MHz). Atoms in each of these two groups are optically pumped into Zeeman and HFS dark states. When the Raman detuning δ_R is not equal to zero (the microwave synthesizer frequency differs from $\nu_g/2$), the HFS-CPT effect is destroyed and the absorption of the cell significantly increases. This explains the observation of narrow central resonances in the cell transmission depicted in Fig. A.7. Under the condition $\delta = 0$ (optical resonance), two counter-propagating light beams drive the same atoms moving almost orthogonally to the wave vectors. The fact that waves exhibit almost equal amplitudes ($E_1 \approx E_2$) and crossed linear polarizations leads to the absence of the dark state on the level $F = 4$ and Zeeman-CPT does not take place. Therefore, absorption of the light field is enhanced at exact optical resonance (compare black and red curves on Fig. A.7 at $\delta_R = 0$).

As it will be shown in the theory section, HFS dark states can be produced by the two counter-propagating beams in some regions of the cell and can be suppressed in other ones, whatever the polarizations. However, when δ_R is far from the two-photon resonance, HFS dark states cannot be produced in the cell. This explains the observation of narrow CPT resonance in the center of the black curve of Fig. A.7. We note that the amplitude of CPT resonances in the case of parallelly polarized counter-propagating beams was measured to be comparable for $\delta = 0$ and $\delta \gg \gamma$ regimes. This is the manifestation of the HFS-CPT and Zeeman-CPT effects, which occur for the resonant velocity groups $\nu = \pm 2\pi\delta/k$ (at $\delta \gg \gamma$) as well as for the group $\nu \approx 0$ ($\delta = 0$).

An additional experiment similar to the one described just above was performed by applying a static magnetic field. Corresponding spectra are reported in Fig. A.8 where crossed polarizations are used. Again, at null optical detuning, the CPT resonance is about not present. At non-null optical detuning, the Zeeman spectrum is clearly visible. The seven peaks observed correspond to two-photon transitions ($\Delta F = 1, \Delta m_F = \pm 2$) involving Zeeman sublevels of different hyperfine ground-state levels $F = 3$ and $F = 4$. We observe that the central transition is narrower than neighboring transitions. This is due to the fact that the magnetic sensitivity of Λ-schemes involved in the central transition is

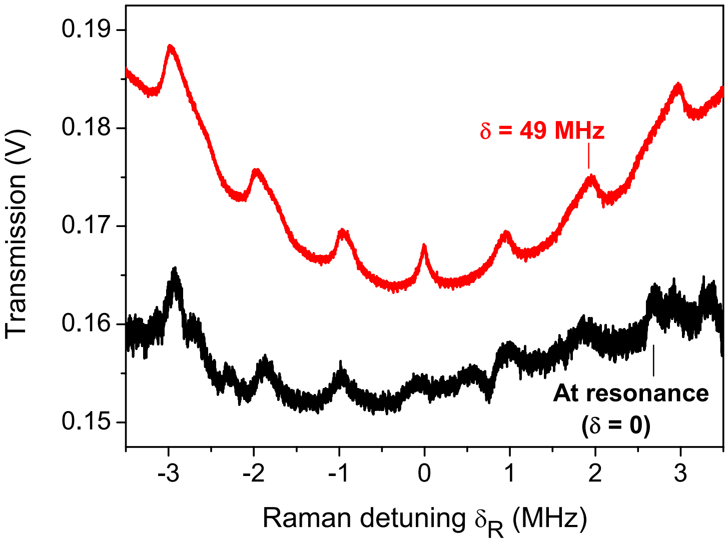

Figure A.8: CPT spectroscopy in the reversed dip for several values of the optical detuning ($\delta = 0.49\,\mathrm{MHz}$) with application of a static magnetic field ($B \sim 1.4\,\mathrm{G}$). Crossed polarizations are used.

lower than the one of Λ-schemes involved in adjacent transitions. Moreover, a residual inhomogeneity of the magnetic field in the cell could affect differently the widths of these resonances.
These experiences demonstrate clearly that at null magnetic field:

- HFS-CPT states are present at null Raman detuning.
- the CPT amplitude is reduced but non-null at optical resonance $\delta = 0$ in crossed polarizations.
- the CPT amplitude is higher for non-null optical detuning.
- HFS-CPT effects can contribute to the observation of the Doppler-free reversed dip in the dual-frequency regime.

A.7 Impact of the HFS-CPT states

The goal of this experiment was to discriminate the effects of Zeeman coherences and HFS coherences on the dip reversal. HFS coherences are not created when both optical sidebands excite two optical transitions without any common excited state, or are nearly cancelled for large Raman detuning, while Zeeman coherences are still present. Here, the MZ EOM is driven by a commercial synthesizer (Rohde-Schwarz SMB100A). The cell is protected by a magnetic shielding and no static magnetic field is applied. Data acquisition is performed as a function of the laser frequency scan, for orthogonally polarized or parallely polarized counter-propagating beams.
Figures A.9a, A.9b, A.9c and A.9d resume measurements performed in different configurations. Each of these figures is obtained for a given Raman detuning value and present two spectra obtained in respective cases of crossed or parallel polarizations. Figures A.9a and A.9b report measurements performed with large Raman detunings (the EOM is driven at $\nu_g/2 \pm \nu_e/2$, with $\nu_e = 1.167$ GHz, the HF splitting of the excited state). For absorption profiles on the left and right sides of the figures, only one laser frequency is resonant with an atomic transition. In such a case a regular saturated absorption resonance (SAR) profile is observed, whose amplitude is reduced by optical pumping in the non-resonant HF ground-state level.
The transitions involved in the central resonance do not share any common excited state, both optical fields are at resonance but with two separate HF excited levels. In this configuration, Zeeman

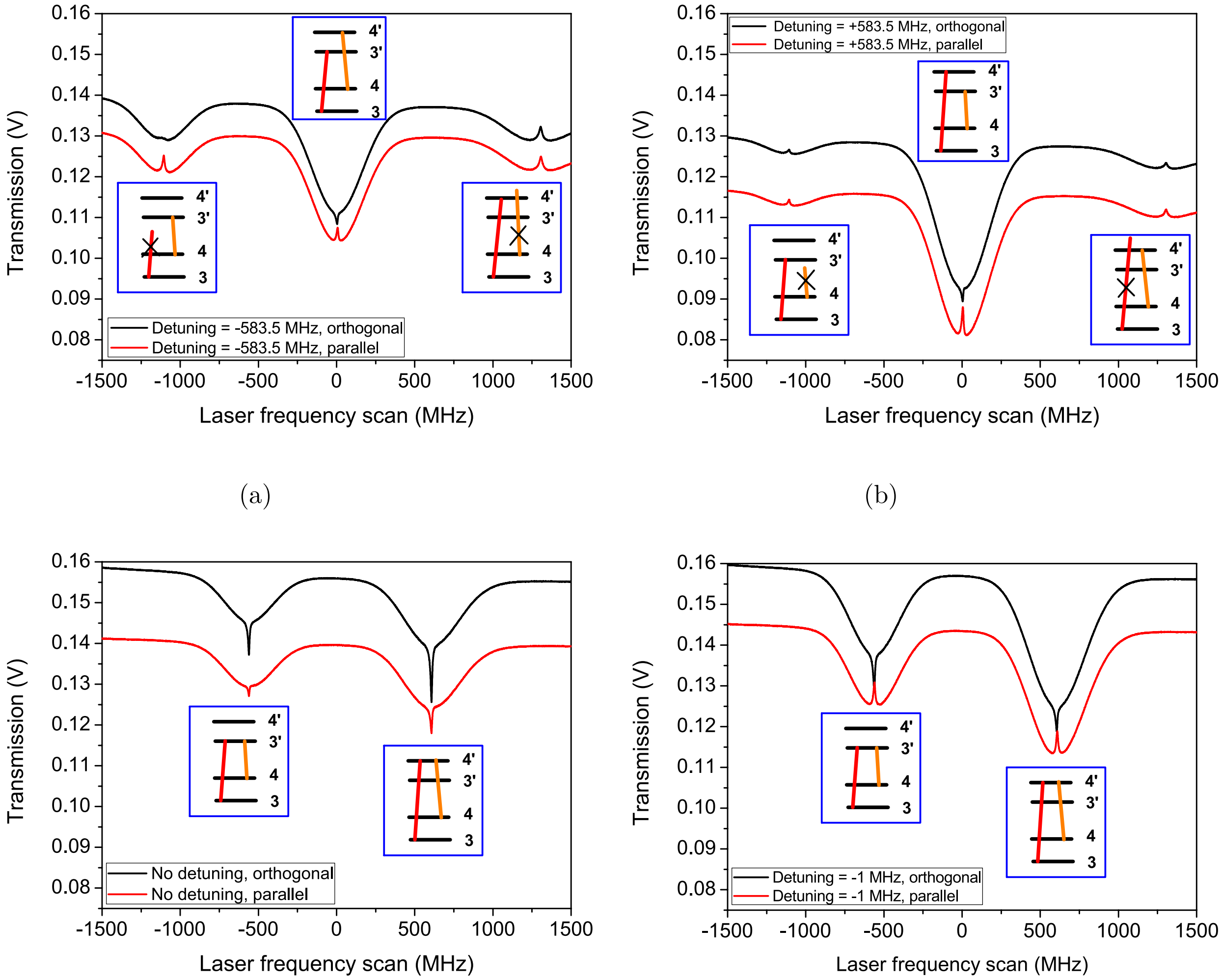

(a) (b)

(c) (d)

Figure A.9: Absorption spectra in the dual-frequency regime for several values of the microwave Raman detuning ((a): $-\nu_e/2$, (b): $+\nu_e/2$, (c): null Raman detuning, (a): $-1\,\text{MHz}$), in crossed or parallel polarization conditions. ν_e is the HF splitting of the excited state. The Raman detuning is null for a synthesizer frequency of $\nu_g/2$. All these figures are plotted with the same y-axis scale to allow the reader to compare the amplitude and background of absorption profiles obtained in respective cases. Insets are added in each figure to show energy transitions involved in each case. Curves obtained with parallel polarizations are always under those obtained with crossed polarized beams. This aspect is not relevant in this study. We observed that some optics were slightly sensitive to polarization. This was checked by removing the cell. In this case, a slight reduction of a few mV on the photodiode signal was observed when orthogonal polarizations were changed to parallelly polarized beams. An offset of 5 mV was added to data (orthogonal) from (a). An offset of 10 mV was added to data (orthogonal) from (b), (c) and (d). This was done to allow the reader to distinguish well the shape and orientation of the dips.

coherences can still be created between sublevels of the same HF level, but HFS coherences cannot. We observe a deeper Doppler profile in the bottom of which a Doppler-free dip is detected (reversed for crossed polarizations, regular for parallel polarizations). The larger Doppler profile is explained by the absence of optical pumping between HF levels of the ground state in this case. This dip is reversed with orthogonal polarizations because Zeeman dark states ($\Delta F = 0, \Delta m_F = 2$) created in each HF level by a travelling wave are destroyed by the counter-propagating wave at null optical detuning, i.e. when a group of atoms "sees" both waves at resonance together. This leads to an increase of the absorbed photon number. The dip is oriented to the top in the parallel polarization case because Zeeman dark states at $\delta = 0$ are common. There is no change at null optical detuning, the regular SAR spectrum is observed.

In both next figures, a common excited state is shared between optical transitions, at null Raman detuning, $\delta_R = 0$, in Fig. A.9c, or with $\delta_R = 1$ MHz in Fig. A.9d. Figure A.9c describes the case addressed in the previous sections. Here, HFS and Zeeman coherences are created together. We observe a modest Doppler profile while the Doppler-free dip is enhanced. The amplitude of the Doppler profile is reduced by CPT states created in the velocity groups for which the fields are at resonance. At optical resonance, in crossed polarizations, HFS and Zeeman dark states are cancelled and the absorption is significantly enhanced leading to the clear high-contrast central reversed dip. In Fig. A.9d, the HFS coherences are nearly canceled, because the Raman detuning is too high, leading to a deeper Doppler profile. With crossed polarizations the dip is still reversed but reduced, only induced by the cancellation of Zeeman coherences.

The effect of HFS coherences is highlighted by comparing Fig. A.9c and Fig. A.9d in the parallel polarization case. Without HFS coherences (Fig. A.9d) the dip is a regular SAR dip, as expected, since there is no increase of absorption by mutual destruction of the Zeeman dark states generated by co-polarized countrapropagating waves at optical resonance. On the contrary, the dip is reversed when HFS dark states are present (Fig. A.9c). This shows that the HFS dark states, or at least an important part of them, are destroyed at optical resonance, even for linear polarizations. At high laser power, this effect is larger than the regular dip which would be induced by Zeeman coherences. This will be explained in section A.9 by the phase shift of both running waves.

In summary, both Zeeman and HFS CPT lead to a reduced Doppler profile for both polarization cases. Zeeman CPT alone (see Fig. A.9a, A.9b, A.9d) leads to a regular SAR dip in parallel polarizations, and an inversed peak in crossed polarizations. HFS CPT reverses the regular dip in parallel polarizations, and increases the size of the absorption peak in crossed polararizations (see Fig. A.9c). These observations are in agreement with predictions of our simplified theoretical model, as discussed in section A.12.

A.8 Theoretical analysis

This theoretical section has been developed and performed by D. Brazhnikov (IPL, Novosibirsk). Full theoretical description of the high-contrast absorption spike observed in the dual-frequency regime (see Fig. A.4b), taking into account the real complex structure of atomic energy levels, light wave polarizations, various optical pumping and nonlinear coherent processes is a quite difficult task. Here, we propose a simplified spectroscopic model based on a three-level Λ-scheme that allows to understand main physical reasons underlying the formation of the high-contrast resonance spike. The scheme is shown on Fig. A.10. Despite its apparent simplicity, this scheme can explain the impact of the static magnetic field, the two-photon (Raman) detuning, light wave polarizations or mutual coherence between the frequency components of the light field observed in the experiments.

We focus here on analyzing the specific case where the highest spike amplitude is obtained. As seen on Fig. A.4b, it is realized when all light waves interact with the excited atomic state $F' = 4$. In general, three physical reasons at least can contribute to the central spike formation. In this section, we consider them separately, based on the Λ-scheme.

Let us first describe the density matrix formalism applied to our system. We assume that the Λ-scheme interacts with a dual-frequency laser field composed of two counter-propagating linearly polarized plane waves. The Cartesian coordinate system is oriented such that the polarization of the first dual-frequency wave (E_1) is directed along the x axis, while the related wave vectors $\mathbf{k_1}$ and $\mathbf{k_2}$ are parallel to the quantization axis z. Under this orientation of the system, linearly polarized light can be represented by two σ^+ and σ^- polarization components in the cyclic basis. If a real atomic transition is considered (taking into account energy levels degeneracy), these two σ components induce corresponding $\sigma^\pm$ optical transitions in the atom. Thus, if the linear polarization has an angle ϕ between the polarization direction and the x axis, the σ^- and σ^+ polarization components acquire additional phase shifts $\exp[\pm i\phi]$. Since we use a simplified spectroscopic model, instead of considering

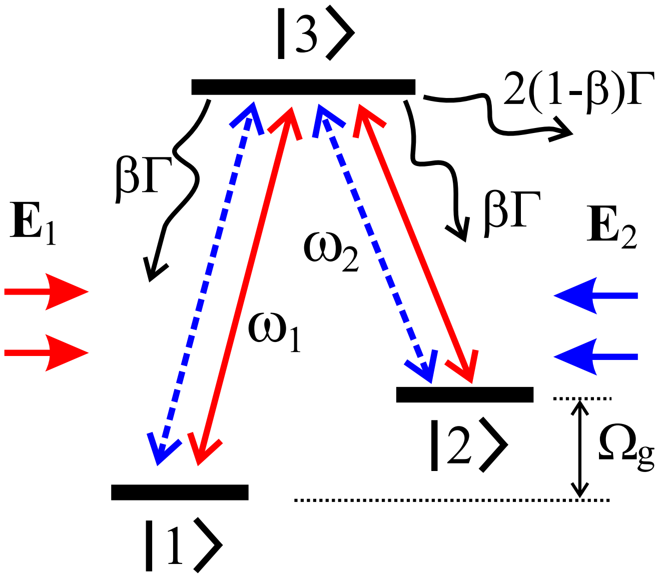

Figure A.10: Λ-scheme of atomic energy levels . Solid vertical arrows denote light-induced transitions by the waves with vectors $\mathbf{k_{1,2}}$, while dashed vertical arrows are attributed to the waves with $-\mathbf{k_{1,2}}$. Wavy black arrows denote spontaneous decay processes. Extracted from [271].

many magnetic sub-levels, the polarization orientation can be included into our model with the help of phase shifts $\exp[\pm i\phi]$ if we assume that $|1\rangle \rightarrow |3\rangle$ and $|2\rangle \rightarrow |3\rangle$ transitions of the Λ-scheme (see Fig. A.10) are induced by σ^+ and σ^- polarization components respectively. Following this, we come to the following expression for the light field:

$$E(z,t) = E_1\big[e^{-i(\omega_1 t - k_1 z)} + e^{-i(\omega_2 t - k_2 z)}\big] + \\ +E_2\big[e^{-i(\omega_1 t + k_1 z - \phi + \phi_1)} + e^{-i(\omega_2 t + k_2 z + \phi + \phi_2)}\big] + c.c. \tag{A.1}$$

We would like to emphasize that the light wave E_1 is travelling in the same direction than the z-axis and has two frequency components (ω_1 and ω_2), while E_2 is a counter-propagating wave having also the same frequency components. As seen from Eq. (A.1), we assume that both frequency components of each waves have equal real amplitudes (just for simplicity). The angle ϕ is the mutual angle between linear polarizations of counter-propagating waves. We will concentrate further on two principal cases: $\phi = 0$ and $\phi = \pi/2$. Since the field E_2 is formed by the reflection of the field E_1, it has a certain space phase shift (actually, two different shifts $\phi_{1,2}$ for each frequency component as the lengths of the wave vectors $\mathbf{k_1}$ and $\mathbf{k_2}$ are different). We would like to note that all frequency parameters in the theory section are measured in radians per second. For example, for optical frequencies of the laser beams from Eq. (A.1) we have $\omega_{1,2} = 2\pi\nu_{1,2}$. The acronym "*c.c.*" stands for the complex conjugate term.
In the case of a dilute gas, collisions between atoms can be neglected. Moreover, we do not take into account linear momentum exchange between an atom and a photon, leading to the recoil effect. Thus, the problem can be considered with the help of a one-atom density matrix in Wigner representation $\widehat{\rho}(z,\upsilon,t)$ according to the equation [166]:

$$\frac{d\widehat{\rho}}{dt} = -\frac{i}{\hbar}\Big[(\widehat{H}_0 + \widehat{V}), \widehat{\rho}\Big] + \widehat{\mathcal{R}}\{\widehat{\rho}\}\,. \tag{A.2}$$

Here $d/dt = \partial/\partial t + \upsilon\,\partial/\partial z$ with υ the projection of atom's velocity on the z axis.
The hamiltonian $\widehat{H}_0$ of a free atom in the basis of eigenfunctions has a diagonal form and can be written by means of Dirac's bra- and ket-vectors:

$$\widehat{H}_0 = \sum_{n=1}^{3} \mathcal{E}_n |n\rangle\langle n|\,, \tag{A.3}$$

where $\mathcal{E}_n$ are energies of the corresponding levels (see Fig. A.10). Further transition frequencies of the Λ-scheme arms will be noted $\omega_{mn} = (\mathcal{E}_m - \mathcal{E}_n)/\hbar$, with $\hbar = h/(2\pi)$, h being the Planck constant. Taking into account Eq. (A.1), nonzero matrix elements of the interaction operator $\widehat{V}$ in the rotating-wave (RWA) and electro-dipole interaction approximations have the following forms:

$$\begin{aligned} V_{31} &= \langle 3|\widehat{V}|1\rangle = -\hbar e^{-i\omega_1 t}\big[\Omega_{R1}e^{ik_1 z} + \Omega_{R2}e^{-i(k_1 z+\phi_1)}\big]\,, \\ V_{32} &= -\hbar e^{-i\omega_2 t}\big[\Omega_{R1}e^{ik_1 z} + \Omega^*_{R2}e^{-i(k_2 z+\phi_2)}\big]\,, \end{aligned} \tag{A.4}$$

where $\Omega_{R1} = d\,E_1/\hbar$, $\Omega_{R2} = (d\,E_2/\hbar)e^{-i\phi}$ are the Rabi frequencies. We assume two arms of the Λ-scheme to have equal and real dipole moments d. Other nonzero matrix elements V_{13} and V_{23} can be obtained from the expressions (A.4) by conjugate transpose operations, because the interaction operator is Hermitian, $\widehat{V} = \widehat{V}^{\dagger}$.

All the relaxation processes are considered in the frame of the widely used relaxation constants approach. The explicit form for the relaxation operator $\widehat{\mathcal{R}}$ is:

$$\begin{aligned} \widehat{\mathcal{R}} = \quad & \Gamma\big[\beta\rho_{11}\widehat{P}_{11} + \beta\rho_{22}\widehat{P}_{22} - 2\rho_{33}\widehat{P}_{33}\big] + \\ & +\Gamma_{eg}\big[\rho_{31}\widehat{P}_{31} + \rho_{32}\widehat{P}_{32} + H.c.\big]\,, \end{aligned} \tag{A.5}$$

For convenience, we assume that the upper state spontaneously relaxes with the total rate 2Γ and $\Gamma_{eg} = \Gamma + G$ is the relaxation rate of optical coherences (see the text below) with G the time-of-flight relaxation rate attributed to the finite time of atom-field interaction ($G \sim \tau^{-1}$, where τ is the mean time of the atomic flight through the laser field area). The branching ratio β is assumed to be equal for both arms of the Λ-scheme. The system of levels can be considered open by taking $\beta < 1$. $\widehat{P}_{nm}$ in (A.5) are the projection operators defined as $\widehat{P}_{nm} = |n\rangle\langle m|$.

Non-diagonal matrix elements ρ_{31}, ρ_{32} and Hermitian conjugate ones $\rho_{13} = \rho^*_{31}$, $\rho_{23} = \rho^*_{32}$ are called optical coherences because they oscillate in time at optical frequencies $\omega_{1,2}$ and describe the atomic light-induced polarization. In general, these elements can be expanded in series of spatial harmonics. In particular, for ρ_{31} and ρ_{32} in RWA we have:

$$\begin{aligned} \rho_{31}(z,t) = e^{-i(\omega_1 t)} \sum_{n=-\infty}^{+\infty}\sum_{m=-\infty}^{+\infty} \rho_{31}^{(nm)}\, e^{i(nk_1+mk_2)z}\,, \\ \rho_{32}(z,t) = e^{-i(\omega_2 t)} \sum_{n=-\infty}^{+\infty}\sum_{m=-\infty}^{+\infty} \rho_{32}^{(nm)}\, e^{i(nk_1+mk_2)z}\,. \end{aligned} \tag{A.6}$$

In fact, we only take into account several harmonics from (A.6), which contribute to the following expansions for other density matrix elements:

$$\rho_{12}(z,t) \approx e^{i\Delta_{12}t}\big[\rho_{12}^{(+)}e^{ik_{12}z} + \rho_{12}^{(-)}e^{-ik_{12}z}\big] \tag{A.7}$$

with $\rho_{21} = \rho^*_{12}$, $\Delta_{12} = \omega_1 - \omega_2$, $k_{12} = k_1 - k_2$, and

$$\rho_{nn}(z) \approx \rho_{nn}^{(0)} + \rho_{nn}^{(+)}e^{2ik_{12}z} + \rho_{nn}^{(-)}e^{-2ik_{12}z}\,, \tag{A.8}$$

where n=1,2,3. As long as we focus on the steady state of the atom, all spatial harmonics of the density matrix elements in (A.6)-(A.8) are assumed to be independent on time t.

As one can see, the populations of atomic levels contain the terms $\rho_{nn}^{(0)}$, which are not dependent on the z-coordinate. These elements can be treated as the space-averaged values of level populations. For instance, if there is only one traveling single-frequency light wave E_1 resonant to the $|1\rangle \to |3\rangle$ transition (see Fig. A.10), the populations ρ_{11} and ρ_{33} will have only zero space harmonics $\rho_{11}^{(0)}$ and $\rho_{33}^{(0)}$. These populations acquire high-order harmonics, when additional light waves with different wave vectors are being injected into the cell. At the same time, we have another situation involving low-frequency coherences ρ_{12} and ρ_{21}. These matrix elements can be only produced by simultaneous action of two mutually coherent light beams with different wave vectors. Therefore, we have only space-dependent harmonics for the low-frequency coherences. An exception occurs when we consider the particular Λ-scheme with a degenerate ground state ($\mathcal{E}_1 = \mathcal{E}_2$). In such a case, two light components with $\mathbf{k_1} = \mathbf{k_2}$ produce coherences ρ_{12} and ρ_{21}, which do not depend on the z-coordinate. The last case is much easier to analyze theoretically (see section A.10).

Optical coherences described in (A.6) can be excluded from the system of equations (A.2). Then, the final system only includes level populations $\rho_{nn}^{(0,\pm)}$ and low-frequency coherences $\rho_{12}^{(\pm)}$, $\rho_{21}^{(\pm)}$. For shortness, we put the final system of equations in Appendix B.

In the experiments, the bichromatic light waves pass the cell in both directions (towards positive and negative z) before reaching the photo-detector. In this case, the absorbed power is proportional to the total fluorescence of the cell. On the other hand, the total fluorescence is proportional to the excited state population averaged over the z-coordinate and velocity distribution of atoms in the gas. Therefore, we analyze the following expression as a spectroscopic signal:

$$W(\Delta) = \langle \rho_{33}^{(0)} \rangle_{\upsilon} + \frac{2\sin(k_{12}L)}{k_{12}L} \mathrm{Re}\big[\langle \rho_{33}^{(+)} \rangle_{\upsilon} e^{ik_{12}L}\big]\,, \tag{A.9}$$

where L is the vapor cell length. The one-photon detuning $\Delta = \omega_1 - \omega_{31} = \omega_2 - \omega_{32}$ is assumed to be the same for both frequency components of the light field and also condition $\Delta = 0$ means that two counter-propagating waves are both in resonance with the atoms at rest. Angle brackets $\langle \dots \rangle_{\upsilon}$ stand for averaging over the Maxwellian velocity distribution such as:

$$\langle f(\upsilon) \rangle_{\upsilon} = \frac{1}{\sqrt{2\pi}\upsilon_0} \int\limits_{-\infty}^{+\infty} f(\upsilon) e^{-\upsilon^2/\upsilon_0^2}\, d\upsilon\,. \tag{A.10}$$

Here $\upsilon_0 = \sqrt{2k_B T/m_0}$ is the most probable thermal velocity of an atom with mass m_0 in a gas with temperature T (k_B is the Boltzmann constant).

We note that, for convenience, spectra extracted from calculations in the theoretical section will be reported in terms of absorption and not in transmission as performed in the experimental section.

A.9 Hyperfine frequency splitting (HFS)-CPT states

In this paragraph, we consider the case where the ground state sub-levels $|1\rangle$ and $|2\rangle$ arise from HF splitting of ground state of the atom. For ^{133}Cs atom, we have $|1\rangle \equiv |F=3\rangle$, $|2\rangle \equiv |F=4\rangle$ and $\Omega_{g,e} = 2\pi\nu_{g,e}$ are the frequency differences between hyperfine levels of the ground and excited states respectively. Magnetic sub-levels are not considered in this paragraph (see section A.10). Before presenting the results of numerical calculations, it is useful to understand the reason of the absorption spike formation on a qualitative level.

In a first approach, we consider the situation where the Raman detuning $\Delta_R = 2\pi\delta_R = 0$ and the one-photon frequency detuning Δ is much larger than the natural linewidth Γ. In this case, each of the dual-frequency fields E_1 and E_2 interacts resonantly with different velocity groups of atoms, as shown on Fig. A.11.

The field E_1 pumps atoms with velocity $-\upsilon$ into the non-coupled state $|\mathrm{NC}_1\rangle$ while the field E_2 pumps those of velocity $+\upsilon$ into the non-coupled state $|\mathrm{NC}_2\rangle$:

$$\begin{aligned} |\mathrm{NC}_1\rangle &= \frac{1}{\sqrt{2}}\big[|1\rangle - e^{ik_{12}z}|2\rangle\big]\,, \\ |\mathrm{NC}_2\rangle &= \frac{1}{\sqrt{2}}\big[|1\rangle - e^{-i(k_{12}z+\phi_{12}+2\phi)}|2\rangle\big]\,. \end{aligned} \tag{A.11}$$

In these non-coupled states, coherent population trapping occurs (see, for example, [123, 272]) and atoms do not absorb any energy from the resonant light field. This implies that absorption (fluorescence) of the vapor cell is low under the condition $\Delta \gg \Gamma$, explaining that atoms are in a so-called dark state. In general, these states are different for two resonant groups of atoms since they interact with different light fields (E_1 or E_2). It is also worth noting that the mutual angle ϕ between linear polarizations of the counter-propagating dual-frequency waves and the relative space phase shift ϕ_{12}

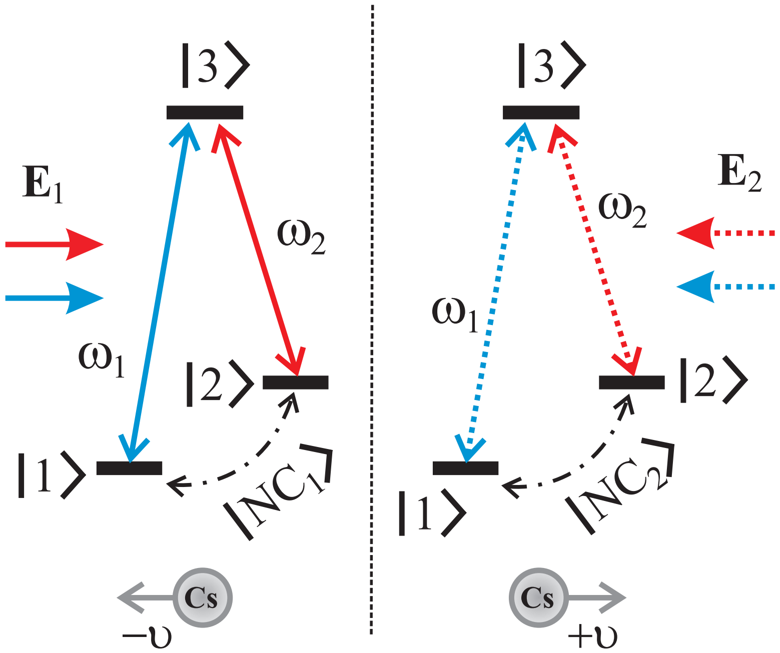

Figure A.11: Two Λ-schemes of atomic energy levels for two resonant groups of atoms. Notations are the same than in Fig. A.10. On this figure, we assume for simplicity $|k_1| \approx |k_2|$. However, in calculations, we took the difference into account. Extracted from [271].

are additive contributions to the non-coupled state $|\mathrm{NC}_2\rangle$ with $\theta = 2\phi + \phi_{12}$ (see the density matrix equations in Appendix B). It means that the cell absorption depends on θ, but not on these angles separately. In other words, by proper changing either ϕ_{12} or ϕ, we can get the same level of absorption. Now, we need to consider the situation where $\Delta \sim \Gamma$ and where the fields E_1 and E_2 start to interact with the same atoms. In this configuration, two principal cases should be analyzed:

1. $|\mathrm{NC}_1\rangle$ and $|\mathrm{NC}_2\rangle$ interfere destructively, i.e. $\langle \mathrm{NC}_1|\mathrm{NC}_2\rangle = 0$;
2. The "competition" between $|\mathrm{NC}_1\rangle$ and $|\mathrm{NC}_2\rangle$ does not destroy the CPT effect, $\langle \mathrm{NC}_1|\mathrm{NC}_2\rangle = 1$.

In the first case, atoms start to absorb intensively and scatter energy from the light field since they are not in the dark state anymore. From the expression (A.11), we can predict that it happens near the coordinates z_{max} satisfying the condition:

$$k_{12} z_{max} = \frac{\pi}{2} - \phi - \frac{\phi_{12}}{2} + \pi n \,, \tag{A.12}$$

with $n = 0, 1, \ldots$
The second condition (2) is satisfied when:

$$k_{12} z_{min} = \pi n - \phi - \frac{\phi_{12}}{2} \,. \tag{A.13}$$

We can conclude that the fluorescence of the cell is inhomogeneous in space. There are areas with intense fluorescence and areas with low fluorescence (see a sketch on Fig. A.12). These regions alternate with the period π/k_{12}:

$$\Delta z = \frac{\pi}{|k_{12}|} \,. \tag{A.14}$$

It is interesting to note that positions of maxima and minima of fluorescence depend on the phases ϕ, ϕ_{12} while the period Δz does not. This induces that for a sufficiently long cell, i.e. $L > \Delta z$, the level of total light-field absorption in the cell almost does not depend neither on the angle between

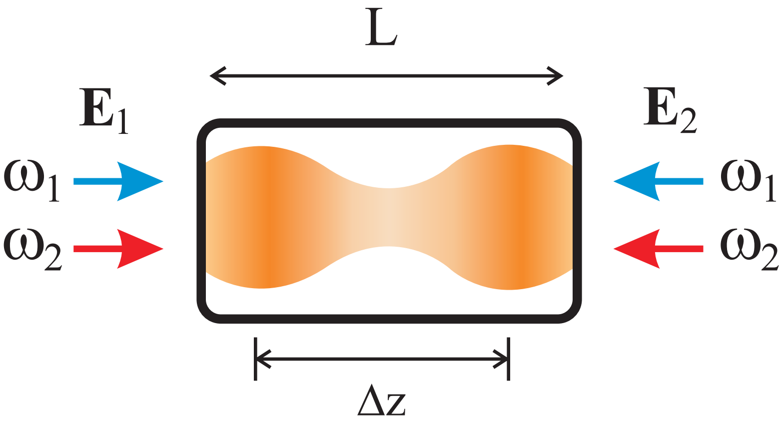

Figure A.12: Picture to demonstrate inhomogeneity of light fluorescence in a vapor cell. Extracted from [271].

the linear polarizations neither on the distance between the cell and the mirror "M" (which produces the field E_2, see Fig. 3.18). Otherwise, the fluorescence of the cell should be much more sensitive to the phases ϕ and ϕ_{12}, when $L \ll \Delta z$. In the particular case of ^{133}Cs, we obtain from Eq. (A.14) that $\Delta z \approx 1.6\,\text{cm}$. It should be noted that the qualitative analysis presented here and based on the non-coupled states formalism is similar to the one previously reported in [273]. In the latter reference, counter-propagating light waves with σ^+ and σ^- polarizations were considered.

Let us support the analysis described above by absorption profiles calculated in several different cases. These profiles have been obtained by solving the density matrix equations whose explicit form can be found in Appendix B. For our numerical calculations, we take slightly different Rabi frequencies of counter-propagating waves due to possible losses during the formation of the backward wave: $\Omega_{R1} = 1.5\,\Gamma$, $\Omega_{R2} = 1.3\,\Gamma$. The time-of-flight relaxation rate is $G = 5 \times 10^{-2}\,\Gamma$. The Doppler width is assumed to be $kv_0 = 94\,\Gamma$. All these values approximately correspond to the experimental conditions. The absorption signal is integrated over the cell length.

The typical resonance is shown on Fig. A.13. Its shape, if converted in transmission, is similar to the experimental one reported on Fig. A.4b. We see that the use of perpendicular polarizations allows to reach a better contrast of the central peak. Nevertheless, a similar result can be obtained assuming $\phi = 0$ and $\phi_{12} = \pi$ (according to Eqs. A.11).

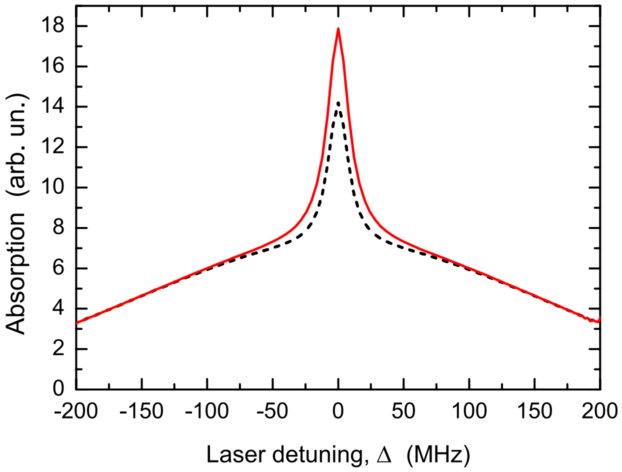

Figure A.13: Absorption of the cell as a function of the one-photon detuning. The red solid curve is obtained for perpendicular polarizations ($\phi = \pi/2$) while the black dashed line is obtained for parallel polarizations ($\phi = 0$). Other parameters are: $\Delta_R = 0$, $\beta = 1$, $L = 2$ cm, $\phi_{12} = 0$. Extracted from [271].

Figure A.14 shows the influence of the cell length on the strength of the central peak. In particular,

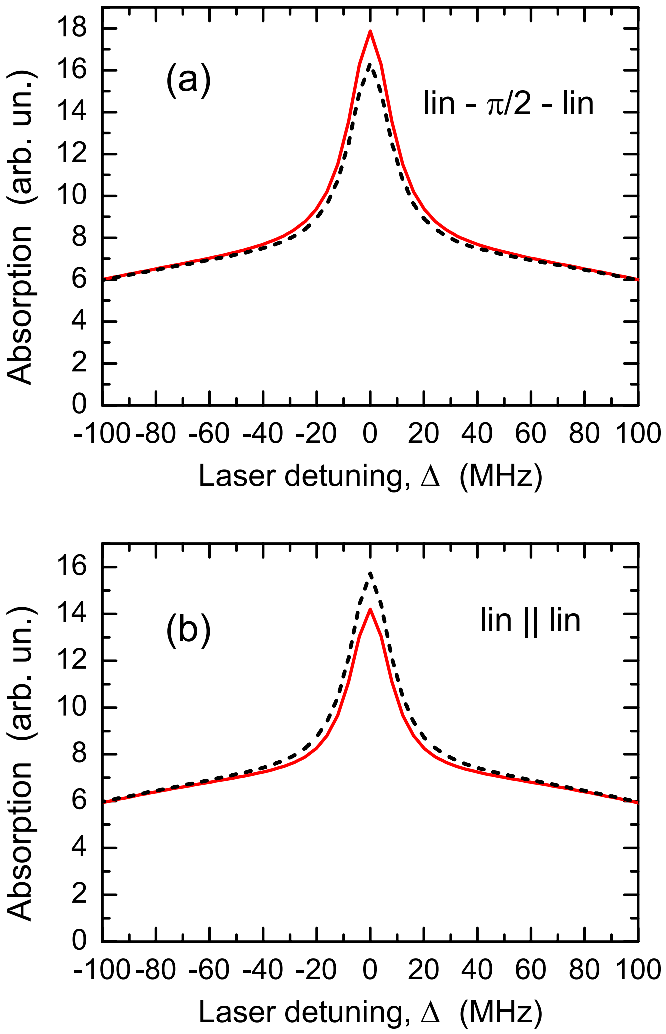

Figure A.14: Illustration of the cell length influence on the resonances in different polarization configurations: (a) perpendicular polarizations, (b) parallel polarizations. Solid red lines are obtained for a cell length $L = 2$ cm. Dashed black lines are obtained for $L = 5$ cm. Other parameters are: $\Delta_R = 0$, $\beta = 1$, $\phi_{12} = 0$. Extracted from [271].

if we take a long cell (compare black dashed curves on Figs A.14 (a) and A.14 (b)), one can see that there is almost no difference between parallel and orthogonal light-wave polarizations. At the same time, using a medium-length cell (as in our experiments, solid lines of Fig. A.14), the effect is sensitive to the light polarizations. Thus, the amplitudes are ≈ 10 on Fig. A.14 (a) and ≈ 6 on Fig. A.14 (b). Figure A.15 helps to understand this sensitivity by showing the influence of the total phase shift $\theta = 2\phi + \phi_{12}$ on the amplitude of the central absorption spike for different cell lengths ($L = 2$ cm or $L = 0.5$ cm). Variations of the spike's amplitude are significantly higher for the short cell with $L = 0.5$ cm. For a sufficiently long cell ($L = 5$ cm and more), variations of the signal are very small and the spike's amplitude is approximately constant. It tends to approach the average level presented on Fig. A.15 as a dash-dotted horizontal line. This average level of absorption is described by the first term in Exp. (A.9). The second term of Exp. (A.9) is responsible for the sensitivity of the spike's amplitude on the total phase θ.

It is interesting to note that we can observe the absorption peak effect for a very wide range of phase θ variations, while the effect is absent only for short cells and for certain θ values in the range 280–330 degree (see Fig. A.15). It means that counter-propagating dual-frequency light waves can have common dark atomic states only in some relatively small regions along the cell, while the other regions give the absorption peak's effect. This circumstance explains why in the case of long cells (several

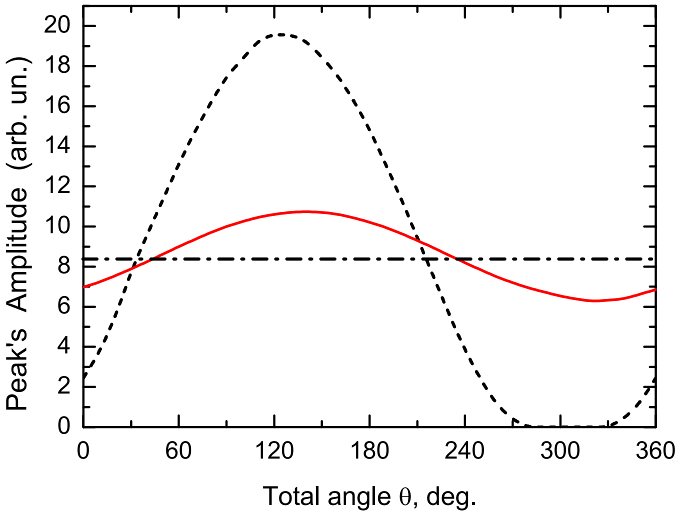

Figure A.15: Influence of the total phase shift $\theta = 2\phi + \phi_{12}$ on the amplitude of the central absorption peak at different cell lengths: L=2 cm (solid red line) and L=0.5 cm (dashed black line). The peak's amplitude tends to oscillate very close to the average level depicted as the dash-dotted horizontal line when the cell length is being increased. The zero gap between $\theta \approx 280$ and 330 degrees means that there is no peak (i.e. the regular dip in the absorption is observed). The Raman detuning is assumed to be zero ($\Delta_R = 0$). Extracted from [271].

cm long), the peak's effect is almost insensitive to the total phase θ. It happens because these dark regions constitute only a small fraction of the total cell length. Otherwise, with a sufficiently small cell, the common dark state can survive throughout the cell length, allowing to observe the low level of fluorescence from the whole cell. For example, the interval $\approx$ 330–280 $= 50^o = 0.87$ radians on Fig. A.15 for a short cell implies that the dark state remains common for both counter-propagating waves at the distance Δz, which can be estimated from the equation $2k_{12}\Delta z = 0.87$. For conditions of Fig. A.15, we immediately get $\Delta z \approx 0.22$ cm. Thus, with a cell of length $L = 0.22$ cm, we should be able to destroy totally the absorption peak's effect by proper choice of the phase θ (for instance, by adjusting the mirror position).

Figure A.16 describes the influence of the atomic transition openness (cases where the branching ratio is $\beta = 1$ or $\beta = 0.5$) on the high-contrast absorption effect. We clearly observe that, in the case of an open transition, the high-contrast spike almost disappears.

Figure A.17 helps to clarify the physical origin of the central spike formation in the considered Λ-scheme. Figure A.17 reflects the situation where the low-frequency coherences ρ_{12} and ρ_{21} are artificially "switched off". In this configuration, the creation of the HFS-CPT phenomenon is prohibited. One can see that there is no peak in the center of the absorption curve (black dashed line). At the opposite, a usual saturated-absorption resonance is observed. Secondly, the background level is found to be much higher when CPT is absent. Thus, from this figure and taking into account all other curves in this paragraph, we can state that the central spike occurs because of a low level of background absorption at $\Delta \gg \Gamma$, the latter becoming "normal" in the vicinity of a spectral line center at $\Delta \sim \Gamma$. This low background level is explained by the CPT phenomenon. For $\Delta \gg \Gamma$, atoms from different velocity groups are pumped into the noncoupled states and do not scatter much light energy from the resonant field. For $\Delta \sim \Gamma$ the light field components start to interact with the same atoms and non-coupled states can be destroyed (see the quantitative analysis in the previous paragraph). When CPT is switched off, only two closed two-level systems with transitions $|1\rangle \leftrightarrow |3\rangle$ and $|2\rangle \leftrightarrow |3\rangle$ are involved. Each of these systems leads to observation of a usual saturated-absorption dip in the center of the resonance curve (see left and right side absorption profiles in Fig. A.9a, A.9b). At optical and Raman resonance, both transitions form a closed system, leading to a deep Doppler absorption profile with a regular SAR dip. Experimentally, the HFS coherences can be avoided by using optical transitions towards two separate excited levels, instead of sharing a common level (see section A.7

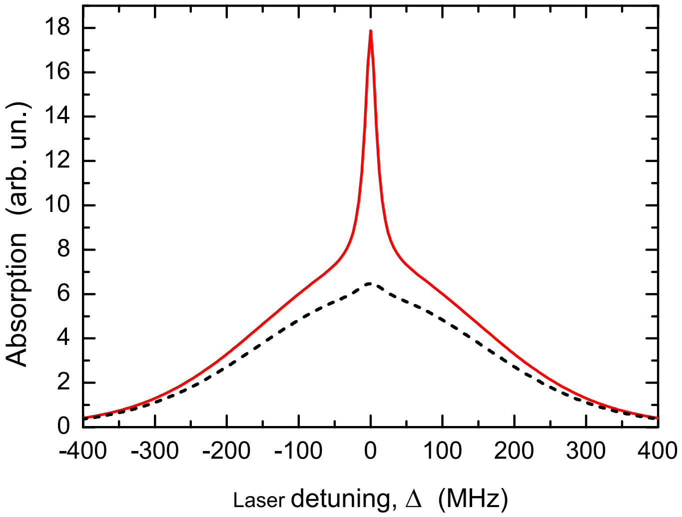

Figure A.16: Influence of the atomic transition openness on the effect of the high-contrast spike: $\beta = 1$ is for the red solid line (closed system of energy levels), $\beta = 0.5$ corresponds to the black solid line (open transition). Other parameters are: $\phi = \pi/2$, $\phi = 0$, $\Delta_R = 0$, $L = 2$ cm. Extracted from [271].

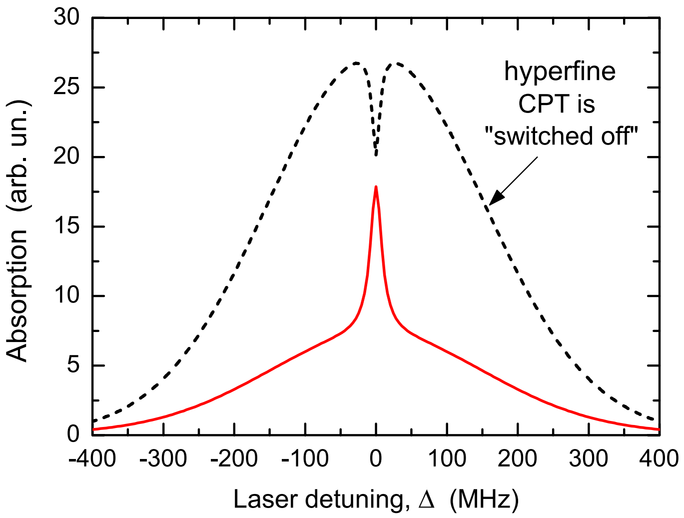

Figure A.17: Resonance curves obtained in same conditions than those depicted for the red solid line of Fig. A.13, but with presence (red solid) or absence (black dashed) of the hyperfine CPT phenomenon. Extracted from [271].

and Fig. A.9a, A.9b) or with a large Raman detuning (see Fig. A.9d). However, even in these cases, CPT states exist between Zeeman sub-levels (see the next section).

In conclusion of this section, we can say that the microwave HF frequency-splitting (HFS)-CPT phenomenon involving different HF-split sub-levels of the ground state in ^{133}Cs, can be a reason of the high-contrast spike effect observed in the experiments. In that sense, the resonance curve shown in Fig. A.18 may appear surprising at first sight. In the latter, conditions are almost the same than those depicted for Fig. A.13 (red solid profile) where a high-contrast resonance is observed. Nevertheless, in the present case, the two-photon (Raman) detuning Δ_R is non-null. Obviously, the spike's effect disappears at $\Delta_R = 2\,\Gamma$ because CPT does not take place (see the blue dash-dotted curve on Fig. A.18). At the same time, the effect comes back for large Raman detunings ($\Delta_R = 20\,\Gamma$ for the black dashed curve on Fig. A.18). In this case, microwave hyperfine CPT is absent. However, a noticeable central spike is detected. This results from the manifestation of another physical process, described in section A.11, linked to some peculiarities of redistribution of atomic energy level populations due to the optical pumping process.

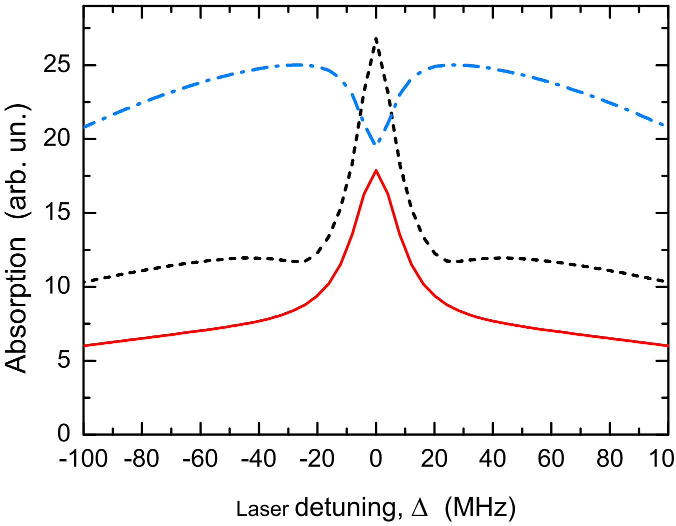

Figure A.18: Absorption as a function of the one-photon detuning, with a Raman detuning $\Delta_R = 0$ (red solid curve), $\Delta_R = 2\,\Gamma$ (blue dash-dotted curve) or $\Delta_R = 20\,\Gamma$ (dashed black). Other parameters are: $\phi = \pi/2$, $\beta = 1$, $L = 2$ cm. Extracted from [271].

A.10 Zeeman CPT states

In the previous paragraph, we have considered the formation of non-coupled states involving different levels of the cesium ground state HF doublet. However, an other type of non-coupled states can be produced during the interaction of dual-frequency counter-propagating light waves with the D_1 line energy structure. This involves $|NC\rangle$-states embracing magnetic (Zeeman) sub-levels of a single HF level [175]. For simplicity, Fig. A.19 reflects the situation where the wave E_1 consists of a single-frequency component ω_1. In this case, the wave can also pump the atoms to the non-coupled state consisting of many magnetic sub-levels. The same frequency component (ω_1) of the counter-propagating wave E_2 (not shown on Fig. A.19) can also lead to the CPT phenomenon on the state $F = 4$. Figure A.19 plots the situation where the state $F' = 4$ is being excited. In this case, $|NC\rangle$-states can be produced only on level with $F = 4$. If we consider the dual-frequency situation where both transitions 3-3' and 4-3' are near resonant, atoms can be driven to $|NC\rangle$-states on both HF-levels $F = 3$, 4. This driving scheme corresponds to the resonance observed in the right of Fig. A.4b.
In an analog way to the previous section, counter-propagating beams interact with different velocity groups of atoms under the condition $\Delta \gg \Gamma$. Each of these groups can be pumped into the non-coupled state and demonstrates a low level of absorption. Near the center of the resonance ($\Delta \sim \Gamma$), the different non-coupled states attributed to different waves start to "compete" with each other and the result depends in particular on the light-waves polarization configuration. For simplicity, we only consider the CPT phenomenon which can take place on the HF level $F = 4$ (see Fig. A.19).

In this section, the situation is very similar to the one described in the previous section. Consequently, a spectroscopic model similar to the previous paragraph (see Fig. A.10) can be considered, but now taking $\Omega_g = 2\Omega$, where $\Omega = \mu_B g_2 B/\hbar$ is the Larmor frequency which characterizes the frequency splitting between magnetic sub-levels of the ground level $F = 4$. B is the static magnetic field applied along the light wave vectors ($B||z$), μ_B is the Bohr magneton and $g_2 = 1/4$ is the Landé g-factor of the state $F = 4$. The Larmor frequency of the excited state can be written as $(g_e/g_2)\Omega$ with $g_e = 1/12$ the g-factor of the state $F' = 4$. Landé factors of the ground HF levels have opposite signs, so that $g_1 = -g_2$.
While this spectroscopic model has many common points with the previous one, it differs in some principal points. First, we consider the interaction of an atom with a light field having a single frequency component. Then, we can assume $\omega_1 = \omega_2 \equiv \omega$. This means also that $\mathbf{k}_1 = -\mathbf{k}_2 \equiv \mathbf{k}$, $\phi_{12} = 0$ and that the vapor fluorescence is homogenous along the cell. These conditions significantly

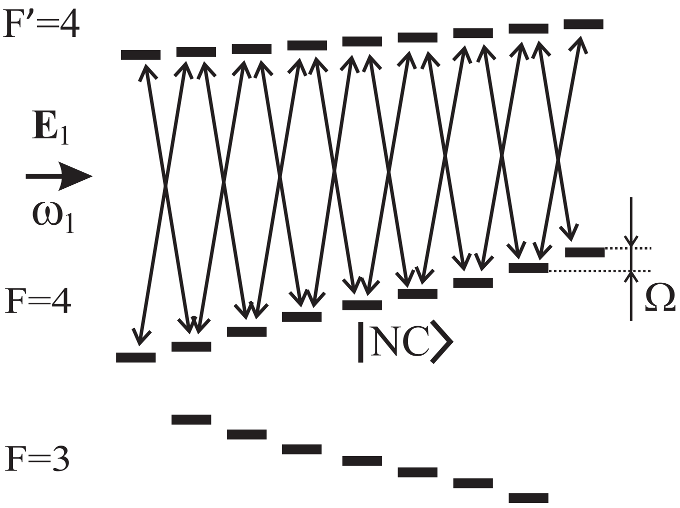

Figure A.19: Traveling light wave $\mathbf{E}_1(\omega_1 t, k_1 z)$ induces dipole σ^+ and σ^- transitions between the magnetic sub-levels of the states $F = 4$ and $F' = 4$ in Cs atom. A weak static magnetic field along the wave vector $\mathbf{k_1}$ is assumed to be switched on. Note that splitting and energy separations are not in scale. Extracted from [271].

simplify the calculations. Expression (A.6) can be simplified by:

$$\begin{aligned} \rho_{31}(z,t) &\approx e^{-i(\omega t)}\,[\rho_{31}^{(1)}\,e^{ikz} + \rho_{31}^{(2)}\,e^{-ikz}]\,, \\ \rho_{32}(z,t) &\approx e^{-i(\omega t)}\,[\rho_{32}^{(1)}\,e^{ikz} + \rho_{32}^{(2)}\,e^{-ikz}]\,, \end{aligned} \tag{A.15}$$

Moreover, the other density matrix elements become homogeneous in space:

$$\rho_{12}(z,t) \approx \rho_{12}^{(0)}\,, \quad \rho_{nn}(z) \approx \rho_{nn}^{(0)}\,. \tag{A.16}$$

These simplifications make the final system of equations much simpler (see Appendix C). In the appendix, we omit the superscript "(0)" for shortness. Space homogeneity of the low-frequency coherence ρ_{12}, for instance, means that we consider it not to be produced by σ-components of polarization of different waves. In other words, the coherence ρ_{12} can be produced by only one wave (travelling along the z-axis or the counter-propagating). Other contributions to ρ_{12} (from simultaneous action of two waves) oscillate very fast in space ($\sim e^{\pm 2ikz}$) and can be neglected.

Let us analyze some figures. The spectroscopic signal can be described now only by the first term of expression (A.9). Figure A.20 shows the resonance curves for parallel and orthogonal linear polarizations of the light waves. The physics of observed signals is similar to the one described in the previous paragraph. At the same time, the cell length now does not impact the strength of the effect (under the approximation of a small medium optical density). The central spike appears (red solid line) when non-coupled states created by both waves are orthogonal: $\langle \mathrm{NC}_1|\mathrm{NC}_2\rangle \approx 0$. This is the case of crossed polarizations (see Fig. A.1b and Fig. A.3a). The dip can be observed (dashed black line) when "dark" states $|\mathrm{NC}_1\rangle$ and $|\mathrm{NC}_2\rangle$ are close to each other (case of parallel polarizations, see Fig. A.1a and Fig. A.4a). Note that a similar effect was discussed in papers [171, 174, 274]. In these references, the goal consisted in studying a vapor-cell absorption under a pump-probe regime. The spectroscopic signal was analyzed as a function of the longitudinal static magnetic field (as in Fig. A.2 and Fig. A.3b in the present work).

Figure A.21 reflects the influence of the Λ-scheme openness. As for Fig. A.16, we can here observe a dramatic suppression of the spike effect for an open transition. Figure A.22 proves clearly that the high-contrast spike creation is connected with the CPT phenomenon (compare with Fig. A.17).

Interesting transformations of the nonlinear spectroscopic signal can be observed by applying a gradual increase of the static magnetic field (see Fig. A.23). One can see that the effect first disappears (for $\Omega > 0.5\,\Gamma$ at the considered conditions) but then comes back (for $\Omega > 2\,\Gamma$). This behavior is similar to the one described in the previous section where the two-photon detuning has been gradually increased.

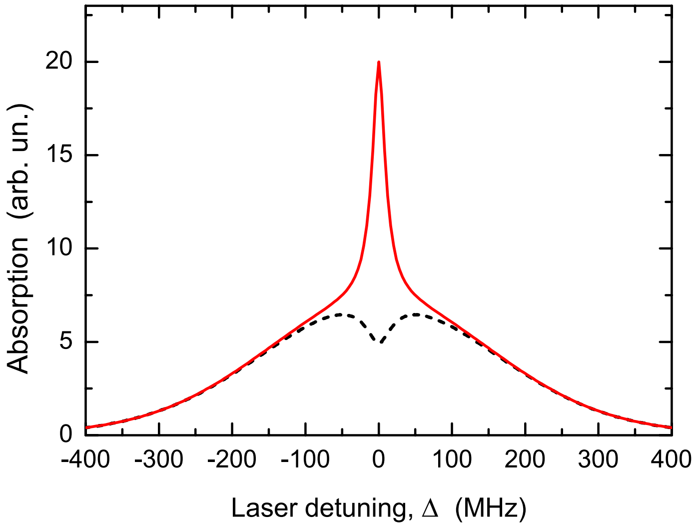

Figure A.20: Absorption curves for parallel ($\phi = 0$, dashed black line) and orthogonal ($\phi = \pi/2$, solid red line) light polarizations. The static magnetic field is zero ($\Omega = 0$). The system of levels is assumed to be closed ($\beta = 1$). Extracted from [271].

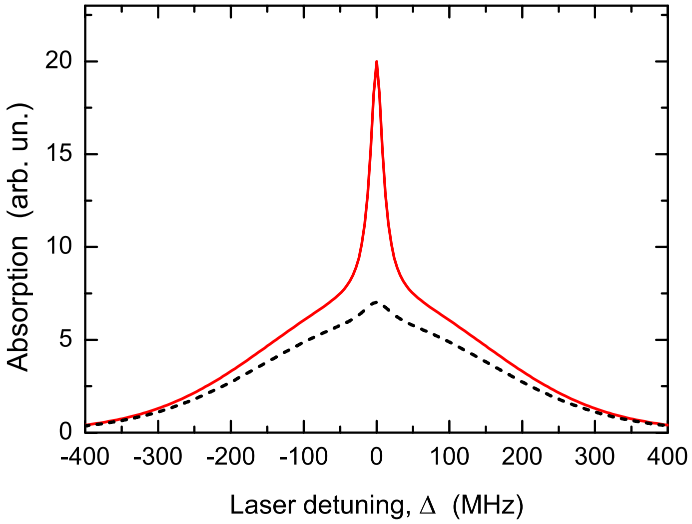

Figure A.21: Influence of atomic transition openness on the effect of high-contrast spike: $\beta = 1$ is for the red solid line (closed system of energy levels), $\beta = 0.5$ corresponds to the black solid line (open transition). Other parameters are: $\phi = \pi/2$, $\Omega = 0$. Extracted from [271].

The behavior of the resonance on Fig. A.23 between $\Omega = 0$ and $\Omega = 2\,\Gamma$ is easy to understand. Under a small magnetic field, the spike formation is linked to the same reason than the one reported in Fig. A.20 (red solid line). The CPT state, linked with the high-contrast spike formation, is destroyed with further increase of the magnetic field. We can estimate the interval of the Larmor frequency where the CPT state survives as $|\Omega| \leq \Omega_R^2/4\Gamma$ (from the power broadening condition). In conditions of Fig. A.23, this means that the CPT state does not influence greatly the absorption profile, when $|\Omega| \gg 0.5\Gamma$. Therefore, the usual saturated-absorption dip is observed on Fig. A.23(d,e), as in Fig. A.1 at high magnetic field. This situation is similar to the one of Fig. A.22 where the CPT is "switched off". However, with further increase of the magnetic field, the spike can be observed again. The reason of this behavior is the same than for Fig. A.18, where a large Raman detuning ($\Delta_R \neq 0$) was considered. Here, the Larmor frequency Ω plays the role of this Raman detuning. The creation of the high-contrast spike under the condition $\Omega \gg \Gamma$ is due to peculiarities of the optical pumping process. This aspect is discussed in the next paragraph.

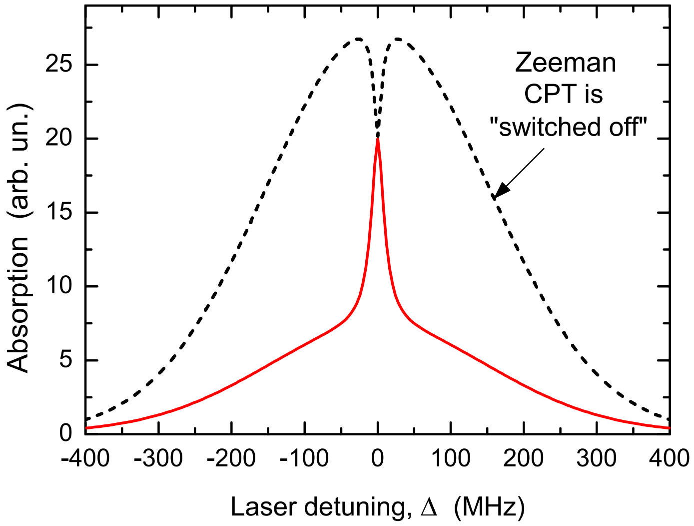

Figure A.22: Influence of the CPT phenomenon on the observation of the central spike in the absorption profile. Parameters are: $\beta = 1$, $\phi = \pi/2$, $\Omega = 0$. Extracted from [271].

A.11 Peculiarities of optical pumping

In this section, we discuss the last physical phenomenon which can contribute to the observation of the high-absorption dip in the center of the absorption profile. This effect can be also understood with the help of a Λ-scheme. As mentioned above, some peculiarities of the optical pumping process can lead to the observation of the peak in cases of Fig. A.18 (black dashed line) or Fig. A.23(f,g,h). Let us consider the case of the peak formation, in the monochromatic case with crossed polarizations, when the Larmor frequency is large enough to destroy the influence of the CPT phenomenon. We also assume that Ω is larger than the natural linewidth of the transition. In other words, we focus on the case of $\Omega = 10\,\Gamma$ where the peak effect is strong enough (see Fig. A.23h).

Figures A.24(a-f) are given to describe qualitatively the physical reason of the peak formation. We assume Δ to be positive as well as the Larmor frequency Ω (i.e., we consider the right part of the curve on Fig. A.23h). When the vapor is being irradiated by a laser field, only specific velocity groups of atoms are excited. This happens due to the Doppler shift of light frequency in the coordinate frame connected with a moving atom. These resonant groups of atoms contribute greatly to the level of absorption at a fixed value of detuning Δ. Therefore, we will consider here the contributions from different resonant velocity groups from different frequency detuning cases. In a first approach, let us compare the cases where $\Gamma \sim \Delta \ll \Omega$ (central part of the absorption curve, see Fig. A.24) and $\Delta \gg \Omega$ (background level). In the former case, there are two symmetrical resonant groups with velocities $\upsilon_{1,2} \approx \mp\Omega/k$ $(\Delta \ll \Omega)$. Each group interacts simultaneously with $\sigma^{+(-)}$ polarization component of one wave and with $\sigma^{-(+)}$ of the other (counter-propagating) wave.

It means that there is a *closed* system of levels, having the following main features: 1) both ground Zeeman sub-levels interact with the field, 2) populations of these sub-levels are almost equal, 3) the upper state is also populated and the fluorescence (absorption) is significant. It should be noted that we do not consider here the influence of CPT-like states which can be produced by counter-propagating waves. Indeed, this state oscillates very fast in space with $\exp[\pm 2ikz]$ and does not affect significantly the absorption of the whole cell. This circumstance is the main difference between this kind of dark state and the dark state considered in the section "HFS-CPT", where two CPT states were created only by wave E_1 *or* E_2 and oscillated in space much slower (according to the low $\exp[\pm ik_{12}z]$).

In the regime $\Delta \gg \Omega$, there are two couples of resonant groups of atoms - each couple is resonant only with E_1 or E_2 wave. The central velocities of these groups are $\upsilon_{3,4} = (\Delta \pm \Omega)/k$ for the E_1 wave and $\upsilon_{5,6} = -(\Delta \pm \Omega)/k$ for the E_2 wave. For shortness, Figs A.24(c,d) reflect the cases for only two of these groups. The main difference between this regime and the one considered above $(\Gamma \sim \Delta \ll \Omega)$ is that we have here four independent resonant groups of atoms which are described by

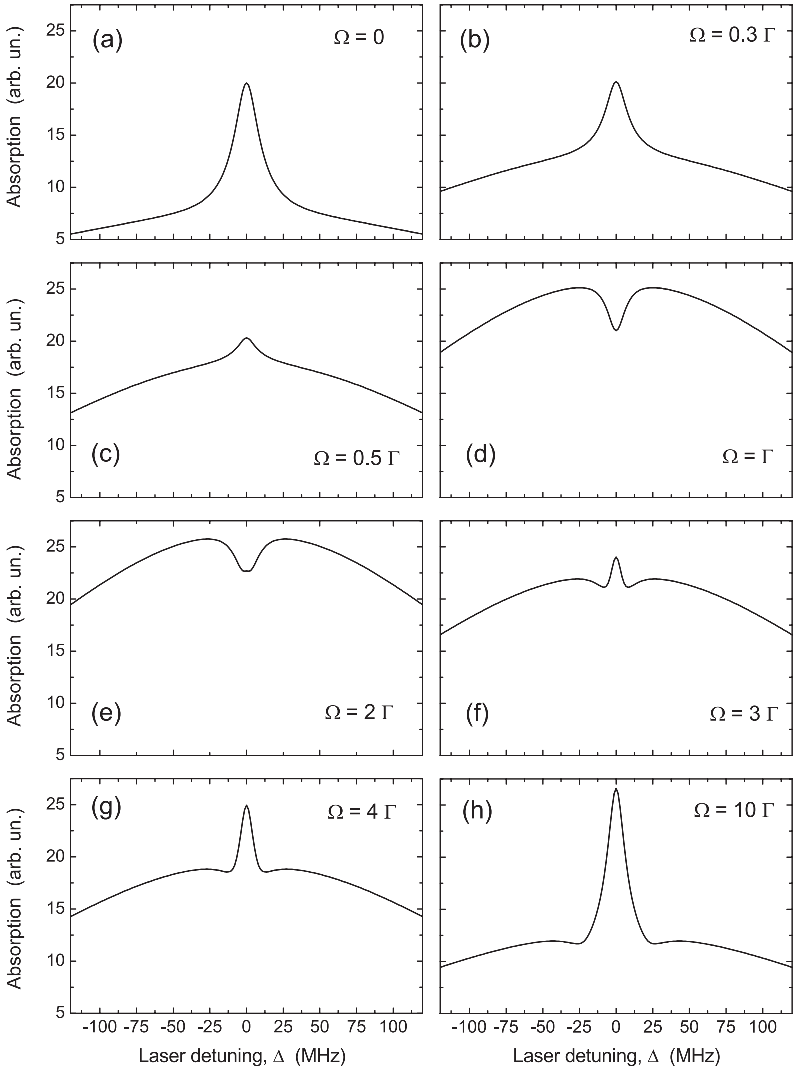

Figure A.23: Influence of a longitudinal static magnetic field (the Larmor frequency Ω) on the creation of the central peak. Parameters are: $\beta = 1$, $\phi = \pi/2$, crossed polarizations. Extracted from [271].

the corresponding Λ-schemes. The main feature of each of these schemes is that they induce "trap" states which accumulate a major part of the atomic population. For example, in the case of Fig. A.24(c), this trap state is $|2\rangle$. We can say that this system is effectively *open* because atoms being trapped in the state $|2\rangle$ do not interact with the field anymore. This leads to a large decrease of the excited state population and the absorption level correspondingly. Therefore, one can observe a strong absorption (a peak) in the center of the resonance and a small background level. This situation is similar to the cases depicted in Figs A.13 or A.20 (solid red curves). In the latter figures, the $|NC\rangle$ states played the same role of trap states for large frequency detunings while these trap states were absent in the center of absorption curves.

An interesting feature to note is the small dip at the substrate of the peaks on Figs A.23(f,g,h). This is explained by Λ-schemes depicted on Fig. A.24(e,f). When $\Delta \approx \Omega$, there is a special resonant group of atoms with zero z-projection ($\upsilon_7 \approx 0$) where two waves act on the same arm of the Λ-scheme (Fig. A.24(e)). In this case, the trap state $|2\rangle$ is better optically pumped than in the situation where only one resonant wave is involved (Figs A.24(c,d)). This means that the upper state suffers from additional reduction of the population and the fluorescence decreases.

The effect considered here is sensitive to the branching ratio. This sensitivity is demonstrated on Fig. A.25. With a slightly open system, the peak does not disappear but its amplitude is much smaller than for a closed system. In a real experiment with ^{133}Cs, the peak-producing reason described here

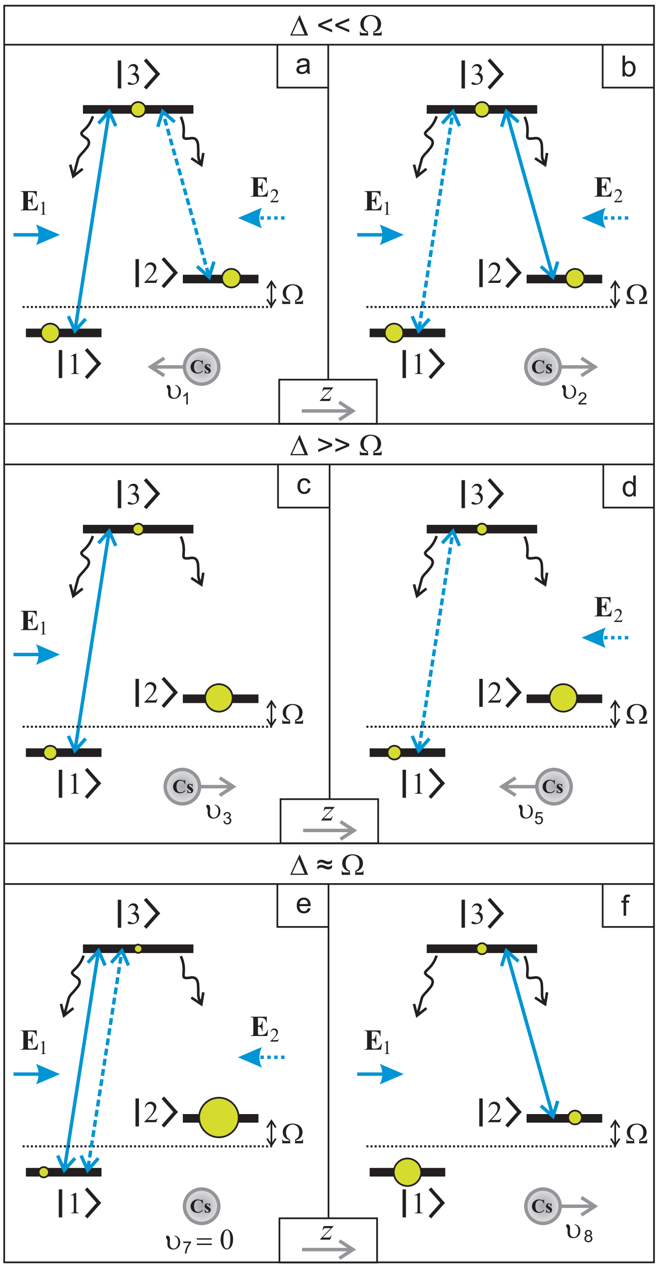

Figure A.24: The three-level Λ-schemes show the peculiarities of population redistributions over atomic energy levels under the resonant light field in the atomic moving frame. The branching ratio is assumed to be equal to unity ($\beta = 1$). Light-induced transitions denoted by solid lines corresponds to E_1, while dashed lines corresponds to the counter-propagating E_2 wave. Extracted from [271].

can be realized separately by the two other mentioned effects by using two independent laser sources (or large Raman detuning δ_R, to kill the HFS-CPT effect) together with a non-zero longitudinal magnetic field B (to "kill" the Zeeman-CPT effect). We should note that a similar effect connected with the optical pumping process was also described with potassium atoms [275].

A.12 Discussions

Let us compare results of the experiments (sections A.2-A.3) and the theoretical analysis described in sections A.9-A.11. First, we are interested by the dual-frequency regime of atom-field interaction. Figure A.4a reports the usual saturated-absorption resonance as a reduction of absorption of the vapor cell near $\Delta = 0$. At the opposite, in the dual frequency regime, a high-contrast enhanced-absorption

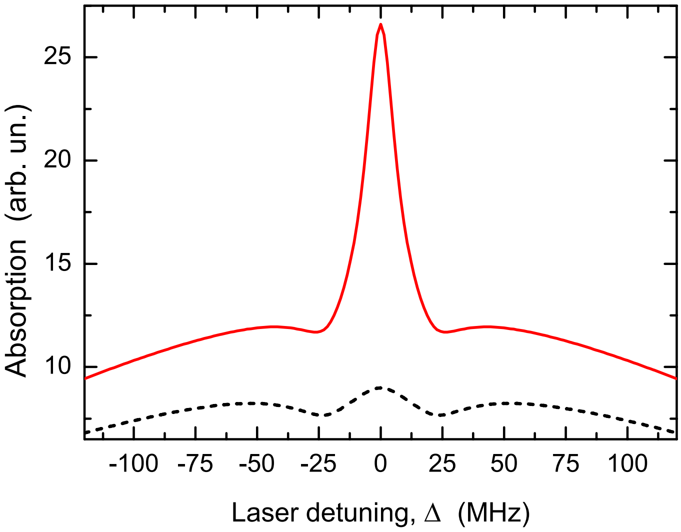

Figure A.25: Study of the influence of openness of energy-levels system on the strength of the effect: $\beta = 1$ is for a closed system (red solid line) and $\beta = 0.5$ is for an open system (black dashed line). Extracted from [271].

peak is detected when both HF ground states with $F = 3$ and $F = 4$ are excited by the counter-propagating waves. We have already described several possible physical reasons underlying this effect. As mentioned above, we focus here on the spike which corresponds to the interaction of the upper state with $F' = 4$. Similar explanations can be provided for the adjacent spike.

When the static magnetic field is close to zero, two main physical reasons can contribute to the absorption peak creation. Both are the manifestations of the coherent population trapping phenomenon. We distinguish the hyperfine-frequency-splitting CPT (HFS-CPT) and the Zeeman-CPT (see sections A.9 and A.10, respectively). Both effects can lead to a reduced absorption over the whole Doppler profile (see Figs A.17 and A.22). The Zeeman-CPT effect leads to a regular SAR dip at the center of the resonance in case of parallel polarizations of the counter-propagating waves, and to an enhanced absorption under the perpendicular polarization case (see Fig. A.20), independently from the cell length. The HFS-CPT effect can result in increased-transmission or increased-absorption resonance under the parallel as well as the perpendicular polarizations. The sign (dip or peak) of the contribution of the HFS-CPT process depends on the cell length L and on the position of the mirror M (Fig. 3.18), i.e. the phase shift ϕ_{12} (see Fig. A.15 and Ref. [272]). For the cell of intermediate lengths (as in our experiments, $L = 2$ cm), both effects have the same sign under the perpendicular light waves polarizations and contribute to the central spike creation. However, when light waves polarizations are parallel, the creation of the absorption peak can be caused only by the HFS-CPT effect (see Fig. A.20). This explains why the peak's amplitude is smaller in the last case than in the case of orthogonally polarized waves (see Fig. A.6a and A.5a for $B = 0$). On the other hand, if we want to understand the role of the Zeeman-CPT effect in the absorption peak creation, we can refer to the experimental figures A.9c and A.9d. On the former figure, both effects take place whereas in the latter case, only Zeeman-CPT occurs because HFS-CPT is eliminated by the non-zero Raman detuning. Analyzing the figures, we can state that both effects (Zeeman-CPT and HFS-CPT) play an important role for the observation of the high-contrast absorption peak.

The reduction of the spike amplitude with presence of a magnetic field is also obvious (see Fig. A.5). Indeed, in the case of ^{133}Cs, the splitting of ground state Zeeman sub-levels (of $F = 3$ or $F = 4$ level) follows the law $|\Omega| = 2\pi \times 0.35$ MHz/G (this law can be easily calculated or revealed directly from Fig. A.8 because the frequency interval between two adjacent transmission peaks corresponds to 2Ω). This means that, under the existence of a non-zero magnetic field in the cell, the non-coupled states $|\mathrm{NC}\rangle$, which are certain superpositions of the magnetic sub-levels m_F of one ground level ($F = 3$ or $F = 4$, see Fig. A.19), can not be created (see section A.10). The critical value of the magnetic field is about $300 - 400$ mG as shown on Fig. A.3b. Therefore, the "Zeeman-CPT" effect does not contribute to the peak formation under the condition $\Omega > \Delta_{\mathrm{CPT}}$, with Δ_{CPT} the width of the Zeeman-CPT resonance (see also Fig. A.23d where the CPT resonance vanishes under $\Omega \sim \Gamma$). In other words, Λ-schemes with two ground magnetic sub-levels belonging to a single HF ground state are very sensitive to the external magnetic field.

At the same time, one could expect that the HFS-CPT effect can contribute to the absorption peak creation even in the presence of a non-null magnetic field. Indeed, Fig. A.26 (solid and dashed red and blue arrows) shows that there are two Λ-schemes, almost insensitive to the magnetic field.

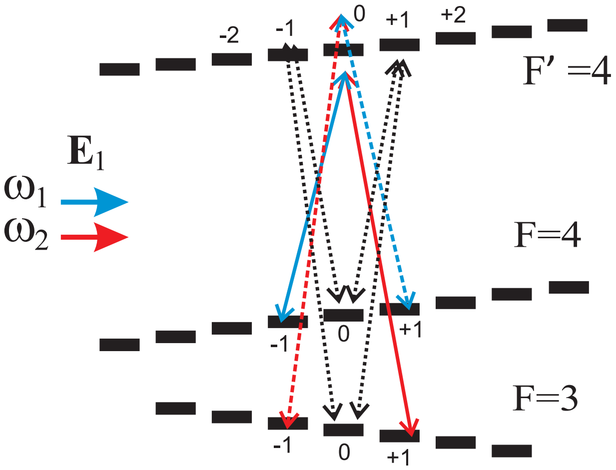

Figure A.26: Two Λ-schemes with low linear sensitivity to external magnetic field (solid and dashed lines are for different schemes), which can be formed by E_1 light wave only. The same schemes are influenced and can be formed by the counter-propagating wave E_2 (it is not shown for simplicity). The dotted black lines denote the schemes that can be neglected due to destructive interference. 0,±1 are the values of magnetic quantum numbers m_F. Extracted from [271].

These schemes embrace the common upper sub-level $|F' = 4, m_{F'} = 0\rangle$ and two pairs of ground-state magnetic sub-levels: $\{|F = 3, m_F = +1\rangle$ & $|F = 4, m_F = -1\rangle\}$ or $\{|F = 3, m_F = -1\rangle$ & $|F = 4, m_F = +1\rangle\}$. The linear sensitivity of these schemes to the magnetic field is only due to the nuclear magnetic momentum (e.g., see [114, 276, 277]). Based on Fig. A.26, one could expect that the absorption peak would survive under a moderate magnetic field value too. Unfortunately, in the case of ^{133}Cs, we cannot distinguish single Λ-schemes under moderate magnetic field values (B ~1 G), which could provide pure and strong HFS-CPT effect. The fact is that, when $\Omega \lesssim \Gamma$, there are additional light-induced σ-transitions in the atom, besides those shown on Fig. A.26. For example, the transition $\{|F = 3, m_F = +1\rangle \rightarrow |F' = 4, m_F = +2\rangle\}$ is also permitted. This transition destroys the CPT state as the superposition of $\{|F = 3, m_F = -1\rangle$ and $|F = 4, m_F = +1\rangle\}$ sub-levels. On the other hand, we could expect that the single Λ-schemes be distinguished with further increase of the magnetic field ($\Omega > \Gamma$), when transitions like $\{|F = 3, m_F = +1\rangle \rightarrow |F' = 4, m_F = +2\rangle\}$ become out of the one-photon resonance and the HFS-CPT effect would occur. Increasing the magnetic field also means that two light waves resonantly interact with atoms having non-zero velocities (Fig. A.27), in contrast to what we have for small magnetic field values (Fig. A.26). Atoms in each of both resonant velocity groups interact with both counter-propagating waves and the pure Λ-schemes can be created. However, the fact is that these Λ-schemes are independent from each other, i.e. each of these schemes is driven only by one wave (E_1 or E_2, see Fig. A.27). Therefore, the waves almost do not "feel" each other under the condition $\Omega > \Gamma$ and there is no reason for the absorption peak creation again. All aforesaid explains why the absorption peak does not survive with increasing the magnetic field in the experiments (for instance, see Fig. A.5a).

Nevertheless, with further increase of the magnetic field, the peak comes back (B ≈2 G under the conditions of our experiments). This happens due to the "pumping" effect described in the previous section. However, the peak's amplitude is not as large as in the case of zero magnetic field because of the considerable openness of the relevant atomic energy levels (especially under the condition $\Omega > \Gamma$),

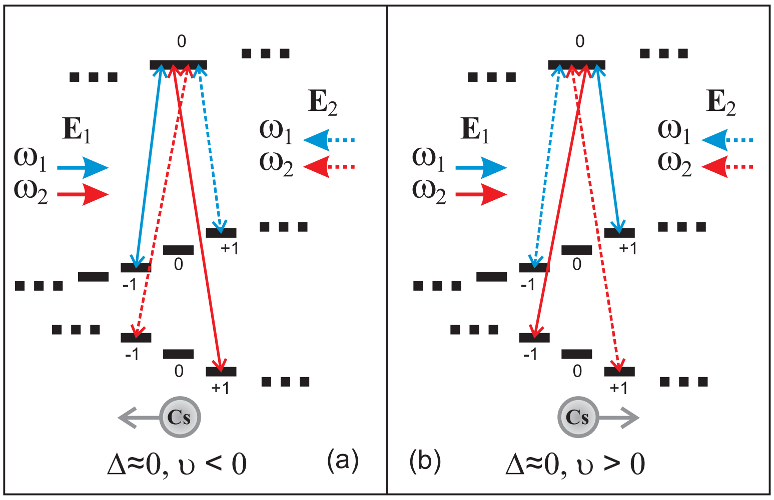

Figure A.27: Two resonant velocity groups of atoms, when $\Delta \approx 0$ (i.e. at the center of resonance) and $\Omega > \Gamma$. (a) $\upsilon = -\Omega/k$, (b) $\upsilon = +\Omega/k$. Extracted from [271].

which harms the absorption peak's effect as shown above (see Fig. A.25). Therefore, when $B > 1$ G, the absorption peak can be observed, but its amplitude is much smaller than under the zero magnetic field.

In principle, two other Λ-schemes are insensitive to the magnetic field (dotted black lines at Fig. A.26). These schemes have common ground-state magnetic sub-levels $|F = 3, m_F = 0\rangle$ and $|F = 4, m_F = 0\rangle$ and are totally insensitive to the linear Zeeman shift (in the sense of a two-photon resonance). However, it can be shown that the $|\mathrm{NC}\rangle$ states cannot be produced in the case of parallelly or orthogonally polarized counter-propagating waves so far as the atom is excited by the two-frequency laser field. Indeed, it is enough to consider just one of the two waves, for example the E_1 wave. If two frequency components ($\omega_{1,2}$) have parallel linear polarizations, the dark state between $|F = 3, m_F = 0\rangle$ and $|F = 4, m_F = 0\rangle$ cannot be created due to the relative phases of the Clebsch-Gordan coefficients (e.g., see [120, 147]). In the case where these components have mutually orthogonal polarizations (for example, if we use two different laser sources or the equivalent push-pull regime [120] of atom excitation), the dark state can be created. However, in our case $\omega_{1,2}$-components of E_1 wave always have equal polarizations and an atom excited by this wave does not exhibit any $|\mathrm{NC}\rangle$ state between $m_F = 0$ sub-levels. The same words can be said for the E_2 wave. Therefore, the Λ-schemes shown at Fig. A.26 as the dotted black lines can be omitted from our consideration. It is interesting to note that the HFS-CPT effect should be more relevant in the case of D_1 line of ^{87}Rb, especially when the $F' = 1$ state is being excited under a dual-frequency regime. Indeed, for ^{87}Rb atoms, there are no unwanted light-induced σ-transitions which can destroy the CPT state between HF levels, even under moderate magnetic field values ($B \sim$1 G). Therefore, in the case of ^{87}Rb, one can expect some new features of the absorption peak creation.

Let us now analyze the influence of the Raman detuning, as focused on experimental curves of Fig. A.9. As measured in the section A.6, the width of HFS-CPT resonances is about 191 kHz. It means that the Raman detuning $\Delta_R = 2\pi \times 1$ MHz is large enough to destroy the influence of this effect on the resonance curves. Comparing Figs A.9c and A.9d, we can state that the HFS-CPT effect can play a relevant role. Indeed, the absorption peak amplitude is noticeably reduced under the single contribution of the Zeeman-CPT effect (Fig. A.9d). In the latter regime, the absorption peak creation follows the laws established in the theory section A.10: in the case of parallel polarizations of counter-propagating light waves, one can observe a regular absorption dip, while the use of orthogonal linear polarizations results in the high-contrast absorption peak. The theoretical calculation reported in Fig. A.18 (blue dash-dotted curve) also demonstrates the destruction of the HFS-CPT effect under the non-zero Raman detuning (equals to 2Γ for the presented figure). Let us note that the HFS-CPT effect can be also "switched off" if optical sidebands are produced by two independent laser sources, instead of using a single modulated laser source as experiments presented here. We inform the reader that some experiments with two independent lasers have been also carried out confirming this point.

Nevertheless, we decided not to provide the results in the current paper for clarity and length of the manuscript.

It is also important to emphasize the difference between small and large Raman detunings. If the Raman detuning is not so large, i.e. $\Delta_R \sim \Gamma$, the counter-propagating light waves are still in resonance with the zero velocity group of atoms and the Zeeman-CPT effect works well. If we tune the microwave synthesizer so that $\Delta_R = \pm\Omega_e/2$, with $\Omega_e = 2\pi\nu_e$ the frequency separation between upper levels, the light waves have also common velocity groups but different transitions are induced (see Fig. A.9a and A.9b). In the latter case, one can also observe absorption peaks which are connected with optical pumping processes. An example of such pumping processes has been considered in the section A.11. However, we should note that the simplified model used in our theory does not take into account the Zeeman coherences of the exited state and their spontaneous transfer to the ground levels. Indeed, the pumping process described in section A.11 always leads to an increase of absorption at $\Delta = 0$, i.e. in the center of resonance curves of Figs A.9a and A.9b, and does not depend qualitatively on the light waves polarizations. However, we can observe a noticeable sensitivity of the nonlinear resonance's sign to the polarizations. At the same time, it is well known that spontaneous transfer of Zeeman coherences can result in the sign reversal effect for the CPT resonances (e.g., see [278]). In our case, this sensitivity to the light polarizations is also due to the coherence spontaneous transfer effect, which occurs between two transitions (see red and orange lines at the insets on Fig. A.9a, A.9b). Light polarization affects the phases of the upper-state Zeeman coherences. Consequently, these coherences are spontaneously transferred to the ground levels $F = 3, 4$ and affect the Zeeman coherences and the CPT phenomenon in the ground state.

A.13 Conclusions

We reported a detailed experimental study on Doppler-free spectroscopy on Cs D_1 line with the use of a dual-frequency optical field. We demonstrated under appropriate conditions the possibility to detect high-contrast natural-linewidth resonances appearing as a sudden increased absorption spike in the center of the Doppler profile. The impact of several experimental parameters onto the shape, sign and amplitude of this resonance was investigated, including the polarizations of the light waves, the static magnetic field, laser or Raman frequency detunings. These experimental results were supported by a detailed theoretical analysis which revealed the effect to be really many-sided. Several simplified spectroscopic models were proposed to explain the results of the experiments due to the variety of physical effects involved into the absorption peak creation. All these models are based on a Λ-scheme of atomic energy levels. It was highlighted that the high-contrast resonance spike appearing in the bottom of the absorption profile is mainly attributed to three physical phenomena including microwave dark-state coherences ("HFS-CPT" effect), dark states composed of coherent superpositions of Zeeman sub-levels of the same hyperfine level ("Zeeman-CPT" effect) and optical pumping processes. In the general case, all these physical reasons contribute constructively and lead to the natural-width bright resonance observed in the vapor cell absorption.

Appendix B

Density matrix elements - HFS-CPT

Numerical calculations of absorption curves presented in the paragraph A.9 are based on the following system of equations for density matrix elements. This system has been derived by substituting (A.3)-(A.8) into the master equation (A.2).

$$\begin{aligned}&\Big(G+2\Gamma_{eg}\big[S_{11}^{(-)}+S_{21}^{(+)}\big]\Big)\rho_{11}^{(0)}-\\&-\Big(\beta\Gamma+2\Gamma_{eg}\big[S_{11}^{(-)}+S_{21}^{(+)}\big]\Big)\rho_{33}^{(0)}+\\&+\Omega_{R1}^2L_1^{(-)}\rho_{12}^{(-)}+\Omega_{R20}^2L_1^{(+)}e^{-i\theta}\rho_{21}^{(+)}+\\&+\Omega_{R1}^2L_1^{(-)*}\rho_{21}^{(+)}+\Omega_{R20}^2L_1^{(+)*}e^{i\theta}\rho_{21}^{(-)}=\frac{G}{2}\,,\end{aligned}\tag{B.1}$$

$$\begin{aligned}&\Big(G+2\Gamma_{eg}\big[S_{12}^{(-)}+S_{22}^{(+)}\big]\Big)\rho_{22}^{(0)}-\\&-\Big(\beta\Gamma+2\Gamma_{eg}\big[S_{12}^{(-)}+S_{22}^{(+)}\big]\Big)\rho_{33}^{(0)}+\\&+\Omega_{R1}^2L_2^{(-)*}\rho_{12}^{(-)}+\Omega_{R20}^2L_2^{(+)*}e^{-i\theta}\rho_{12}^{(+)}+\\&+\Omega_{R1}^2L_2^{(-)}\rho_{21}^{(+)}+\Omega_{R20}^2L_2^{(+)}e^{i\theta}\rho_{21}^{(-)}=\frac{G}{2}\,,\end{aligned}\tag{B.2}$$

$$\begin{aligned}&\Big(G+\Omega_{R1}^2M_{12}^{(+)}+\Omega_{R20}^2M_{12}^{(-)*}+2ik_{12}v\Big)\rho_{11}^{(+)}-\\&-\Big(\beta\Gamma+\Omega_{R1}^2M_{12}^{(+)}+\Omega_{R20}^2M_{12}^{(-)*}\Big)\rho_{33}^{(+)}+\\&+\Omega_{R1}^2M_{12}^{(+)}\rho_{12}^{(+)}+\Omega_{R20}^2M_{12}^{(-)*}e^{i\theta}\rho_{21}^{(+)}=0\,.\end{aligned}\tag{B.3}$$

Taking into account the connection $\rho_{11}^{(-)}{=}\rho_{11}^{(+)*}$, we immediately get

$$\begin{aligned}&\Big(G+\Omega_{R1}^2M_{12}^{(+)*}+\Omega_{R20}^2M_{12}^{(-)}-2ik_{12}v\Big)\rho_{11}^{(-)}-\\&-\Big(\beta\Gamma+\Omega_{R1}^2M_{12}^{(+)*}+\Omega_{R20}^2M_{12}^{(-)}\Big)\rho_{33}^{(-)}+\\&+\Omega_{R1}^2M_{12}^{(+)*}\rho_{21}^{(-)}+\Omega_{R20}^2M_{12}^{(-)}e^{-i\theta}\rho_{12}^{(-)}=0\,.\end{aligned}\tag{B.4}$$

For harmonics $\rho_{22}^{(\pm)}$ we have

$$\begin{aligned}&\Big(G+\Omega_{R1}^2M_{21}^{(+)*}+\Omega_{R20}^2M_{21}^{(-)}+2ik_{12}v\Big)\rho_{22}^{(+)}-\\&-\Big(\beta\Gamma+\Omega_{R1}^2M_{21}^{(+)*}+\Omega_{R20}^2M_{21}^{(-)}\Big)\rho_{33}^{(+)}+\\&+\Omega_{R1}^2M_{21}^{(+)*}\rho_{12}^{(+)}+\Omega_{R20}^2M_{21}^{(-)}e^{i\theta}\rho_{21}^{(+)}=0\,,\end{aligned}\tag{B.5}$$

$$\begin{aligned}
&\Big(G+\Omega_{R1}^2 M_{21}^{(+)}+\Omega_{R20}^2 M_{21}^{(-)*}-2ik_{12}\upsilon\Big)\rho_{22}^{(-)}-\\
&\quad-\Big(\beta\Gamma+\Omega_{R1}^2 M_{21}^{(+)}+\Omega_{R20}^2 M_{21}^{(-)*}\Big)\rho_{33}^{(-)}+\\
&\quad+\Omega_{R1}^2 M_{21}^{(+)}\rho_{21}^{(-)}+\Omega_{R20}^2 M_{21}^{(-)*}e^{-i\theta}\rho_{12}^{(-)}=0\,.
\end{aligned}\tag{B.6}$$

For low-frequency coherences:

$$\begin{aligned}
&\Big\{G+\Omega_{R1}^2\big[M_{21}^{(+)*}+M_{12}^{(+)}\big]+\Omega_{R20}^2\big[L_2^{(+)*}+L_1^{(+)}\big]+\\
&+i(\Delta_R+k_{12}\upsilon)\Big\}\rho_{12}^{(+)}+\Omega_{R20}^2 L_1^{(+)}e^{i\theta}\rho_{11}^{(0)}+\\
&+\Omega_{R20}^2 L_2^{(+)*}e^{i\theta}\rho_{22}^{(0)}+\Omega_{R1}^2 M_{12}^{(+)}\rho_{11}^{(+)}+\Omega_{R1}^2 M_{21}^{(+)*}\rho_{22}^{(+)}-\\
&-\Omega_{R20}^2\big[L_2^{(+)*}+L_1^{(+)}\big]e^{i\theta}\rho_{33}^{(0)}-\\
&\qquad-\Omega_{R1}^2\big[M_{21}^{(+)*}+M_{12}^{(+)}\big]\rho_{33}^{(+)}=0\,,
\end{aligned}\tag{B.7}$$

and, since $\rho_{21}^{(-)}{=}\rho_{12}^{(+)*}$, we have

$$\begin{aligned}
&\Big\{G+\Omega_{R1}^2\big[M_{21}^{(+)}+M_{12}^{(+)*}\big]+\Omega_{R20}^2\big[L_2^{(+)}+L_1^{(+)*}\big]-\\
&-i(\Delta_R+k_{12}\upsilon)\Big\}\rho_{21}^{(-)}+\Omega_{R20}^2 L_1^{(+)*}e^{-i\theta}\rho_{11}^{(0)}+\\
&+\Omega_{R20}^2 L_2^{(+)}e^{-i\theta}\rho_{22}^{(0)}+\Omega_{R1}^2 M_{12}^{(+)*}\rho_{11}^{(-)}+\Omega_{R1}^2 M_{21}^{(+)}\rho_{22}^{(-)}-\\
&-\Omega_{R20}^2\big[L_2^{(+)}+L_1^{(+)*}\big]e^{-i\theta}\rho_{33}^{(0)}-\\
&\qquad-\Omega_{R1}^2\big[M_{21}^{(+)}+M_{12}^{(+)*}\big]\rho_{33}^{(-)}=0\,.
\end{aligned}\tag{B.8}$$

Analogically, for $\rho_{12}^{(-)}$ and $\rho_{21}^{(+)}{=}\rho_{12}^{(-)*}$ we can derive the following:

$$\begin{aligned}
&\Big\{G+\Omega_{R1}^2\big[L_2^{(-)*}+L_1^{(-)}\big]+\Omega_{R20}^2\big[M_{21}^{(-)*}+M_{12}^{(-)}\big]+\\
&+i(\Delta_R-k_{12}\upsilon)\Big\}\rho_{12}^{(-)}+\Omega_{R20}^2 M_{21}^{(-)*}e^{i\theta}\rho_{22}^{(-)}+\\
&+\Omega_{R20}^2 M_{12}^{(-)}e^{i\theta}\rho_{11}^{(-)}+\Omega_{R1}^2 L_1^{(-)}\rho_{11}^{(0)}+\Omega_{R1}^2 L_2^{(-)*}\rho_{22}^{(0)}-\\
&-\Omega_{R20}^2\big[M_{21}^{(-)*}+M_{12}^{(-)}\big]e^{i\theta}\rho_{33}^{(-)}-\\
&\qquad-\Omega_{R1}^2\big[L_2^{(-)*}+L_1^{(-)}\big]\rho_{33}^{(0)}=0\,,
\end{aligned}\tag{B.9}$$

$$\begin{aligned}
&\Big\{G+\Omega_{R1}^2\big[L_2^{(-)}+L_1^{(-)*}\big]+\Omega_{R20}^2\big[M_{21}^{(-)}+M_{12}^{(-)*}\big]-\\
&-i(\Delta_R-k_{12}\upsilon)\Big\}\rho_{21}^{(+)}+\Omega_{R20}^2 M_{21}^{(-)}e^{-i\theta}\rho_{22}^{(+)}+\\
&+\Omega_{R20}^2 M_{12}^{(-)*}e^{-i\theta}\rho_{11}^{(+)}+\Omega_{R1}^2 L_1^{(-)*}\rho_{11}^{(0)}+\Omega_{R1}^2 L_2^{(-)}\rho_{22}^{(0)}-\\
&-\Omega_{R20}^2\big[M_{21}^{(-)}+M_{12}^{(-)*}\big]e^{-i\theta}\rho_{33}^{(+)}-\\
&\qquad-\Omega_{R1}^2\big[L_2^{(-)}+L_1^{(-)*}\big]\rho_{33}^{(0)}=0\,.
\end{aligned}\tag{B.10}$$

In these equations, the two-photon (Raman) detuning $\Delta_R{=}\omega_1{-}\omega_2{-}\Omega_g$ and absolute value of the Rabi frequency $\Omega_{R20}{=}|\Omega_{R2}|$ have been introduced. The following notations for saturation parameters (S) and complex Lorentzian (L and M) have been also exploited:

$$
\begin{aligned}
S_{mn}^{\pm} &= \frac{|\Omega_{Rn}|^2}{\Gamma_{eg}^2 + (\omega_m - \omega_{3m} \pm k_m \upsilon)^2}\,, \\
L_m^{\pm} &= \frac{1}{\Gamma_{eg} + i(\omega_m - \omega_{3m} \pm k_m \upsilon)}\,, \\
M_{mn}^{\pm} &= \frac{1}{\Gamma_{eg} + i(\omega_m - \omega_{3m} \pm [k_m - 2k_n]\upsilon)}\,.
\end{aligned}
$$

It is also convenient to replace $\omega_1{-}\omega_{31}{=}\Delta{+}\Delta_R/2$ and $\omega_2{-}\omega_{32}{=}\Delta{-}\Delta_R/2$ with Δ the one-photon detuning from the state $|3\rangle$, which has been scanned in the experiments to observe the absorption profiles.

Instead of the analogous equations for the space harmonics of excited-state population ρ_{33} (which are pretty long), the following common equation can be derived by summing the equations for the populations of all states ρ_{33}, ρ_{22} and ρ_{11} from (A.2):

$$
\begin{aligned}
\Big(\frac{\partial}{\partial t} + \upsilon\frac{\partial}{\partial z} + G\Big)\,[\rho_{11} + \rho_{22} + \rho_{33}] &+ \\
+2\Gamma(1-\beta)\rho_{33} &= G\,.
\end{aligned}
$$

In particular, for zero space harmonics, we get:

$$
\rho_{11}^{(0)} + \rho_{22}^{(0)} + \rho_{33}^{(0)} = 1 - 2\Gamma\tau(1-\beta)\rho_{33}^{(0)} \tag{B.11}
$$

with $\tau{\equiv}G^{-1}$. This equation has a very clear sense. In the case of an open system of atomic energy levels ($\beta{<}1$), full track of density matrix $\widehat{\rho}^{(0)}$ over the time τ decreases in the value $2\Gamma(1{-}\beta)\rho_{33}^{(0)}{\times}\tau$. For a closed system of levels ($\beta{=}1$), we have the obvious expression $\mathrm{Tr}[\widehat{\rho}^{(0)}]{=}1$. For the other harmonics, equations are also very simple:

$$
\begin{aligned}
(G - 2ik_{12}\upsilon)\,[\rho_{11}^{(-)} + \rho_{22}^{(-)} + \rho_{33}^{(-)}] &+ \\
+2\Gamma(1-\beta)\rho_{33}^{(-)} &= 0\,,
\end{aligned} \tag{B.12}
$$

and

$$
\begin{aligned}
(G + 2ik_{12}\upsilon)\,[\rho_{11}^{(+)} + \rho_{22}^{(+)} + \rho_{33}^{(+)}] &+ \\
+2\Gamma(1-\beta)\rho_{33}^{(+)} &= 0\,,
\end{aligned} \tag{B.13}
$$

Finally, the system of equations (B.1)-(B.13) can be written in the vector form:

$$
\widehat{\mathcal{L}}\boldsymbol{\rho} = \mathbf{C_0}\,, \tag{B.14}
$$

where we introduce the vector:

$$
\boldsymbol{\rho} = \{\rho_{11}^{(0)}, \rho_{22}^{(0)}, \rho_{33}^{(0)}, \rho_{11}^{(-)}, \rho_{22}^{(-)}, \rho_{33}^{(-)}, \rho_{12}^{(-)}, \ldots, \rho_{21}^{(+)}\}^{\mathrm{T}}\,.
$$

The vector $\mathbf{C_0}$ has a simple structure:

$$
\mathbf{C}_0 = \{G/2, G/2, G, 0, \ldots, 0\}^{\mathrm{T}}\,,
$$

and the matrix elements of the Liouvillian $\widehat{\mathcal{L}}$ can be defined from the explicit forms of the equations written above. Then the solution of the system is $\boldsymbol{\rho}{=}\widehat{\mathcal{L}}^{-1}\mathbf{C_0}$.

Appendix C

Density matrix elements - Zeeman CPT

This appendix contains the system of equations for the density matrix elements, which must be numerically solved to obtain the absorption profiles presented in the subsection A.10. As the system presented in Appendix B, the following system has been derived by substituting (A.3)-(A.5) and (A.15, A.16) into the master equation (A.2). Thus, for the upper state population we can take the simple equation:

$$G\Big(\rho_{11}+\rho_{22}+\rho_{33}\Big)+2\Gamma(1-\beta)\rho_{33}=G\,. \tag{C.1}$$

For the ground state sub-levels we get:

$$\begin{aligned}&\Big(G+2\Gamma_{eg}\big[S_{-1}+S_{-2}\big]\Big)\rho_{11}-\\&\qquad-\Big(\beta\Gamma+2\Gamma_{eg}\big[S_{-1}+S_{-2}\big]\Big)\rho_{33}+\\&+\Big\{(\Omega_{R1}^2L_{-1}+\Omega_{R2}^2L_{-2})\rho_{12}+c.c.\Big\}=\frac{G}{2}\,,\end{aligned} \tag{C.2}$$

and

$$\begin{aligned}&\Big(G+2\Gamma_{eg}\big[S_{+1}+S_{+2}\big]\Big)\rho_{22}-\\&\qquad-\Big(\beta\Gamma+2\Gamma_{eg}\big[S_{+1}+S_{+2}\big]\Big)\rho_{33}+\\&+\Big\{(\Omega_{R1}^2L_{+1}^*+\Omega_{R2}^2L_{+2}^*)\rho_{12}+c.c.\Big\}=\frac{G}{2}\,.\end{aligned} \tag{C.3}$$

For the low-frequency (Zeeman) coherence, we have:

$$\begin{aligned}&(\Omega_{R1}^2L_{-1}+\Omega_{R2}^{2*}L_{-2})\rho_{11}+(\Omega_{R1}^2L_{+1}^*+\Omega_{R2}^{2*}L_{+2}^*)\rho_{22}-\\&\qquad-\Big[\Omega_{R1}^2(L_{-1}+L_{+1}^*)+\Omega_{R2}^{2*}(L_{-2}+L_{+2}^*)\Big]\rho_{33}+\\&+\Big[G-2i\Omega+\Omega_{R1}^2(L_{-1}+L_{+1}^*)+\\&\qquad\qquad+\Omega_{R20}^2(L_{-2}+L_{+2}^*)\Big]\rho_{12}=0\,.\end{aligned} \tag{C.4}$$

The equation for $\rho_{21}{=}\rho_{12}^*$ can be obtained by complex conjugation of the last one. The new notations for complex Lorenzians and saturation parameters have been introduced:

$$S_{\pm1,2}=\frac{|\Omega_{R1,2}|^2}{\Gamma_{eg}^2+(\Delta_{1,2}\pm\Omega)^2}\,,$$

$$L_{\pm1,2}=\frac{1}{\Gamma_{eg}+i(\Delta_{1,2}\pm\Omega)}\,,$$

where $\Delta_{1,2}=\Delta\mp kv$ are the one-photon detunings for counter-propagating waves.
By analogy with Appendix B, we can compose the vector

$$\boldsymbol{\rho} = \left\{\rho_{11}, \rho_{22}, \rho_{33}, \rho_{12}, \rho_{21}\right\}^{\mathrm{T}},$$

and rewrite the system in the matrix form again

$$\widehat{\mathcal{L}}\boldsymbol{\rho} = \mathbf{C_0}\,, \tag{C.5}$$

Now the Liouvillian $\widehat{\mathcal{L}}$ is much shorter than in the case of the spectroscopic model described in paragraph A.9 and Appendix B. The solution of the presented system of equations can be found in the same way: $\boldsymbol{\rho}=\widehat{\mathcal{L}}^{-1}\mathbf{C_0}$.

Appendix D

Electronic diagrams

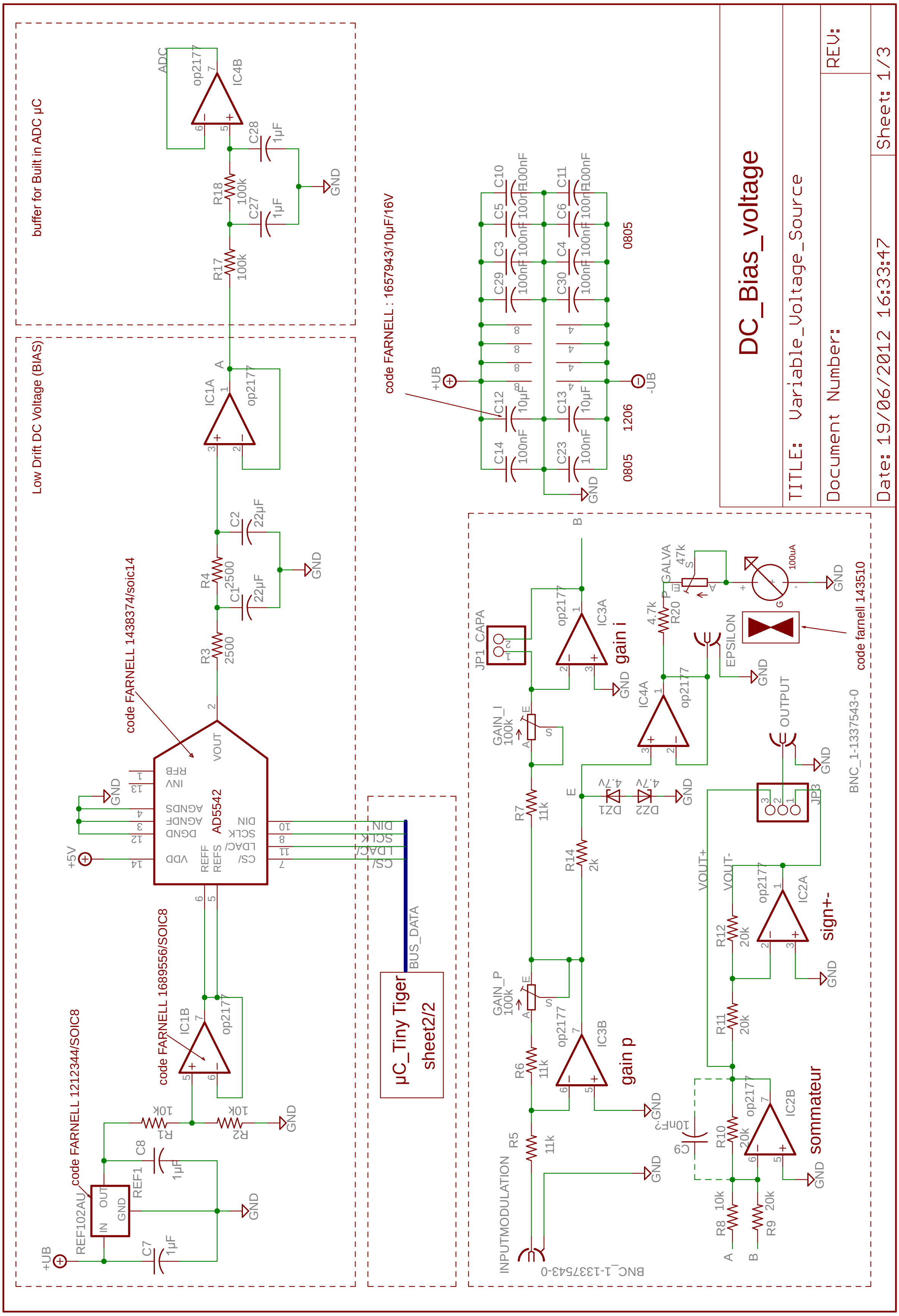

Figure D.1: Diagram of the EOM carrier suppression stabilization electronics. Design by C. Rocher and R. Boudot (FEMTO-ST).

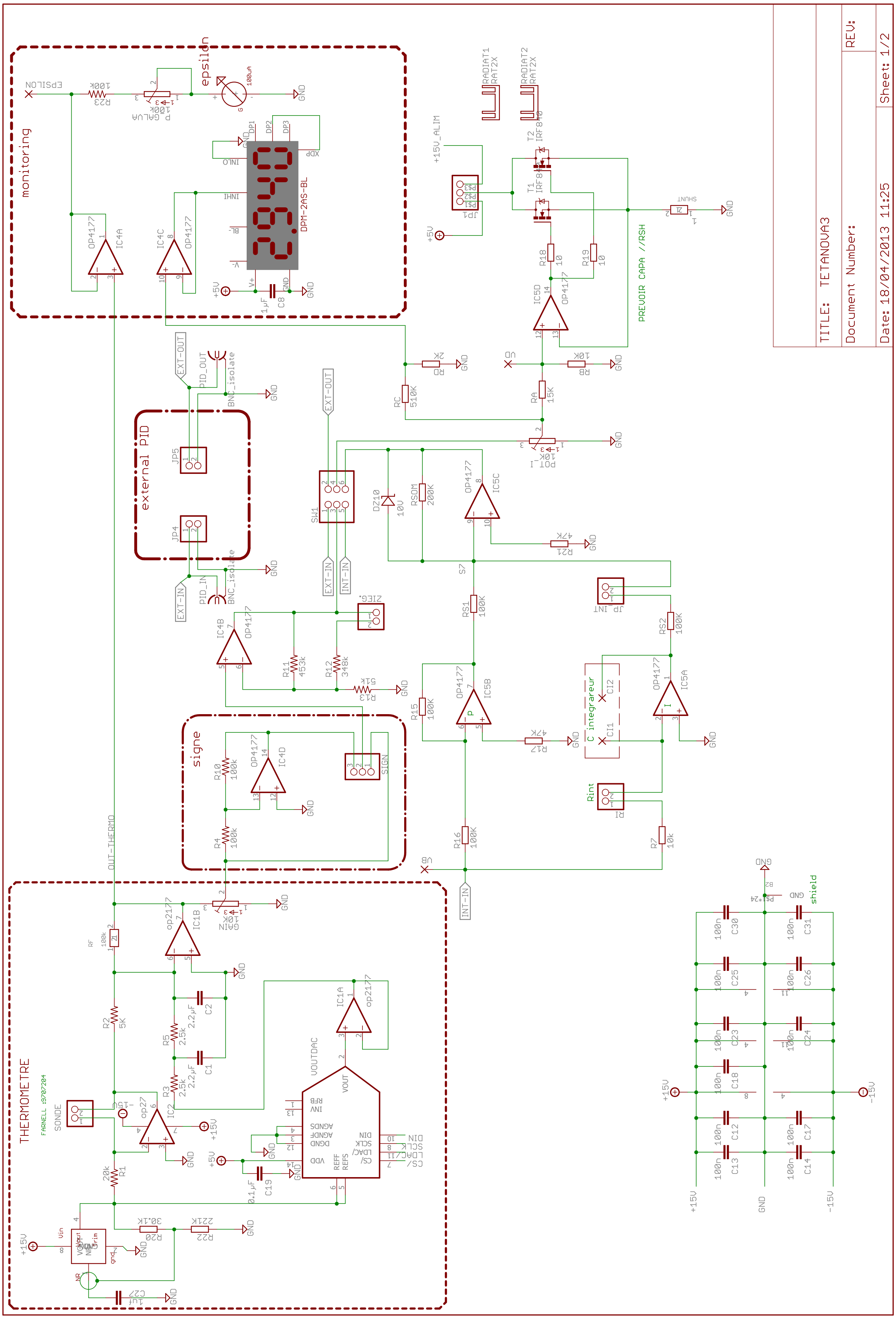

Figure D.2: Electronic diagram of the EOM temperature controller. Design by C. Rocher, E. Rubiola and R. Boudot (FEMTO-ST).

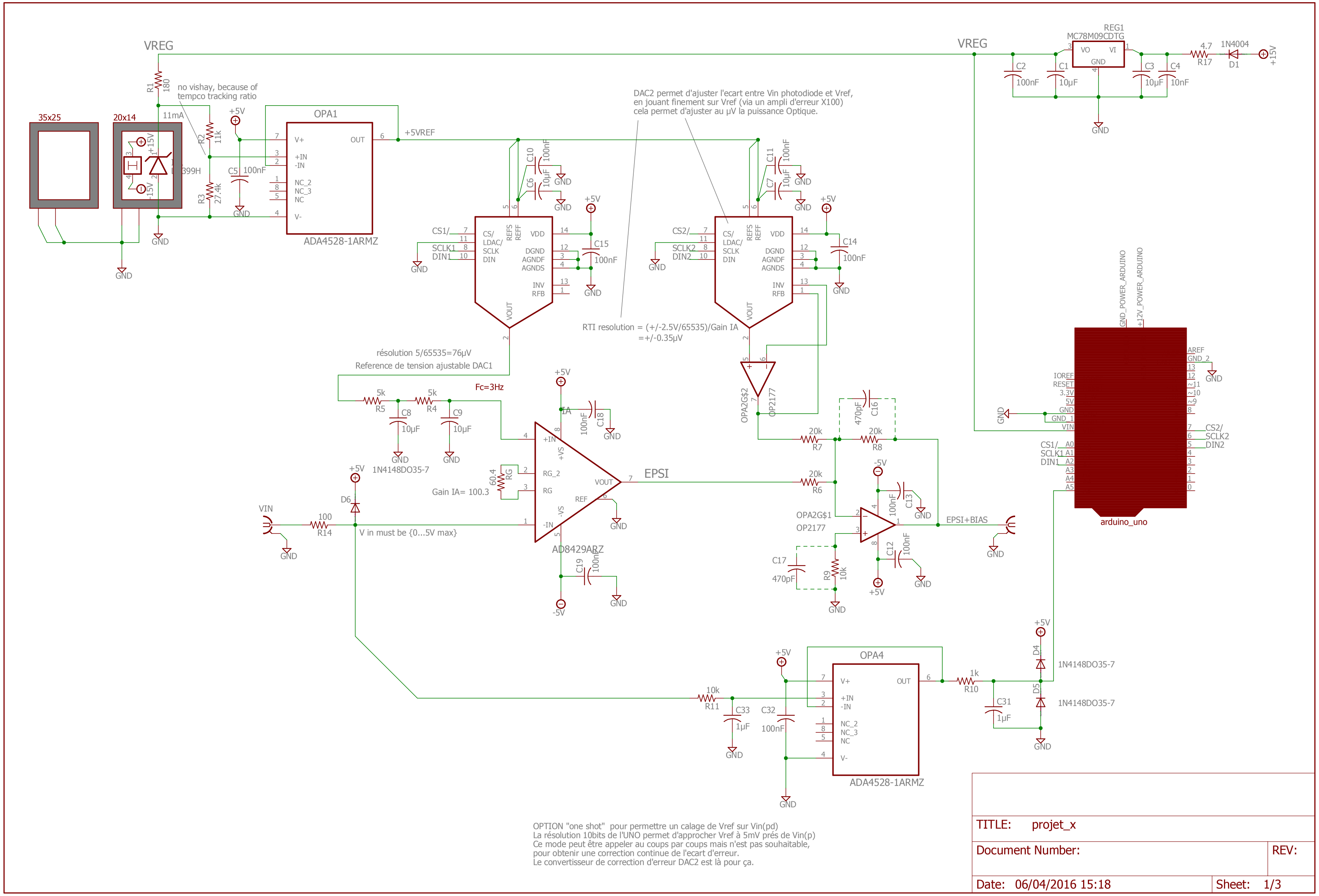

DAC2 permet d'ajuster l'ecart entre Vin photodiode et Vref, en jouant finement sur Vref (via un ampli d'erreur X100) cela permet d'ajuster au µV la puissance Optique.

RTI resolution = (+/-2.5V/65535)/Gain IA
=+/-0.35µV

OPTION "one shot" pour permettre un calage de Vref sur Vin(pd)
La résolution 10bits de l'UNO permet d'approcher Vref à 5mV prés de Vin(p)
Ce mode peut être appeler au coups par coups mais n'est pas souhaitable,
pour obtenir une correction continue de l'ecart d'erreur.
Le convertisseur de correction d'erreur DAC2 est là pour ça.

TITLE: projet_x
Document Number:
REV:
Date: 06/04/2016 15:18
Sheet: 1/3

Figure D.3: Electronic diagram of the LPSS. Design by C. Rocher (FEMTO-ST).

Bibliography

[1] C. Cohen-Tannoudji, B. Diu, and F. Laloë. *Quantum Mechanics*. Wiley, 1977. ISBN 978-0-471-16432-6.

[2] L. Essen and J. V. L. Parry. An Atomic Standard of Frequency and Time Interval: A Cæsium Resonator. *Nature*, 176(4476):280–282, August 1955. ISSN 0028-0836. doi:10.1038/176280a0.

[3] A. Kastler. Optical methods of atomic orientation and of magnetic resonance. *JOSA*, 47(6): 460–465, 1957.

[4] C. E. Wieman and L. Hollberg. Using diode lasers for atomic physics. *Review of scientific instruments*, 62(1):1–20, 1991.

[5] S. Chu. The manipulation of neutral particles. *Reviews of Modern Physics*, 70(3):685, 1998.

[6] C. N. Cohen-Tannoudji. Manipulating atoms with photons. *Reviews of Modern Physics*, 70(3): 707, 1998.

[7] W. D. Phillips. Laser cooling and trapping of neutral atoms. *Reviews of Modern Physics*, 70 (3):721, 1998.

[8] M. H. Anderson, J. R. Ensher, M. R. Matthews, C. E. Wieman, and E. A. Cornell. Observation of Bose-Einstein Condensation in a Dilute Atomic Vapor. *Science*, 269(5221):198–201, July 1995. ISSN 0036-8075, 1095-9203. doi:10.1126/science.269.5221.198.

[9] K. B. Davis, M. O. Mewes, M. R. Andrews, N. J. van Druten, D. S. Durfee, D. M. Kurn, and W. Ketterle. Bose-Einstein Condensation in a Gas of Sodium Atoms. *Physical Review Letters*, 75 (22):3969–3973, November 1995. ISSN 0031-9007, 1079-7114. doi:10.1103/PhysRevLett.75.3969.

[10] C. C. Bradley, C. A. Sackett, J. J. Tollett, and R. G. Hulet. Evidence of Bose-Einstein condensation in an atomic gas with attractive interactions. *Physical Review Letters*, 75(9):1687, 1995.

[11] T. Kessler, C. Hagemann, C. Grebing, T. Legero, U. Sterr, F. Riehle, M. J. Martin, L. Chen, and J. Ye. A sub-40-mHz-linewidth laser based on a silicon single-crystal optical cavity. *Nature Photonics*, 6(10):687–692, September 2012. ISSN 1749-4885, 1749-4893. doi:10.1038/nphoton.2012.217.

[12] R. W. P. Drever, J. L. Hall, F. V. Kowalski, J. Hough, G. M. Ford, A. J. Munley, and H. Ward. Laser phase and frequency stabilization using an optical resonator. *Applied Physics B*, 31(2): 97–105, 1983.

[13] S. A. Diddams, D. J. Jones, J. Ye, S. T. Cundiff, J. L. Hall, J. K. Ranka, R. S. Windeler, R. Holzwarth, T. Udem, and T. W. Hänsch. Direct link between microwave and optical frequencies with a 300 THz femtosecond laser comb. *Physical Review Letters*, 84(22):5102, 2000.

[14] M. Schioppo, R. C. Brown, W. F. McGrew, N. Hinkley, R. J. Fasano, K. Beloy, T. H. Yoon, G. Milani, D. Nicolodi, J. A. Sherman, N. B. Phillips, C. W. Oates, and A. D. Ludlow. Ultrastable optical clock with two cold-atom ensembles. *Nature Photonics*, 11(1):48–52, November 2016. ISSN 1749-4885, 1749-4893. doi:10.1038/nphoton.2016.231.

[15] B. J. Bloom, T. L. Nicholson, J. R. Williams, S. L. Campbell, M. Bishof, X. Zhang, W. Zhang, S. L. Bromley, and J. Ye. An optical lattice clock with accuracy and stability at the 10^{-18} level. *Nature*, 506(7486):71–75, January 2014. ISSN 0028-0836, 1476-4687. doi:10.1038/nature12941.

[16] Y. Y. Jiang, A. D. Ludlow, N. D. Lemke, R. W. Fox, J. A. Sherman, L.-S. Ma, and C. W. Oates. Making optical atomic clocks more stable with 10^{-16}-level laser stabilization. *Nature Photonics*, 5(3):158–161, March 2011. ISSN 1749-4885, 1749-4893. doi:10.1038/nphoton.2010.313.

[17] C. Chou, D. Hume, J. Koelemeij, D. Wineland, and T. Rosenband. Frequency Comparison of Two High-Accuracy Al^{+} Optical Clocks. *Physical Review Letters*, 104(7), February 2010. ISSN 0031-9007, 1079-7114. doi:10.1103/PhysRevLett.104.070802.

[18] R. Tyumenev, M. Favier, S. Bilicki, E. Bookjans, R. L. Targat, J. Lodewyck, D. Nicolodi, Y. L. Coq, M. Abgrall, J. Guéna, L. D. Sarlo, and S. Bize. Comparing a mercury optical lattice clock with microwave and optical frequency standards. *New Journal of Physics*, 18(11):113002, November 2016. ISSN 1367-2630. doi:10.1088/1367-2630/18/11/113002.

[19] S. M. F. Raupach, A. Koczwara, and G. Grosche. Optical frequency transfer via a 660 km underground fiber link using a remote Brillouin amplifier. *Optics Express*, 22(22):26537, November 2014. ISSN 1094-4087. doi:10.1364/OE.22.026537.

[20] S. Droste, F. Ozimek, T. Udem, K. Predehl, T. W. Hänsch, H. Schnatz, G. Grosche, and R. Holzwarth. Optical-Frequency Transfer over a Single-Span 1840 km Fiber Link. *Physical Review Letters*, 111(11), September 2013. ISSN 0031-9007, 1079-7114. doi:10.1103/PhysRevLett.111.110801.

[21] C. Lisdat, G. Grosche, N. Quintin, C. Shi, S. Raupach, C. Grebing, D. Nicolodi, F. Stefani, A. Al-Masoudi, S. Dörscher, S. Häfner, J.-L. Robyr, N. Chiodo, S. Bilicki, E. Bookjans, A. Koczwara, S. Koke, A. Kuhl, F. Wiotte, F. Meynadier, E. Camisard, M. Abgrall, M. Lours, T. Legero, H. Schnatz, U. Sterr, H. Denker, C. Chardonnet, Y. Le Coq, G. Santarelli, A. Amy-Klein, R. Le Targat, J. Lodewyck, O. Lopez, and P.-E. Pottie. A clock network for geodesy and fundamental science. *Nature Communications*, 7:12443, August 2016. ISSN 2041-1723. doi:10.1038/ncomms12443.

[22] J. Camparo. The rubidium atomic clock and basic research. *Physics Today*, 60(11):33–39, November 2007. ISSN 0031-9228, 1945-0699. doi:10.1063/1.2812121.

[23] V. Formichella, J. Camparo, and P. Tavella. Influence of the ac-Stark shift on GPS atomic clock timekeeping. *Applied Physics Letters*, 110(4):043506, January 2017. ISSN 0003-6951, 1077-3118. doi:10.1063/1.4975071.

[24] S. Micalizio, C. E. Calosso, A. Godone, and F. Levi. Metrological characterization of the pulsed Rb clock with optical detection. *Metrologia*, 49(4):425–436, August 2012. ISSN 0026-1394, 1681-7575. doi:10.1088/0026-1394/49/4/425.

[25] J.-M. Danet, M. Lours, S. Guérandel, and E. De Clercq. Dick effect in a pulsed atomic clock using coherent population trapping. *IEEE Transactions on Ultrasonics, Ferroelectrics, and Frequency Control*, 61(4):567–574, April 2014. ISSN 0885-3010. doi:10.1109/TUFFC.2014.2945.

[26] T. Bandi, C. Affolderbach, C. Stefanucci, F. Merli, A. K. Skrivervik, and G. Mileti. Compact high-performance continuous-wave double-resonance rubidium standard with 1.4 10^{-13} $\tau^{-1/2}$ stability. *IEEE Transactions on Ultrasonics, Ferroelectrics, and Frequency Control*, 61(11): 1769–1778, November 2014. ISSN 0885-3010. doi:10.1109/TUFFC.2013.005955.

[27] IND55 Mclocks - European Metrology Research Programme (EMRP). http://www.inrim.it/Mclocks/.

[28] Muquans. MuClock A high-performance frequency standard based on cold atoms. https://www.muquans.com/images/stories/muquans_muclock.pdf.

[29] G. Alzetta, A. Gozzini, L. Moi, and G. Orriols. An experimental method for the observation of rf transitions and laser beat resonances in oriented Na vapour. *Il Nuovo Cimento B (1971-1996)*, 36(1):5–20, 1976.

[30] H. Schuh and D. Behrend. VLBI: A fascinating technique for geodesy and astrometry. *Journal of Geodynamics*, 61:68–80, October 2012. ISSN 02643707. doi:10.1016/j.jog.2012.07.007.

[31] Symmetricom. Better Undersea Sensing with the Quantum^{TM} SA.45s Chip Scale Atomic Clock (CSAC). `http://www.scientific-devices.com.au/pdfs/WeTransfer-NZvJB6Cw/Frequency/Better%20Undersea%20Sensing%20using%20Chip%20Scale%20Atomic%20Clock.pdf`.

[32] D. Rogers. *Broadband Quantum Cryptography*. Morgan & Claypool Publishers, November 2010. ISBN 978-1-60845-060-2.

[33] A. V. Sergienko. *Quantum Communications and Cryptography*. CRC Press, November 2005. ISBN 978-1-4200-2660-3.

[34] M.-A. Russon. Atomic clock invention syncs orders ultra-quickly to prevent high-frequency trading fraud. *International Business Times*, August 2016.

[35] L. Shen. This Legendary Hedge Fund Hopes to Use Physics to Battle Wall Street's Speed Demons. *FORTUNE*, July 2016.

[36] R. Bouchendira, P. Cladé, S. Guellati-Khélifa, F. Nez, and F. Biraben. New Determination of the Fine Structure Constant and Test of the Quantum Electrodynamics. *Physical Review Letters*, 106(8), February 2011. ISSN 0031-9007, 1079-7114. doi:10.1103/PhysRevLett.106.080801.

[37] J. D. Anderson, G. Schubert, V. Trimble, and M. R. Feldman. Measurements of Newton's gravitational constant and the length of day. *EPL (Europhysics Letters)*, 110(1):10002, April 2015. ISSN 0295-5075, 1286-4854. doi:10.1209/0295-5075/110/10002.

[38] G. Rosi, F. Sorrentino, L. Cacciapuoti, M. Prevedelli, and G. M. Tino. Precision measurement of the Newtonian gravitational constant using cold atoms. *Nature*, 510(7506):518–521, June 2014. ISSN 0028-0836, 1476-4687. doi:10.1038/nature13433.

[39] G. Gräff, H. Kalinowsky, and J. Traut. A direct determination of the proton electron mass ratio. *Zeitschrift für Physik A: Atoms and Nuclei*, 297(1):35–39, March 1980. ISSN 0340-2193, 1434-601X. doi:10.1007/BF01414243.

[40] J. Vanier and C. Audoin. *The Quantum Physics of Atomic Frequency Standards*. A. Hilger, 1989. ISBN 978-0-85274-433-8.

[41] J. Rutman and F. L. Walls. Characterization of frequency stability in precision frequency sources. *Proceedings of the IEEE*, 79(7):952–960, 1991.

[42] J. R. Vig. Introduction to quartz frequency standards. Technical report, DTIC Document, 1992.

[43] M. Lombardi. Time and Frequency from A to Z, H. https://www.nist.gov/time-and-frequency-services/h, 2010-05-12T13:12-04:00.

[44] E. Rubiola. *Phase Noise and Frequency Stability in Oscillators*. The Cambridge RF and microwave engineering series. Cambridge University Press, November 2008.

[45] Bureau International des Poids et Mesures. Treizième conférence générale des poids et mesures. Technical report, Paris, 1967, 1968.

[46] S. Falke, H. Schnatz, J. S. R. V. Winfred, T. Middelmann, S. Vogt, S. Weyers, B. Lipphardt, G. Grosche, F. Riehle, U. Sterr, and C. Lisdat. The ^{87}Sr optical frequency standard at PTB. *Metrologia*, 48(5):399–407, October 2011. ISSN 0026-1394, 1681-7575. doi:10.1088/0026-1394/48/5/022.

[47] R. Le Targat, L. Lorini, Y. Le Coq, M. Zawada, J. Guéna, M. Abgrall, M. Gurov, P. Rosenbusch, D. G. Rovera, B. Nagórny, R. Gartman, P. G. Westergaard, M. E. Tobar, M. Lours, G. Santarelli, A. Clairon, S. Bize, P. Laurent, P. Lemonde, and J. Lodewyck. Experimental realization of an optical second with strontium lattice clocks. *Nature Communications*, 4, July 2013. ISSN 2041-1723. doi:10.1038/ncomms3109.

[48] A. D. Ludlow, T. Zelevinsky, G. K. Campbell, S. Blatt, M. M. Boyd, M. H. G. de Miranda, M. J. Martin, J. W. Thomsen, S. M. Foreman, J. Ye, T. M. Fortier, J. E. Stalnaker, S. A. Diddams, Y. Le Coq, Z. W. Barber, N. Poli, N. D. Lemke, K. M. Beck, and C. W. Oates. Sr Lattice Clock at 1 10^{-16} Fractional Uncertainty by Remote Optical Evaluation with a Ca Clock. *Science*, 319 (5871):1805–1808, March 2008. ISSN 0036-8075, 1095-9203. doi:10.1126/science.1153341.

[49] T. L. Nicholson, M. J. Martin, J. R. Williams, B. J. Bloom, M. Bishof, M. D. Swallows, S. L. Campbell, and J. Ye. Comparison of Two Independent Sr Optical Clocks with 1 10^{-17} Stability at 10^3 s. *Physical Review Letters*, 109(23), December 2012. ISSN 0031-9007, 1079-7114. doi:10.1103/PhysRevLett.109.230801.

[50] A. A. Madej, P. Dubé, Z. Zhou, J. E. Bernard, and M. Gertsvolf. ^{88}Sr$^+$ 445-THz Single-Ion Reference at the 10^{-17} Level via Control and Cancellation of Systematic Uncertainties and Its Measurement against the SI Second. *Physical Review Letters*, 109(20), November 2012. ISSN 0031-9007, 1079-7114. doi:10.1103/PhysRevLett.109.203002.

[51] N. Huntemann, M. Okhapkin, B. Lipphardt, S. Weyers, C. Tamm, and E. Peik. High-Accuracy Optical Clock Based on the Octupole Transition in ^{171}Yb$^+$. *Physical Review Letters*, 108(9), February 2012. ISSN 0031-9007, 1079-7114. doi:10.1103/PhysRevLett.108.090801.

[52] Bureau International des Poids et Mesures. 22e Conférence générale des poids et mesures. Technical report, 2003.

[53] D. W. Allan. Statistics of atomic frequency standards. *Proceedings of the IEEE*, 54(2):221–230, 1966. ISSN 0018-9219. doi:10.1109/PROC.1966.4634.

[54] R. Szmuk, V. Dugrain, W. Maineult, J. Reichel, and P. Rosenbusch. Stability of a trapped-atom clock on a chip. *Physical Review A*, 92(1), July 2015. ISSN 1050-2947, 1094-1622. doi:10.1103/PhysRevA.92.012106.

[55] S. Knappe, V. Shah, P. D. D. Schwindt, L. Hollberg, J. Kitching, L.-A. Liew, and J. Moreland. A microfabricated atomic clock. *Applied Physics Letters*, 85(9):1460–1462, August 2004. ISSN 0003-6951, 1077-3118. doi:10.1063/1.1787942.

[56] Y. Zhang, W. Yang, S. Zhang, and J. Zhao. Rubidium chip-scale atomic clock with improved long-term stability through light intensity optimization and compensation for laser frequency detuning. *Journal of the Optical Society of America B*, 33(8):1756, August 2016. ISSN 0740-3224, 1520-8540. doi:10.1364/JOSAB.33.001756.

[57] Microsemi. Quantum SA.45s CSAC. https://www.microsemi.com/document-portal/doc_download/133305-quantum-sa-45s-csac, .

[58] J. D. Prestage, Meirong Tu, S. K. Chung, and P. MacNeal. Compact microwave mercury ion clock for space applications. pages 651–654. IEEE, May 2008. ISBN 978-1-4244-1794-0. doi:10.1109/FREQ.2008.4623080.

[59] C. Lacroûte, M. Souidi, P.-Y. Bourgeois, J. Millo, K. Saleh, E. Bigler, R. Boudot, V. Giordano, and Y. Kersalé. Compact Yb $^+$ optical atomic clock project: Design principle and current status. *Journal of Physics: Conference Series*, 723:012025, June 2016. ISSN 1742-6588, 1742-6596. doi:10.1088/1742-6596/723/1/012025.

[60] J. Cao, P. Zhang, J. Shang, K. Cui, J. Yuan, S. Chao, S. Wang, H. Shu, and X. Huang. A transportable ^{40}Ca$^+$ single-ion clock with 7.7 10^{-17} systematic uncertainty. *arXiv preprint arXiv:1607.03731*, 2016.

[61] S. B. Koller, J. Grotti, S. Vogt, A. Al-Masoudi, S. Dörscher, S. Häfner, U. Sterr, and C. Lisdat. Transportable Optical Lattice Clock with 7 10^{-17} Uncertainty. *Physical Review Letters*, 118(7), February 2017. ISSN 0031-9007, 1079-7114. doi:10.1103/PhysRevLett.118.073601.

[62] Oscilloquartz. OSA 3705 Passive Hydrogen Maser. http://www.oscilloquartz.com/files/1383126925-da_3705.pdf, .

[63] Microsemi. 5071A Primary Frequency Standard. http://www.microsemi.com/document-portal/doc_download/133269-5071a, .

[64] V. Hermann, M. Gazard, P. Berthoud, S. Lecomte, R. Ruffieux, C. Audoin, R. Barillet, E. de Clercq, and S. Guerandel. OSCC project: A space Cs beam optically pumped atomic clock for Galileo. In *Frequency Control Symposium, 2007 Joint with the 21st European Frequency and Time Forum. IEEE International*, pages 77–80. IEEE, 2007.

[65] C. Berthoud, C. Audoin, R. Barillet, M. Gazard, M. Haldimann, V. Hermann, S. Lecomte, and R. Ruffieux. Optically-pumped space cesium clock for Galileo : First results of the breadboard. 2008.

[66] E. De Clercq. L'étalon primaire de fréquence à jet de césium du BNM-SYRTE. *125*, 2004(2), 2004.

[67] D. B. Sullivan, J. C. Bergquist, J. J. Bollinger, R. E. Drullinger, W. M. Itano, S. R. Jefferts, W. D. Lee, D. Meekhof, T. E. Parker, F. L. Walls, and others. Primary atomic frequency standards at NIST. *Journal of Research of the National Institute of Standards and Technology*, 106(1):47, 2001.

[68] M. Lombardi. Time and Frequency from A to Z, C to Ce. https://www.nist.gov/time-and-frequency-services/c-ce, 2010-05-12T12:52-04:00.

[69] Oscilloquartz. OSA 3030B EUDICS. http://www.oscilloquartz.com/files/1396965064-Br_3030B%20EUDICS.pdf, .

[70] T4Science. pH Maser 1008 Passive hydrogen maser clock. https://www.t4science.com/wp-content/uploads/2016/09/pH-Maser_Clock_Spec.pdf, .

[71] J. Li, J. Zhang, Y. Bu, C. Cao, W. Wang, and H. Zheng. Space passive hydrogen maser a passive hydrogen maser for space applications. In *Frequency Control Symposium (IFCS), 2016 IEEE International*, pages 1–5. IEEE, 2016.

[72] F. Droz, P. Mosset, Q. Wang, P. Rochat, M. Belloni, M. Gioia, A. Resti, and P. Waller. Space passive hydrogen maser-Performances and lifetime data. In *2009 IEEE International Frequency Control Symposium Joint with the 22nd European Frequency and Time Forum*, pages 393–398. IEEE, 2009.

[73] J. Camparo, I. Sesia, V. Formichella, G. Signorile, L. Galleani, and P. Tavella. Rubidium clock lamplight variations and long-term frequency instability: First analyses of multiyear GPS data. In *Proc. 2016 Precise Time and Time Interval Meeting*, 2016.

[74] J. Vanier and C. Mandache. The passive optically pumped Rb frequency standard: The laser approach. *Applied Physics B*, 87(4):565–593, June 2007. ISSN 0946-2171, 1432-0649. doi:10.1007/s00340-007-2643-5.

[75] Microsemi. Portfolio of High-Performance Rubidium Oscillators. http://www.microsemi.com/document-portal/doc_view/134379-high-performance-rubidium-oscillators, .

[76] spectratime. Low Cost & Profile Frequency Rubidium Standard (LPFRS). http://www.spectratime.com/uploads/documents/isource/iSource_LPFRS%20Spec.pdf, 2014.

[77] M. Lombardi. Time and Frequency from A to Z, Re to Ru. https://www.nist.gov/time-and-frequency-services/re-ru, 2010-05-12T17:38-04:00.

[78] R. J. Carpenter, E. C. Beaty, P. L. Bender, S. Saito, and R. O. Stone. A prototype rubidium vapor frequency standard. *IRE Transactions on Instrumentation*, 1(2):132–135, 1960.

[79] T4Science. iMaser 3000 Smart active hydrogen maser clock. https://www.t4science.com/wp-content/uploads/2016/06/iMaser_Clock_Spec.pdf, .

[80] T. Bandi, C. Affolderbach, C. E. Calosso, and G. Mileti. High-performance laser-pumped rubidium frequency standard for satellite navigation. *Electronics letters*, 47(12):698–699, 2011.

[81] C. Stefanucci, T. Bandi, F. Merli, M. Pellaton, C. Affolderbach, G. Mileti, and A. K. Skrivervik. Compact microwave cavity for high performance rubidium frequency standards. *Review of Scientific Instruments*, 83(10):104706, 2012. ISSN 00346748. doi:10.1063/1.4759023.

[82] T. Bandi, C. Affolderbach, and G. Mileti. Laser-pumped paraffin-coated cell rubidium frequency standard. *Journal of Applied Physics*, 111(12):124906, June 2012. ISSN 0021-8979, 1089-7550. doi:10.1063/1.4729570.

[83] C. E. Calosso, A. Godone, F. Levi, and S. Micalizio. Enhanced temperature sensitivity in vapor-cell frequency standards. *IEEE Transactions on Ultrasonics, Ferroelectrics and Frequency Control*, 59(12):2646–2654, December 2012. ISSN 0885-3010. doi:10.1109/TUFFC.2012.2505.

[84] N. F. Ramsey. A molecular beam resonance method with separated oscillating fields. *Physical Review*, 78(6):695, 1950.

[85] A. Godone, S. Micalizio, F. Levi, and C. Calosso. Physics characterization and frequency stability of the pulsed rubidium maser. *Physical Review A*, 74(4), October 2006. ISSN 1050-2947, 1094-1622. doi:10.1103/PhysRevA.74.043401.

[86] S. Micalizio, A. Godone, C. Calosso, F. Levi, C. Affolderbach, and F. Gruet. Pulsed optically pumped rubidium clock with high frequency-stability performance. *IEEE Transactions on Ultrasonics, Ferroelectrics and Frequency Control*, 59(3):457–462, March 2012. ISSN 0885-3010. doi:10.1109/TUFFC.2012.2215.

[87] S. Micalizio, A. Godone, F. Levi, B. François, C. E. Calosso, A. Battisti, M. Gioia, and A. Borella. The pulsed optically pumped Rb frequency standard: A proposal for a space atomic clock. In *Metrology for Aerospace (MetroAeroSpace), 2015 IEEE*, pages 384–388. IEEE, 2015.

[88] G. A. Pitz, D. E. Wertepny, and G. P. Perram. Pressure broadening and shift of the cesium D_1 transition by the noble gases and N_2, H_2, HD, D_2, CH_4, C_2H_6, CF_4, and ^{3}He. *Physical Review A*, 80(6), December 2009. ISSN 1050-2947, 1094-1622. doi:10.1103/PhysRevA.80.062718.

[89] B. François, C. E. Calosso, J.-M. Danet, and R. Boudot. A low phase noise microwave frequency synthesis for a high-performance cesium vapor cell atomic clock. *Review of Scientific Instruments*, 85(9):094709, September 2014. ISSN 0034-6748, 1089-7623. doi:10.1063/1.4896043.

[90] B. François, C. E. Calosso, M. Abdel Hafiz, S. Micalizio, and R. Boudot. Simple-design ultra-low phase noise microwave frequency synthesizers for high-performing Cs and Rb vapor-cell atomic clocks. *Review of Scientific Instruments*, 86(9):094707, September 2015. ISSN 0034-6748, 1089-7623. doi:10.1063/1.4929384.

[91] S. Kang, M. Gharavipour, C. Affolderbach, F. Gruet, and G. Mileti. Demonstration of a high-performance pulsed optically pumped Rb clock based on a compact magnetron-type microwave cavity. *Journal of Applied Physics*, 117(10):104510, March 2015. ISSN 0021-8979, 1089-7550. doi:10.1063/1.4914493.

[92] J. Lin, J. Deng, Y. Ma, H. He, and Y. Wang. Detection of ultrahigh resonance contrast in vapor-cell atomic clocks. *Optics letters*, 37(24):5036–5038, 2012.

[93] G. Dong, J. Deng, J. Lin, S. Zhang, H. Lin, and Y. Wang. Recent improvements on the pulsed optically pumped rubidium clock at SIOM. *Chinese Optics Letters*, 15(4):040201, 2017.

[94] N. Cyr, M. Tetu, and M. Breton. All-optical microwave frequency standard: A proposal. *IEEE Transactions on Instrumentation and Measurement*, 42(2):640–649, April 1993. ISSN 00189456. doi:10.1109/19.278645.

[95] S. Knappe, R. Wynands, J. Kitching, H. G. Robinson, and L. Hollberg. Characterization of coherent population-trapping resonances as atomic frequency references. *JOSA B*, 18(11):1545–1553, 2001.

[96] M. Merimaa, T. Lindvall, I. Tittonen, and E. Ikonen. All-optical atomic clock based on coherent population trapping in 85 Rb. *JOSA B*, 20(2):273–279, 2003.

[97] S. Khripunov, D. Radnatarov, and S. Kobtsev. Atomic clock based on a coherent population trapping resonance in ^{87}Rb with improved high-frequency modulation parameters. volume 9378, pages 93780A–93780A–6, 2015. doi:10.1117/12.2080165.

[98] S. Knappe. Emerging Topics : MEMS Atomic Clocks. In *Comprehensive Microsystems*, volume 3, pages 571–612. Elsevier, Oxford, 2008. ISBN 978-0-444-52190-3.

[99] J. Haesler, L. Balet, J.-A. Porchet, T. Overstolz, J. Pierer, R. J. James, S. Grossmann, D. Ruffieux, and S. Lecomte. The integrated swiss miniature atomic clock. pages 579–581. IEEE, July 2013. ISBN 978-1-4799-0342-9. doi:10.1109/EFTF-IFC.2013.6702125.

[100] E. Kroemer, J. Rutkowski, V. Maurice, R. Vicarini, M. Abdel Hafiz, C. Gorecki, and R. Boudot. Characterization of commercially available vertical-cavity surface-emitting lasers tuned on Cs D_1 line at 894.6 nm for miniature atomic clocks. *Applied Optics*, 55(31):8839, November 2016. ISSN 0003-6935, 1539-4522. doi:10.1364/AO.55.008839.

[101] M. Zhu. High contrast signal in a coherent population trapping based atomic frequency standard application. In *Frequency Control Symposium and PDA Exhibition Jointly with the 17th European Frequency and Time Forum, 2003. Proceedings of the 2003 IEEE International*, pages 16–21. IEEE, 2003.

[102] P. Yun, F. Tricot, C. E. Calosso, S. Micalizio, B. François, R. Boudot, S. Guérandel, and E. de Clercq. High-performance coherent population trapping clock with polarization modulation. *arXiv preprint arXiv:1610.00170*, 2016.

[103] P. Yun, J.-M. Danet, D. Holleville, E. de Clercq, and S. Guérandel. Constructive polarization modulation for coherent population trapping clock. *Applied Physics Letters*, 105(23):231106, December 2014. ISSN 0003-6951, 1077-3118. doi:10.1063/1.4903862.

[104] P. Yun, S. Guérandel, and E. de Clercq. Coherent population trapping with polarization modulation. *Journal of Applied Physics*, 119(24):244502, June 2016. ISSN 0021-8979, 1089-7550. doi:10.1063/1.4954690.

[105] M. Huang and J. C. Camparo. Coherent population trapping under periodic polarization modulation: Appearance of the CPT doublet. *Physical Review A*, 85(1), January 2012. ISSN 1050-2947, 1094-1622. doi:10.1103/PhysRevA.85.012509.

[106] A. Godone, F. Levi, S. Micalizio, and C. Calosso. Coherent-population-trapping maser: Noise spectrum and frequency stability. *Physical Review A*, 70(1), July 2004. ISSN 1050-2947, 1094-1622. doi:10.1103/PhysRevA.70.012508.

[107] S. Guérandel, J.-M. Danet, P. Yun, and E. De Clercq. High performance compact atomic clock based on coherent population trapping. In *2014 IEEE International Frequency Control Symposium (FCS)*, pages 1–5. IEEE, 2014.

[108] F. Tricot, P. Yun, B. Francois, S. Mejri, J.-M. Danet, M. Lours, S. Guerandel, and E. de Clercq. Progress on a pulsed CPT clock: Reduction of the main noise source contributions. pages 1–3. IEEE, April 2016. ISBN 978-1-5090-0720-2. doi:10.1109/EFTF.2016.7477813.

[109] N. Castagna, S. Guérandel, F. Dahes, T. Zanon, E. De Clercq, A. Clairon, and N. Dimarcq. Frequency stability measurement of a Raman-Ramsey Cs clock. In *2007 IEEE International Frequency Control Symposium Joint with the 21st European Frequency and Time Forum*, pages 67–70. IEEE, 2007.

[110] S. Guérandel, T. Zanon, N. Castagna, F. Dahes, E. de Clercq, N. Dimarcq, and A. Clairon. Raman-Ramsey Interaction for Coherent Population Trapping Cs Clock. *IEEE Transactions on Instrumentation and Measurement*, 56(2):383–387, April 2007. ISSN 0018-9456. doi:10.1109/TIM.2007.891124.

[111] R. Boudot, S. Guerandel, E. De Clercq, N. Dimarcq, and A. Clairon. Current Status of a Pulsed CPT Cs Cell Clock. *IEEE Transactions on Instrumentation and Measurement*, 58(4): 1217–1222, April 2009. ISSN 0018-9456. doi:10.1109/TIM.2008.2009918.

[112] J. E. Thomas, P. R. Hemmer, S. Ezekiel, C. C. Leiby Jr, R. H. Picard, and C. R. Willis. Observation of Ramsey fringes using a stimulated, resonance Raman transition in a sodium atomic beam. *Physical Review Letters*, 48(13):867, 1982.

[113] T. Zanon, S. Guerandel, E. de Clercq, D. Holleville, N. Dimarcq, and A. Clairon. High Contrast Ramsey Fringes with Coherent-Population-Trapping Pulses in a Double Lambda Atomic System. *Physical Review Letters*, 94(19), May 2005. ISSN 0031-9007, 1079-7114. doi:10.1103/PhysRevLett.94.193002.

[114] O. Kozlova, J.-M. Danet, S. Guerandel, and E. de Clercq. Limitations of Long-Term Stability in a Coherent Population Trapping Cs Clock. *IEEE Transactions on Instrumentation and Measurement*, 63(7):1863–1870, July 2014. ISSN 0018-9456, 1557-9662. doi:10.1109/TIM.2014.2298672.

[115] F.-X. Esnault, E. Blanshan, E. N. Ivanov, R. E. Scholten, J. Kitching, and E. A. Donley. Cold-atom double- λ coherent population trapping clock. *Physical Review A*, 88(4), October 2013. ISSN 1050-2947, 1094-1622. doi:10.1103/PhysRevA.88.042120.

[116] F.-X. Esnault, D. Holleville, N. Rossetto, S. Guérandel, and N. Dimarcq. High-stability compact atomic clock based on isotropic laser cooling. *Physical Review A*, 82(3), September 2010. ISSN 1050-2947, 1094-1622. doi:10.1103/PhysRevA.82.033436.

[117] F.-X. Esnault, N. Rossetto, D. Holleville, J. Delporte, and N. Dimarcq. HORACE: A compact cold atom clock for Galileo. *Advances in Space Research*, 47(5):854–858, March 2011. ISSN 02731177. doi:10.1016/j.asr.2010.12.012.

[118] M. Abdel Hafiz, G. Coget, P. Yun, S. Guérandel, E. de Clercq, and R. Boudot. A high-performance Raman-Ramsey Cs vapor cell atomic clock. *Journal of Applied Physics*, March 2017.

[119] X. Liu. *High Contrast Coherent Population Trapping Resonances in Cs Vapour Cells with A Simple-Architecture Laser System.* PhD thesis, Université de Franche-Comté, December 2013.

[120] X. Liu, J.-M. Mérolla, S. Guérandel, C. Gorecki, E. de Clercq, and R. Boudot. Coherent-population-trapping resonances in buffer-gas-filled Cs-vapor cells with push-pull optical pumping. *Physical Review A*, 87(1), January 2013. ISSN 1050-2947, 1094-1622. doi:10.1103/PhysRevA.87.013416.

[121] Y.-Y. Jau, E. Miron, A. B. Post, N. N. Kuzma, and W. Happer. Push-Pull Optical Pumping of Pure Superposition States. *Physical Review Letters*, 93(16), October 2004. ISSN 0031-9007, 1079-7114. doi:10.1103/PhysRevLett.93.160802.

[122] V. Maurice. *Design, Microfabrication and Characterization of Alkali Vapor Cells for Miniature Atomic Frequency References.* PhD thesis, Besançon, July 2016.

[123] E. Arimondo and E. Wolf. Coherent population trapping in laser spectroscopy. *Progress in Optics*, 35, 1996.

[124] V. Shah and J. Kitching. Advances in Coherent Population Trapping for Atomic Clocks. In *Advances In Atomic, Molecular, and Optical Physics*, volume 59, pages 21–74. Elsevier, 2010. ISBN 978-0-12-381021-2.

[125] J. Dalibard, S. Reynaud, and C. Cohen-Tannoudji. La cascade radiative de l'atome habillé. In *Interaction of Radiation with Matter, a Volume in Honor of Adriano Gozzini*, pages 29–48. Pisa, Italy, scuola normale superiore edition, 1987.

[126] J. Vanier, A. Godone, and F. Levi. Coherent population trapping in cesium: Dark lines and coherent microwave emission. *Physical review A*, 58(3):2345, 1998.

[127] T. Zanon-Willette, E. de Clercq, and E. Arimondo. Ultrahigh-resolution spectroscopy with atomic or molecular dark resonances: Exact steady-state line shapes and asymptotic profiles in the adiabatic pulsed regime. *Physical Review A*, 84(6), December 2011. ISSN 1050-2947, 1094-1622. doi:10.1103/PhysRevA.84.062502.

[128] O. Kozlova. *Caractérisation d'une horloge à piégeage cohérent de population dans une vapeur thermique de césium. Principaux effets pouvant affecter la stabilité de fréquence à moyen-long terme.* PhD thesis, Université Pierre et Marie Curie - Paris VI, January 2012.

[129] R. H. Dicke. The Effect of Collisions upon the Doppler Width of Spectral Lines. *Physical Review*, 89(2):472–473, January 1953. doi:10.1103/PhysRev.89.472.

[130] J. Vanier. Atomic clocks based on coherent population trapping: A review. *Applied Physics B*, 81(4):421–442, August 2005. ISSN 0946-2171, 1432-0649. doi:10.1007/s00340-005-1905-3.

[131] N. Beverini, P. Minguzzi, and F. Strumia. Foreign-gas-induced cesium hyperfine relaxation. *Physical Review A*, 4(2):550, 1971.

[132] N. Beverini, P. Minguzzi, and F. Strumia. Foreign-Gas-Induced Cesium Hyperfine Relaxation. *Physical Review A*, 5(2):993–993, February 1972. ISSN 0556-2791. doi:10.1103/PhysRevA.5.993.

[133] F. A. Franz and C. E. Sooriamoorthi. Spin relaxation within the 6 $^2P_{1/2}$ and 6 $^2S_{1/2}$ states of cesium measured by white-light optical pumping. *Physical Review A*, 10(1):126, 1974.

[134] G. Breit and I. I. Rabi. Measurement of Nuclear Spin. *Physical Review*, 38(11):2082–2083, December 1931. ISSN 0031-899X. doi:10.1103/PhysRev.38.2082.2.

[135] D. A. Steck. Cesium D line data. *Theoretical Division*, 2008.

[136] J. Vanier, R. Kunski, N. Cyr, J. Y. Savard, and M. Têtu. On hyperfine frequency shifts caused by buffer gases: Application to the optically pumped passive rubidium frequency standard. *Journal of Applied Physics*, 53(8):5387–5391, August 1982. ISSN 0021-8979, 1089-7550. doi:10.1063/1.331467.

[137] F. Strumia, N. Beverini, A. Moretti, and G. Rovera. Optimization of the Buffer Gas Mixture for Optically Pumped CS Frequency Standards. pages 468–472. IEEE, 1976. doi:10.1109/FREQ.1976.201353.

[138] N. Beverini, F. Strumia, and G. Rovera. Buffer gas pressure shift in the mF= 0→ mF= 0 ground state hyperfine line in Cs. *Optics Communications*, 37(6):394–396, 1981.

[139] O. Kozlova, S. Guérandel, and E. de Clercq. Temperature and pressure shift of the Cs clock transition in the presence of buffer gases: Ne, N_2 , Ar. *Physical Review A*, 83(6), June 2011. ISSN 1050-2947, 1094-1622. doi:10.1103/PhysRevA.83.062714.

[140] R. Boudot, D. Miletic, P. Dziuban, C. Affolderbach, P. Knapkiewicz, J. Dziuban, G. Mileti, V. Giordano, and C. Gorecki. First-order cancellation of the Cs clock frequency temperature-dependence in Ne-Ar buffer gas mixture. *Optics express*, 19(4):3106–3114, 2011.

[141] W. HAPPER. Optical Pumping. *Reviews of Modern Physics*, 44(2):169–249, April 1972. doi:10.1103/RevModPhys.44.169.

[142] C. Cohen-Tannoudji, J. Dupont-Roc, and G. Grynberg, editors. *Atom—Photon Interactions*. Wiley-VCH Verlag GmbH, Weinheim, Germany, April 1998. ISBN 978-3-527-61719-7 978-0-471-29336-1. doi:10.1002/9783527617197.

[143] D. Miletic. *Light-Shift and Temperature-Shift Studies in Atomic Clocks Based on Coherent Population Trapping*. PhD thesis, Université de Neuchâtel, 2013.

[144] W. Demtröder. *Laser Spectroscopy: Vol. 2: Experimental Techniques*. Springer Science & Business Media, July 2008. ISBN 978-3-540-74954-7.

[145] M. Stähler, R. Wynands, S. Knappe, J. Kitching, L. Hollberg, A. Taichenachev, and V. Yudin. Coherent population trapping resonances in thermal ^{85}Rb vapor: D_1 versus D_2 line excitation. *Optics letters*, 27(16):1472–1474, 2002.

[146] A. Kastler. Le bilan du moment cinétique et les règles de polarisation en spectroscopie. Application à la diffusion de la lumière et à la fluorescence. *Journal de Physique et le Radium*, 4(7): 406–420, 1933. ISSN 0368-3842. doi:10.1051/jphysrad:0193300407040600.

[147] A. V. Taichenachev, V. I. Yudin, V. L. Velichansky, and S. A. Zibrov. On the unique possibility of significantly increasing the contrast of dark resonances on the D1 line of ^{87}Rb. *Journal of Experimental and Theoretical Physics Letters*, 82(7):398–403, 2005.

[148] K.-i. Watabe, T. Ikegami, A. Takamizawa, S. Yanagimachi, S.-i. Ohshima, and S. Knappe. High-contrast dark resonances with linearly polarized light on the D_1 line of alkali atoms with large nuclear spin. *Applied Optics*, 48(6):1098, February 2009. ISSN 0003-6935, 1539-4522. doi:10.1364/AO.48.001098.

[149] Y.-Y. Jau. *New Studies of Optical Pumping, Spin Resonances, and Spin Exchange in Mixtures of Inert Gases and Alkali-Metal Vapors*. PhD thesis, Ph. D. dissertation, Princeton University, Princeton, NJ, 2005.

[150] T. Zanon, S. Tremine, S. Guerandel, E. deClercq, D. Holleville, N. Dimarcq, and A. Clairon. Observation of Raman–Ramsey Fringes With Optical CPT Pulses. *IEEE Transactions on Instrumentation and Measurement*, 54(2):776–779, April 2005. ISSN 0018-9456. doi:10.1109/TIM.2004.843400.

[151] F. A. Camargo, J. Barrientos, G. Baili, L. Morvan, D. Dolfi, D. Holleville, S. Guerandel, I. Sagnes, P. Georges, and G. Lucas-Leclin. Coherent Dual-Frequency Emission of a Vertical External-Cavity Semiconductor Laser at the Cesium D_2 Line. *IEEE Photonics Technology Letters*, 24(14):1218–1220, July 2012. ISSN 1041-1135, 1941-0174. doi:10.1109/LPT.2012.2199103.

[152] P. Dumont, F. Camargo, J.-M. Danet, D. Holleville, S. Guerandel, G. Pillet, G. Baili, L. Morvan, D. Dolfi, I. Gozhyk, G. Beaudoin, I. Sagnes, P. Georges, and G. Lucas-Leclin. Low-Noise Dual-Frequency Laser for Compact Cs Atomic Clocks. *Journal of Lightwave Technology*, 32(20): 3817–3823, October 2014. ISSN 0733-8724, 1558-2213. doi:10.1109/JLT.2014.2318179.

[153] P. Yun, F. Tricot, C. E. Calosso, S. Micalizio, B. François, R. Boudot, S. Guérandel, and E. de Clercq. High-Performance Coherent Population Trapping Clock with Polarization Modulation. *Physical Review Applied*, 7(1):014018, January 2017. doi:10.1103/PhysRevApplied.7.014018.

[154] Y. Yano and S. Goka. High-contrast coherent population trapping based on crossed polarizers method. *IEEE Transactions on Ultrasonics, Ferroelectrics, and Frequency Control*, 61(12): 1953–1960, December 2014. ISSN 0885-3010. doi:10.1109/TUFFC.2014.006623.

[155] X. L. Sun, J. W. Zhang, P. Cheng, C. Xu, L. Zhao, and L. J. Wang. Investigation of Ramsey spectroscopy in a lin-par-lin Ramsey coherent population trapping clock with dispersion detection. *Optics Express*, 24(5):4532, March 2016. ISSN 1094-4087. doi:10.1364/OE.24.004532.

[156] M. Rosenbluh, V. Shah, S. Knappe, and J. Kitching. Differentially detected coherent population trapping resonances excited by orthogonally polarized laser fields. *Optics express*, 14(15):6588–6594, 2006.

[157] V. I. Yudin, A. V. Taichenachev, D. I. Sevostianov, V. L. Velichansky, V. V. Vasiliev, A. A. Zibrov, A. S. Zibrov, and S. A. Zibrov. Feedback spectroscopy of atomic resonances. *Physical Review A*, 87(6), June 2013. ISSN 1050-2947, 1094-1622. doi:10.1103/PhysRevA.87.063806.

[158] eagleyard PHOTONICS. EYP-DFB-0852-00150-1500-TOC03-000x. http://www.eagleyard.com/fileadmin/downloads/data_sheets/EYP-DFB-0852-00150-1500-TOC03-0000.pdf.

[159] X. Liu and R. Boudot. A Distributed-Feedback Diode Laser Frequency Stabilized on Doppler-Free Cs D_1 Line. *IEEE Transactions on Instrumentation and Measurement*, 61(10):2852–2855, October 2012. ISSN 0018-9456, 1557-9662. doi:10.1109/TIM.2012.2196399.

[160] G. Di Domenico, S. Schilt, and P. Thomann. Simple approach to the relation between laser frequency noise and laser line shape. *Applied optics*, 49(25):4801–4807, 2010.

[161] N. Bucalovic, V. Dolgovskiy, C. Schori, P. Thomann, G. Di Domenico, and S. Schilt. Experimental validation of a simple approximation to determine the linewidth of a laser from its frequency noise spectrum. *Applied optics*, 51(20):4582–4588, 2012.

[162] Photline Technologies. LiNbO3 Intensity Modulators Bias Control and Modulation Driving. https://photonics.ixblue.com/files/files/pdf/LiNb03_BiasControl_%26_Driving.pdf, 2014.

[163] J. C. Camparo. Conversion of laser phase noise to amplitude noise in an optically thick vapor. *JOSA B*, 15(3):1177–1186, 1998.

[164] C. Cohen-Tannoudji and D. Guéry-Odelin. *Advances in Atomic Physics: An Overview*. WORLD SCIENTIFIC, September 2011. ISBN 978-981-277-496-5 978-981-277-498-9.

[165] A. L. Schawlow. Spectroscopy in a new light. *Reviews of Modern Physics*, 54(3):697, 1982.

[166] V. S. Letokhov. Saturation spectroscopy. In P. D. K. Shimoda, editor, *High-Resolution Laser Spectroscopy*, number 13 in Topics in Applied Physics, pages 95–171. Springer Berlin Heidelberg, 1976. ISBN 978-3-540-07719-0 978-3-540-38237-9. doi:10.1007/3540077197_20.

[167] D. Budker and M. Romalis. Optical magnetometry. *Nature Physics*, 3(4):227–234, April 2007. ISSN 1745-2473, 1745-2481. doi:10.1038/nphys566.

[168] P. G. Pappas, M. M. Burns, D. D. Hinshelwood, M. S. Feld, and D. E. Murnick. Saturation spectroscopy with laser optical pumping in atomic barium. *Physical Review A*, 21(6):1955, 1980.

[169] O. Schmidt, K.-M. Knaak, R. Wynands, and D. Meschede. Cesium saturation spectroscopy revisited: How to reverse peaks and observe narrow resonances. *Applied Physics B*, 59(2): 167–178, 1994.

[170] J. J. McFerran. An inverted crossover resonance aiding laser cooling of ^{171}Yb. *Journal of the Optical Society of America B*, 33(6):1278, June 2016. ISSN 0740-3224, 1520-8540. doi:10.1364/JOSAB.33.001278.

[171] D. V. Brazhnikov, A. V. Taichenachev, and V. I. Yudin. Polarization method for controlling a sign of electromagnetically-induced transparency/absorption resonances. *The European Physical Journal D*, 63(3):315–325, August 2011. ISSN 1434-6060, 1434-6079. doi:10.1140/epjd/e2011-20112-6.

[172] N. Beverini, K. Ernst, M. Inguscio, and F. Strumia. Optogalvanic nonlinear hanle effect by a single frequency laser: A quantitative analysis. *Applied Physics B*, 37(1):17–29, 1985.

[173] E. De Clercq and P. Mangin. Optical pumping of a caesium beam and population trapping. page 281, Besançon, France, 1989.

[174] D. V. Brazhnikov, A. V. Taichenachev, A. M. Tumaikin, V. I. Yudin, I. I. Ryabtsev, and V. M. Entin. Effect of the polarization of counterpropagating light waves on nonlinear resonances of the electromagnetically induced transparency and absorption in the Hanle configuration. *JETP Letters*, 91(12):625–629, June 2010. ISSN 0021-3640, 1090-6487. doi:10.1134/S0021364010120039.

[175] V. S. Smirnov, A. M. Tumaikin, and V. I. Yudin. Stationary coherent states of atoms in a resonant interaction with elliptically polarized light. Coherent trapping of populations (general theory). *Zh. Eksp. Teoret. Fiz*, 69:913, 1989.

[176] T. Lindvall and I. Tittonen. Effect of optical pumping on alkali-atom Doppler-limited spectra. *Journal of Modern Optics*, 54(18):2779–2793, December 2007. ISSN 0950-0340, 1362-3044. doi:10.1080/09500340701243566.

[177] C. Audoin, V. Candelier, and N. Dimarcq. A limit to the frequency stability of passive frequency standards. In *Precision Electromagnetic Measurements, 1990. CPEM'90 Digest., Conference On*, page 93. IEEE, 1990.

[178] G. J. Dick. Local oscillator induced instabilities in trapped ion frequency standards. Redondo Beach, CA, 1987. DTIC Document.

[179] G. Santarelli, C. Audoin, A. Makdissi, P. Laurent, G. J. Dick, and A. Clairon. Frequency stability degradation of an oscillator slaved to a periodically interrogated atomic resonator. *IEEE Transactions on Ultrasonics, Ferroelectrics, and Frequency Control*, 45(4):887–894, July 1998. ISSN 0885-3010. doi:10.1109/58.710548.

[180] T. M. Fortier, M. S. Kirchner, F. Quinlan, J. Taylor, J. C. Bergquist, T. Rosenband, N. Lemke, A. Ludlow, Y. Jiang, C. W. Oates, and S. A. Diddams. Generation of ultrastable microwaves via optical frequency division. *Nature Photonics*, 5(7):425–429, June 2011. ISSN 1749-4885, 1749-4893. doi:10.1038/nphoton.2011.121.

[181] A. Hati, C. W. Nelson, C. Barnes, D. Lirette, T. Fortier, F. Quinlan, J. A. Desalvo, A. Ludlow, S. A. Diddams, and D. A. Howe. State-of-the-art RF signal generation from optical frequency division. *IEEE Transactions on Ultrasonics, Ferroelectrics, and Frequency Control*, 60(9):1796–1803, September 2013. ISSN 0885-3010. doi:10.1109/TUFFC.2013.2765.

[182] S. Grop, P.-Y. Bourgeois, R. Boudot, Y. Kersalé, E. Rubiola, and V. Giordano. 10 GHz cryocooled sapphire oscillator with extremely low phase noise. *Electronics Letters*, 46(6):1, 2010.

[183] V. Giordano, S. Grop, B. Dubois, P.-Y. Bourgeois, Y. Kersalé, G. Haye, V. Dolgovskiy, N. Bucalovic, G. Di Domenico, S. Schilt, J. Chauvin, D. Valat, and E. Rubiola. New-generation of cryogenic sapphire microwave oscillators for space, metrology, and scientific applications. *Review of Scientific Instruments*, 83(8):085113, August 2012. ISSN 0034-6748, 1089-7623. doi:10.1063/1.4747456.

[184] D. Chambon, S. Bize, M. Lours, F. Narbonneau, H. Marion, A. Clairon, G. Santarelli, A. Luiten, and M. Tobar. Design and realization of a flywheel oscillator for advanced time and frequency metrology. *Review of Scientific Instruments*, 76(9):094704, 2005. ISSN 00346748. doi:10.1063/1.2018567.

[185] G. D. Rovera, G. Santarelli, and A. Clairon. Frequency synthesis chain for the atomic fountain primary frequency standard. *IEEE transactions on ultrasonics, ferroelectrics, and frequency control*, 43(3):354–358, 1996.

[186] R. Boudot, S. Guerandel, and E. de Clercq. Simple-Design Low-Noise NLTL-Based Frequency Synthesizers for a CPT Cs Clock. *IEEE Transactions on Instrumentation and Measurement*, 58(10):3659–3665, October 2009. ISSN 0018-9456, 1557-9662. doi:10.1109/TIM.2009.2019306.

[187] J. Lautier, M. Lours, and A. Landragin. A compact micro-wave synthesizer for transportable cold-atom interferometers. *Review of Scientific Instruments*, 85(6):063114, 2014.

[188] Pascall Electronics. `http://www.pascall.co.uk/content/S635144040796327285/pascall%20OCXOoct11.pdf`, 2011.

[189] E. Rubiola and V. Giordano. Correlation-based phase noise measurements. *Review of Scientific Instruments*, 71(8):3085, 2000. ISSN 00346748. doi:10.1063/1.1304871.

[190] E. Rubiola and R. Boudot. The effect of AM noise on correlation phase-noise measurements. *IEEE Transactions on Ultrasonics, Ferroelectrics and Frequency Control*, 54(5):926–932, May 2007. ISSN 0885-3010. doi:10.1109/TUFFC.2007.338.

[191] C. W. Nelson, A. Hati, and D. A. Howe. A collapse of the cross-spectral function in phase noise metrology. *Review of Scientific Instruments*, 85(2):024705, February 2014. ISSN 0034-6748, 1089-7623. doi:10.1063/1.4865715.

[192] R. Boudot and E. Rubiola. Phase noise in RF and microwave amplifiers. *IEEE Transactions on Ultrasonics, Ferroelectrics and Frequency Control*, 59(12):2613–2624, December 2012. ISSN 0885-3010. doi:10.1109/TUFFC.2012.2502.

[193] Pascall Electronics. http://www.pascall.co.uk/.

[194] T. E. Parker. Characteristics and sources of phase noise in stable oscillators. In *41st Annual Symposium on Frequency Control. 1987*, pages 99–110. IEEE, 1987.

[195] S. Brandt, A. Nagel, R. Wynands, and D. Meschede. Buffer-gas-induced linewidth reduction of coherent dark resonances to below 50 Hz. *Physical Review A*, 56(2):R1063–R1066, August 1997. doi:10.1103/PhysRevA.56.R1063.

[196] A. Andalkar and R. B. Warrington. High-resolution measurement of the pressure broadening and shift of the Cs D1 and D2 lines by N_2 and He buffer gases. *Physical Review A*, 65(3), February 2002. ISSN 1050-2947, 1094-1622. doi:10.1103/PhysRevA.65.032708.

[197] J. F. Kielkopf. Semiempirical potentials for alkali-noble gas interactions. *The Journal of Chemical Physics*, 61(11):4733–4739, 1974.

[198] M. V. Romalis, E. Miron, and G. D. Cates. Pressure broadening of Rb D_1 and D_2 lines by ^{3}He, ^{4}He, N_2, and Xe: Line cores and near wings. *Physical Review A*, 56(6):4569, 1997.

[199] M. Weel and A. Kumarakrishnan. Laser-frequency stabilization using a lock-in amplifier. *Canadian Journal of Physics*, 80(12):1449–1458, December 2002. ISSN 0008-4204. doi:10.1139/p02-084.

[200] ANALOG DEVICES. Low Noise, Precision Operational Amplifier. http://www.analog.com/media/en/technical-documentation/data-sheets/OP27.pdf, 2016.

[201] HAMAMATSU. Si photodiodes - S1337 series. `https://www.hamamatsu.com/resources/pdf/ssd/s1337_series_kspd1032e.pdf`, 2015.

[202] J. C. Camparo and W. F. Buell. Laser PM to AM conversion in atomic vapors and short term clock stability. In *Frequency Control Symposium, 1997., Proceedings of the 1997 IEEE International*, pages 253–258. IEEE, 1997.

[203] D. Miletic, C. Affolderbach, M. Hasegawa, R. Boudot, C. Gorecki, and G. Mileti. AC Stark-shift in CPT-based Cs miniature atomic clocks. *Applied Physics B*, 109(1):89–97, October 2012. ISSN 0946-2171, 1432-0649. doi:10.1007/s00340-012-5121-7.

[204] R. Boudot, P. Dziuban, M. Hasegawa, R. K. Chutani, S. Galliou, V. Giordano, and C. Gorecki. Coherent population trapping resonances in Cs–Ne vapor microcells for miniature clocks applications. *Journal of Applied Physics*, 109(1):014912, January 2011. ISSN 0021-8979, 1089-7550. doi:10.1063/1.3530951.

[205] M. Zhu and L. S. Cutler. Theoretical and experimental study of light shift in a CPT-based Rb vapor cell frequency standard. Technical report, DTIC Document, 2001.

[206] V. Shah, V. Gerginov, P. D. D. Schwindt, S. Knappe, L. Hollberg, and J. Kitching. Continuous light-shift correction in modulated coherent population trapping clocks. *Applied Physics Letters*, 89(15):151124, October 2006. ISSN 0003-6951, 1077-3118. doi:10.1063/1.2360921.

[207] J.-M. Danet. *Horloge atomique à piégeage cohérent de population du césium en cellule : limitations à la stabilité de fréquence.* PhD thesis, Université Pierre et Marie Curie - Paris VI, March 2014.

[208] X. Liu, J.-M. Mérolla, S. Guérandel, E. de Clercq, and R. Boudot. Ramsey spectroscopy of high-contrast CPT resonances with push-pull optical pumping in Cs vapor. *Optics Express*, 21 (10):12451–12459, May 2013. ISSN 1094-4087. doi:10.1364/OE.21.012451.

[209] N. Castagna, R. Boudot, S. Guerandel, E. Clercq, N. Dimarcq, and A. Clairon. Investigations on continuous and pulsed interrogation for a CPT atomic clock. *IEEE Transactions on Ultrasonics, Ferroelectrics and Frequency Control*, 56(2):246–253, February 2009. ISSN 0885-3010. doi:10.1109/TUFFC.2009.1033.

[210] E. Blanshan, S. M. Rochester, E. A. Donley, and J. Kitching. Light shifts in a pulsed cold-atom coherent-population-trapping clock. *Physical Review A*, 91(4), April 2015. ISSN 1050-2947, 1094-1622. doi:10.1103/PhysRevA.91.041401.

[211] V. I. Yudin, A. V. Taichenachev, C. W. Oates, Z. W. Barber, N. D. Lemke, A. D. Ludlow, U. Sterr, C. Lisdat, and F. Riehle. Hyper-Ramsey spectroscopy of optical clock transitions. *Physical Review A*, 82(1), July 2010. ISSN 1050-2947, 1094-1622. doi:10.1103/PhysRevA.82.011804.

[212] N. Huntemann, B. Lipphardt, M. Okhapkin, C. Tamm, E. Peik, A. V. Taichenachev, and V. I. Yudin. Generalized Ramsey Excitation Scheme with Suppressed Light Shift. *Physical Review Letters*, 109(21), November 2012. ISSN 0031-9007, 1079-7114. doi:10.1103/PhysRevLett.109.213002.

[213] R. Hobson, W. Bowden, S. A. King, P. E. G. Baird, I. R. Hill, and P. Gill. Modified hyper-Ramsey methods for the elimination of probe shifts in optical clocks. *Physical Review A*, 93(1), January 2016. ISSN 2469-9926, 2469-9934. doi:10.1103/PhysRevA.93.010501.

[214] T. Zanon-Willette, E. de Clercq, and E. Arimondo. Probe light-shift elimination in generalized hyper-Ramsey quantum clocks. *Physical Review A*, 93(4), April 2016. ISSN 2469-9926, 2469-9934. doi:10.1103/PhysRevA.93.042506.

[215] V. I. Yudin, A. V. Taichenachev, M. Y. Basalaev, and T. Zanon-Willette. Synthetic frequency protocol for Ramsey spectroscopy of clock transitions. *Physical Review A*, 94(5), November 2016. ISSN 2469-9926, 2469-9934. doi:10.1103/PhysRevA.94.052505.

[216] N. F. Ramsey. A new molecular beam resonance method. *Physical Review*, 76(7):996, 1949.

[217] M. Abdel Hafiz and R. Boudot. A coherent population trapping Cs vapor cell atomic clock based on push-pull optical pumping. *Journal of Applied Physics*, 118(12):124903, September 2015. ISSN 0021-8979, 1089-7550. doi:10.1063/1.4931768.

[218] M. Gharavipour, C. Affolderbach, S. Kang, T. Bandi, F. Gruet, M. Pellaton, and G. Mileti. High performance vapour-cell frequency standards. *Journal of Physics: Conference Series*, 723: 012006, June 2016. ISSN 1742-6588, 1742-6596. doi:10.1088/1742-6596/723/1/012006.

[219] E. Kuchina, E. E. Mikhailov, and I. Novikova. Effect of atomic diffusion on the Raman–Ramsey coherent population trapping resonances. *Journal of the Optical Society of America B*, 33(4): 610, April 2016. ISSN 0740-3224, 1520-8540. doi:10.1364/JOSAB.33.000610.

[220] Y. Yano, W. Gao, S. Goka, and M. Kajita. Theoretical and experimental investigation of the light shift in Ramsey coherent population trapping. *Physical Review A*, 90(1), July 2014. ISSN 1050-2947, 1094-1622. doi:10.1103/PhysRevA.90.013826.

[221] G. S. Pati, Z. Warren, N. Yu, and M. S. Shahriar. Computational studies of light shift in a Raman–Ramsey interference-based atomic clock. *Journal of the Optical Society of America B*, 32(3):388, March 2015. ISSN 0740-3224, 1520-8540. doi:10.1364/JOSAB.32.000388.

[222] C. J. Bordé. Density Matrix Equations and Diagrams for High Resolution Non-Linear Laser Spectroscopy: Application to Ramsey Fringes in the Optical Domain. In F. T. Arecchi, F. Strumia, and H. Walther, editors, *Advances in Laser Spectroscopy*, pages 1–70. Springer US, Boston, MA, 1983. ISBN 978-1-4613-3717-1 978-1-4613-3715-7. doi:10.1007/978-1-4613-3715-7_1.

[223] E. Kroemer, M. Abdel Hafiz, V. Maurice, B. Fouilland, C. Gorecki, and R. Boudot. Cs vapor microcells with Ne-He buffer gas mixture for high operation-temperature miniature atomic clocks. *Optics Express*, 23(14):18373, July 2015. ISSN 1094-4087. doi:10.1364/OE.23.018373.

[224] R. Chutani, V. Maurice, N. Passilly, C. Gorecki, R. Boudot, M. Abdel Hafiz, P. Abbé, S. Galliou, J.-Y. Rauch, and E. de Clercq. Laser light routing in an elongated micromachined vapor cell with diffraction gratings for atomic clock applications. *Scientific Reports*, 5:14001, September 2015. ISSN 2045-2322. doi:10.1038/srep14001.

[225] E. Kroemer. *Étude Du Déplacement Collisionnel de La Fréquence d'horloge Du Césium En Présence Du Gaz Tampon Hélium Ou Xénon. Applications Pour Microcellules à Haute Température.* PhD thesis, Institut FEMTO-ST, 2015.

[226] I. K. Kominis, T. W. Kornack, J. C. Allred, and M. V. Romalis. A subfemtotesla multichannel atomic magnetometer. *Nature*, 422(6932):596–599, April 2003. ISSN 0028-0836. doi:10.1038/nature01484.

[227] B. Julsgaard, A. Kozhekin, and E. S. Polzik. Experimental long-lived entanglement of two macroscopic objects. *Nature*, 413(6854):400–403, September 2001. ISSN 0028-0836. doi:10.1038/35096524.

[228] H. Krauter, D. Salart, C. A. Muschik, J. M. Petersen, H. Shen, T. Fernholz, and E. S. Polzik. Deterministic quantum teleportation between distant atomic objects. *Nature Physics*, 9(7): 400–404, June 2013. ISSN 1745-2473, 1745-2481. doi:10.1038/nphys2631.

[229] D. Budker, D. F. Kimball, S. M. Rochester, and V. V. Yashchuk. Nonlinear Magneto-optics and Reduced Group Velocity of Light in Atomic Vapor with Slow Ground State Relaxation. *Physical Review Letters*, 83(9):1767–1770, August 1999. ISSN 0031-9007, 1079-7114. doi:10.1103/PhysRevLett.83.1767.

[230] Y. Xiao, M. Klein, M. Hohensee, L. Jiang, D. F. Phillips, M. D. Lukin, and R. L. Walsworth. Slow Light Beam Splitter. *Physical Review Letters*, 101(4), July 2008. ISSN 0031-9007, 1079-7114. doi:10.1103/PhysRevLett.101.043601.

[231] M. A. Bouchiat, J. Guena, L. Hunter, and L. Pottier. Observation of a parity violation in cesium. *Physics Letters B*, 117(5):358–364, November 1982. ISSN 0370-2693. doi:10.1016/0370-2693(82)90736-5.

[232] A. Kuzmich, L. Mandel, and N. P. Bigelow. Generation of Spin Squeezing via Continuous Quantum Nondemolition Measurement. *Physical Review Letters*, 85(8):1594–1597, August 2000. ISSN 0031-9007, 1079-7114. doi:10.1103/PhysRevLett.85.1594.

[233] N. F. Ramsey. Resonance Experiments in Successive Oscillatory Fields. *Review of Scientific Instruments*, 28(1):57–58, January 1957. ISSN 0034-6748, 1089-7623. doi:10.1063/1.1715708.

[234] H. G. Robinson, E. S. Ensberg, and H. G. Dehmelt. *Bull. Am. Phys. Soc.*, 3(9), 1958.

[235] R. G. Brewer. Study of Atom—Wall Collisions by Optical Pumping. *The Journal of Chemical Physics*, 38(12):3015–3020, June 1963. ISSN 0021-9606, 1089-7690. doi:10.1063/1.1733636.

[236] M. A. Bouchiat and J. Brossel. Relaxation of Optically Pumped Rb Atoms on Paraffin-Coated Walls. *Physical Review*, 147(1):41–54, July 1966. ISSN 0031-899X. doi:10.1103/PhysRev.147.41.

[237] D. Budker, W. Gawlik, D. F. Kimball, S. M. Rochester, V. V. Yashchuk, and A. Weis. Resonant nonlinear magneto-optical effects in atoms. *Reviews of Modern Physics*, 74(4):1153–1201, November 2002. ISSN 0034-6861, 1539-0756. doi:10.1103/RevModPhys.74.1153.

[238] H. G. Robinson and C. E. Johnson. Narrow ^{87}Rb hyperfine-structure resonances in an evacuated wall-coated cell. *Applied Physics Letters*, 40(9):771–773, May 1982. ISSN 0003-6951, 1077-3118. doi:10.1063/1.93279.

[239] M. V. Balabas, K. Jensen, W. Wasilewski, H. Krauter, L. S. Madsen, J. H. Müller, T. Fernholz, and E. S. Polzik. High quality anti-relaxation coating material for alkali atom vapor cells. *Optics Express*, 18(6):5825, March 2010. ISSN 1094-4087. doi:10.1364/OE.18.005825.

[240] M. V. Balabas, T. Karaulanov, M. P. Ledbetter, and D. Budker. Polarized Alkali-Metal Vapor with Minute-Long Transverse Spin-Relaxation Time. *Physical Review Letters*, 105(7), August 2010. ISSN 0031-9007, 1079-7114. doi:10.1103/PhysRevLett.105.070801.

[241] E. P. Corsini, T. Karaulanov, M. Balabas, and D. Budker. Hyperfine frequency shift and Zeeman relaxation in alkali-metal-vapor cells with antirelaxation alkene coating. *Physical Review A*, 87 (2), February 2013. ISSN 1050-2947, 1094-1622. doi:10.1103/PhysRevA.87.022901.

[242] D. Budker, L. Hollberg, D. F. Kimball, J. Kitching, S. Pustelny, and V. V. Yashchuk. Microwave transitions and nonlinear magneto-optical rotation in anti-relaxation-coated cells. *Physical Review A*, 71(1), January 2005. ISSN 1050-2947, 1094-1622. doi:10.1103/PhysRevA.71.012903.

[243] S. J. Seltzer, D. J. Michalak, M. H. Donaldson, M. V. Balabas, S. K. Barber, S. L. Bernasek, M.-A. Bouchiat, A. Hexemer, A. M. Hibberd, D. F. J. Kimball, C. Jaye, T. Karaulanov, F. A. Narducci, S. A. Rangwala, H. G. Robinson, A. K. Shmakov, D. L. Voronov, V. V. Yashchuk, A. Pines, and D. Budker. Investigation of antirelaxation coatings for alkali-metal vapor cells using surface science techniques. *The Journal of Chemical Physics*, 133(14):144703, October 2010. ISSN 0021-9606, 1089-7690. doi:10.1063/1.3489922.

[244] J. A. Dziuban. *Bonding in Microsystem Technology.* Springer Science & Business Media, January 2007. ISBN 978-1-4020-4589-9.

[245] S. J. Seltzer and M. V. Romalis. High-temperature alkali vapor cells with antirelaxation surface coatings. *Journal of Applied Physics*, 106(11):114905, December 2009. ISSN 0021-8979, 1089-7550. doi:10.1063/1.3236649.

[246] S. J. Seltzer, P. J. Meares, and M. V. Romalis. Synchronous optical pumping of quantum revival beats for atomic magnetometry. *Physical Review A*, 75(5), May 2007. ISSN 1050-2947, 1094-1622. doi:10.1103/PhysRevA.75.051407.

[247] S. J. Seltzer, D. M. Rampulla, S. Rivillon-Amy, Y. J. Chabal, S. L. Bernasek, and M. V. Romalis. Testing the effect of surface coatings on alkali atom polarization lifetimes. *Journal of Applied Physics*, 104(10):103116, November 2008. ISSN 0021-8979, 1089-7550. doi:10.1063/1.2985913.

[248] Y. W. Yi, H. G. Robinson, S. Knappe, J. E. Maclennan, C. D. Jones, C. Zhu, N. A. Clark, and J. Kitching. Method for characterizing self-assembled monolayers as antirelaxation wall coatings for alkali vapor cells. *Journal of Applied Physics*, 104(2):023534, 2008. ISSN 00218979. doi:10.1063/1.2958329.

[249] J. C. Camparo, R. P. Frueholz, and B. Jaduszliwer. Alkali reactions with wall coating materials used in atomic resonance cells. *Journal of Applied Physics*, 62(2):676–681, July 1987. ISSN 0021-8979, 1089-7550. doi:10.1063/1.339741.

[250] R. Straessle, M. Pellaton, C. Affolderbach, Y. Pétremand, D. Briand, G. Mileti, and N. F. de Rooij. Microfabricated alkali vapor cell with anti-relaxation wall coating. *Applied Physics Letters*, 105(4):043502, July 2014. ISSN 0003-6951, 1077-3118. doi:10.1063/1.4891248.

[251] M. Hasegawa, R. K. Chutani, C. Gorecki, R. Boudot, P. Dziuban, V. Giordano, S. Clatot, and L. Mauri. Microfabrication of cesium vapor cells with buffer gas for MEMS atomic clocks. *Sensors and Actuators A: Physical*, 167(2):594–601, June 2011. ISSN 0924-4247. doi:10.1016/j.sna.2011.02.039.

[252] J. Fedchak, P. Cabauy, W. Cummings, C. Jones, and R. Kowalczyk. Silane coatings for laser-driven polarized hydrogen sources and targets. *Nuclear Instruments and Methods in Physics Research Section A: Accelerators, Spectrometers, Detectors and Associated Equipment*, 391(3): 405–416, June 1997. ISSN 01689002. doi:10.1016/S0168-9002(97)00571-8.

[253] M. Stephens, R. Rhodes, and C. Wieman. Study of wall coatings for vapor-cell laser traps. *Journal of Applied Physics*, 76(6):3479–3488, September 1994. ISSN 0021-8979, 1089-7550. doi:10.1063/1.358502.

[254] W. Franzen. Spin Relaxation of Optically Aligned Rubidium Vapor. *Physical Review*, 115(4): 850–856, August 1959. ISSN 0031-899X. doi:10.1103/PhysRev.115.850.

[255] A. Javan, O. Kocharovskaya, H. Lee, and M. O. Scully. Narrowing of electromagnetically induced transparency resonance in a Doppler-broadened medium. *Physical Review A*, 66(1), July 2002. ISSN 1050-2947, 1094-1622. doi:10.1103/PhysRevA.66.013805.

[256] M. Radonjić, D. Arsenović, Z. Grujić, and B. M. Jelenković. Coherent population trapping linewidths for open transitions: Cases of different transverse laser intensity distribution. *Physical Review A*, 79(2), February 2009. ISSN 1050-2947, 1094-1622. doi:10.1103/PhysRevA.79.023805.

[257] G. Kazakov, B. Matisov, A. Litvinov, and I. Mazets. Coherent population trapping in a finite-size buffer-less cell. *Journal of Physics B: Atomic, Molecular and Optical Physics*, 40(19): 3851–3860, October 2007. ISSN 0953-4075, 1361-6455. doi:10.1088/0953-4075/40/19/006.

[258] J. B. Taylor and I. Langmuir. Vapor Pressure of Caesium by the Positive Ion Method. *Physical Review*, 51(9):753–760, May 1937. ISSN 0031-899X. doi:10.1103/PhysRev.51.753.

[259] H. M. Goldenberg, D. Kleppner, and N. F. Ramsey. Atomic beam resonance experiments with stored beams. *Physical Review*, 123(2):530, 1961.

[260] J. Vanier, J.-F. Simard, and J.-S. Boulanger. Relaxation and frequency shifts in the ground state of Rb 85. *Physical Review A*, 9(3):1031, 1974.

[261] C. Rahman and H. Robinson. Rb 0-0 hyperfine transition in evacuated wall-coated cell at melting temperature. *IEEE Journal of Quantum Electronics*, 23(4):452–454, April 1987. ISSN 0018-9197. doi:10.1109/JQE.1987.1073365.

[262] E. Breschi, G. Kazakov, C. Schori, G. Di Domenico, G. Mileti, A. Litvinov, and B. Matisov. Light effects in the atomic-motion-induced Ramsey narrowing of dark resonances in wall-coated cells. *Physical Review A*, 82(6), December 2010. ISSN 1050-2947, 1094-1622. doi:10.1103/PhysRevA.82.063810.

[263] M. Klein, M. Hohensee, D. F. Phillips, and R. L. Walsworth. Electromagnetically induced transparency in paraffin-coated vapor cells. *Physical Review A*, 83(1), January 2011. ISSN 1050-2947, 1094-1622. doi:10.1103/PhysRevA.83.013826.

[264] T. Bandi, C. Affolderbach, G. Mileti, C. E. Calosso, C. Stefanucci, F. Merli, and A. K. Skrivervik. Laser-pumped high-performance compact gas-cell Rb standard with 3 10^{-13} $\tau^{-1/2}$ stability. In *European Frequency and Time Forum (EFTF), 2012*, pages 494–496. IEEE, 2012.

[265] T. Zanon-Willette, V. I. Yudin, and A. V. Taichenachev. Generalized hyper-Ramsey resonance with separated oscillating fields. *Physical Review A*, 92(2), August 2015. ISSN 1050-2947, 1094-1622. doi:10.1103/PhysRevA.92.023416.

[266] T. Zanon-Willette, M. Minissale, V. Yudin, and A. Taichenachev. Composite pulses in Hyper-Ramsey spectroscopy for the next generation of atomic clocks. *Journal of Physics: Conference Series*, 723:012057, June 2016. ISSN 1742-6588, 1742-6596. doi:10.1088/1742-6596/723/1/012057.

[267] J. L. Hall, C. J. Bordé, and K. Uehara. Direct optical resolution of the recoil effect using saturated absorption spectroscopy. *Physical Review Letters*, 37(20):1339, 1976.

[268] S. N. Bagaev, A. K. Dmitriev, Y. V. Nekrasov, and B. N. Skvortsov. Optical spectroscopy free of quadratic Doppler effect. *Soviet Journal of Experimental and Theoretical Physics Letters*, 50: 194, August 1989. ISSN 0021-3640.

[269] J. Ishikawa, F. Riehle, J. Helmcke, and C. J. Bordé. Strong-field effects in coherent saturation spectroscopy of atomic beams. *Physical Review A*, 49(6):4794, 1994.

[270] V. V. Vasil'ev, V. L. Velichanskii, S. A. Zibrov, A. V. Sivak, D. V. Brazhnikov, A. V. Taichenachev, and V. I. Yudin. Dual structure of saturated absorption resonance at an open atomic transition. *Journal of Experimental and Theoretical Physics*, 112(5):770–779, May 2011. ISSN 1063-7761, 1090-6509. doi:10.1134/S1063776111040248.

[271] M. Abdel Hafiz, D. Brazhnikov, G. Coget, A. Taichenachev, V. Yudin, E. de Clercq, and R. Boudot. High-contrast sub-Doppler absorption spikes in a hot atomic vapor cell exposed to a dual-frequency laser field. *New Journal of Physics*, 19(7):073028, July 2017. ISSN 1367-2630. doi:10.1088/1367-2630/aa7258.

[272] C. Affolderbach, S. Knappe, R. Wynands, A. V. Taĭchenachev, and V. I. Yudin. Electromagnetically induced transparency and absorption in a standing wave. *Physical Review A*, 65(4), March 2002. ISSN 1050-2947, 1094-1622. doi:10.1103/PhysRevA.65.043810.

[273] S. V. Kargapoltsev, J. Kitching, L. Hollberg, A. V. Taichenachev, V. L. Velichansky, and V. I. Yudin. High-contrast dark resonance in σ_+ - σ_- optical field. *Laser Physics Letters*, 1(10): 495–499, October 2004. ISSN 1612-2011, 1612-202X. doi:10.1002/lapl.200410107.

[274] D. V. Brazhnikov, A. M. Tumaĭkin, V. I. Yudin, A. V. Taĭchenachev, I. I. Ryabtsev, and V. M. Éntin. Level-crossing resonance in the field of counterpropagating elliptically polarized light waves. *Journal of Optical Technology*, 77(10):606–607, October 2010. doi:10.1364/JOT.77.000606.

[275] D. Bloch, M. Ducloy, N. Senkov, V. Velichansky, and V. Yudin. Doppler-Free Spectroscopy of the D_1 Line of Potassium. *LASER PHYSICS-LAWRENCE-*, 6:670–678, 1996.

[276] G. Kazakov, B. Matisov, I. Mazets, G. Mileti, and J. Delporte. Pseudoresonance mechanism of all-optical frequency-standard operation. *Physical Review A*, 72(6), December 2005. ISSN 1050-2947, 1094-1622. doi:10.1103/PhysRevA.72.063408.

[277] S. A. Zibrov. Experimental Investigation of the Dark Pseudoresonance on the D1 Line of the ^{87}Rb Atom Excited by a Linearly Polarized Field. *JETP Letters*, 82(8):477, 2005. ISSN 00213640. doi:10.1134/1.2150865.

[278] A. V. Taichenachev, A. M. Tumaikin, and V. I. Yudin. Electromagnetically induced absorption in a four-state system. *Physical Review A*, 61(1):011802, 1999.

Publications in peer-reviewed journals

- M. Abdel Hafiz, V. Maurice, R. Chutani, N. Passilly, C. Gorecki, S. Guérandel, E. De Clercq and R. Boudot, Journ. Appl. Phys. 117, 184901 (2015).
- E. Kroemer, M. Abdel Hafiz, V. Maurice, B. Fouilland, C. Gorecki and R. Boudot, Opt. Express 23, 14, 18373-18380 (2015).
- R. Chutani, V. Maurice, N. Passilly, C. Gorecki, R. Boudot, M. Abdel Hafiz, P. Abbé, S. Galliou, J. Y. Rauch and E. De Clercq, Nature Sci. Rep. 5, 14001 (2015).
- B. Francois, C. E. Calosso, M. Abdel Hafiz, S. Micalizio and R. Boudot, Rev. Sci. Instr. 86, 094707 (2015).
- M. Abdel Hafiz and R. Boudot, Journ. Appl. Phys. 118, 124903 (2015).
- M. Abdel Hafiz, G. Coget, E. De Clercq and R. Boudot, Opt. Lett. 41, 13, 2982-2985 (2016).
- M. Abdel Hafiz, X. Liu, S. Guérandel, E. De Clercq and R. Boudot, Journal of Physics: Conference Series, 723 (1), 012013 (2016).
- E. Kroemer, J. Rutkowski, V. Maurice, R. Vicarini, M. Abdel Hafiz, C. Gorecki and R. Boudot, Applied Optics 55, 31, 8839-8847 (2016).
- M. Abdel Hafiz, G. Coget, P. Yun, S. Guérandel, E. De Clercq and R. Boudot, A high-performance Raman-Ramsey Cs vapor cell atomic clock, Journal of Applied Physics 121, 104903 (2017).
- M. Abdel Hafiz, D. Brazhnikov, G. Coget, A. Taichenachev, V. I. Yudin, E. De Clercq and R. Boudot, High-contrast sub-Doppler absorption spikes in a hot atomic vapor cell exposed to a dual-frequency laser field, submitted to New Journal of Physics (2017).

International conferences

- M. Abdel Hafiz, R. Boudot Progress in the evaluation of a Cs cell CPT clock using push-pull optical pumping, Proceedings of the European Frequency Time Forum , 24-26 June 2014, Neuchatel (Switzerland).
- M. Abdel Hafiz, R. Boudot Preliminar results of a Cs vapor cell atomic clock using push-pull optical pumping, Proceedings of the European Frequency Time Forum International Frequency Control Symposium, 12-17 April 2015, Denver, Colorado.
- M. Abdel Hafiz, V. Maurice, R. Chutani, C. Gorecki, E. De Clercq, S. Guérandel and R. Boudot, Spectroscopy and hyperfine clock frequency shift measurements in Cs vapor cells coated with octadecyltrichlorosilanes (OTS), Proceedings of the European Frequency Time Forum International Frequency Control Symposium, 12-17 April 2015, Denver, Colorado.
- S. Micalizio, F. Levi, A. Godone, C. E. Calosso, B. Francois, S. Guerandel, D. Holleville, E. De Clercq, L. De Sarlo, P. Yun, JM. Danet, M. Langlois, R. Boudot, M. Abdel Hafiz, E. Sahin, C. Affolderbach, S. Kang, F. Gruet, M. Gharavipour, G. Mileti and B. Desruelle Compact clocks for industrial applications : the EMRP project IND55 MClocks , Proceedings of the European Frequency Time Forum International Frequency Control Symposium, 12-17 April 2015, Denver, Colorado.
- M. Abdel Hafiz, X. Liu, S. Guérandel, E. De Clercq and R. Boudot A CPT-based Cs vapor cell atomic clock with a short-term fractional frequency stability of 3 10-13 tau-1/2 , Proceedings Frequency Standards and Metrology, October 2015, Potsdam, Germany.

- P. Yun, S. Mejri, F. Tricot, M. Abdel Hafiz, R. Boudot, E. De Clercq and S. Guérandel High-stability double modulation CPT cesium compact clock , Proceedings Frequency Standards and Metrology, October 2015, Potsdam, Germany

- Vincent Maurice, Ravinder Chutani, Nicolas Passilly, Rodolphe Boudot, Serge Galliou, M. Abdel Hafiz, Philippe Abbé, Emeric De Clercq and Christophe Gorecki A novel alkali vapor microcell architecture for miniature atomic clocks, Proceedings of the European Frequency Time Forum , 04-07 April 2016, York (UK).

- M. Abdel Hafiz and Rodolphe Boudot A high-performance CPT-based Cs vapor cell atomic clock using push-pull optical pumping, Proceedings of the European Frequency Time Forum , 04-07 April 2016, York (UK).

- M. Abdel Hafiz and Rodolphe Boudot A high-performance CPT-based Cs cell atomic clock, Proceedings of the International Frequency Control Symposium , 09-12 May 2016, New-Orleans, Louisiana (USA).

Résumé :

Ce travail de thèse, financé par le LabeX FIRST-TF et la Région de Franche-Comté, effectué dans le cadre du projet européen MClocks (http://www.inrim.it/mclocks), reporte le développement et la caractérisation métrologique d'une horloge atomique à cellule de césium de haute performance basée sur le phénomène de piégeage cohérent de population (CPT). Cette horloge combine une diode laser DFB accordée sur la raie D$_1$ du césium (894.6 nm), un modulateur électro-optique Mach-Zehnder fibré, un modulateur acousto-optique, un système Michelson, une cellule à vapeur de césium avec gaz tampon et un bloc électronique. L'horloge exploite un schéma de pompage CPT optimisé, nommé push-pull optical pumping (PPOP), permettant la détection de résonances CPT à fort contraste sur la transition d'horloge 0-0. Une caractérisation détaillée des différents éléments de l'horloge est reportée. Dans une première partie de cette étude, l'horloge fut exploitée en mode continu (CW). Dans une seconde étape, fut implémentée une technique d'interrogation pulsée type Ramsey. Dans cette configuration, les atomes interagissent avec une séquence d'impulsions lumineuses CPT séparées par un temps d'évolution libre T$_R$ « dans le noir », conduisant à la détection de franges de Ramsey-CPT. Dans les deux modes de fonctionnement, l'horloge démontre une stabilité relative de fréquence de l'ordre de $2\ 10^{-13}\ \tau^{-1/2}$ jusque 100 s d'intégration, principalement limitée par des effets de puissance laser. L'interaction pulsée permet de réduire significativement la sensibilité de la fréquence d'horloge aux variations de puissance laser, en particulier pour les fortes valeurs de T$_R$. Cette horloge atomique, parmi les meilleures horloges à cellule développées à travers le monde, pourrait trouver des applications pour les systèmes de télécommunications, d'instrumentation, de défense ou navigation par satellite.

Cette thèse reporte aussi une technique originale de stabilisation de fréquence laser par spectroscopie sub-Doppler bi-fréquence en cellule. Une étude expérimentale et théorique, menée en profondeur, fut réalisée pour identifier les phénomènes physiques complexes mis en jeu dans ce type de schéma, mettant en avant la contribution significative d'états noirs CPT et d'effets de pompage optique. La plateforme constituée par l'horloge a été utilisée pour mener des tests de physique plus amont, incluant la caractérisation par spectroscopie CPT d'une cellule de césium avec un revêtement anti-relaxant OTS (octadecyltrichlorosilane) ou la caractérisation de microcellules à vapeur de césium avec gaz tampon développées à FEMTO-ST pour des horloges atomiques miniatures.

Mots-clés : Horloge à cellule de vapeur de césium, piégeage cohérent de population, spectroscopie laser, stabilité relative de fréquence

Abstract:

This thesis work, funded by LabeX FIRST-TF and Région de Franche-Comté and performed in the frame of the MClocks European project (http://www.inrim.it/mclocks), reports the development and metrological characterization of a high-performance Cs vapor cell atomic clock based on coherent population trapping (CPT). This clock combines basically a distributed feedback diode laser tuned on the Cs D$_1$ line (894.6 nm), a pigtailed Mach-Zehnder electro-optic modulator, an acousto-optic modulator, a Michelson system, a cm-scale buffer gas-filled Cs cell and electronics. The clock uses an optimized CPT pumping scheme, named push-pull optical pumping (PPOP), allowing the detection of high-contrast CPT resonances on the 0-0 magnetic-field insensitive clock transition. A detailed characterization of key components of the clock is reported. In a first phase, the clock was operated in the continuous-wave (CW) regime. In a second phase, a Ramsey-like pulsed interrogation technique was implemented. In this configuration, atoms interact with a sequence of optical CPT pulses separated by a free-evolution time T$_R$ "in the dark", conducting to the detection of high-contrast and narrow Ramsey-CPT fringes. In both regimes, the clock demonstrates a short-term fractional frequency stability at the level of $2\ 10^{-13}\ \tau^{-1/2}$ up to 100 s averaging time, mainly limited by laser power effects. The pulsed interaction allows to reduce significantly the clock frequency sensitivity to laser power variations, especially for high values of the free evolution time T$_R$. This CPT clock, ranking among the best microwave vapor cell atomic frequency standards, could find applications in telecommunication, instrumentation, defense or satellite-based navigation systems.

This thesis reports also a novel laser frequency stabilization technique using dual-frequency sub-Doppler spectroscopy in a vapor cell. An in-depth experimental and theoretical investigation was performed to describe underlying physical processes of this setup, highlighting the relevant contribution of CPT states and velocity-selective optical pumping effects. The clock "platform" has also been used to perform using CPT spectroscopy the characterization of a Cs vapor cell coated with octadecyltrichlorosilane (OTS) or original buffer-gas filled Cs vapor micro-fabricated cells developed in FEMTO-ST for CPT-based miniature atomic clocks.

Keywords: Cs vapor cell atomic clock, coherent population trapping, push-pull optical pumping, laser spectroscopy, frequency stability

■ École doctorale SPIM 1 rue Claude Goudimel F - 25030 Besançon cedex
■ tél. +33 (0)3 81 66 66 02 ■ **ed-spim@univ-fcomte.fr** ■ www.ed-spim.univ-fcomte.fr

UFC
UNIVERSITÉ
DE FRANCHE-COMTÉ